UNIVERSITÀ DEGLI STUDI DI UDINE
hic sunt futura

www.uniud.it

Doctor of Philosophy degree in Environmental and Energy Engineering Science

Cycle XXX

Title

"Computational Study of Compounds with Biological Activity and their Interaction with Nano-Materials"

Ph. D. candidate
Daniele Veclani

Supervisor
Prof. Andrea Melchior

Co-supervisor
Prof. Marilena Tolazzi

2018

UNIVERSITÀ DEGLI STUDI DI UDINE
hic sunt futura

www.uniud.it

Doctor of Philosophy degree in Environmental and Energy Engineering Science

Cycle XXX

Title

"Computational Study of Compounds with Biological Activity and their Interaction with Nano-Materials"

Ph. D. candidate
Daniele Veclani

Supervisor
Prof. Andrea Melchior

Co-supervisor
Prof. Marilena Tolazzi

2018

‹‹Just remember what ol' Jack Burton does when the earth quakes,
and the poison arrows fall from the sky, and the pillars of Heaven shake.
Yeah, Jack Burton just looks that big ol' storm right square in the eye
and he says, "Give me your best shot, pal. I can take it."››
cit. Kurt Russell (Jack Burton) from Big Trouble in Little China

Abstract

In the last few decades, computer simulation became a potent tool to study experimental systems such as chemical reactions and adsorption mechanisms in more detail. Every day, developments in computers and computational software are made to increase the computational power and study more complex systems. Nowadays, computational chemistry is used in many different ways, and one of the important fields in which computational chemistry is used is drugs design. In this thesis, computational methods (the quantum mechanics method and molecular dynamics simulations in particular) were used to study the reactivity of two classes of pharmaceutical compounds and their interaction with carbon-based materials; the two classes are platinum-based antitumor drugs (chapter 3) and fluoroquinolones antimicrobials compounds (chapter 4).

The first part of chapter 3 focuses on the hydrolysis reaction of *cis*-[Pt(PMe_3)$_2$(etga)], cis-[Pt(PMe_3)$_2$(3-Hfl)]$^+$ containing ethyl gallate (etga) and 3-Hydroxyflavone(3-Hfl), designed to try to limit the side effects of cisplatin, studied by means of density functional theory (DFT) calculations. The calculations showed that the rate determining step is the first step of the hydrolysis reaction and that the formation of the hydroxo species is observed in both complexes. Moreover, the activation energies are significantly lower than those calculated for cisplatin, with consequent high hydrolysis reaction rate that might make such complexes subject to fast degradation, causing potentially poor pharmacological activity; indeed, the complexes present lower cytotoxic activity compared to cisplatin.

In the second part of chapter 3 the complete mechanism of action (hydrolysis reaction, reaction with DNA bases and reaction with cysteine) of phenanthriplatin, a monofunctional platinum complex, was studied by means of DFT calculations. Moreover, a comparison between phenanthriplatin and cisplatin was made with the aim of understanding why phenanthriplatin presents a higher cytotoxicity activity compared to cisplatin. The hydrolysis reaction showed that phenanthriplatin's activation energy barrier is close to the energy barriers obtained for the first hydrolysis of cisplatin. Unlike cisplatin, phenanthriplatin reacts with both guanine and adenine bases; with the latter, the formation of two products, N7 and N1, occurs, and the reaction rate follows the order N7-guanine > N7-adenine > N1-adenine; moreover, the reaction with guanine is kinetically

favoured in phenanthriplatin in respect to cisplatin. Finally, the reaction between phenanthriplatin and cysteine showed that such reaction is disadvantageous, both kinetically and thermodynamically, in phenanthriplatin in respect to cisplatin. This can explain why phenanthriplatin is more cytotoxic than cisplatin.

In the last part of chapter 3 the non-covalent interaction between graphene prototypes, new candidates as drugs delivery systems, and cisplatin were investigated through MP2 and DFT calculation. Different orientations of cisplatin in respect to the circumcoronene, one parallel and three perpendicular, were taken into account and different DFT functional were tested and compared with the interaction energy obtained from MP2 calculations. The best DFT functional is M62X-D3, which was used to obtain the energy profiles. The parallel orientation presents the highest value of interaction energy in vacuum. The density of states (DOS) analysis showed that when cisplatin is adsorbed with perpendicular orientations a destabilization of the circumcoronene electronic structure is observed. Finally, the introduction of the solvent does not drastically change the interaction energy profiles between cisplatin and circumcoronene. Thus, a favourable adsorption of cisplatin on graphene can be predicted.

As regards the fluoroquinolones (FQs) antimicrobials compounds, in the first part of chapter 4 the relative stability and photochemical behaviour of the different protonation states of ciprofloxacin (CFX) in gas phase and in water was studied by means of molecular dynamics simulations and DFT calculations. This work confirm the predominance of the zwitterionic form in water in respect to the neutral form, thanks to the introduction of a discrete-continuum approach (obtained by placing some water molecules around the protonated groups of the solute); the result was further confirmed through the calculated absorption UV-Vis spectra. Finally, the protonation sequence was confirmed through the comparison with the crystalline structures found in the literature, through the calculation of the relative stability for such species and the calculated absorption UV-Vis spectra.

In the last part of chapter 4 the adsorption of both neutral and zwitterionic forms of CFX to the inner and outer surface of carbon nano-tubes (CNTs) in vacuum and in water was studied through molecular dynamics simulations. The simulation results showed that CFX remains adsorbed to the surface of CNT both in vacuum and in water thanks to π-π interactions. However, a change in CNT-CFX morphology was observed after the solvent was added; CFX molecules tend to form fewer hydrogen bonds between themselves and

more with water, leading to a dispersion of the molecules on the CNT surface. Finally, the adsorption Gibbs free energy were carried out for the adsorbed zCFX and nCFX using the umbrella sampling technique, finding out that adsorption is thermodynamically favoured and CFX molecules seem to interact more strongly with the inner surface than with the outer surface of CNT. Moreover, these values are in good agreement with the data reported in the literature. In conclusion, the use of computational chemistry can help to rationalize the experimental data and to investigate various mechanicistic hypothesis.

Index

List of Figures

Chapter 2 Theory

Chapter 3 Platinum-based antitumor Drugs: Theoretical Study of the mechanism of action and Interaction with Graphene

Chapter 4 Fluoroquinolones: Study of the Chemical Properties and the Adsorption Mechanism on Carbon Nano Tube

Appendix A

List of Tables

Appendix A

Appendix B

Abbreviations

QM	Quantum mechanics calculations
MM	Molecular mechanics calculations
PES	Potential energy surface
E	Energy
V	Potential energy
G	Gibbs free energy
GDISS	Geometry optimization direct inversion of the iterative subspace
HF	Hartree-Fock
RHF	Restricted Hartree-Fock calculations
UHF	Unrestricted Hartree-Fock calculations
SCF	Self Consistent Field procedure
MP	Møller-Plesset perturbation theory calculations
DFT	Density Functional Theory
LDA	Local density approximation
LSDA	Local spin-density approximation
GGA	Generalised gradient approximation
STOs	Slater-type orbitals
GTOs	Gaussian-type orbitals
ECP	Effective Core Potential
ZPVE	Zero-Point vibrational energy
SCRF	Self-consistent reaction field models
PCM	Polarizable Continuum Model
COSMO	Conductor-like Screening Model
FF	Force Field
US FDA	US Food and Drug Administration
NER	Nucleotide excision repair machinery
HMGB	High-mobility group box proteins
HAS	Human serum albumin

GSH	Glutathione
MT	Metallothioneins proteins
SAR	Structures activity relationships
3-Hlf	3-Hydroxyflavone
etga	Ethyl gallate
Que	Quercetin
SDD	Stuttgart– Dresden pseudopotential
Esd	Estimated standard deviations
R	Reagent
RA	Reagent adduct
TS	Transitions states
PA	Product adduct
P	Product
MAE	Mean absolute error index
RMSD	Root-mean-square deviation index
Me-GUA	9-methylguanine
Me-Ade	9-methyladenine
H-bond	Hydrogen bond
GO	Graphene oxide
rGO	Reduced graphene oxide
COM	Centre of mass
BSSE	Basis set superposition error
E_{int}	Interaction energy
DOS	Density of states
FQ	Fluoroquinolones
Topo IV	Topoisomerase IV enzyme
QRDR	Quinolone resistance-determining region
CFX	Ciproflocaxin
LINCS	LINear Constraint Solver
UFF	Universal force field
TD-DFT	Time-dependent formalism
NOR	Norfloxacin

OFL	Ofloxacin
OXY	Oxytetracycline
CNT	Carbon nanotubes
SW-CNT	Single-walled CNT
MW-CNT	Multi-walled CNT
PMF	Potential of mean force
US	Umbrella Sampling technique
G54A7	GROMOS 54A7 force field
ATB	Automated topology bulider
E_{hyd}	Hydration energy
WHAM	Weighted Histogram Analysis Method
RDF	Radial distribution function curves
LJ	Lennard-Jones potential
SDF	Spatial distribution function

Acknowledgements

First of all I want to thank my supervisor, Professor Andrea Melchior, and my co-supervisor, Professor Marilena Tolazzi, without whom nothing would have been possible. I would like to thank them especially for all the help and the advice they provided me, as well as for their patience and the efforts they put into helping me get where I am now.

I am also thankful to the people of the Thermodynamics and Modeling group, past and present, who have all made a contribution to my achievements (Pierluigi Polese, Cristian Grazioli, Sara Isabel Gràcia Lanas, Georgina Faura Muñoz); in particular, I want to thank Ph.D. student Matteo Busato for the computational support he gave me during the last year of my Ph.D. I would also like to thank Professor José Pedro Ceròn Carrasco for having guided me during my experience in Spain at the group of Bioinformatics and High Performance Computing Research Group (Catholic University of Murcia UCAM), for his invaluable advice and for all the help he generously provided me. I would also like to thank Professor Marco Bortoluzzi, who made me discover and appreciate computational chemistry. I also have to give special thanks to Professor Salvatore Daniele who with his advice has guided me throughout my university education.

Finally, I would like to thank the people in my life who are not related to the chemistry world but whose presence has contributed to my work and to getting me where I am today. They all had a positive influence on me during these three years, helping me overcome the obstacles arisen during my Ph.D. I would like to start by thanking my parents for your support. I want to thank my girlfriend Magda who have always given me great advice and have always been there to support me. Many times she made me realize that things were not as bad as I may have thought in the first place. I also want to thank Giulia Zanin for the linguistic support she gave me for writing this thesis. I am also grateful to Massimo Aurelio Ceccato and Alvise Zennaro for the hours spent talking about the NERD world that made these three years less heavy. Finally, I want to thank QDSS channel and the McFit fitness center for keeping me physically and mentally healthy during these three years of PhD. It is thanks to all these people that these three years were, for me, a personal achievement.

Chapter 1

Introduction to Computational Chemistry

Anyone can do calculations nowadays.

Anyone can also operate a scalpel.

That doesn't mean all our medical problems are solved.

Cit. "Karl Irikura"

1.1 Introduction

The use of computers in chemistry can be dated back to the beginning of the 50s, when the first software became available.[1] With the progressing development of theoretical methods and the improvement of computer codes, the interest in employing computational models for solving various chemical problems increased.[2] Recent years have witnessed an increase in the number of people using computational chemistry, facilitated by the development of a computer software that is increasingly easy to use. Indeed, computational chemistry is now very approachable, because calculations can be performed without knowing the underlying principles. As a result, many people do not understand even the most basic concepts involved in a calculation and their work results largely unfocused and remains often unknown.[3]

The term theoretical chemistry could be defined as the mathematical description of chemistry; it is generally used when a mathematical method is sufficiently well developed to be automated for implementation on a computer. It is important to note that the words “exact” and “perfect” do not appear in these definitions. Indeed, almost every aspect of chemistry has been described by qualitative or approximate computational schemes. Therefore, the biggest mistake a computational chemist can make is to assume that any computed number is exact. However, if the researcher understands what can or cannot be predicted, an approximate or qualitative calculation can give useful information.[3]

1.2 Uses of Computational Chemistry

Nowadays, computational chemistry is used in many different ways. For example, one way is to model a molecular system prior to synthesizing a molecule in the laboratory; in fact, computational models are good enough to eliminate most of the possible compounds not suitable for the intended purpose. The information provided is very useful, because synthesizing a single compound could require months of labour and a large quantity of raw materials and generate toxic waste. Computational chemistry is also used to understand a problem more completely. For example, there are some properties of a molecule, such as molecular bonding, absolute and relative (interaction) energies, electronic charge density distributions, dipoles and higher multipole moments, vibrational frequencies, reactivity and other spectroscopic quantities, which are easier to obtain

computationally than by experimental means.[3] Another important field in which computational chemistry is used is drugs design.[4–6] The design of a new drug is an incredibly difficult and frustrating task, because it does not entail a unique scientific technique, but a collaborative process in which all available techniques (experimental and computational) are used to achieve the desired results. The reality is that the use of computers and computational methods now permeates all aspects of drug discovery. In drug discovery campaign, such methods are usually used for three major purposes:

- Filter a large compound into smaller sets of predicted active compounds that can be tested experimentally.
- Guide the optimization of the compounds to increase its affinity or to optimize drug metabolism and pharmacokinetics properties, including absorption, distribution, metabolism, excretion, and the potential for toxicity.
- Design novel compounds, either by "growing" starting molecules one functional group at a time or by piecing fragments together into novel chemotypes.

Moreover, the use of these techniques allows researchers to save both money and time, because many compounds predicted to be inactive can be skipped, while those predicted to be active can be prioritized. This way, the cost and the workload are reduced without compromising lead discovery.[5]

1.3 Outline

The purpose of this thesis is to study, by computational chemistry techniques, the mechanism of action and adsorption of two classes of drugs on carbon-based materials; the two classes are the platinum-based chemotherapeutic compounds and the antimicrobials fluoroquinolones.

Chapter 2 starts by presenting the basics of quantum mechanics simulation and molecular dynamics, the main methods used in this work. It describes the basic theory of both quantum and classical simulation, then goes on to discuss two different problem areas that have been addressed in this thesis. In chapter 3 the results of the investigation of the mechanisms of action and interaction of platinum-based chemotherapeutic compounds on graphene are presented. Chapter 4 discusses the acid-base properties and the

adsorption of fluoroquinolones on carbon nanotubes. Overall, the leading thread of this thesis is the interaction of the above-mentioned drugs with carbon-based surfaces; a brief introduction on carbon-based materials is provided in Chapters 3 and 4.

1.4 References

[1] C. J. Cramer, *Essentials of Computational Chemistry Theories and Models*, John Wiley & Sons Ltd, Chichester, England, **2004**.

[2] F. Jensen, *Introduction to Computational Chemistry*, John Wiley & Sons Ltd, Chichester, England, **2007**.

[3] D. C. Young, *Computational Chemistry: A Pratical Giude for Applying Techniques to Real World Problems*, John Wiley & Sons, Inc., New York, USA, **2001**.

[4] G. Sliwoski, S. Kothiwale, J. Meiler, E. W. J. Lowe, *Pharmacol. Rev.* **2014**, *66*, 334–395.

[5] C. A. Lipinski, F. Lombardo, B. W. Dominy, P. J. Feeney, *Adv. Drug Deliv. Rev.* **2001**, *46*, 3–26.

[6] W. L. Jorgensen, *Science* **2004**, *303*, 1813–1818.

Chapter 2

Theory

The mathematical framework of quantum theory
has passed countless successful tests
and is now universally accepted as a consistent
and accurate description of all atomic phenomena.
Cit "Erwin Schrödinger"

2.1 Modelling a Molecular System

The systems that can be considered in molecular modelling[1–3] include a very wide range of molecules, from small isolated molecules to biological macromolecules (such as proteins and DNA) and solids. The nature as well as the dimension of the studied system guides the type of approach that will be used to study it. The two most common computational approaches are quantum mechanics (QM) and molecular mechanics (MM). The first one is based on an approximate solution of the Schrödinger equations, while the second one is based on a classical description of the atoms (Newton's laws). Both computational approaches provide the total energy for a given atomic configuration. The QM and MM approaches have been used in this thesis with different levels of theory and different algorithms; a short discussion on the most common method will be discussed in this chapter, along with the computational procedure chosen to obtain the best geometrical arrangement (the one with the lowest energy), the reaction pathway, the behaviour of systems as a function of time and the value of various observables useful to rationalize or even predict, experimental data. A description of the computational procedures is also provided in the following chapter.

2.2 Potential Energy Surfaces (PES) and Geometry Optimization

A potential energy surface (PES) is a hypersurface definition of the potential energy (V) of a set of atoms, obtained by varying their relative position.[1,2,4] PES, in addition to the potential energy coordinate, has 3N-3 (N is the number of total atoms) Cartesian coordinates negligence to define the positions of all atoms. Such coordinates can be matched to the geometric parameters of the molecules, such as interatomic distances, angles and dihedral angles, called internal coordinates when the total number of the coordinates is 3N-6. The most important points of a PES are:

- Local minima: correspond to optimal molecular geometries.
- Saddle point: characterized by having a downward concavity along one coordinate, upward concavities for all the other coordinates and slope = 0 in all directions.

Saddle points are the lowest energy barriers in a path between two local minima and correspond to the chemical concept of transition state. An example of PES is reported in Figure 1.

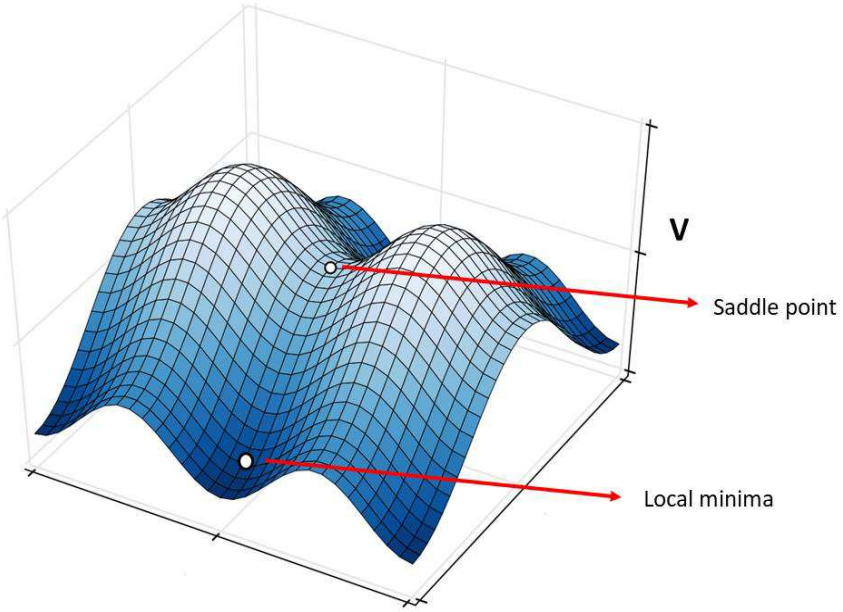

Figure 1 Diagram of potential energy surface (PES).

The calculation of V for a coordinate set $\vec{q}^k$ (q is a vector consisting of all the cartesian or internal coordinates needed to define the positions of the atoms) is called single point calculation; in order to obtain a minimum energy as a function of $\vec{q}^k$ a geometry optimization will be performed. The aim of geometry optimization is to generate the optimal (lowest energy) structure of a molecule from an arbitrary starting state. There are several algorithms to find the minimum of PES[5], for example; Newton or Newton–Raphson method, conjugate gradient method and geometry optimization direct inversion of the iterative subspace (GDIIS).

2.3 Quantum Mechanics Calculations

2.3.1 Introduction to quantum mechanics methods

In 1926, Schrödinger provided a complete mathematical description of a generic molecular system through the known Schrödinger equation[6]:

$$\hat{\mathrm{H}}\,\Psi = E\,\Psi$$

(eq1)

In this equation Ψ is the wave-function (eigen-function for a given Hamiltonian), which describes the system, $\hat{\mathrm{H}}$ is the Hamiltonian operator and E is the energy of the system. Moreover, Ψ takes as variables the positions of electrons and nuclei in the system:

$$\hat{\mathrm{H}}\,\Psi_i\left(\vec{x}_1,\dots,\vec{x}_N,\vec{R}_1,\dots,\vec{R}_M\right) = E\,\Psi_i\left(\vec{x}_1,\dots,\vec{x}_N,\vec{R}_1,\dots,\vec{R}_M\right)$$

(eq2)

where $\vec{x}_N$ describes the positions of the electrons, N is the number of the electron, $\vec{R}_M$ describes the positions of the nuclei and M is the number of the nuclei. The system's properties can be deduced from the knowledge of Ψ, which must be chosen to be orthogonal and normalised (orthonormal) over the whole space:

$$\langle\Psi_i|\Psi_J\rangle = \delta_{ij}$$

(eq3)

where δ_{ij} is the Kronecker symbol and takes value of 1 when i = j, while when i ≠ j it takes value of 0. Considering a generic molecule $\widehat{H}$ is composed of 5 contributions:

$$H = T_e + T_n + V_{ne} + V_{ee} + V_{nn}$$

(eq4)

where T_e and T_n are the kinetic energies for the electrons and the nuclei respectively; V_{ne} represents the attractive potential between electrons and nuclei, V_{ee} and V_{nn} the inter-electronic and inter-nuclear repulsion potentials. Such term is represented with the following equation:

$$\widehat{T_e} = -\frac{1}{2}\sum_{i=1}^{N}\nabla_i^2\ ; \qquad \widehat{T_n} = -\frac{1}{2}\sum_{A=1}^{M}\frac{1}{M_A}\nabla_A^2$$

$$\widehat{V_{ne}} = -\sum_{i=1}^{N}\sum_{A=1}^{M}\frac{Z_A}{r_{iA}}$$

$$\widehat{V_{ee}} = \sum_{i=1}^{N}\sum_{j>i}^{N}\frac{1}{r_{ij}}\,; \qquad \widehat{V_{nn}} = \sum_{A=1}^{M}\sum_{B>A}^{M}\frac{Z_A Z_B}{R_{AB}}$$

(eq5)

where the index i and j denote the N electrons, A and B denote the M nuclei, M_A is the mass of the nucleus, Z_A and Z_b are the atomic numbers of the nuclei, r_{iA} is the distance between the i electron and the A nucleus, r_{ij} is the distance between electrons and R_{AB} is the distance between nuclei. Then Hamiltonian will be:

$$\widehat{H} = -\frac{1}{2}\sum_{i=1}^{N}\nabla_i^2 \; -\frac{1}{2}\sum_{A=1}^{M}\frac{1}{M_A}\nabla_A^2 \; -\sum_{i=1}^{N}\sum_{A=1}^{M}\frac{Z_A}{r_{iA}} + \sum_{i=1}^{N}\sum_{j>i}^{N}\frac{1}{r_{ij}} + \sum_{A=1}^{M}\sum_{B>A}^{M}\frac{Z_A Z_b}{R_{AB}}$$

(eq6)

2.3.2 Born-Oppenheimer approximation

The Schrödinger equation described above is so complex that it can be unsolvable even for very simple systems such as the H_2 molecule. In particular, all attractive and repulsive relationships between the particles represent an enormous obstacle, since the particles' motions are not independent. This non-independence is often referred to as correlation. A general approximation is given by the approximation of Born-Oppenheimer.[7] As previously reported, the wave-functions are functions of the positions of both the nuclei and the electrons of the system. The approximation is based on the fact that a nucleus is much heavier than an electron (approximately 1800 times more) and its movements, compared to the electrons', are negligible. Therefore, the nuclei can be considered to be frozen, with their kinetic energy set to zero, but they still contribute to the potential energy of the system. Consequently, Ψ depends only on T_e, V_{ne} and V_{ee}, so the Hamiltonian becomes:

$$\widehat{H} = -\frac{1}{2}\sum_{i=1}^{N}\nabla_i^2 \; -\sum_{i=1}^{N}\sum_{A=1}^{M}\frac{Z_A}{r_{iA}} + \sum_{i=1}^{N}\sum_{j>i}^{N}\frac{1}{r_{ij}} + V_{nn}$$

(eq7)

where V_{nn} represents the nucleus-nucleus repulsion and is a constant. Moreover, eq.7 is factorisable:

$$\widehat{H_{el}} = \sum_i \left(-\frac{1}{2} \nabla_i^2 - \sum_A \frac{Z_A}{r_{iA}} + \sum_{j>i} \frac{1}{r_{ij}} \right)$$

(eq8)

We can observe that the wave-function now depends only on the electronic coordinates (Ψ_{el}); this equation is called electronic Schrödinger equation and returns the electronic energy (E_{el}):

$$\widehat{H_{el}}\, \Psi_{el}\left(\vec{x}_1, \vec{x}_2 \ldots, \vec{x}_i, \vec{x}_j, \ldots, \vec{x}_N\right) = E_{el}\, \Psi_{el}\left(\vec{x}_1, \vec{x}_2 \ldots, \vec{x}_i, \vec{x}_j, \ldots, \vec{x}_N\right)$$

(eq9)

Moreover, the electrons are also described by their spin quantum number, which can assume two values, −1/2 or 1/2, defined by the alignment of the spin with respect to an arbitrary axis. The two types of spin are called α and β and are orthonormalised:

$$\langle \alpha | \alpha \rangle = \langle \beta | \beta \rangle = 1$$
$$\langle \alpha | \beta \rangle = \langle \beta | \alpha \rangle = 0$$

Both a spatial and a spin component describe the wave-function:

$$\Psi(\vec{x}) = \psi(\vec{r})\sigma \qquad \sigma = \alpha \; or \; \beta$$

(eq10)

2.3.3 Slater determinant

The antisymmetry principle: Ψ itself is not observable, but the expression:

$$|\Psi(\vec{x}_1, \vec{x}_2 \ldots, \vec{x}_N)|^2 \, d\vec{x}_1 d\vec{x}_2 \ldots d\vec{x}_N$$

(eq11)

$d\vec{x}_N$ denotes a small volume, which represents the probability of finding an electron at a given point in space. Since electrons are indistinguishable, the exchange of two electrons does not change the probability but leads to a change of sign of the wave-function; Ψ is antisymmetric with respect to electron change. Such behaviour represents the quantum-mechanical generalisation of the Pauli's exclusion principle (two or more fermions,

particles with spin = ½ such as electrons, cannot occupy the same state within a quantum system simultaneously).

The exact wavefunction is unknown, therefore a trial wave-function that obeys the antisymmetry principle is necessary; in order to generate the trial wave-function, the N-electron wave-function is expressed as an antisymmetric product of N one-electron wave-functions $\chi_i(\vec{x}_i)$ ($\chi_i = \Psi^*\sigma$). This product is indicated with ϕ_{SD}, called Slater determinant,[8] and presents this form:

$$\Phi_{SD} = \frac{1}{\sqrt{N!}} \begin{vmatrix} \chi_1(\vec{x}_1) & \chi_2(\vec{x}_1) & \dots & \chi_N(\vec{x}_1) \\ \chi_1(\vec{x}_2) & \chi_2(\vec{x}_2) & \dots & \chi_N(\vec{x}_2) \\ \vdots & \vdots & \ddots & \vdots \\ \chi_1(\vec{x}_N) & \chi_2(\vec{x}_N) & \dots & \chi_N(\vec{x}_N) \end{vmatrix}$$

(eq12)

The columns are single electron wave-functions (orbitals), while the rows are the electron indices.

2.3.4 Variational method

The equation eq9 is solved with the Rayleigh-Ritz variational method or, more simply, the variational method. The variational theorem states that the value calculated for the total energy of a trial wave-function can only be greater than or equal to the ground-state energy, E_0:

$$E = \langle \Psi | H | \Psi \rangle \geq E_0$$

(eq13)

Such method provides a criterion for establishing the "best" wave-function, subject to a given set of constants. The two methods based on the variational method are the Hartree-Fock method and Density functional theory; both will be described in this chapter.

2.3.5 Hartree-Fock theory (HF)

The approximation of Born-Oppenheimer[7] greatly simplifies the Schrödinger equation[6]. However, the equation still contains the term regarding inter-electronic repulsion, the calculation of which is difficult, being the motion of various electrons correlated to each

other. The Hartree-Fock (HF) method[1,2] is one of the most widely used computational approaches for the determination of the wave-function within the molecular orbital model. In the HF method, the Hamiltonian can be divided into two parts:

- A core Hamiltonian $H^c(i)$ describing the kinetic energy and the electron-nuclei attraction potential.
- A part that describe the electron-electron repulsion.

$$H = \sum_i \left[H^c(i) + \sum_{j>i} \frac{1}{r_{ij}} \right] \quad H^c(i) = -\frac{1}{2} \nabla^2 - \sum_A \frac{Z_A}{r_{Ai}}$$

(eq14)

The core Hamiltonian can be solved exactly, whereas the electron-electron repulsion part can only be treated in an average way, in which each electron is considered to be moving independently from the others in an average field created by the other electrons. The application of the variational method to a single Slater determinant allows the calculation of the lowest possible energy through the optimisation of the orbitals χ_i. The resulting equations are called Hartree-Fock equations; their solution determines the best spin orbitals for which E will reach its lowest value.

$$\hat{f}\chi_i = \varepsilon_i \chi_i$$

(eq15)

where χ_i is an eigen-function of the operator $\hat{f}$, called Fock operator and ε_i is the corresponding energy and represents the orbital energy. The negative of the eigen-value, $-\varepsilon i$, corresponds to the ionisation potential according to Koopmans' theorem. The Fock operator has the following form:

$$\hat{f} = -\frac{1}{2} \nabla_i^2 - \sum_A \frac{Z_A}{r_{ij}} + V_{HF}(i)$$

(eq16)

V_{HF} is the Hartree-Fock potential and represents the average repulsive potential experienced by each electron due to the other N-1 electrons. V_{HF} has replaced the $1/r_{ij}$ operator, which was too complex to be solved. Summing up the electronic repulsions of

different electrons in an average potential, the equation is now solvable. V_{HF} consists of two terms:

$$V_{HF} = \sum_j \left(\hat{J}_j(\overrightarrow{x_1}) - \hat{K}_j(\overrightarrow{x_1}) \right)$$

(eq17)

$$\hat{J}_j(\overrightarrow{x_1}) = \int |\chi_j(\overrightarrow{x_2})|^2 \frac{1}{r_{12}} \, d\overrightarrow{x_2}$$

(eq18)

$$\hat{K}_j(\overrightarrow{x_1})\chi_i(\overrightarrow{x_1}) = \int \chi_j{}^*(\overrightarrow{x_2}) \frac{1}{r_{12}} \chi_i(\overrightarrow{x_2}) d\overrightarrow{x_2} \, \chi_j(\overrightarrow{x_1})$$

(eq19)

The operator $\hat{J}_j$ represents the potential experienced by an electron at position $\overrightarrow{x_i}$ due to the average charge distribution of another electron in the spin orbital χ_i. The operator $\hat{K}_j$ leads to an exchange of the variables in the two spin orbitals introducing the exchange potential. If two electrons have the same spin state, such energy reduces the electrostatic repulsion between them in different molecular orbitals (see Figure 2). The contribution due to the exchange energy is correctly calculated by the HF method.

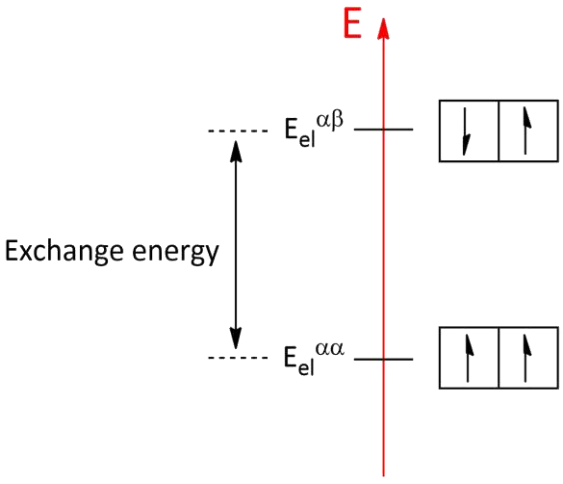

Figure 2 Exchange energy contribution.

Finally, two methods can be used to solve the HF equation depending on the system. If the system contains an equal number of paired electrons it is solved using the RHF (Restricted Hartree-Fock) formalism. If the system contains an odd number of electrons

or an equal number, but with some unpaired electrons, the UHF (Unrestricted Hartree-Fock) formalism can be used. In the RHF method, the equations of Roothan-Hall[9,10] are used to resolve the equation, whereas in the case of UHF the equation is resolved using the Berthier-Pople-Nesbert equations[11,12].

Moreover, the solution of the Hartree-Fock equations, even in RHF formulation, is not trivial, being the Fock operator a function of the molecular orbitals themselves, corresponding to the solutions of the eigenvalues equations. The algorithm used to solve the Roothaan-Hall equations[9,10] is an iterative approach (Figure 3) called Self Consistent Field (SCF) procedure[13]. According to this algorithm, an initial guess for the Fock matrix is built using the molecular orbitals obtained at a lower level of theory (for instance Extended Huckel or semiempirical methods, not discussed in this thesis). Then, the Roothaan-Hall equations[9,10] are solved to give atomic coefficients for each orbital and the relative energies and, consequently, the total energy. The procedure is repeated using the new coefficients to build a new Fock matrix and a new value of energy is obtained. The new total energy value is compared to the previous one. The procedure stops when this energy difference is smaller than a chosen value.

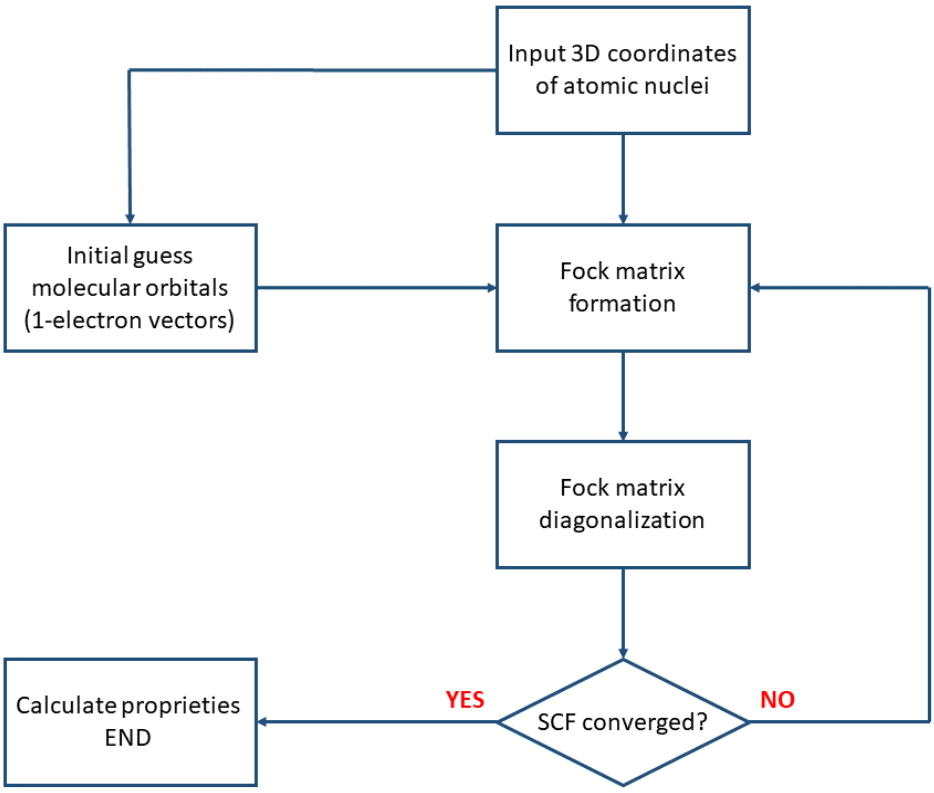

Figure 3 Self Consistent Field (SCF) procedure.

2.3.6 Correlation energy

The main problem of the HF method is that the total energy obtained is always higher than the real energy. Indeed, in the HF method the electrons are considered to move in an average electronic field, so the correlated motion of each electron with the others is omitted. The difference between the real energy and the HF energy is designated as the correlation energy:

$$E_{correlation} = E_{tot} - E_{HF}$$

(eq20)

Correlation energy, in many cases, is approximately 1% of the total energy of the system. However, this small amount of the total energy could have a large influence on the properties of the calculated system. The usual method used to introduce the correlation takes into account the excitation of one or more electrons from one or more occupied orbitals to one or more virtual orbitals higher in energy (see Figure 4).

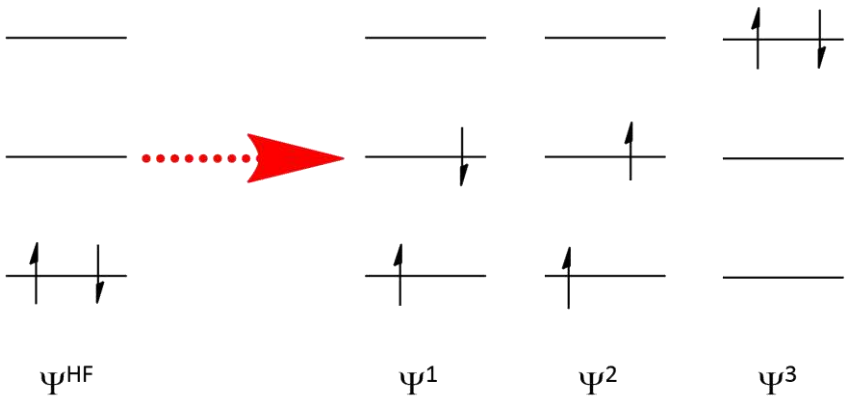

Figure 4 Possible electronic configuration derived from Ψ^{HF}.

Each state is described by a Slater determinant, and the combination of them gives the new trial function, which should be closer to the real system than the original determinant.

$$\Psi = c_i \Phi_{HF} + \sum_{i=1} c_i \Phi_i$$

(eq21)

where the sum is over all the possible excited states and c_i is the coefficient defining the contribution of each exited state to the wave-function.

2.3.7 Møller-Plesset perturbation theory (MP)

Møller-Plesset perturbation theory[14] (MP) is one of the most popular quantum chemistry post-Hartree-Fock *ab*-initio method. Rayleigh-Schrödinger perturbation theory (RS-PT) is used to improve the HF energy. The acronyms MP2, MP3, MP4 and so on are used to denote a truncation of the perturbation series up to second, third, fourth order, respectively. The MP2 method, despite being more computationally expensive than HF, is often used to treat systems where electronic correlation effects play a key role. For instance, weak interactions like dispersion (London) forces or π-stacking interactions between aromatic compounds can be properly described at MP2 level.

2.3.8 Density Functional Theory (DFT)

Unlike the HF theory, density functional theory (DFT) is based on electron density, ρ, rather than on wave-functions. The electronic density can be expressed as a function of the molecular orbital by summing the molecular orbital squares.

$$\rho = \sum_i |\Psi_i|^2$$

(eq22)

The integration of ρ over all space gives the total number of electrons N:

$$N = \int \rho(\vec{r}) d\vec{r}$$

(eq23)

The use of electron density associated with the correct Hamiltonian operator allows a complete description of the energy of the system.

In 1964 Hohenberg and Kohn[15] postulated two fundamental theorems, which today represent the heart of the DFT method. The first theorem states that the external potential $V_{ext}(\vec{r})$ applied on the system is defined as a unique functional of the electronic density, ρ(r). V_{ext} represents the attraction to the nuclei given by the usual expression. In turn, V_{ext} fixes $\widehat{H}$, which is therefore a unique functional of $\rho(\vec{r})$.

$$\rho_0 \rightarrow \{N, Z, R\} \rightarrow V_{ext} \rightarrow \hat{H} \rightarrow \Psi_0 \rightarrow E_0$$

(eq24)

where N is the number of electrons, R is the electron-nucleus distance, Z is the nuclear charge; the "$_0$" index represents the system in its ground state and, consequently, the energy of the system in this state is written as:

$$E_0 = T[\rho_0] + E_{ee}[\rho_0] + E_{Ne}[\rho_0]$$

(eq25)

The T[ρ] and E_{ee}[ρ] parts of the equation are independent from the variables N, R and Z, while E_{Ne} depends on them. Equation 25 can be re-written as following:

$$E_0[\rho_0] = T[\rho_0] + E_{ee}[\rho_0] + \int \rho_0(\vec{r})\, V_{Ne} d(\vec{r})$$

(eq26)

The first part (T[ρ_0] + Eee[ρ_0]) is universally valid, while the second part (the part concerning the integral) depends on the system. This first part can be embedded in a new quantity, called Hohenberg-Kohn functional:

$$F_{HK}[\rho] = T[\rho_0] + E_{ee}[\rho_0]$$

(eq27)

The knowledge of the form of the F_{HK} functional allows the calculation of E_0. However, the explicit forms of the two terms that compose this functional are unknown. The E_{ee} term can be divided in two terms: a Coulomb part, J[ρ] and a term containing all the non-classical contributions to the electron-electron interaction, E_{ncl}[ρ].

The second Hohenberg-Kohn theorem simply consists in the variational theory applied to the electronic density. When an approximate electronic density $\tilde{\rho}(\vec{r})$ associated with an external potential V_{ext}, is used, the resulting energy will always be greater than or equal to the exact ground state energy:

$$E[\tilde{\rho}] = T[\tilde{\rho}] + E_{ee}[\tilde{\rho}] + E_{Ne}[\tilde{\rho}] \geq E_{exact}$$

(eq28)

As reported above, the Hohenberg-Kohn theorems are the heart of the modern DFT. Despite being extremely powerful, the Hohenberg-Kohn theorems do not offer a way of

computing the ground-state density of a system in practice. The success of modern DFT methods derives from the suggestion made by Kohn and Sham in 1965 that most of the problems are connected with the way the kinetic energy is described. The solution consisted in introducing the idea of a fictitious system built from a set of orbitals (one electron functions), where the electrons are non-interacting, so each electron is submitted to an average repulsion field coming from the other electrons. The total energy is divided as follows:

$$E[\rho] = T_s[\rho] + \int \left[\widehat{V_{ext}}(r) + \hat{J}(r)\right]\rho(r)dr + E_{XC}[\rho]$$

(eq29)

$T_S[\rho]$ corresponds to the electron kinetic energy for the hypothetical system; ρ is equivalent to the real system but refers to non-interacting electrons. $\hat{J}(r)$ represents the classical Coulomb interaction between electrons and $\widehat{V_{ext}}$. This last operator presents this form:

$$\hat{J}(r) = \int \frac{\rho(r)}{|r - r'|} dr'$$

(eq30)

$$\widehat{V_{ext}} = \sum_A \frac{Z_A}{|R_A - r|}$$

(eq31)

where r and r' are the coordinates of the two electrons. Kinetic energy can be expressed in terms of a one-electron function:

$$T_s[\rho] = -\frac{1}{2}\sum_{i=1}^{N} \langle \varphi_i | \nabla^2 | \varphi_i \rangle$$

(eq32)

Finally, E_{XC} is a term which encompasses all the contributions to the energy not accounted for in the previous terms, such as electron exchange, correlation energy and correction for the self-interaction included in the Coulomb term, as well as the portion of the kinetic

energy which corresponds to the differences between the non-interacting and the real system.

At this point, a new Hamiltonian can be obtained by taking into account only the non-interacting system:

$$\widehat{H_s} = -\frac{1}{2}\sum_i^N \nabla_i^2 + \sum_i^N V_{s(\vec{r_i})}$$

(eq33)

One-electron functions are reintroduced in DFT in the form of Kohn-Sham orbitals φi, determined by:

$$\widehat{f^{KS}}\varphi_i = \varepsilon_i\varphi_i \quad where \quad \widehat{f^{KS}} = -\frac{1}{2}\nabla^2 + V_s(\vec{r})$$

(eq34)

$\widehat{f^{KS}}$, known as the Kohn-Sham operator, is a one-electron operator, while φ_i is the Kohn-Sham orbital. $V_s(\vec{r})$ describes the effective potential of the non-interacting reference system. The non-interacting system is related to the real system by choosing an effective potential V_S so that:

$$\rho_s(\vec{r}) = \sum_i^N |\varphi_i(\vec{r})|^2 = \rho_0(\vec{r})$$

(eq35)

Returning to the original system:

$$E_{DFT}[\rho] = T[\rho] + E_{Ne}[\rho] + J[\rho] + E_{XC}[\rho]$$

(eq36)

where the E_{XC} has the following form:

$$E_{XC}[\rho] = (T[\rho] - T_s[\rho]) + (E_{ee}[\rho] - J[\rho]) = T_c[\rho] + E_{ncl}[\rho]$$

(eq37)

Now the computation of the major part of the kinetic energy is possible. The Hohenberg-Kohn functional then becomes:

$$F[\rho(\vec{r})] = T_s[\rho(\vec{r})] + J[\rho(\vec{r})] + E_{XC}[\rho(\vec{r})]$$

(eq38)

The E_{XC} term contains both the residual kinetic energy and the repulsion terms. As mentioned above, E_{XC} is an unknown term of the equation that can be obtained only if approximated. In the Functionals session (2.2.10) the different approximation methods used to model the functional will be described. Finally, the resolution of eigenvalues equations based on Kohn-Sham operators, such as the equations underlying the HF method, require an interactive method of SCF type (see Figure 3).[16]

2.3.9 Functionals

Finding effective expressions for the functional $E_{xc}[\rho]$ is one of the crucial issues of DFT methods, and the development of new functionals is an ongoing and active area of research. As reported above, the $E_{XC}[\rho]$ functional contains the non-classical contributions to the potential energy due to the electron-electron interaction and the difference between the kinetic energy of the real system and the kinetic energy related to the non-interacting system. The functionals described here represent different approximations to this exchange-correlation functional.

2.3.9.1 Local Density Approximation (LDA)

The local density approximation[17] (LDA) is one of the first methods used to calculate E_{XC}; it is defined using the electronic density of a uniform electron gas. However, the constant value of the electronic density does not reflect the rapid variation of densities in a molecule. Although LDA is a rough approximation, it is the only system through which the density is defined, by $\rho = N/V$ (N represents the number of electrons and V represents the volume of the gas); the form of the exchange and correlation energy functionals are known either exactly or with a very high accuracy. In systems including spin polarization (open-shell systems) the electronic density ρ is replaced by the spin electronic densities ρα and ρβ, so that $\rho = \rho\alpha + \rho\beta$; in this case, the approximation is called local spin-density approximation (LSDA). One of the most famous LDA functional is VWN, developed by Vosko, Wilk and Nusair[17], based on high-level quantum Monte Carlo calculations for

uniform electron gases. The use of LDA functionalities provides more accurate results than the HF method for determining molecular properties such as structures, vibration frequencies, charge moments, elastic modules. However, it shows some defects in the case of energy details such as bond energies and energy barriers in chemical reactions, which are poorly characterised by using this type of functional.

2.3.9.2 Generalised Gradient Approximation (GGA)

The LDA approximation describes the energies rather badly, so a new type of functional, the generalised gradient approximation (GGA)[17] has been introduced. These functionals include the gradient of the electron density, ∇ρ, which better describes the non-homogeneity of electron density.

The GGA is usually divided into two terms: one regarding exchange energy and the other one related to correlation energy. The two terms can be solved individually.

$$E_{XC}^{GGA} = E_{X}^{GGA} + E_{c}^{GGA}$$

(eq39)

A list of the most efficient GGA functionals commonly used in computational chemistry is provided below:

- B is an exchange functional developed by Becke.[18] It is a gradient correction to the LSDA exchange energy. It includes a single parameter fitted on known atomic data from the rare gas atoms.
- P86 is a correlation functional developed by Perdew.[19] It is a popular gradient correction to LSDA, which includes one empirical parameter fitted for the neon atom.
- PW91 is a modification of the P86 functional developed by Perdew, Wang and Burke.[20,21]
- PBE is an exchange-correlation functional developed by Perdew, Burke and Ernzerhof.[22]
- LYP is a correlation functional developed by Lee, Yang and Parr.[24,25] It is the most extensively used GGA correlation functional. It contains four empirical parameters fitted to the helium atom.

Usually, a combination of exchange and correlation function is created to try to fully describe the systems. Some of the most common combinations are: BLYP, BP86 and BPW91.

$\nabla^2\rho$, the laplacian of the electron density or the local kinetic energy density, could be used to achieve a better approximation of E_C and E_x. The approach is called meta-GGA and is an expansion of the normal GGA.

2.3.9.3 Hybrid functionals

The problem with LDA and GGA approaches consist in the lack of a description of the exchange part, due to a problem of electronic self-interaction. However, the exchange part is defined exactly in HF. Therefore, an alternative approach would be to use a mix of DFT and HF to describe the exchange energy, although this type of approach gives poor results (worse than GGA). The final solution to this problem is the use of a combination of HF, GGA and LSDA functionals to describe the exact exchange and correlation terms; such approach is known as hybrid functional. The main element of these functionals come from GGA functionals, so they are often called GGA hybrid functionals. A list of the most used hybrid functionals is reported below:

- B3 contains exact exchange and by Becke.[26] It is a combination of LSDA and GGA functionals.
- PBE0, also called PBE1PBE, was developed by Adamo and Barone.[27] It is a combination of 75% of PBE GGA exchange functional and 25% of HF exchange functional.
- B97 and B98 were first developed by Becke (B97),[28] then modified by Becke and Schmider (B98).[29]

A famous example of exchange and correlation combination is B3LYP, one of the more often used hybrid functionals.[29] The B3LYP functional is a mix between LDA and GGA functionals resulted from DFT and HF methods. In B3LYP scheme, Perdew-Wang gradient-corrected correlation energy[21,23] is replaced by Lee-Yang-Parr correlation energy. B3LYP exchange-correlation energy functional is described with:

$$E_{XC} = E_X^{LSDA}(1 - a_0) + a_0 E_X^{exact} + a_X \Delta E_X^{B88} + E_C^{LSDA} + a_C \Delta E_C^{LYP}$$

(eq40)

in which the local spin-density functional of Vosko, Wilk, and Nusair[30] is used for E_X^{LSDA} and E_C^{LSDA} . E_X^{exact} is the exact nonlocal HF exchange energy. ΔE_X^{B88} and ΔE_C^{LYP} are Becke's[26] and Lee-Yang-Parr's gradient corrections[24,25] for local exchange and correlation energies respectively. The weight coefficients for gradient-corrected correlation energy, local exchange energy, and the exact HF exchange terms were determined by a linear least-square fitting of the thermochemical properties of some atoms and molecules to the experiments.

Another important family of hybrid functionals is the Minnesota family (M), developed by Zhao and Truhlar, in particular the M06 family.[31,32] Specifically, M06 functional is based on LSDA components, GGA functional PBE and MGGA functional VSXC. The percentage of HF component for exchange energy is 27% in M06, 54% in M06-2X, 100% in M06-HF and 0% in M06-L. Moreover, M06 is a functional with good accuracy "across-the-board" for transition metals, main group thermochemistry, medium-range correlation energy and barrier heights. M06-2X has an excellent performance for main group chemistry, predicts accurate valence and Rydberg electronic excitation energies and it is an excellent functional for aromatic-aromatic stacking interactions. M06-L is not as accurate as M06 for barrier heights but it is the most accurate functional for transition metals and the only local functional with better across-the-board average performance than B3LYP. M06-HF has good performance for valence, Rydberg, and charge transfer excited states with minimal sacrifice of ground-state accuracy.

2.3.10 Basis sets

The simplest way to represent a molecular orbital (Ψ_i) is by a linear combination of atomic orbitals (LCAO). The mathematical expression for atomic orbitals (ϕ) and the dependence of ϕ at the distance r from the nucleus is:

$$\Phi \propto e^{-r}$$

(eq41)

The mathematical expression for the combination of atomic orbitals to obtain a molecular orbital is:

$$\Psi_i = \sum_m a_m \phi_m$$

(eq42)

The a_m coefficients have a decisive role in the calculation of the electronic structure of a system; in fact, during the SCF process; the a_m are varied at each cycle by generating a new molecular orbital.

Basis functions are used to create atomic orbitals (AO) or molecular orbitals (MO). These basis functions can be classified into two main types:

- Slater-type orbitals (STOs) have the exponential dependence of $e^{-\zeta r}$ and are very close in their mathematical expression to the real AO:

$$\eta^{STO} = N\, r^{n-1} e^{\zeta r} Y_{lm}(\Theta, \phi)$$

(eq43)

  where N is a factor of normalisation, ζ is the exponent, r, Θ and ϕ are spherical coordinates and Y_{lm} is the angular momentum part (function describing the "shape"). Finally, n, l and m are the classical quantum numbers.

- the Gaussian-type orbitals (GTOs) have the exponential dependence $e^{-\alpha r^2}$:

$$\eta^{GTO} = N\, x^l y^m z^n e^{-\alpha r^2}$$

(eq44)

  where x, y and z are Cartesian coordinates and other symbols have the same meaning as in STO.

STOs appropriately describe the behaviour of atomic hydrogen orbital, because they exhibit a cusp at r = 0 and a good exponential decay. On the contrary, GTOs do not show a cusp at r = 0 and decrease too rapidly to obtain large values of r. However, STOs are computationally more expensive than GTOs, because the product of two GTOs centred on two different atoms is a third one situated between them, which cannot be obtained with STOs. A number of GTOs can be combined to approximate a STO, a procedure that often proves to be more efficient than using the STO itself.

The precision of a basic set (and, therefore, its degree of complexity) is defined by the number of contracted functions (CGFs) used to represent each atomic orbital. For example, the STO-3G basis set (where G indicates a combination of contracted Gaussian

functions) is formed by a linear combination of three CGFs for each basis function, so as to resemble an STO. A better description of the system can be provided by using two or more functions to describe each type of orbital; triple-zeta and quadruple-zeta basis sets are usually characterized by a good precision.

Valence electrons are more involved in the formation of chemical bonds, so a flexible description of such electrons is more useful than one of the core electrons. Basis sets where the core and valence orbitals are treated differently are called split valence basis sets. One of the most used split valence basis set is the 6-311G basis set. The nomenclature of this type of basis set (*A*-*BCD*G) is provided below:

- *A* represents the number (six in this case) of primitives GTOs used to describe one single contracted Gaussian function of the core.
- *B*, *C* and *D* represent the number of primitives GTOs describing the valence orbitals. In this case, the basis set is composed of three functions, one containing three primitives and the others containing only one.

In addition, polarization and/or diffused functions can be added for greater accuracy of the basis set. Polarization is caused by to the deformation of the electronic cloud around each atom when atoms form a bond. The effect is achieved when functions with higher angular momentum are added to the basis set. Usually, a *p* polarisation function can be added to H atoms, a *d* function to a base set containing *p* valence orbital, and an *f* functions to d-valence orbitals. For example, a 6-311G basis set that implement *p* and *d* polarisation functions became 6-311G(d,p). Diffusion functions describe the part of atomic orbitals distant from the nuclei and can have a very important role when considering, for example, anions or diffuse electronic clouds in second or third row transition metals. The function is represented by a "+", thus a basis set implementing it became 6-311+G or 6-311++G. Moreover, the inner core of transition metals is very large, therefore the number of basic functions used to describe it would be very high. However, the problem can be solved by replacing the core basis function with an Effective Core Potential (ECP). ECPs are functions that represent electrostatic effects due to the electronic cloud of core orbits. Besides reducing the computational demand, the use of such functions, may also introduce some relativistic effects on the studied system, because the functions are generated from relativistic atomic calculations.

2.3.11 Molecular vibrations

The vibrational states[4] of a molecule are experimentally observed by means of IR (Infra-Red) and Raman spectroscopy and give precious information about the molecular structure and the environment.

However, assigning any observed peak to a defined molecular motion is often difficult. The calculation of vibrational frequencies can be of great help in peak assignment and also in the calculation of some important thermodynamic parameters (molecular enthalpy, entropy, and free energy). The simplest description of a vibration is a harmonic oscillator:

$$V_{harm} = k(x - x_0)^2 \qquad \text{(eq45)}$$

where V_{harm} is the potential energy, and x_0 the equilibrium position. Better results can be achieved by using a more sophisticated potential, such as the Morse functional form.

Vibrational frequencies and vibrational energy levels for a molecular system can be directly obtained from the Hessian matrix, which can be computed either analytically or numerically by means of a finite difference procedure applied to analytical first derivatives. As seen above, a geometric optimization calculation leads to a minimum energy value. However, the system can never reach such energy value because it always maintains a vibrational motion.

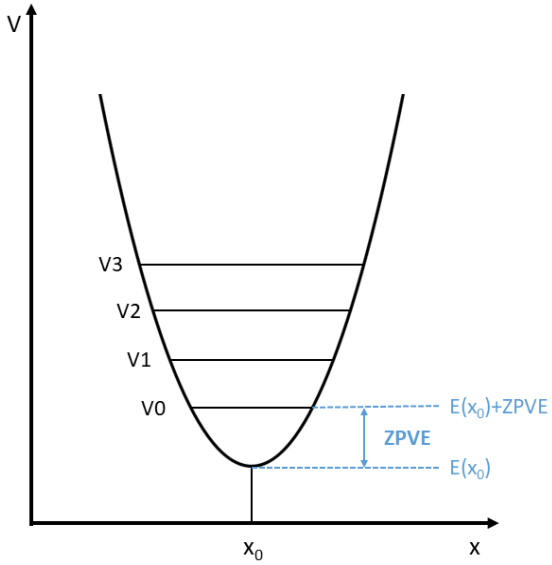

Figure 5 Schematic representation of a harmonic potential energy function and first vibrational levels. The Zero Point Energy (ZPE) is indicated.

A more accurate value can be obtained through the evaluation of the energy associated with the lowest vibrational level (Zero-Point vibrational energy or ZPVE, see Figure 5), which is then summed to the potential energy to obtain. This is of particular importance when comparing the energy of different critical points of the surface (different conformers or in the investigation of a chemical reaction).

2.3.12 Implicit solvation

Most of the chemical processes take place in liquid media, so the properties of the solvent are often considered in computational studies in order to avoid unrealistic results. However, an explicit approach where a large number of solvent molecules is introduced around the solute makes the calculations computationally impossible. Therefore, some implicit, continuum treatment is typically used. A large number of implicit solvation models have been developed,[33] and their common feature is solute placed in a cavity in an otherwise continuous and polarizable medium with a dielectric constant; the solvation energy is given by:

$$\Delta G_{sol} = \Delta G_{cav} + \Delta G_{disp} + \Delta G_{el}$$

(eq46)

where ΔG_{cav} is the energetic penalty for creating the solvent cavity around the solute, the shape of which can be determined in several ways,[33] ΔG_{disp} is an energy contribution due to the dispersion interaction between solvent and solute and ΔG_{el} is the variation of free energy associated with electrostatic interactions between solute and solvent. The two last terms in eq46 are typically stabilizing, due to simulated weak interactions and the solvent's polarization aligning with the solute's dipole moment. Normally, the non-polar terms are separated from the electrostatic term, whose contribution to total energy is found through modified Hamiltonians:

$$\hat{H} = \hat{H}_0 + \phi(\vec{r})$$

(eq47)

$\phi(\vec{r})$ is the electrostatic potential due to the polarization solvent and can be found by solving the Poisson equation:[2]

$$\nabla[\varepsilon(\vec{r})\nabla\phi(\vec{r})] = -4\pi\rho(\vec{r})$$

(eq48)

where $\rho(\vec{r})$ is the charge density. Eq 48 can be simplified in different ways, depending on the assumptions made for $\varepsilon(\vec{r})$ and $\rho(\vec{r})$.

In the Poisson-Boltzmann (PB) methods, a 'reaction field' is generated by computing ϕ for vacuum and solvent dielectric constant and taking $\phi_{reac} = \phi_{solv} - \phi_{\varepsilon=1}$. ϕ_{reac} is then used to obtain ΔG_{el} by integration (or summation) over the charge density (or point charges).

$$\Delta G_{el}^{PB} = \frac{1}{2}\int \rho(\vec{r})\,\phi_{reac}(\vec{r})d(\vec{r})$$

(eq49)

The equation is further reduced in the Generalized Born (GB) model, where all atoms are treated as point charges q_i interacting with each other and with the surrounding continuum. The two very different types of interactions are combined as in the following equation:

$$\Delta G_{el}^{GB} = \frac{1}{2}\left(1 - \frac{1}{\epsilon_{solv}}\right)\sum_i \sum_{j=i} \frac{q_i q_j}{f_{ij}}$$

(eq50)

where the Born radii f_{ij} depends on the atom pairs' positions and their positions relative to the cavity. The polarization of the solvent affects the electronic structure of the solute. The modified wave function, in turn, changes $\phi(\vec{r})$ and so on, in a self-consistent way. Methods that carry out such iterations are called self-consistent reaction field (SCRF) models. Furthermore, more sophisticated implementations construct a molecular shape-induced cavity and, therefore, have to divide them into segments, or tesserae, which have a partial charge density $\sigma_s(\vec{r_s})$. The potential for each tesserae is then given by:

$$\phi_s(\vec{r}) = \int \frac{\sigma_s(\vec{r_s})}{r - r_s} d\vec{r_s}$$

(eq51)

In the Polarizable Continuum Model (PCM),[34,35] the Conductor-like Screening Model (COSMO)[36,37] and the related C-PCM models[38] the cavity is determined by empirically scaled van der Walls radii, and the electrostatic effects are calculated as in eq48. They are all similar, but in the conductor-like models the continuum outside the cavity has a dielectric constant set to infinity. However, implicit solvation models cannot account for explicit solvation effects such as hydrogen bonding and electron pair coordination to cations. Such effects can have a great influence in predicting the properties of a solute in solution; an example is reported in Chapter 4, where the stability of the neutral and zwitterionic form of ciprofloxacin has been studied.

2.4 Molecular Dynamics Simulation (MD)

The molecular dynamics simulation method (MD) is based on Newton's second law. This method assumes that each particle constituting the system behaves like a Newtonian particle, and quantum behaviour is completely ignored. This means that electronic motions are not considered, electrons are assumed to remain in their ground state and adjust their dynamics instantly when atomic positions change (Born-Oppenheimer approximation) and the motion of the particles is described only through classical mechanics. The equation of motion:

$$\vec{F} = m\vec{a} \qquad \text{(eq52)}$$

is applied on the particles where $\vec{F}$ is the force, m is mass and $\vec{a}$ is the acceleration of the particle.

Once the speeds and position of each atom are known, the state of the system can be predicted and new positions and speeds can be calculated. The procedure can be repeated several times, thereby defining an atomic trajectory. Several algorithms can be used to solve Newton's equations of motion by integration; two common algorithms are the Verlet integrator and the leap-frog integrator, both implemented in GROMACS software.[39]

2.4.1 The Verlet and velocity Verlet algorithm

The Verlet algorithm[40] uses positions and accelerations at time t and positions from time (t-Δt) to calculate new positions at time (t + Δt). The Verlet algorithm uses no explicit velocities and it is a two-step method, because it estimates x (t+Δt)v from the current position x(t) and the previous position x(t-Δt). Therefore, it is not self-starting: initial positions x(0) and velocities v(0) are not sufficient to begin a calculation, and a backward Euler method must be used at t = 0 to get x(-Δt).

$$x(t+\Delta t) = \frac{1}{2}a\Delta t^2 + v(t)\Delta t + x(t) \tag{eq53}$$

$$x(t-\Delta t) = \frac{1}{2}a\Delta t^2 - v(t)\Delta t - x(t) \tag{eq54}$$

$$x(t+\Delta t) = a\Delta t^2 - x(t-\Delta t)\Delta t + 2x(t) \tag{eq55}$$

Velocity Verlet algorithm[41] is the complete form of Verlet algorithm. In this algorithm, both the atomic positions and velocities are calculated at the same time. Positions and velocities at time t are used to integrate the equations of motion. Therefore, positions, velocities and accelerations at time t + Δt are obtained from the same quantities at time t.

$$x(t+\Delta t) = \frac{\Delta t^2}{2m}F(t) + v(t)\Delta t + x(t) \tag{eq56}$$

$$v(t+\Delta t) = \frac{\Delta t}{2m}[F(t) + F(t+\Delta t)] + v(t) \tag{eq57}$$

2.4.2 Leap-frog algorithm

The leap-frog algorithm[41] is similar to the Verlet algorithm, since it is made of two steps. First, the velocities are calculated at time $\left(t + \frac{1}{2}\Delta t\right)$; by using such velocity as an initial

velocity the position x can be calculated at time (x+Δt). In this way, the velocities leap over the positions, then the positions leap over the velocities.

$$x(t+\Delta t) = v\left(t+\frac{1}{2}\Delta t\right) + x(t) \tag{eq58}$$

$$v\left(t+\frac{1}{2}\Delta t\right) = v\left(t-\frac{1}{2}\Delta t\right) + a(t)\Delta t \tag{eq59}$$

$$v(t) = \frac{1}{2}\left[v\left(t-\frac{1}{2}\Delta t\right) + v\left(t+\frac{1}{2}\Delta t\right)\right] \tag{eq60}$$

2.4.3 Empirical force field

The crucial step in MD simulations is describing the atomic interactions of a molecular system, called the force field (FF). The FF cover all relevant molecular interactions that will model the important degrees of freedom. So, first of all, the forces need to be evaluated. As described above, the force $\vec{F_i}$ at time t is determined by the gradient of the potential energy E with respect to the position coordinates of the particle i according to:

$$\vec{F_i} = -\nabla_i V \tag{eq61}$$

The potential energy can be calculated as bonded (intra-molecular) and non-bonded (intermolecular) interactions:

$$V = \sum\nolimits_{bonded} V_i + \sum\nolimits_{non-bonded} V_i \tag{eq62}$$

In Figure 6 the energy terms described in the force field are reported, while the bonded and non-bonded interaction will be explained below.

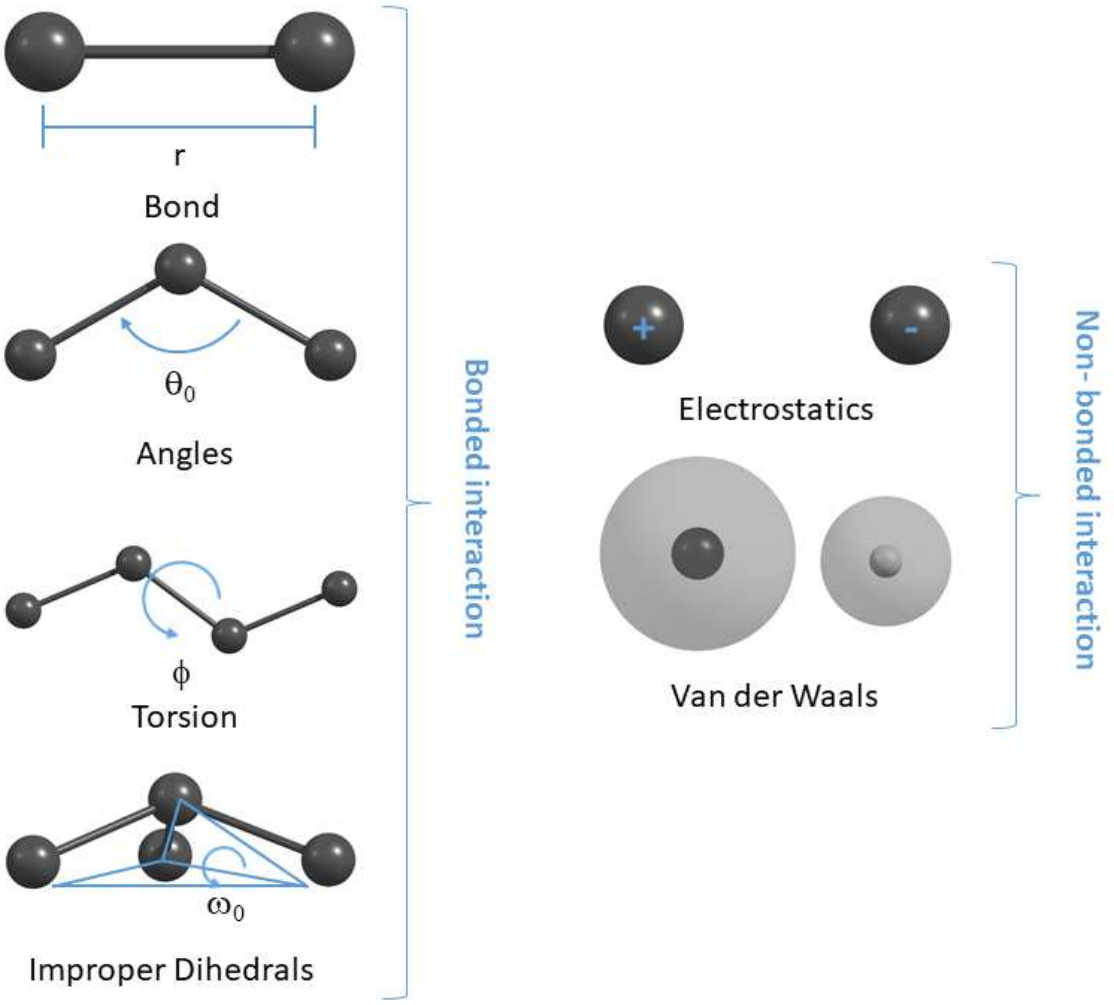

Figure 6 Graphic illustrations of the energy terms described in the force-field terms.

2.4.4 Bonded interactions

As reported in Figure 6, there are four types of interactions between bonded atoms:

- Stretching along the bond (V_{str}).
- Bending between bonds (V_b).
- Planar distortion or improper dihedrals (V_{imp}).
- Torsion (V_{tor}).

V_{str} represents the energy required to stretch or compress a covalent bond. The bond is considered as a spring having its own equilibrium length, r_0 (i.e., the bond distance where the molecule is at a minimum energy level), and the energy required to stretch or compress the bond can be approximated by Hooke's law (for an ideal spring):

$$V_{str} = \frac{1}{2} k_{str,ij} (r_{ij} - r_0)^2$$

(eq63)

V_b is the energy required to bend a bond from its equilibrium angle, θ_0. Bending can also be modelled by a spring; the energy is given by Hooke's law with respect to angle:

$$V_b = \frac{1}{2} k_{b,ijk} (\theta_{ijk} - \theta_0)^2$$

(eq64)

V_{imp} is the energy required to deform a planar group of atoms from its equilibrium angle (ω_o), usually equal to zero. The system also can be modelled by a spring, and the energy is given by Hooke's law with respect to planar angle:

$$V_{imp} = \frac{1}{2} k_{imp,ijkl} (\omega_{ijkl} - \omega_0)^2$$

(eq65)

V_{tor} is the energy needed to rotate around the bonds. Torsional interactions are modelled by the potential:

$$V_{tor} = \sum_{1-4\ pairs} K_\phi (1 - \cos(n\phi - \delta))$$

(eq66)

where ϕ is the angle, δ is the phase and n is the number of peaks in a full rotation. In the equations, i, j, k, l are the various atoms or particles.

2.4.5 Non-bonded interactions

There are two potential functions to be concerned about between non-bonded atoms:

- Columbic interactions between electrostatic charges.
- Lennard-Jones interaction energy, which reflects the van der Waals interaction between atoms.

In electrostatic interactions, atom charges are involved. Opposite atom charges attract and, like atom charges, repel each other.

In this potential, the force of the attraction is inversely proportional to the square of the distance:

$$\vec{F} = \frac{q_1 q_2}{4\pi\varepsilon_0 r^2}$$

(eq67)

where q_1 and q_2 are the partial atomic charge of the atoms or particles, ε_0 is the dielectric constant of the medium, r is the distance between the two atoms. In van der Waals interactions, (V_{VdW}) two atoms not having a moment of electrical multipole interact attractively among themselves thanks to an interaction known as induced dipole-dipole interaction. Such interaction gets stronger the more the atoms are polarizable and the closer they are to each other. However, the two atoms cannot approach the infinite, and for very short distances the repulsive force becomes dominant. The potential is defined, called Lennad Jones potential (LJ) as:

$$V_{ij} = 4\varepsilon_{ij}\left(\left(\frac{\sigma_{ij}}{r_{ij}}\right)^{12} - \left(\frac{\sigma_{ij}}{r_{ij}}\right)^{6}\right)$$

(eq68)

where ε is the depth of the potential well, σ is the finite distance at which the inter-particle potential is zero and r is the distance between atom i and atom j.

Most of the force field parameters are taken from experimental data on small molecules, while others are taken from theoretical calculations. In general, crystallographic data are useful to obtain reference bond lengths and angles. Indeed, spectroscopic data can provide force constants to bonds, angles and improper dihedral. Dihedral parameters and partial atomic charges are usually derived from quantum chemical calculations. The parameters for the Lennard-Jones function are usually derived from knowledge of diffusion, viscosity and heats of vaporization in the condensed phase and refined by molecular dynamics simulations.

2.5 References

[1] C. J. Cramer, *Essentials of Computational Chemistry Theories and Models*, John Wiley & Sons Ltd, Chichester, England, **2004**.

[2] F. Jensen, *Introduction to Computational Chemistry*, John Wiley & Sons Ltd, Chichester, England, **2007**.

[3] D. C. Young, *Computational Drug Design A Guide for Computational and Medicinal Chemists*, JohnWiley & Sons, Inc., Hoboken, New Jersey Published, **2009**.

[4] D. C. Young, *Computational Chemistry: A Pratical Giude for Applying Techniques to Real World Problems*, John Wiley & Sons, Inc., New York, USA, **2001**.

[5] H. B. Schlegel, *Adv. Rev.* **2011**, *1*, 790–809.

[6] E. Schrödinger, *Phys. Rev.* **1926**, *28*, 1049–1070.

[7] M. Born, R. Oppenheimer, *Ann. Phys.* **1927**, *389*, 457–484.

[8] J. C. Slater, *Phys. Rev.* **1929**, *34*, 1293–1322.

[9] C. C. J. Roothaan, *Rev. Mod. Phys.* **1951**, *23*, 69–89.

[10] G. G. Hall, *Proc. R. Soc. A* **1951**, *205*, 541–552.

[11] J. A. Pople, R. K. Nesbet, *J. Chem. Phys.* **1954**, *22*, 571–572.

[12] F. Bertaut, A. Durif, *C. R. Hebd. Seances Acad. Sci.* **1954**, *238*, 2173–2175.

[13] S. M. Blinder, *Am. J. Phys.* **1965**, *33*, 431–443.

[14] C. Møller, M. S. Plesset, *Phys. Rev.* **1934**, *46*, 618–622.

[15] P. Hohenberg, W. Kohn, *Phys. Rev. B* **1973**, *7*, 1912–1919.

[16] W. Kohn, L. J. Sham, *Phys. Rev.* **1965**, *140*, A1133–A1138.

[17] W. Kohn, L. J. Sham, *Phys. Rev.* **1965**, *137*, A1697–A1705.

[18] A. D. Becke, *Phys. Rev. A* **1988**, *38*, 3098–3100.

[19] J. P. Perdew, *Phys. Rev. B* **1986**, *33*, 8822–8824.

[20] J. P. Perdew, K. Burke, Y. Wang, *Phys. Rev. B* **1996**, *54*, 533–539.

[21] J. Perdew, J. Chevary, S. Vosko, K. Jackson, M. Pederson, D. Singh, C. Fiolhais, *Phys. Rev. B* **1992**, *46*, 6671–6687.

[22] J. P. Perdew, K. Burke, M. Ernzerhof, *Phys. Rev. Lett.* **1996**, *77*, 3865–3868.

[23] J. P. Perdew, K. Burke, M. Ernzerhof, *Phys. Rev. Lett.* **1996**, *77*, 3865–3868.

[24] C. Lee, W. Yang, R. G. Parr, *Phys. Rev. B* **1988**, *37*, 785–789.

[25] B. Miehlich, A. Savin, H. Stoll, H. Preuss, *Chem. Phys. Lett.* **1989**, *157*, 200–206.

[26] A. D. Becke, *J. Chem. Phys.* **1993**, *98*, 1372–1377.

[27] C. Adamo, V. Barone, *J. Chem. Phys.* **1999**, *110*, 6158–6170.

[28] A. D. Becke, *J. Chem. Phys.* **1997**, *107*, 8554–8560.

[29] H. L. Schmider, A. D. Becke, *J. Chem. Phys.* **1998**, *109*, 8188–8199.

[30] S. H. Vosko, L. Wilk, M. Nusair, *Can. J. Phys.* **1980**, *58*, 1200–1211.

[31] Y. Zhao, D. G. Truhlar, *Theor. Chem. Acc.* **2008**, *120*, 215–241.

[32] Y. Zhao, D. G. Truhlar, *Accounts Chem. reserch* **2008**, *41*, 157–167.

[33] J. Tomasi, B. Mennucci, R. Cammi, *Chem. Rev.* **2005**, *105*, 2999–3093.

[34] M. Cossi, V. Barone, R. Cammi, J. Tomasi, *Chem. Phys. Lett.* **1996**, *255*, 327–335.

[35] M. Cossi, G. Scalmani, N. Rega, V. Barone, *J. Chem. Phys.* **2002**, *117*, 43–54.

[36] A. Klamt, *J. Phys. Chem.* **1995**, *99*, 2224–2235.

[37] A. Klamt, G. Schüürmann, *J. Chem. Soc., Perkin Trans. 2* **1993**, *2*, 799–805.

[38] M. Cossi, N. Rega, G. Scalmani, V. Barone, *J. Comput. Chem.* **2003**, *24*, 669–681.

[39] M. J. Abraham, T. Murtola, R. Schulz, S. Páll, J. C. Smith, B. Hess, E. Lindah, *SoftwareX* **2015**, *1–2*, 19–25.

[40] L. Verlet, *Phys. Rev.* **1967**, *159*, 98–103.

[41] W. C. Swope, H. C. Andersen, P. H. Berens, K. R. Wilson, *J. Chem. Phys.* **1982**, *76*, 637–649.

Chapter 3

Platinum-based Antitumor Drugs: Theoretical Study of the Mechanism of Action and Interaction with Graphene

For years I've been saying cisplatin is the first platinum-based drug we discovered. It can't possibly be the best one! It's disappointing that the scientific community has not been able to find better one
Cit. "Barnett Rosenberg"

3.1 Introduction

3.1.1 A brief history of platinum-based antitumor drugs

The history of platinum-based antitumor drugs started by accident over 50 years ago in the laboratory of the physicist Barnett Rosenberg at Michigan State University. Rosenberg was studying the effect of electromagnetic radiation on bacterial and mammalian cells in a growth chamber. In the early experiments using Escherichia coli (E. coli), a set of platinum electrodes (considered to be inert) was included in the growth chamber, and after the electric field was activated the bacteria grew up to 300 times their normal length, becoming very long filaments. Such effect has been shown to be due to electrolysis products derived from platinum electrodes rather than to the electric field. Detailed chemical analysis later identified the diamminedichloroplatinum(II) [$Pt(NH_3)_2Cl_2$] complex as responsible for the phenomenon.

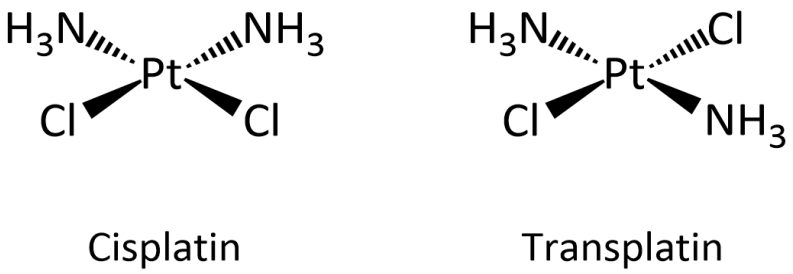

Scheme 1 Schematic representation of cisplatin and transplatin.

Rosenberg and his co-workers published the discovery in 1965[1] and, in order to further clarify it, they synthesised both *cis* and *trans* isomers of the [$Pt(NH_3)_2Cl_2$] and tested their activity on E. coli, thereby finding out that the *cis* isomer caused an efficient inhibition of cell division, whereas the *trans* isomer was rather inefficient at inhibiting it. Hence, the *cis* isomer (the active complex) is now called cisplatin, while the *trans* isomer is now referred to as transplantin (see Scheme 1).[2–4]

In 1968, following further tests against various bacteria, cisplatin was administered to mice possessing tumour sarcoma-180 at the non-lethal dose of 8 mg per kg, and was shown to cause marked tumour regression. In 1971, after a long series of tests, cisplatin was used to treat the first patients , and in 1978 it was finally approved by US Food and

Drug Administration (US FDA).[3] The discovery resulted in a revival of inorganic chemistry and led to the synthesis and biological evaluation of many thousands of molecules similar to cisplatin; it also led to an in-depth investigation of other elements close in the periodic table (eg. palladium and gold).[5–7] Currently, cisplatin is primarily used to treat testicular, ovarian, and bladder cancers, but it has also been used in the treatment of head and neck cancers, lung cancer, malignant pleural mesothelioma, neuroblastoma, tumors of the brain, and esophageal and cervical cancers.[8,9]

3.1.2 Mechanism of action of cisplatin

The generalized mechanism of action involves four key steps (Figure 1): (1) cellular uptake, (2) activation by the hydrolysis reactions, (3) DNA binding and (4) cellular processing of DNA lesions leading to cell death .[10,11]

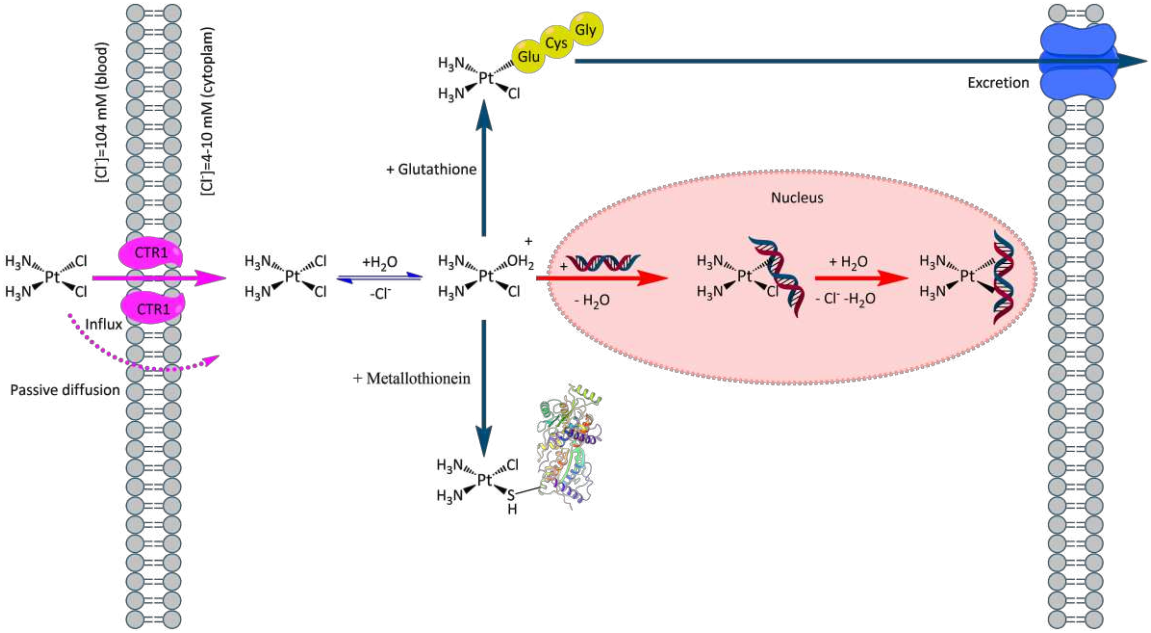

Figure 1 Extracellular and intracellular events that influence cisplatin activity.

Cisplatin could enter the cell through two pathways by passive diffusion through the plasma membrane and by active transport mediated by membrane proteins.[12,13] The particular structure of cisplatin, characterized by a small size and a square-planar geometry, has long been cited as supportive of passive diffusion. Indeed, cisplatin uptake does not saturate with increasing concentration and is proportional to the administered concentration.[13] On the contrary, other studies suggest that the predominant mechanism of uptake is

active transport. Indeed, many works focus on the importance of copper transporters, such as CTR1, which can mediate the uptake of cisplatin.[14,15] A combination of both passive and active transport best explains the data accrued to date, but the relative importance of these pathways and the extent to which they influence each other remain to be determined.

Besides affecting cisplatin uptake, the square-planar geometry of cisplatin facilitates the ligand substitution, which is indispensable for it to form the DNA lesions that characterize its activity. Upon entry into the cell, cisplatin becomes 'activated' by the ligand substitution, in which chloride ligands are replaced by water molecules to form *cis*-$[PtCl(H_2O)(NH_3)_2]^+$ and *cis*-$[Pt(H_2O)_2(NH_3)_2]^{2+}$. A schematic representation of the hydrolysis reaction is reported in Scheme 2.

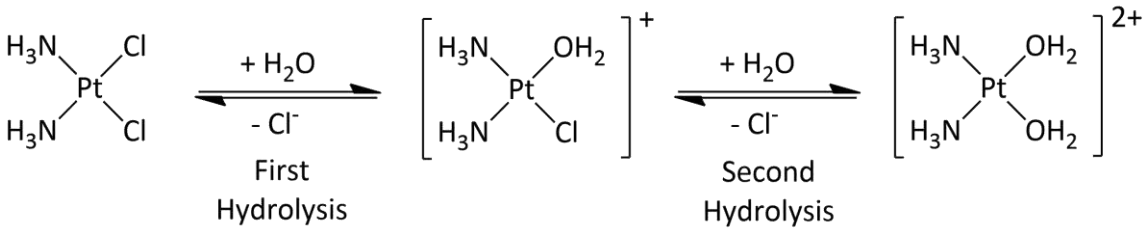

Scheme 2 The hydrolysis reaction of cisplatin. The first hydrolysis reaction replaces a chloride ligand with a water molecule giving a net positive charge. The second stage hydrolysis reaction replaces the second chloride ligand with another water molecule which gives a 2+ net positive charge.

Depending on the pH of the solution, the coordinated water molecules may deprotonate to give hydroxo complexes. Experimental evidence indicates that such aquation is suppressed in the bloodstream, where the chloride ion concentration is high (~100 mM), but occurs more readily in the cytoplasm, where the chloride ion concentration falls below 20 mM.[4,16,17] The positive charge on the aquated platinum complex can attract it to the negatively charged nuclear DNA. There is general agreement that DNA is a key biological target of cisplatin[18,19], based on experiments in which DNA repair-deficient prokaryotic and eukaryotic cells were found to exhibit a hypersensitivity to cisplatin treatment.[20,21] Although decades of research have supported the hypothesis that nuclear DNA is the functional target of platinum drugs, interactions with proteins and RNA have also been suggested as possible targets.[22–24] Activated cisplatin can enter the nucleus, and the coordinated water molecule can be substituted by a heterocylic DNA base, being the Pt-

OH_2 bond much more reactive than Pt-Cl. The most nucleophilic sites of DNA are the N7 atoms of the imidazole ring of DNA purine bases (guanine and adenine, see Scheme 3), which are preferentially platinated.

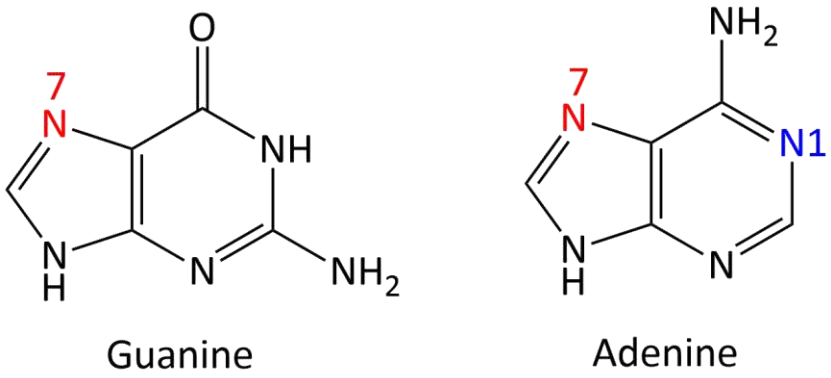

Scheme 3 Schematic representation of the guanine and adenine purine bases.

Spectroscopic experiments revealed that cisplatin first forms monofunctional adducts on DNA. Following this event, the remaining water ligand is substituted for a second guanine base, forming a cross-link on the DNA. The majority of DNA adducts result from the binding of cisplatin to adjacent purine bases on the same strand of the DNA helix; they are called intrastrand DNA adducts and they are the significant sites of cisplatin's biological effectiveness and anti-tumour activity. However, a smaller proportion of its biological activity is attributed to DNA adducts formed at AG, GA and GC sequences.[25–27] An experiment was conducted on DNA fractions to assess the amount of cisplatin bound to DNA. 1,2 GG intrastrand adducts (formed between two adjacent guanine bases on the same DNA strand) are the most prevalent lesions, and account for approximately 65% of all DNA adducts. 1,2 AG intrastrand adducts (formed between adjacent adenine and guanine bases on the same DNA strand) account for about 25% of all adducts, and 1,3 GG intrastrand adducts (formed between two non-adjacent guanine bases on the same DNA strand) account for about 10 % of all adducts.[28,29] GG interstrand adducts (where platinum binds to guanine bases on opposite strands of the DNA) was also detected. Such adducts are considerably less common than intrastrand DNA adducts, accounting for only 2% of all adducts formed by cisplatin .[29,30] The four different types of DNA adducts formed by cisplatin are shown in Figure 2.

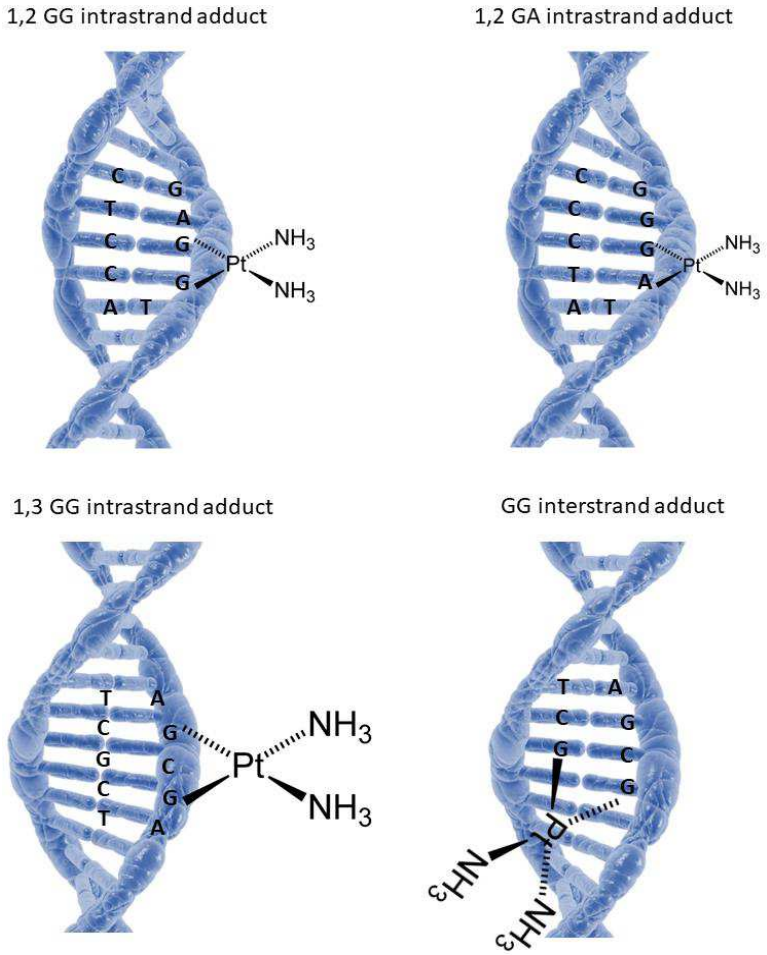

Figure 2 Images showing the four different types of DNA adducts formed by cisplatin. The 1,2 GG intrastrand adduct is formed by cisplatin binding to two adjacent guanine bases on the same DNA strand. The 1,2 GA intrastrand adduct is formed by cisplatin binding to adjacent guanines and adenines on the same DNA strand. The 1,3 GG intrastrand adduct is formed by cisplatin binding to two non-adjacent guanines on the same DNA strand. The GG interstrand adduct is formed upon cisplatin binding to two guanines on opposite strands of the DNA helix.

These DNA adducts distort the structure of DNA in a substantial manner, resulting in the bending and unwinding of the double helix upon platination.[28] Atomic resolution structures of many adducts formed by different platinum anticancer agents are now available; some of them , relative to cisplatin, are reported in Figure 3.[31] Cells with DNA presenting these distortions arrest at the G2/M transition of the cell cycle and attempt to repair the platinated DNA. Lesions formed by cisplatin inhibit RNA polymerase II, the enzyme responsible for transcription of mRNA precursors that ultimately form proteins in humans.[32] If the polymerase becomes stalled at the platinum adduct, additional proteins are recruited to repair the damage. Cisplatin lesions are effectively removed by the

nucleotide excision repair (NER) machinery, and enhanced NER can produce cells that resist platinum treatment.[33,34] The repair machinery must be able to access the lesion, but there are some proteins, not involved in DNA repair, that bind to a platinum lesion and can effectively shield it from repair.

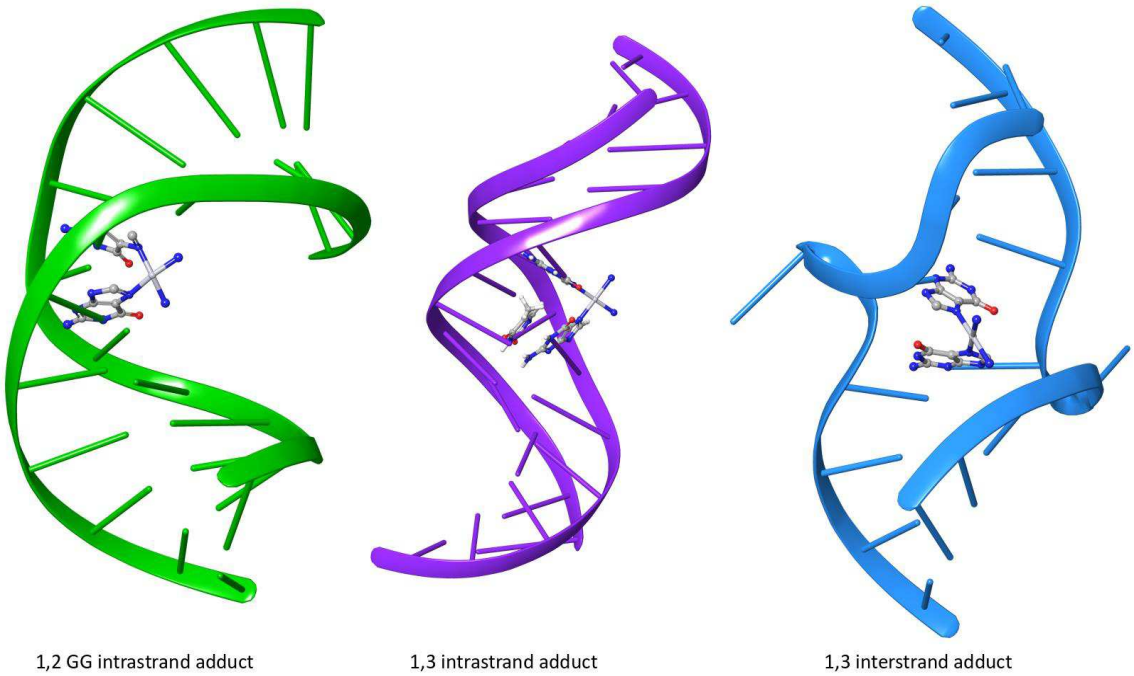

Figure 3 Structures of double-stranded DNA adducts of cisplatin determined by X-ray crystallography or NMR spectroscopy. Cisplatin 1,2 GG intrastrand cross-link (PDB 1AIO). Cisplatin 1,3 GTG intrastrand cross-link (PDB 1DA4). Cisplatin interstrand cross-link (PDB 1A2E).

One class of proteins includes the high-mobility group (HMG) box proteins, that recognize and bind distorted DNA. Indeed, cisplatin induces distortions in the DNA double helix resembling those recognized by some HMG proteins.[35] The HMGB proteins are among the most abundant proteins in the nucleus[36] and display a particular affinity to $[Pt(NH_3)_2]^{2+}$ 1,2 GG intrastrand cross-links, the most abundant lesions.[37] The proteins' ability to shield the platinum lesions could contribute to the cisplatin sensitivity of the cancer cells that overexpress them. However, the cellular redox environment can influence the interaction of HMGB with the platinated DNA and suggest that the redox state HMGB is a potential factor in regulating the role of the protein in modulating the activity of cisplatin as an anticancer drug.[38] If the cell is unable to repair the platinum-DNA lesion, the expression of pro-apoptotic proteins increases, prompting the release of

cytochrome C and the activation of intracellular caspases, a family protease enzymes playing an essential role in programmed cell death. Such proteases effectively degrade the cell in a process of programmed cell death known as apoptosis.[39]

However, there are many pathways in which platinum complexes can be deactivated to prevent the apoptosis.[40] The current platinum drugs are all administered intravenously and can interact with blood components, one of which is human serum albumin (HAS), the most abundant protein in the human bloodstream. This protein contains a cysteine residue that can interact with platinum complexes.[41] However, the main interaction of cisplatin with HAS seems to involve the thionester side chains of methionine residues rather than the cysteine thiol groups.[42] Moreover, once inside the cell and after hydrolysis reaction, platinum complexes can interact with biomolecules other than DNA. Cisplatin reacts with molecules containing sulfur atoms such as tripeptide glutathione (GSH) and metallothioneins (MT) (5), species rich in amino acids like cysteine and methionine, eventually causing the inactivation of cisplatin.[33] Reactions with biomolecules other than DNA are among the possible causes of generation of drug resistance. As part of the cellular detoxification program, platinum-glutathione adducts are removed by dedicated export pumps from the cytoplasm.

3.1.3 Other platinum(II) compounds with a mechanism of action similar to cisplatin's

Following the initial reports of the anticancer activity of cisplatin, inorganic chemists started preparing a variety of platinum complexes with different ligands and testing their anti-neoplastic effects. The results of these studies have revealed a set of rules governing the molecular structure, necessary for a platinum complex to have an activity.[43] The structures activity relationships (SARs) reveal that platinum complexes must have a square-planar geometry, be neutrally-charged, contain two *cis* amine ligands and have two *cis* anionic ligands. The anionic ligands cannot bind the platinum too tightly, otherwise its activity could be reduced. Moreover, the two amine ligands and the two anionic ligands can be replaced by a chelating diamine or chelating dicarboxylate respectively. Extensive drug discovery programs relying on systematic variation of ligands have been initiated according to such rules.[5–7,44,45] Many efforts have been made to find novel platinum

complexes that could be safer than cisplatin for patients. Indeed, although on the one hand cisplatin shows high antiproliferative activity, on the other hand it shows many side effects, including nephrotoxicity, ototoxicity, neurotoxicity, myelotoxicity, haematological toxicity and gastrointestinal reactions (see Figure 4).[8,33,46]

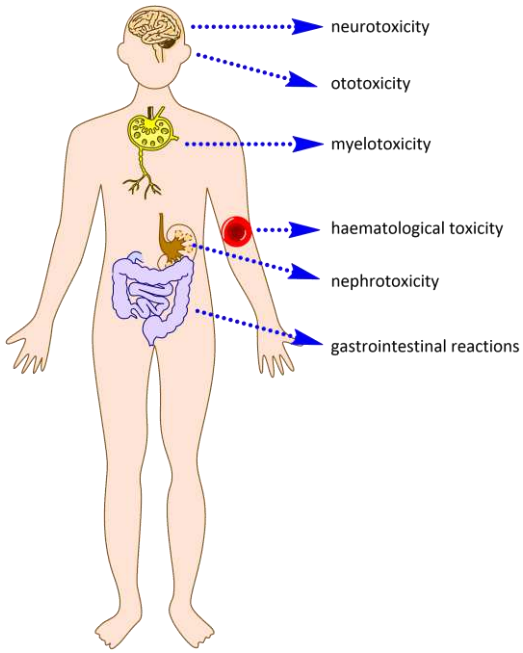

Figure 4 Toxicities associated with treatment with platinating agents

Unfortunately, most of the newly-found compounds were rejected in the preclinical stage; only carboplatin and oxaliplatin are now in world-wide clinical use (see scheme 4), while nedaplatin, heptaplatin and lobaplatin are marketed platinum antitumor drugs.[39] The toxicity of platinum-based drugs is directly related to the ease with which the leaving ligands are replaced by water molecules. Platinum complexes that present highly labile ligands, such as water or nitrate, are very toxic, whereas ligands such as bis-carboxylates, where the hydrolysis process is very slow, are significantly less toxic. Diammine [1,1-cyclobutanedicarboxylato(2-)-O,O'] platinum(II), now known as carboplatin, was designed specifically to reduce the side effects associated with cisplatin treatment. In carboplatin, the chloride ligands were replaced with 1,1-cyclobutanedicarboxylate, leading to a reduced hydrolysis rate constant in respect to cisplatin (10^{-8} s^{-1} for carboplatin and 10^{-5} s^{-1} for cisplatin).[47,48] Carboplatin is used primarily to treat ovarian cancer but has also found use in treating retinoblastomas, neuroblastomas, nephroblastomas and brain tumors, as

well as cancers of the head and neck and endometrium, cervix, testes, breast, lung and bladder cancers.[9]

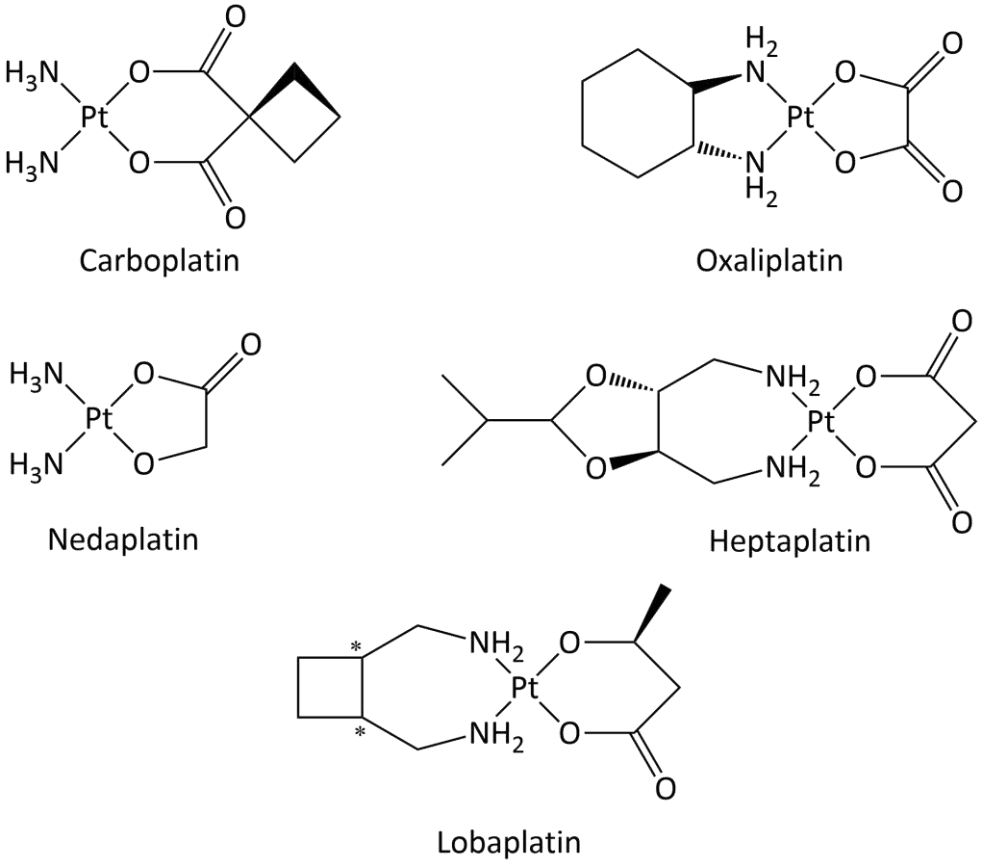

Scheme 4 Schematic representation of carboplatin and oxaliplatin and marketed platinum antitumor drugs.

[Oxalate(2-)-O,O'][1R,2R-cyclohexanediamine-N,N'] platinum(II), now known as oxaliplatin, was the first drug capable of overcoming cisplatin resistance to be approved. In oxaliplatin the two ammine ligands have been replaced by a single bidentate ligand, (1R,2R)-cyclohexane-1,2-diamine(R,R-dach).[3] Oxaliplatin is thought to overcome cisplatin resistance through the different adducts it forms with DNA.[49] Oxaliplatin, like cisplatin, does form GG intrastrand adducts, but the bulky hydrophobic ligand points into the DNA major groove and prevents the formation of the bond with proteins repairing DNA.[50] Moreover, the oxalate ligand greatly reduces the severity of the side effects of the drug compared with cisplatin.[49] Currently, Oxaliplatin is widely approved for the treatment of adjuvant and metastatic colorectal cancers when used in combination with 5-FU (5-fluorouracil) and folinic acid.[51] Diammine [hydroxyacetato(2-)-O,O'] platinum(II), nedaplatin, is a second-generation platinum analogue ten times more water soluble than

cisplatin, and significantly less nephrotoxic than both cisplatin and carboplatin.[52,53] Preclinical and clinical studies demonstrated that nedaplatin's anticancer activity is superior to carboplatin's and equivalent to cisplatin's.[53,54] Since its approval in 1995, nedaplatin has been used in the treatment of oesophageal cancer and head and neck cancers .[53,55]

Heptaplatin was selected for clinical trials because its in vitro and in vivo cytotoxicity was equal or superior to cisplatin in various cell lines. Moreover, it also displayed high stability in solution, no remarkable toxicity and a potent anticancer activity towards cisplatin-resistant cell.[56–58]

Lobaplatin is a third-generation platinum anticancer drug delivered as a diastereomeric mixture of S,S and R,R configurations of the carrier ligand and presents less side effects than cisplatin and carboplatin.[59] Although our understanding of cisplatin and other novel anti-cancer drugs has advanced through an array of discoveries determined from past research investigations, further study and characterisation is much needed. The goal is to provide a greater understanding of DNA-drug interactions and potentially enable the design of enhanced anti-cancer drugs to overcome the cytotoxic effects and tumour resistance associated with cisplatin.

3.2 Hydrolysis reaction in Triphenylphosphane Pt(II) Complexes Containing Biologically Active Natural Polyphenols: DFT Study.

3.2.1 Introduction

The antitumor activity of dietary flavonoids comprising a massive group of polyphenolic compounds[60,61] has recently been reviewed.[62] The pharmacological effects of flavonoids include induction of apoptosis, antiproliferation, antimetastatic and antiangiogenesis.[62] Because of structural differences, flavonoids are divided into eight different groups, flavonols being one of them. 3-Hydroxyflavone (3-Hlf, Scheme 5) is the backbone of all flavonols.[63] Due to their polyphenolic structure, flavonols are effective metal ion chelators, playing a key role in the initiation of free radical and antioxidant processes.[64] Moreover, flavonols can intercalate into DNA as well as covalently bind to DNA and proteins.[65,66] As a result of such characteristics, flavonols have complex biological

interactions and are combined in some therapies with cisplatin, increasing efficacy over individual treatments[67] and reducing side effects.[68] However, the combinations of flavonols with platinum are poorly.[69] Like flavonols, plant phenols such as ethyl gallate (etga, Scheme 5) also have an antitumor activity and can effectively bind metal ions.[70,71]

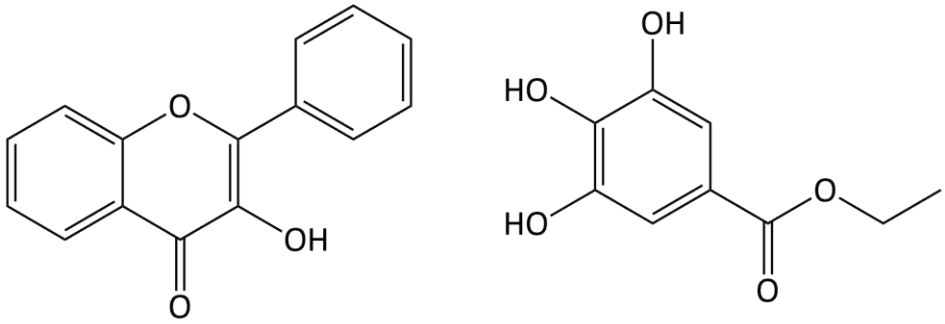

Scheme 5 Schematic representation of 3-Hydroxyflavone and ethyl gallate.

In some cases, phosphane ligands with a hydrophobic character have been shown to increase the cytotoxicity of their platinum complexes, due to a possible enhancement of the cellular membrane transfer process.[72] In previous works,[73,74] interesting results were obtained by synthetizing platinum compounds bearing two mutually *cis*-triphenyl-phosphanes with bioactive ligands. The studies reported that Pt(II) complexes containing PPh_3 have a remarkable cytotoxic activity on some cancer cell lines. However, a total replacement of the usually employed amine carrier ligands with air and water stable triaryl-phosphanes may exhibit some disadvantages, the major of which being tertiary phosphane's inability to establish any hydrogen bond with the DNA backbone. However, triaryl-phosphane ligands may stabilize DNA-Pt adducts through π-π interactions occurring between the phosphane phenyl groups and the nucleobases.[75]

In 2016 Dell'Anna[76] and co-workers synthetized and characterized three triphenyl-phosphane Pt(II) complexes containing quercetin (Que) *cis*-$[Pt(Que)(PPh_3)_2]$, etga *cis*-$[Pt(etga)(PPh_3)_2]$ and 3-Hfl *cis*-$[Pt(3\text{-}Hfl)(PPh_3)_2]^+$ and they have been biologically characterized 3-Hfl *cis*-$[Pt(3\text{-}Hfl)(PPh_3)_2]^+$ and *cis*-$[Pt(etga)(PPh_3)_2]$ (Table 1).

Table1 Cytotoxicity of hydroxyflavone, ethyl gallate, *cis*-[Pt(3-Hfl)$(PPh_3)_2]^+$, *cis*-[Pt(etga)$(PPh_3)_2$], *cis*-[$PtCl_2(PPh_3)_2$] and cisplatin toward U87 and MCF-7 cancer cell lines.

	IC_{50} (μM)	
Compound	U87	MCF-7
cis-[Pt(3-Hfl)$(PPh_3)_2]^+$	26.3 ± 2.1	55.2 ± 1.7
3-Hydroxyflavone	27.5 ± 2.3	108.1 ±3.5
cis-[Pt(etga)$(PPh_3)_2$]	123.7 ± 3.8	>200
Ethyl gallate	97.7 ± 2.6	>200
cis-[$PtCl_2(PPh_3)_2$]	>200	>200
cisplatin	1.76 ± 0.22	14. ± 3

As reported in Table 1, cell cycle studies (in the dark) of the complexes in two human cell cancers lines (U87, MCF-7) revealed that the cytotoxic activity of the complex bearing 3-Hfl is higher than the one exhibited by 3-Hfl alone in MCF-7 cancer cell. *cis*-[Pt(etga)$(PPh_3)_2$], instead, presents less cytotoxic activity than etga alone. However, both these complexes exhibit much lower cytotoxicity than cisplatin, while *cis*-[$PtCl_2(PPh_3)_2$] results totally inert.

The ligand released by hydrolysis, a key-step for DNA-adduct formation, attracted numerous experimental studies.[25] However, the results obtained through experimental studies do not always offer the same insight provided by computational studies. Therefore, the hydrolysis reaction of cisplatin and many other platinum-based drugs have been extensively studied using computational techniques, in particular the DFT approach.[53,77–88]

Chval *et al.*[77] made one of the first computational works related to the study of the hydrolysis reaction in 2000. Their work investigated the hydrolysis reaction for cisplatin using MP2 and DFT calculations. The first and second step of the hydrolysis reactions belong to the class of second-order nucleophilic substitution (S_N2) reactions. The reactions for square-planar complexes proceed via a collision between the reactant and two consecutive nucleophilic species, attacking the metal centre to release the ionic ligand. In such process, a transition state adopts a substantially trigonal bipyramid geometry, in which the entering molecule and the leaving group result weakly bound to the metal atom, suggesting an associative mechanism. The activation barrier attains 21.3 kcal mol^{-1} in the first step and 26.1 kcal mol^{-1} in the second.

In 2005 Burda *et al.*[78] studied the thermodynamic and kinetic aspects of the hydrolysis reactions of cisplatin and transplatin. The hydration of Pt complexes was considered in two steps. In each of them concurrent reactions of dechlorination and deammination were expected. An associative mechanism was assumed for the reaction course, in which a trigonal bipyramidal structure of TS was determined. Results showed that the determined rate constants of the dechlorination process are by several (three to four) orders of magnitude larger than the constants of the deamination process, indicating that the deamination is highly disadvantaged.

In 2009 Alberto *et al.*[53] studied the first and the second hydrolysis of Nedaplatin, using DFT calculation combined with CPCM approach, corresponding to the ring opening followed by the loss of the ligand, in neutral and acid conditions respectively. In addition to the reactive water molecule, their models featured an explicit water molecule, which could assist the degradation processes. They found out that the rate determining step in neutral conditions is the first hydrolysis process and, consequently, the double hydrated complex is suggested to be the species reacting with the DNA purine bases, while in acid conditions the trend is different, with the second hydrolysis process being the rate limiting step.

In 2011 Melchior *et al.*[83] made a comparative study of the hydrolysis of cisplatin and the third-generation platinum anticancer compound picoplatin *cis*-[$PtCl_2(NH_3)$-(2-picoline)] using the DFT calculations. Solvent effects were taken into account either by applying the PCM approach or by introducing a cluster of water molecules solvating the complex. Results show that the steric hindrance of 2-picoline has a minimum impact on the activation barriers for picoplatin hydrolysis. Moreover, the authors demonstrated that the use of separated reactants as a reference for the energy barrier gives satisfactory results and produces correct relative magnitudes of the first and second hydrolysis rate constants for each compound. However, the approach is not able to predict the faster hydrolysis observed experimentally on cisplatin with respect to picoplatin, while the discrete solvation model is able to correctly predict a slightly slower hydrolysis of picoplatin.

In 2017 Mitra *el al.*[87] studied the hydrolysis processes of cytotoxic Pt(II) and Pd(II) complexes bearing benzimidazole moieties combining DFT with CPCM approach. The results revealed that the rate-limiting step is the second aquation, suggesting that the monohydrated complex is most likely to react with the DNA bases. The results provided

detailed energy profiles for the hydrolysis mechanism, which help understanding the interaction of such anticancer agents with their ultimate cellular target.

3.2.2 Aim of this work

The aim of this work is to study the hydrolysis reaction in *cis*-[Pt(PMe$_3$)$_2$(etga)] and in *cis*-[Pt(PMe$_3$)$_2$(3-Hfl)]$^+$ by means of DFT calculations. A detailed computational study of the hydrolysis reaction could clarify the causes of the poor cytotoxicity of such complexes. In order to study the platinum complexes with two flavonols, two different hydrolysis pathways have been considered (Scheme 6), due to the asymmetry of the starting complex. Finally, the activation energy obtained for *cis*-[Pt(PMe$_3$)$_2$(etga)] and *cis*-[Pt(PMe$_3$)$_2$(3-Hfl)]$^+$ has been compared with the activation energies obtained for cisplatin and no-active *cis*-[Pt(Cl)$_2$(PMe$_3$)$_2$].

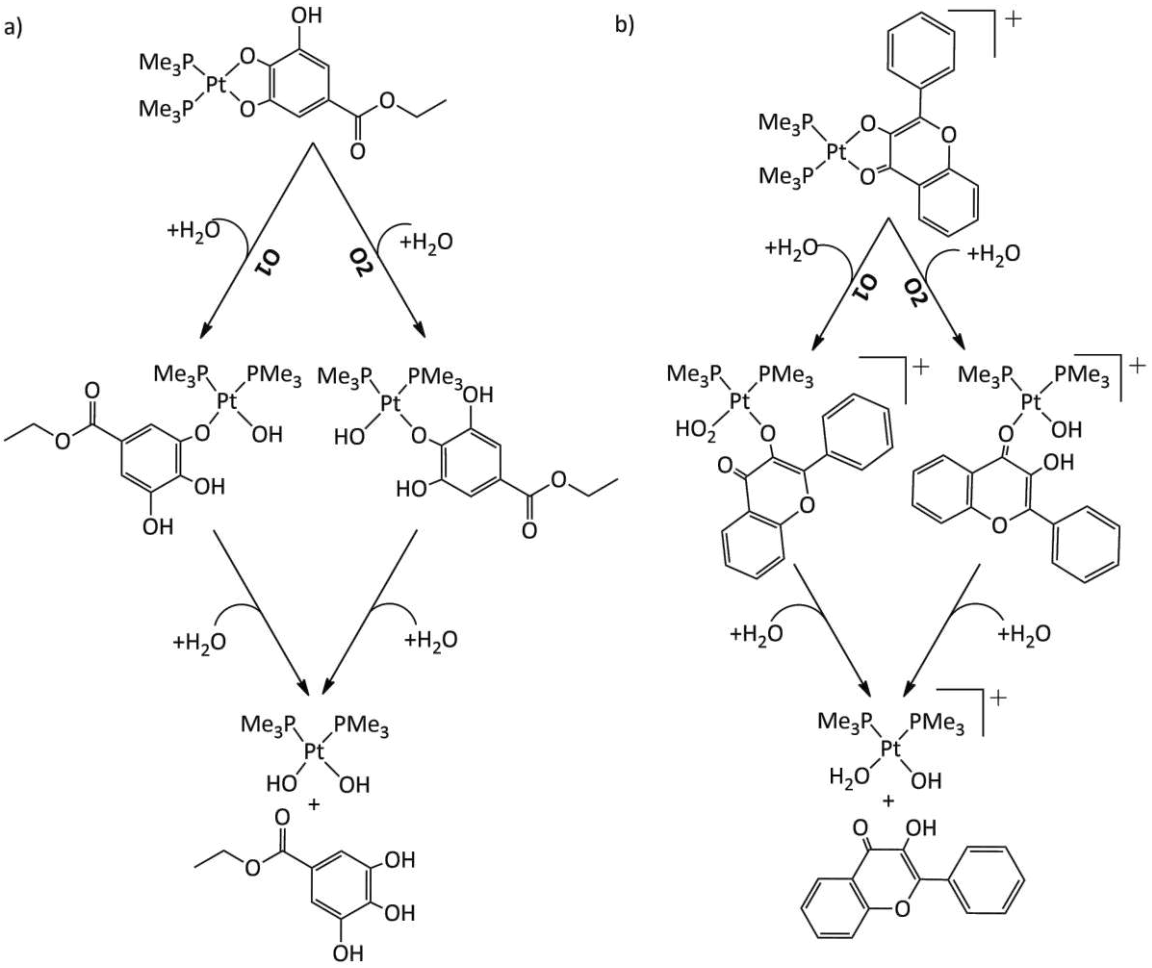

Scheme 6 Hydrolysis reaction in (a) *cis*-[Pt(PMe$_3$)$_2$(etga)] and in (b) *cis*-Pt[(PMe$_3$)$_2$(3-Hfl)]$^+$.

3.2.3 Computational details

In this work we studied the hydrolysis reaction for *cis*-[Pt(PMe_3)$_2$(etga)], *cis*-[Pt(PMe_3)$_2$(3-Hfl)]$^+$, cispatin, and *cis*-[$PtCl_2$(PMe_3)$_2$] by means of DFT calculations using mPW1PW91 functional, which had been previously demonstrated to provide reliable structures and energies for cisplatin and its derivatives.[83] For computational convenience, Phenyls were replaced in PPh_3 groups by methyl (Me) groups. Geometry optimizations were carried out in vacuum, with a 6-31+G(d) basis set for all atoms except the platinum atom, which was described by the quasi-relativistic Stuttgart– Dresden pseudopotential (SDD).[89] In order to confirm that stationary points were actually minima or transition state geometries, analytical calculations of second derivatives of the energy and vibrational frequency analysis were carried out. The frequencies are related to the eigenvalues of the Hessian matrix, which contains second derivatives. If the eigenvalues are all positive, then the frequencies are all real and the stationary point is a local minimum. If one eigenvalue is negative and one imaginary frequency is present, then the stationary point is a transition structure. The character of the transition states was confirmed by existence of a single negative eigenvalue of the hessian matrix corresponding to the appropriate antisymmetric stretching mode. Due to the key role of solvation in influencing thermodynamic and kinetic parameters in metal complex reactivity,[90–92] environmental effects were introduced by representing water surrounding the reagents, transition states and products as a polarizable continuum method (PCM).[93] Since the solvent is also the reagent, it has been represented as an explicit H_2O molecule added to the initial reagent (R).[76,83] The initial position of the molecule is between the O atom of the leaving ligands and the P atom of the ancillary ligand, 3.0 Å to 3.5 Å from the Pt atom. Such adduct is called reactants adduct (RA). After the TS, the leaving Cl atom are in proximity of the *acquo*-complex (products adduct, PA); in the final product (P), the Cl atom have been separated. Potential energy profiles were estimated from total electronic energies adding zero ZPVE and thermal corrections at 298.15 K. Total electronic energies plus thermal corrections (instead of free energies) are reported in order to uniform our data to those obtained in previous works.[53,83] DFT calculations were performed with the Gaussian 09 program.[94]

3.2.4 Results and discussion

The notion of hydrolysis of platinum(II) anticancer complexes as a bimolecular nucleophilic substitution S_N2 has been widely accepted on the basis of a large number of experimental data. The initial square-planar complex is converted to a bipyramidal (5-coordinated) transition state (TS), in which the incoming water molecule and the leaving chloride are weakly bound to the metal.[77] The structural features of this trigonal bipyramid are relevant for determining the hydrolysis activation barrier.

The first hydrolysis (first step) leads to the ring-opening process, with the 3-Hfl and etga derivatives remaining mono-coordinated to the metal ion center. The second hydrolysis (second step) leads to the complete release of 3-Hfl and etga. The reaction profile of the hydrolysis reaction in *cis*-[Pt(PMe_3)$_2$(etga)] is discussed in paragraph 3.2.4.1, while the reaction profile for the hydrolysis reaction in *cis*-[Pt(PMe_3)$_2$(3-Hfl)]$^+$ is discussed in paragraph 3.2.4.2.

3.2.4.1 Hydrolysis reaction in cis-[Pt(PMe_3)$_2$(etga)]

In Table 2 some selected bond lengths and angles along with the experimental data (with relative estimated standard deviations (esd)) for *cis*-[Pt(PMe_3)$_2$(etga)] are reported (Figure 5).[76] The calculated bond lengths and angles are in good agreement with the experimental ones, confirming the reliability of the used computational protocol; the mean absolute error (MAE) and root-mean-square deviation (RMSD) index[95] calculated on bond lengths are 0.002 Å and 0.006 Å respectively.

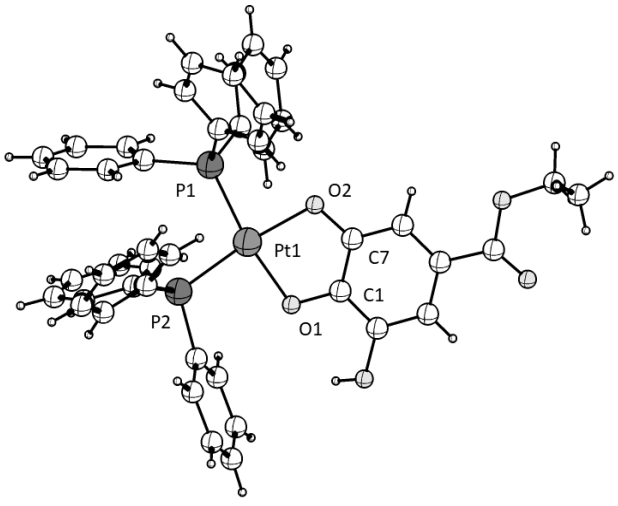

Figure 5 Crystal structures of *cis*-[Pt(PPh_3)$_2$(etga)].

Table 2 Comparison selected bond lengths (Å) and angles (°) in *cis*-[Pt(PMe_3)$_2$(etga)] (optimized structures) and in *cis*-[Pt(PPh_3)$_2$(etga)] (experimental X-ray structures) with relative esd (in parentheses).

Bond distances			Angles		
	Exp.	Calc.		Exp.	Calc.
Pt1-P1	2.257(2)	2.255	P1-Pt1-P2	99.2(9)	103.16
Pt1-P2	2.261(2)	2.256	P1-Pt1-O2	87.4(2)	83.24
Pt1-O2	2.050(8)	2.033	P2-Pt1-O2	172.3(2)	173.55
Pt1-O1	2.031(7)	2.041	P1-Pt1-O1	169.7(2)	166.75
C7-O2	1.358(1)	1.351	P2-Pt1-O1	90.6(2)	90.07
C1-O1	1.353(1)	1.348	Pt1-O1-C1	110.5(6)	101.43

The investigated reaction paths for the hydrolysis of *cis*-[Pt(PMe_3)$_2$(etga)] shown in Scheme 6a are reported in Figure 6, while energy (E) profiles are reported in Figure 7. Energy (E) values are referred to separated reactants (R) rather than reactant adducts (RA) (Figure 6) since it is widely accepted that, at the beginning of the reaction, the water molecule in the second coordination shell of the metal is possible only in vacuum, but it seems an artifact in solution.[83] Relevant bond distances of all optimized complexes are reported in Table A1 and A2 in appendix A. The energy values corresponding to Figure 7 are reported in Table A3 in appendix A. The detachment of the etga ligand in the first hydrolysis can occur in two different ways (Scheme 6a): by breaking the bond connecting the oxygen in α position to the OH group (O1 path) or by breaking the other P-O bond (O2 path). Both O1 and O2 paths (Figure 6a) showed a proton transfer from the incoming water molecule to the closer oxygen of the ligand (OL). The result obtained through DFT calculations had been previously reported for the hydrolysis of other platinum drugs in neutral conditions.[82,96] The products obtained in the second step of the hydrolysis reaction (Figure 6b) are the di-hydroxo complex and the formation of free etga. Mono- and di-hydroxo complexes should form under physiological conditions, but it has been reported that the local pH in the vicinity of macromolecules could be different from the physiological one.[97,98] The energy profiles for the first step (Figure 7a) show that the formation of the reactant adducts (RA1-O1 and RA1-O2) is energetically favored, although the RA1 obtained for the O2 path is slightly more stable (Figure 6a and Table A3 in appendix A).

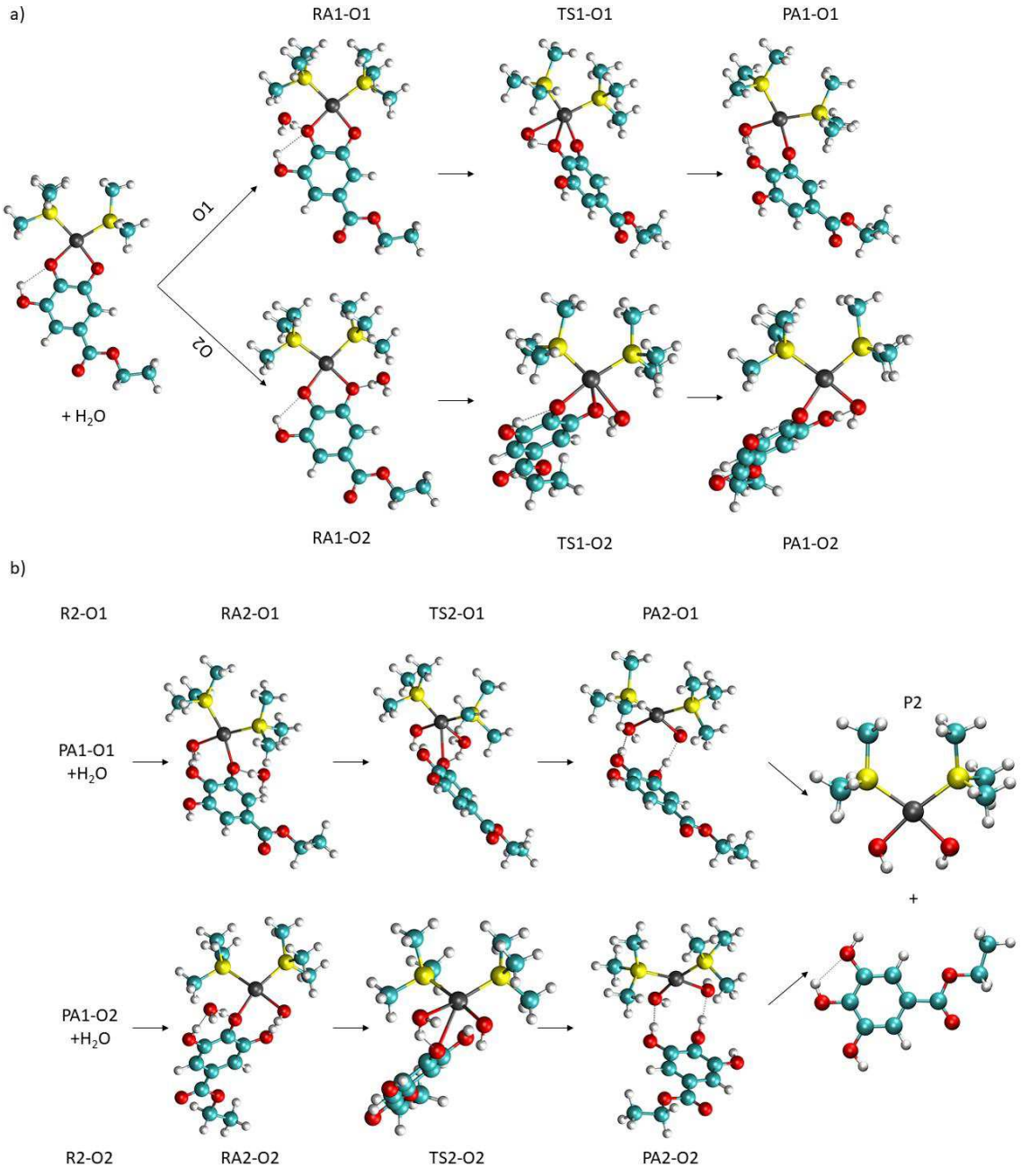

Figure 6 a) Optimized structures for the first step of the hydrolysis of *cis*-[Pt(PMe_3)$_2$(etga)]; b) optimized structures for the second step of the hydrolysis of *cis*-[Pt(PMe_3)$_2$(etga)].

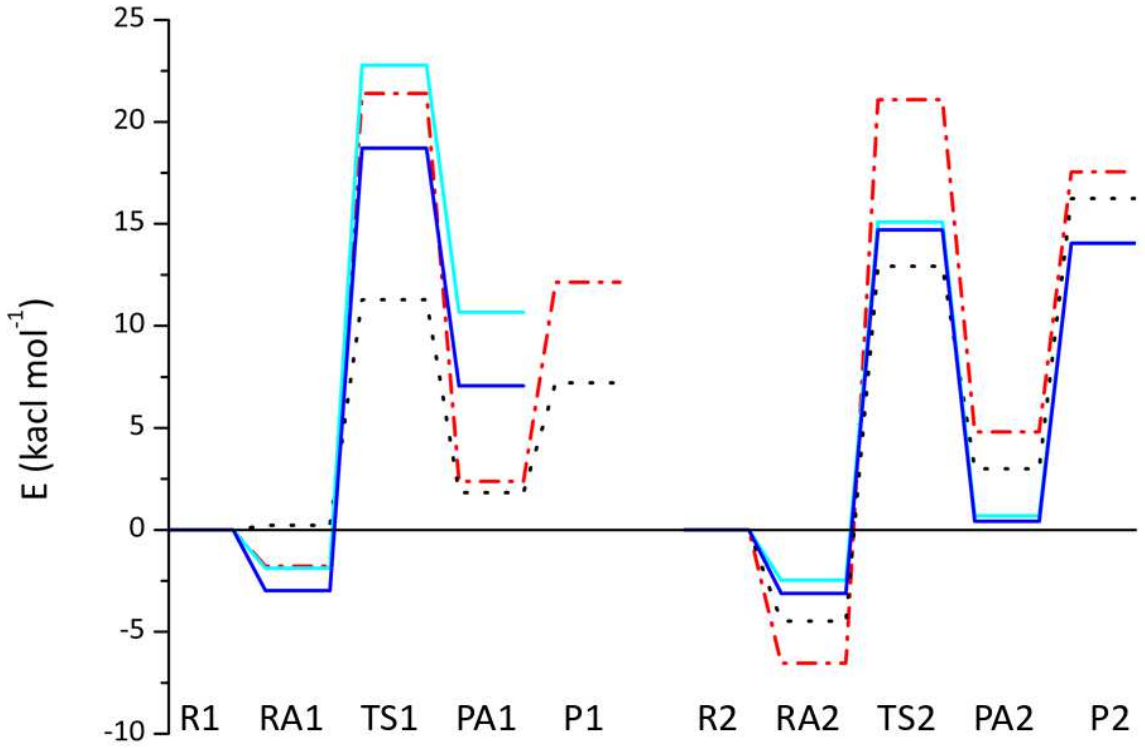

Figure 7 Activation energy profiles for the hydrolysis of *cis*-[Pt(PMe$_3$)$_2$(etga)] in PCM water. The E_a of Cisplatin and *cis*-[PtCl$_2$(PMe$_3$)$_2$] are reported for comparison.

Both transition states, TS1-O1 and TS1-O2, show a penta-coordinated structure according with an associative S_N2 reaction. The imaginary frequencies observed in the transition states are about 99.7 cm^{-1} for TS1-O1 and 157.8 cm^{-1} for TS1-O2. The analysis of such vibrational modes clearly indicates the rupture of the bond between platinum and the etga ligand (Pt-OL) and the formation of the metal-water bond. The activation energies ($E_a = E_{transition\ state} - E_{reactants}$) for the two paths are rather different: E_a = 22.8 kcal mol^{-1} for the O1 path and a E_a = 18.7 kcal mol^{-1} for the O2 path (Table A3 in appendix A). According to the results, the release of etga upon opening of the Pt-O2 bond is kinetically preferred. Furthermore, such pathway leads to the most stable product ($\Delta E = E_{PA1\text{-}O1} - E_{PA1\text{-}O2}$ = 3.6 kcal mol^{-1}). The difference could be due to the formation of a hydrogen bond (H-bond) between OH and the oxygen in α to OH (Figure 8) in TS and in products.

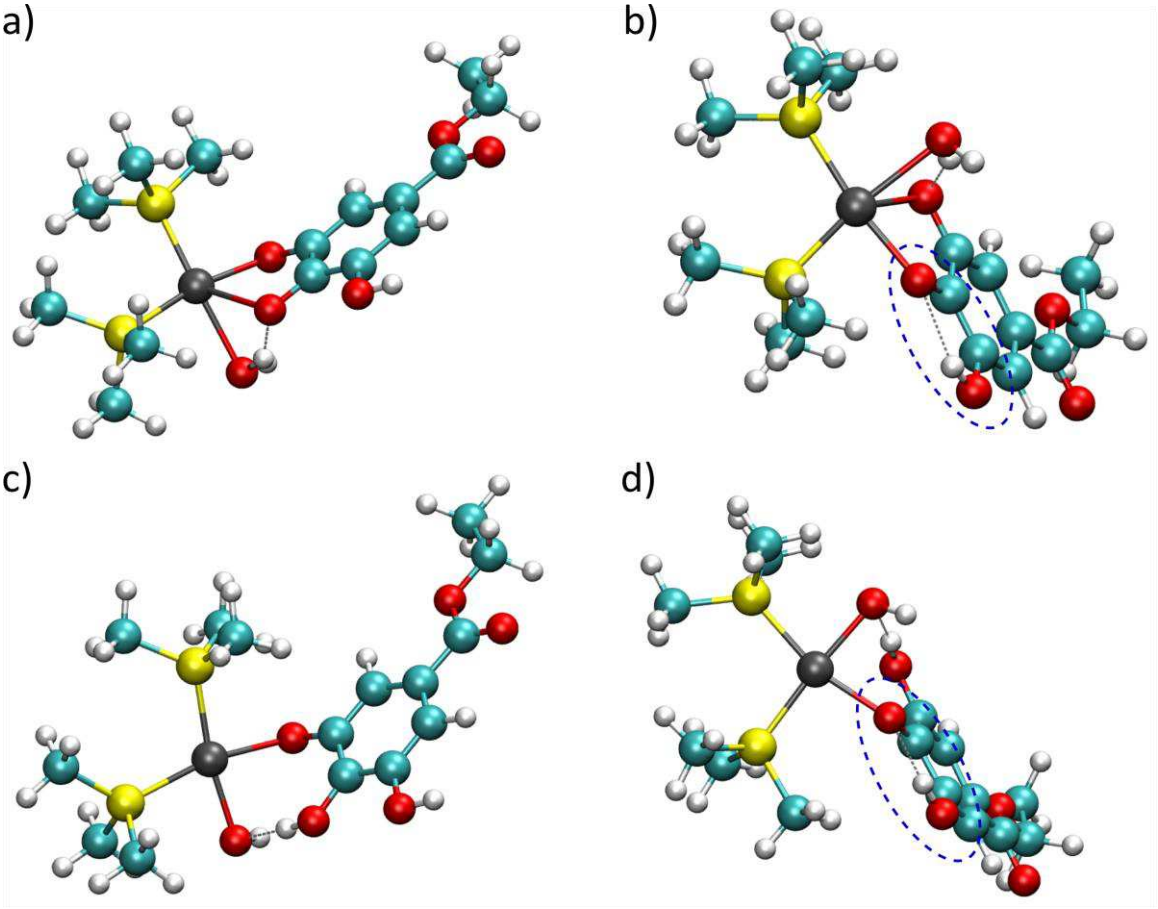

Figure 8 Optimized structures of a) TS1-O1, b) TS1-O2, c) PA1-O1 and d) PA1-O2, the most important hydrogen bonds are highlighted in blue.

The transition states in the second hydrolysis have a penta-coordinated structure with imaginary frequencies of 103.9 cm^{-1} for TS2-O1 and 101.7 cm^{-1} for TS2-O2 (Figure 6b). The analysis of the two vibrational modes clearly indicates the rupture of the bond between platinum and the etga ligand (Pt-OL) and the formation of the metal-water bond.

The calculated profiles (Figure 7b) show that the two reaction paths have comparable activation energy ($\Delta E_a = E_{aTS2\text{-}O1} - E_{aTS2\text{-}O2}$ = 0.4 kcal mol^{-1}, Table A3 in appendix A). In addition, the final products (P2) do not show a significant energy difference (Table A3 in appendix A).

As shown in Figure 7 (Table A3 in appendix A), the first hydrolysis step has a higher E_a compared to the second step, irrespective of the ring opening order; thus, the first hydrolysis process is the rate determining step (RDS) of the whole reaction leading to the release of etga in the solution.

When comparing the energy profiles of *cis*-[Pt(PMe_3)$_2$(etga)] with those of the highly cytotoxic cisplatin in the first hydrolysis (Figure 7a), the E_a in the O2 path appears to be lower than the E_a of cisplatin ($\Delta E_a = E_{a\text{-}TS1\text{-}O2} - E_{a\text{-}cisplatin}$ =−2.7 kcalmol^{-1}). On the contrary, the E_a in the O1 path is higher than the one calculated for cisplatin (ΔE_a = +1.4 kcal mol^{-1}) (Figure 7a, Figure A1, Table A3 and Table A4 in appendix A). In the second hydrolysis step, E_a values for both O1 and O2 paths are much lower than cisplatin E_a value (ΔE_a = −6 kcal mol^{-1} for O1 path and ΔE_a = −6.4 kcal mol^{-1} for O2 path) (Figure 7b, Figure A2, Table A3 and Table A5 in appendix A). The results obtained suggest that *cis*-[Pt(PMe_3)$_2$(etga)] leads to a mono-hydroxo complex with etga mono-coordinated to the metal, which promptly reacts with another water molecule, giving the di-hydroxo species. The mono-hydroxo and di-hydroxo species are considered poorly reactive for DNA coordination, therefore their formation can limit the efficacy of a platinum metallodrug.[4] Furthermore, the low activation energy barriers of the second step and the consequent high hydrolysis reaction rate might make this complex subject to fast degradation, causing potentially poor pharmacological activity.[99] The obtained E_a value (11.3 kcal mol^{-1}) calculated for the first hydrolysis of *cis*-[$PtCl_2(PMe_3)_2$], analogue of the cisplatin but biologically inactive, is much lower than the E_a calculated for *cis*-[Pt(PMe_3)$_2$(etga)] and cisplatin (Figure 7 and Table A3 in appendix A). Finally, the E_a calculated for the second hydrolysis of *cis*-[Pt(PMe_3)$_2$(etga)] is close to the E_a of *cis*-[$PtCl_2(PMe_3)_2$] (Figure 7) and much lower than cisplatin. On the basis of the DFT calculations, the complex *cis*-[Pt(PMe_3)$_2$(etga)] should not be expected to be highly cytotoxic.

3.2.4.2 Hydrolysis reaction in cis-[Pt(PMe$_3$)$_2$(3-Hfl)]$^+$

The investigated reaction paths for the hydrolysis of *cis*-[Pt(PMe$_3$)$_2$(3-Hfl)]$^+$ (Scheme 6b) are reported in Figure 9, while the energy profiles are reported in Figure 10. The energy values corresponding to Figure 10 profiles and the relevant bond distances of all optimized complexes are reported in Table A3-A6 and in Table A7 in appendix A.

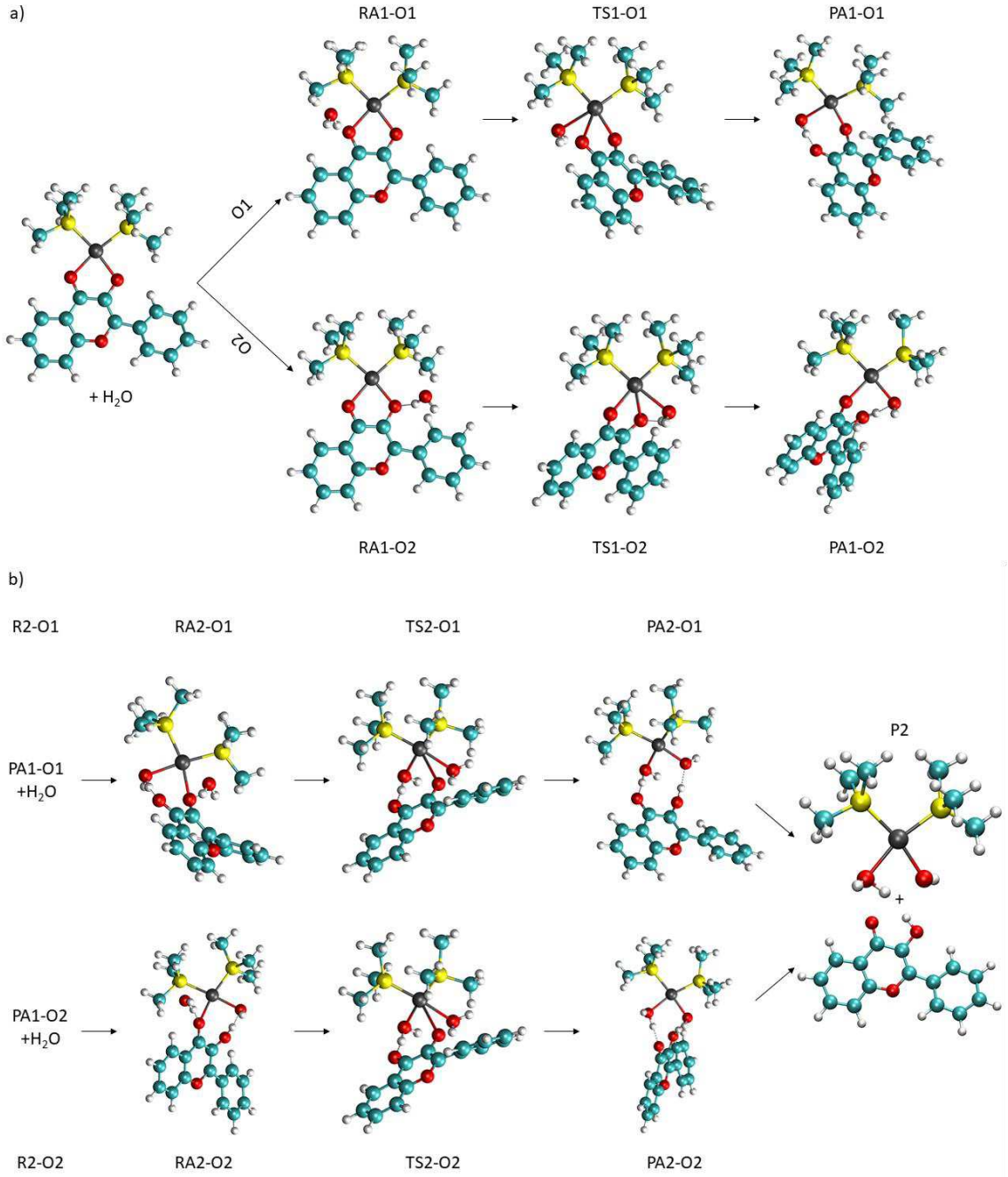

Figure 9 a) Optimized structures for the first step the hydrolysis of *cis*-[Pt(PMe$_3$)$_2$(3-Hfl)]$^+$; b) optimized structures for the second step the hydrolysis of *cis*-[Pt(PMe$_3$)$_2$(3-Hfl)]$^+$.

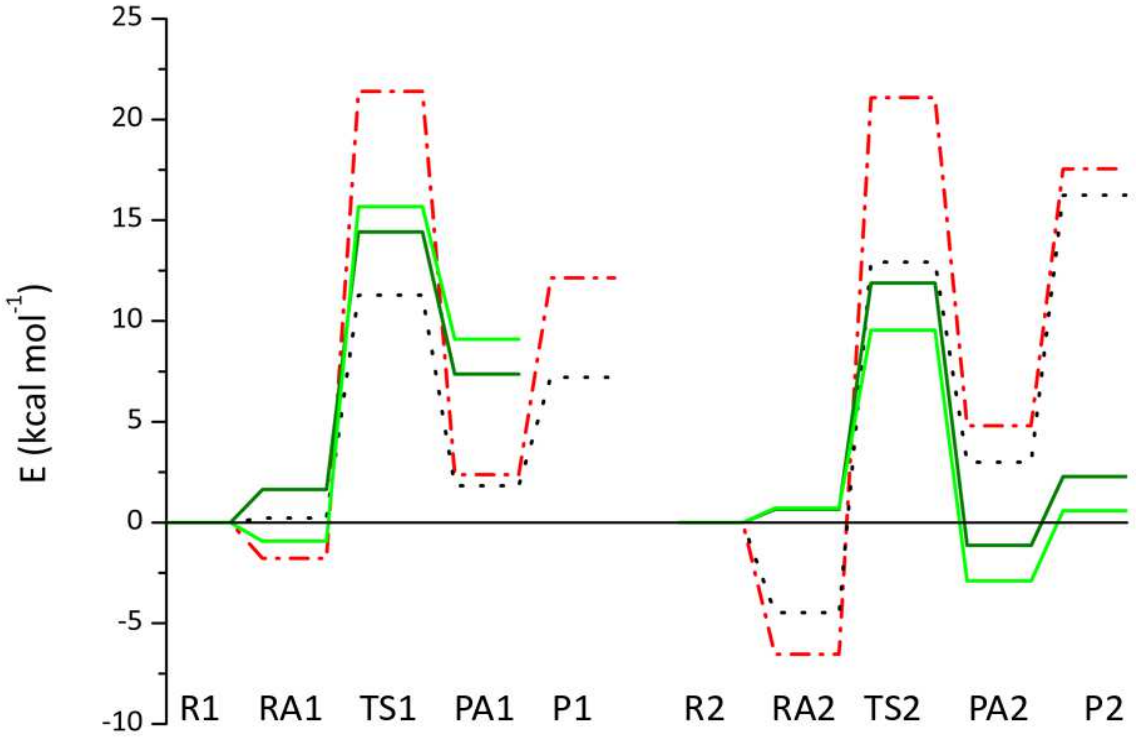

Figure 10 Activation energy profiles for the hydrolysis of *cis*-$[Pt(PMe_3)_2(3\text{-Hfl})]^+$ in PCM water. The E_a of Cisplatin and *cis*-$[PtCl_2(PMe_3)_2]$ are reported for comparison.

The formation of the intermediate RA1-O2 is slightly energetically favored, while RA1-O1 formation energy is slightly positive. The difference is probably due to the stronger interaction between the O atom of the 3-Hfl ligand and the H atom of the incoming water present in RA1-O2. Indeed, an H-bond between such atoms is observed in RA1-O2, but not in RA1-O1 (see Figure 9a); the distance between O and H is 1.883 Å in RA1-O2 and 2.116 Å in RA1-O1.

As in the previous case, the transition states of both O1 and O2 paths have a penta-coordinated structure with imaginary frequencies of 87 cm^{-1} for TS-O1 and 78 cm^{-1} for TS-O2. The calculated E_a value is 15.7 kcal mol^{-1} for the O2 path and E_a = 14.4 kcal mol^{-1} for the O1 path. The O1 opening produces a mono-*aquo* derivative, while in the O2 path a proton transfer leading to the mono-hydroxo complex occurs. The PA1-O1 is also more stable than PA1-O2 ($\Delta E = E_{PA1\text{-}O1} - E_{PA1O2}$ = -1.7 kcal mol^{-1}, Table A3 in appendix A). Here again, the difference could be related to the formation of an H-bond between the O atom of the 3Hfl ligand and the coordinated water; the distance between the atoms is 1.443 Å in PA1-O1 and 1.542 Å in PA1-O2. In conclusion, in the first hydrolysis step the O1 path,

leading to a mono-aqua Pt complex, should be more favored than the O2 path (which leads to a mono-hydroxo Pt complex).

In the second hydrolysis (Figure 10b), transition states with a penta-coordinated Pt geometry are characterized by a single imaginary frequency (imaginary frequencies: 89 cm^{-1} for TS2-O1 and 83 cm^{-1} for TS2-O2). The calculated E_a values are 11.9 kcal mol^{-1} and 9.5 kcal mol^{-1} for the O1 and O2 path respectively (Table A3 in appendix A). Therefore, first hydrolysis is the rate determining step of the process leading to the complete release of the 3-Hfl for *cis*-$[Pt(PMe_3)_2(3\text{-Hfl})]^+$ too. Furthermore, a comparison between the obtained E_a (Figures 7 and 10, Table A3 in appendix A) shows that in both the first and the second step the hydrolysis reactions for *cis*-$[Pt(PMe_3)_2(3\text{-Hfl})]^+$ proceed faster than the reactions for cisplatin (Figure 7 and Table A3 in appendix A). On the contrary, the hydrolysis of *cis*-$[Pt(PMe_3)_2(3\text{-Hfl})]^+$ is slower than the hydrolysis of *cis*-$[PtCl_2(PMe_3)_2]$ in the first step and faster in the second one. In the O1 path, the final product shows a proton transfer from the water molecule bonded to platinum to the closest oxygen of the ligand, while in the O2 path such transfer does not occur. The final product of *cis*-$[Pt(PMe_3)_2(3\text{-Hfl})]^+$ hydrolysis is the mono-*aquo*-mono-hydroxo complex *cis*-$[Pt(PMe_3)_2(H_2O)(OH)]^+$ (see Figure 9b). On the one hand, on the basis of the DFT calculations, some synergic cytotoxic effect between the platinum center and the 3-Hfl leaving group effect might be expected for *cis*-$Pt[(PMe_3)_2(3\text{-Hfl})]^+$, because the mono-*aquo* platinum species formed in both the first and second hydrolysis steps could coordinate DNA.[25] On the other hand, the theoretical hydrolysis activation energy, mainly affected by the *trans* influence of the carrier ligand, is significantly lower with respect to cisplatin (Figure 10) and could lead to a fast deactivation of the platinum compound and, thus, to a poorer biological activity.[99]

3.2.5 Conclusions

In the case of *cis*-$[Pt(PMe_3)_2(etga)]$, the formation of the hydroxo species has been observed in both steps and both reactive pathways (Figure 6). In the case of *cis*-$Pt[(PMe_3)_2(3\text{-Hfl})]^+$, the formation of a mono-*acquo* species can be observed in the O1 path, while in the O2 path the formation of mono-hydroxo occurs (Figure 9a). The opposite behavior takes place in the second step, with the formation of *cis*-$[Pt(PMe_3)_2(H_2O)(OH)]^+$ as the final product. In both complexes, the rate determining step

is the first step of the hydrolysis reaction, the one controlling the release of the polyphenols. The activation energies (except for the O1 opening in the *cis*-[$Pt(PMe_3)_2$(etga)] first hydrolysis) are significantly lower than those calculated for cisplatin and closer to the *cis*-[$PtCl_2(PMe_3)_2$] complex. The results suggest that tuning the hydrolysis rate is fundamental to design an effective combined platinum-polyphenol drug.

3.3 Phenanthriplatin, a Unconventional Platinum Drug: Disentangling the Hydrolysis and DNA-binding Mechanisms by Theoretical Calculations

3.3.1 Introduction

Despite the clinical success enjoyed by cisplatin, carboplatin, and oxaliplatin, the treatment with such compounds causes a number of deleterious side effects that have already been discussed.[8,33,46] Moreover, another serious limitation of the current platinum-based drugs lies in the fact that some types of cancer are inherently resistant to treatment and many others develop resistance with time.[100] In an effort to circumvent the mechanisms that give rise to such inherent or acquired resistance and to mitigate other side-effects, platinum compounds deviating in structure from the prescripts of the traditional SARs have been investigated. The hypothesis is that a difference in structure will result in an altered mechanism of action and, consequently, in a different spectrum of anticancer activity.

Several different strategies have been used to design drugs that could be more selective and less toxic than traditional metallodrugs, e.g., complexes with *trans*-stereochemistry, polyplatinum molecules, platinum-tethered intercalators, and monofunctional complexes.[7] Moreover, Pt(IV) complexes have also been studied and are believed to act primarily as prodrugs that release active Pt(II) species following their intracellular reduction.[101] Among them, the monofunctional platinum complexes have emerged as promising *non*-classical platinum drug candidates.[102] The *cis*-$[Pt(NH_3)_2(pyridine)Cl]^+$ cation, called pyriplatin, was the first monofunctional platinum compound to be studied. Pyriplatin contains only a single leaving chloride ligand so, unlike cisplatin, can only form a monofunctional adduct on DNA after the activation by the hydrolysis reaction. The

nature of such adduct was revealed by an X-ray crystallographic analysis and is reported in Figure 11 together with the schematic structure of pyriplatin.[103] Compared with cisplatin-DNA adducts (see Figure 3), pyriplatin only causes a little distortion of the DNA structure. However, the pyriplatin lesion can inhibit the RNA polymerase II enzyme and, consequently, the transcription in cells as readily as the site-specific bifunctional cisplatin lesion.[104] The polymerase was unable to extend the RNA transcript past the pyriplatin lesion. In order to better understand the interaction of the pyriplatin lesion with RNA polymerase II, the crystal structure of the enzyme stalled at the lesion was solved.[105] The X-ray analysis shows that the growing RNA strand terminated at the post-translocation step of transcription. Such result stands in contrast to similar stalling induced by cisplatin, which block RNA polymerase II procession at the translocation step.[106] Detailed analysis of the crystal structure indicated the steric bulk of the pyridine ligand to be instrumental in blocking subsequent translocation. Moreover, the monofunctional lesions formed by pyriplatin are repaired by NER, but not with the same fidelity as bifunctional lesions.[104]

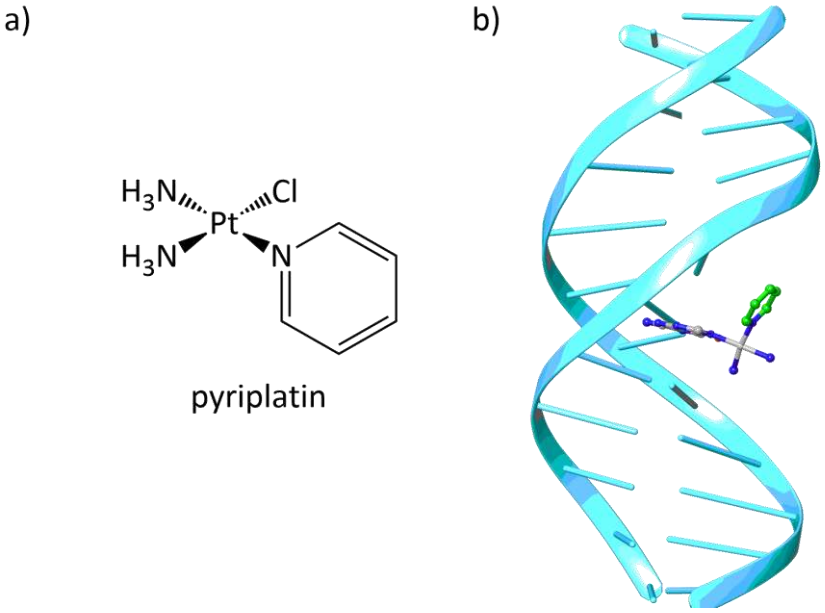

Figure 11 a) Schematic structure of pyriplatin, b) X-ray pyriplatin-DNA adduct[103].

However, the cytotoxicity of pyriplatin was found to be much lower than the cytoxicity of cisplatin.[107] The structural studies with RNA polymerase II highlighted the importance of steric hindrance on enzyme action by the pyridine ligand. In order to improve its efficacy, different N-heterocyclic Am of *cis*-$[Pt(NH_3)_2(Am)Cl]^+$ was systematically varied with an

emphasis on increasing steric bulk.[108] The results of these studies indicated that the most potent compound was the one in which Am was phenanthridine (see Scheme 7).

Such complex, called phenanthriplatin, exhorts a significantly greater cytotoxicity than cisplatin in the NCI60 panel of cancer cells.[7,40,102,103,108] The panel is made of the 60 human cancer cell lines used by the National Cancer Institute (NCI) to screen compounds for anticancer activity.[109] The mechanism of action of phenanthriplatin is analogous to those described above for pyriplatin, even though the large, planar structure of the aromatic phenanthridine ligand may indicate a possible interaction with DNA by an intercalative mechanism. However, experimental evidence reports that phenanthriplatin binds to DNA in a purely covalent manner, like cisplatin.[7,40]

It is worth noting that the latest experimental evidences hint that phenanthriplatin not only reacts with guanosine residues (similar to cisplatin), but also forms adducts with adenine residues (the most nucleophilic site after guanosine), a behaviour which has never been observed for cisplatin.[110] More specifically, the experimental measures reveal that phenanthriplatin binds to the N1 or N7 position of 9-methyladenine (see Scheme 3), while the reaction with 9-methylguanine mainly leads to the formation of the N7 adduct. Furthermore, due to the rotation of the aromatic ligands, the N1 and N7 adducts of 9-methyladenine exist as two diastereomeric species, and their activation energies for ligand rotation are comparable. In the end, kinetic analysis show that phenanthriplatin reacts more rapidly with 9-methylguanine than with 9-methyladenine, indicating that the distribution of lesions formed on DNA is kinetically controlled.

3.3.2 Aim of this work

As reported above, many theoretical studies have been done to define the reaction energy profiles of hydrolysis reaction.[53,77–88] Moreover, the reaction between Pt complexes and DNA bases like guanine and adenine has been extensity studied,[111–117] as well as the reaction with sulfur molecule.[118,119]

In 2003 Baik and his co-workers studied the reaction between mono-aqua cisplatin and guanine or adenine bases using DFT calculation. The results show that guanine is 3-4 orders of magnitude more reactive toward cisplatin than adenine. Such difference is due to two effects: firstly, the transition state is characterized by a strong hydrogen bond between the ammine-hydrogen of cisplatin and the O=C moiety of guanine while when adenine is binds, only a weak hydrogen bond is formed between the chloride ligand of cisplatin and the H_2N-C group of adenine. Secondly, a significantly stronger molecular orbital interaction is identified for guanine compared to adenine.

To the best of our knowledge, however, no theoretical comparison work between phenanthriplatin and cisplatin, which could help to design a new generation of monofunctional drugs, is reported in the literature, where only a few theoretical works studying the diastereoselectivity of phenanthriplatin can be found. In 2014 Johnstone ad co-workers[120] performed a set of molecular mechanics and DFT calculation to study such topic. They found out that the energetic difference between the two diastereomeric forms is small. The origin of the diastereoselectivity seems to result from the rotation of the phenanthridine ligand, which relieves steric congestion over one face of the platinum complex. Herein, we present a computational study of the chloride hydrolysis of phenanthriplatin, and the reaction between such complex and 9-methyladenine, 9-methylguanine, cysteine in comparison with cisplatin (see scheme 7). Given the great potential of the complex, the purpose of my work is to clarify the reaction mechanisms of phenanthriplatin and to confront them with those obtained for cisplatin by means of DFT calculations.

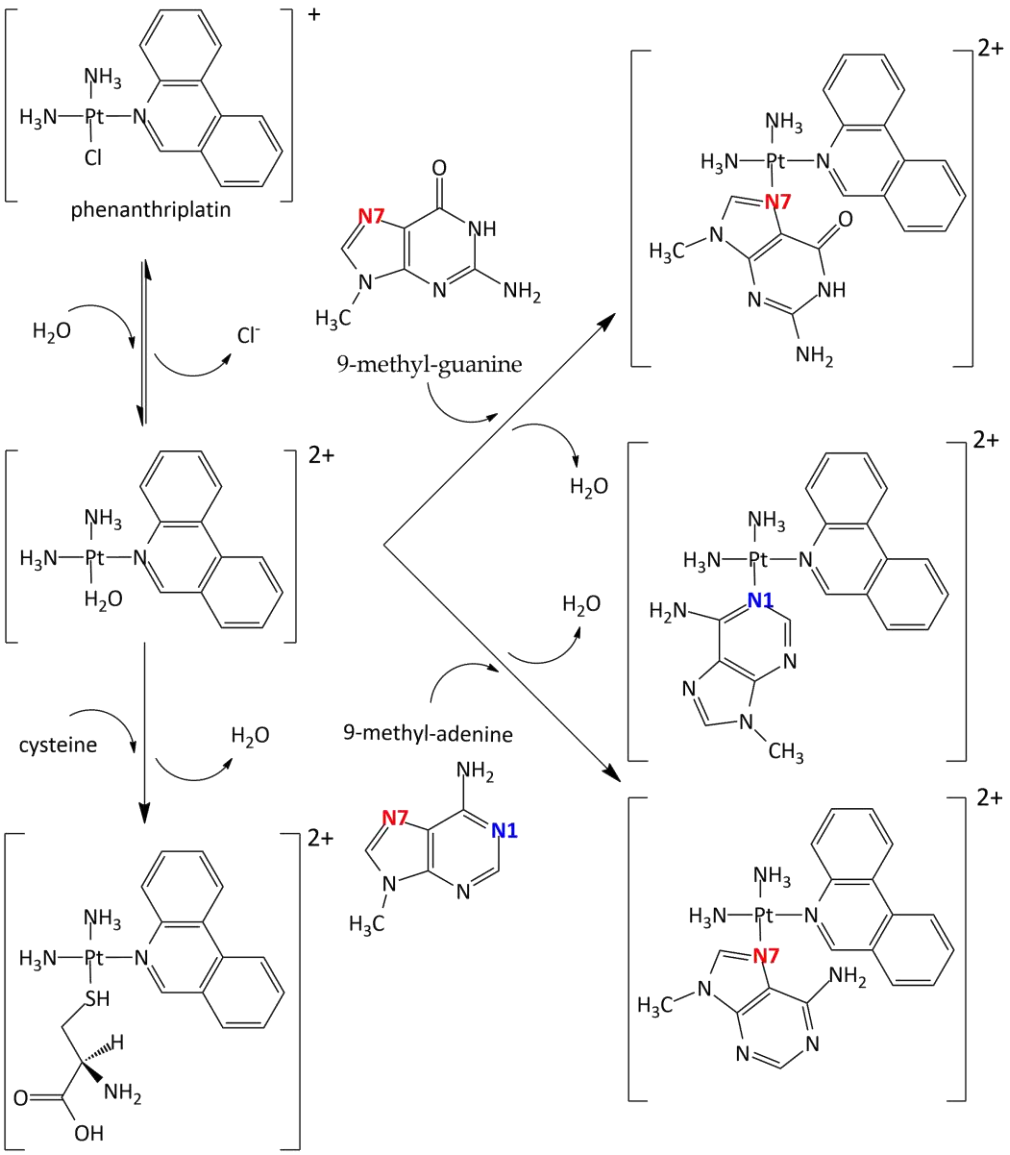

Scheme 7 Schematic representation of phenanthriplatin and the reaction studied in this thesis.

3.3.3 Computational details

All DFT calculations were performed at the M06 level of theory[121,122] using Gaussian 09 program.[94] Previous works have shown that M06 hybrid density functional provides reliable results for thermochemistry and kinetics of organometallic compounds.[123–128] However, the reaction between phenanthriplatin and the bases was also investigated using M06 and B3LYP[129] functionals with the inclusion of the latest dispersion contribution correction (D3) of Grimme.[130]

Geometry optimizations were carried out in vacuum with a 6-311+G(d,p) basis set for all atoms except the platinum atom, which was described by the quasi-relativistic Stuttgart-

Dresden pseudopotential (SDD).[89] In order to confirm that stationary points were actually minima or transition state (TS) geometries, analytical calculations of second derivatives of the energy and vibrational frequency analysis were carried out. The character of the transition states was confirmed by existence of a single negative eigenvalue of the hessian matrix corresponding to the appropriate antisymmetric stretching mode. Due to the key role of solvation in influencing thermodynamic and kinetic parameters in metal complex reactivity, environmental effects were introduced by representing water surrounding the reagents, transition states and products as a polarizable continuum method (PCM).[93] Single point calculations on the gas phase optimized geometries were performed using PCM on the M06, M06-D3 and B3LYP-D3/6-311+G(d,p)/SDD level of theory. All solvation calculations were carried out in water. Since the solvent is also the reagent, it has been represented as an explicit H_2O molecule added to the initial reagent (R).[76,83] The initial position of the molecule is between the N atom and the Cl atom at about 3.5 Å from the Pt atom (RA). After the TS, the leaving Cl atom are in proximity of the *aqua*-complex (products adduct, PA); in the final product (P) the Cl atom has been separated.

3.3.4 Results and discussion

Phenanthriplatin could exist as two isomers (P and M) arising from the rotation of the phenanthridine ligand along the Pt--N bond (see Scheme 8a). Aiming to provide a complete picture of the phenanthriplatin reactivity, we included both structures in our computational approach and calculated the reaction involving isomer P and insomer M of phenanthriplatin to understand how a different stereochemistry can influence the activation energy barriers.

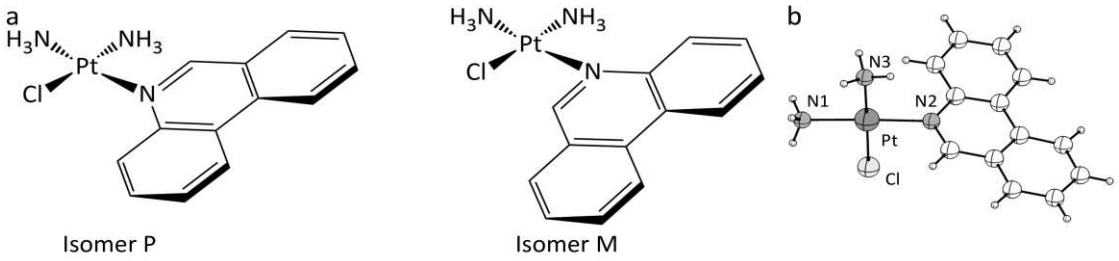

Scheme 8 a) The two possible phenanthriplatin isomers, labelled as P and M depending on the orientation of the phenanthridine ring b) X-ray structures of structures of phenanthriplatin.

3.3.4.1 Hydrolysis reaction

The work started by analysing the similarities and differences between the hydrolysis of phenanthriplatin and cisplatin, which is the rate-determining step of the process during the attack to DNA.[25] Since the structural features of the pentacoordinated structure have been shown to govern the hydrolysis activation barrier,[131,132] the accuracy of the selected computational protocol were initially assessed by comparing the optimized DFT structure with the available X-ray data (see scheme 8b and Table 3).[120] The calculated bond lengths and angles are in good agreement with the experimental ones, confirming the reliability of the used computational protocol, as can be seen from the MAE and RMSD indexes[95] calculated on bond lengths (0.027 Å and 0.044 Å respectively).

Table 3 Comparison selected bond lengths (Å) and angles (°) in phenanthriplatin, with relative esd (in parentheses) for experimental measurements.

Bond distance	Exp.	Calc.	Angles	Exp.	Calc.
Pt1-Cl	2.296(7)	2.308	Cl1-Pt1-N1	90.25(6)	85.44
Pt1-N1	2.039(2)	2.105	Cl1-Pt1-N2	87.71(6)	89.82
Pt1-N2	2.025(2)	2.062	N1-Pt1-N3	89.08(8)	95.70
Pt1-N3	2.047(2)	2.145	N2-Pt1-N3	92.95(8)	89.02

The optimized structures of R, RA, PA, P and TS are shown in Figure 12 while the structure of cisplatin is reported in Figure A3. Relevant bond distances and angles of the optimized complexes are reported in Table A8-A10 in appendix A (see also Figure A4 in appendix A). The Gibbs reaction free energy (G) profiles are shown in Figure 13 (see also Table A11 in appendix A). This activation energy will then be compared to the one obtained for the first hydrolysis of cisplatin.

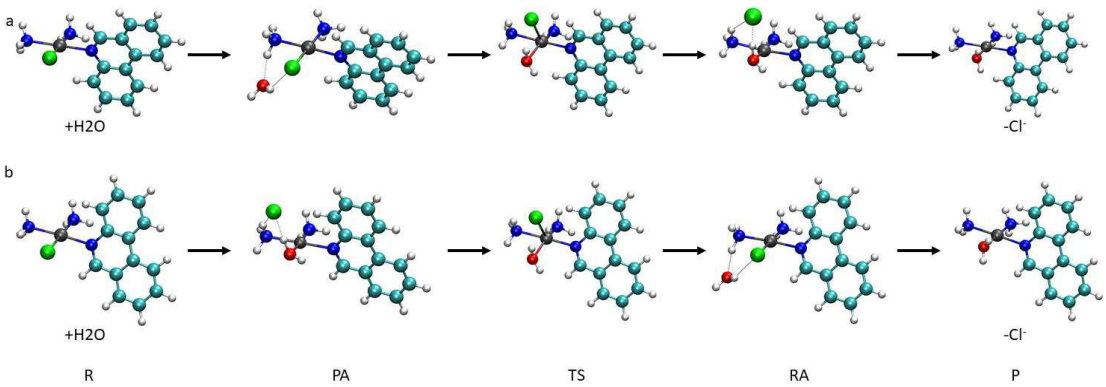

Figure 12 Optimized structures for the hydrolysis reaction of isomers P (a) and isomers M (b).

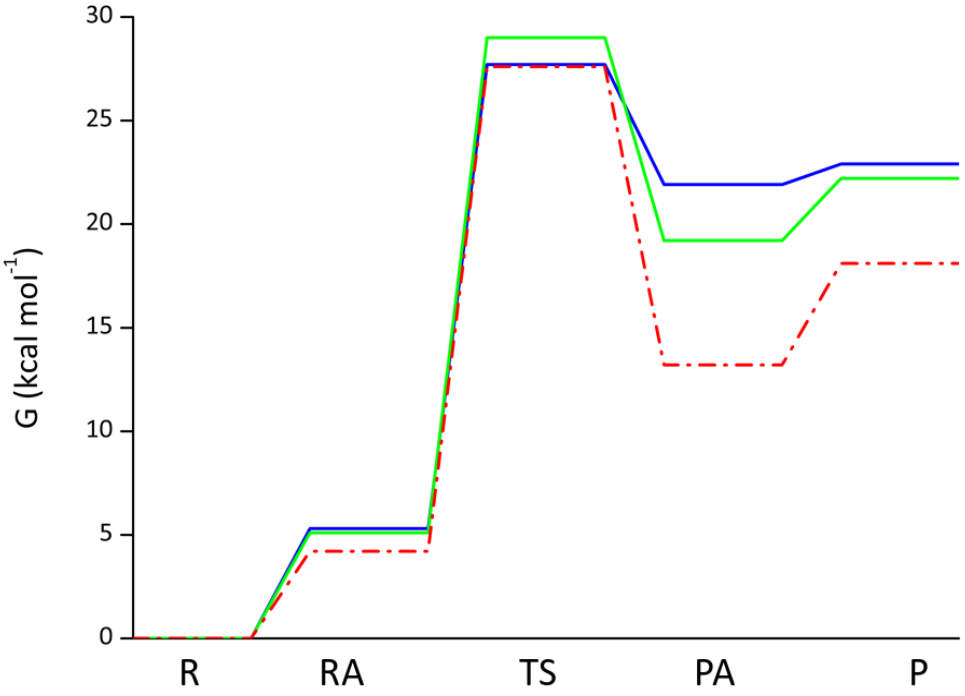

Figure 13 Activation Gibbs free energy profiles of isomers P (blue line) and isomers M (green line) and first step (red dot line) of the hydrolysis of cisplatin in PCM water.

The G energy profiles (Figure 13) for the hydrolysis reaction show that the RAs of isomers P and M of phenanthriplatin lie above the reactant molecules and present similar values (5.3 and 5.1 kcal mol^{-1} respectively see also Table A11 in appendix A). In both cases, the formation of a hydrogen bond (H-bond) between the O atom of the water and the H atom of the ammonia group (Figure 12) is observed.

As expected, the initial square-planar complexes become a bipyramidal TS. The analysis of the single-imaginary vibrational mode (144.77i cm^{-1} for isomer P and 151.09i cm^{-1} for isomer M) confirms the rupture of the bond between platinum and the chloride ligand and the simultaneous formation of the metal-water bond. As shown in Figure 13, the activation Gibbs free energy barrier for isomers P and M are slightly different: isomer P has $G_a = G_{TS} - G_{RA}$ = 22.4 kcal mol^{-1}, while isomer M shows G_a = 23.9 kcal mol^{-1} (see Table S5).

The rate constants (k) for the hydrolysis reaction have been calculated by means of the Eyring equation at 298.15 K:

$$k = \frac{k_b T}{h} e^{-\frac{G_a}{RT}}$$

(eq1)

k_B is Boltzmann's constant, and h is Planck's constant. These values are k = 2.37*10^{-4} s^{-1} for isomer P and k = 1.89*10^{-5} s^{-1} for isomer M. According to the results, the release of Cl^- ligands is slightly kinetically favoured in complex P moreover the G profiles confirm that the relative position of the phenanthridine ring does not impact on the activation step of the monovalent platinum drug. Isomer M conduces to the most stable PA, where the G energy difference (ΔG_{PA} = $G_{PA\text{-isomer P}}$ - $G_{PA\text{-isomer M}}$) is 2.7 kcal mol^{-1} (see Table A11 in appendix A), probably due to the stronger interaction present in isomer M between the H atom of the coordinated water and the Cl^- ion. Indeed, an H-bond between such atoms is observed in both complexes (Figure 12), but in isomer M the distance between H and Cl^- is 1.796 Å, whereas in isomer P it is 1.873 Å. The final P is less stable in isomer P than in isomer M (ΔG_P = $G_{P\text{-isomer P}}$ – $G_{P\text{-isomer M}}$ is +0.7 kcal mol^{-1}).

The comparison between the energy profiles for the first hydrolysis reaction of cisplatin (Figure 13 and Table A11 in appendix A) and the hydrolysis of isomer P and isomer M shows that the RA for cisplatin lies above the reactant molecules and seems more stable; the ΔG_{RA} = $G_{RA\text{-isomer P or M}}$ - $G_{RA\text{-cisplatin}}$ is 1.1 kcal mol^{-1} for isomer P and 0.9 kcal mol^{-1} for isomer M (see table A11 in appendix A). Moreover, the G_a in isomer P is slightly lower than the one in cisplatin (ΔG_a = $G_{a\text{-TS-isomer P}}$ - $G_{a\text{-TS-cisplatin}}$ = -1.0 kcal mol^{-1}); on the contrary, the G_a in isomer M is slightly higher than the one calculated for cisplatin (ΔG_a = +0.5 kcal mol^{-1}) (Figure 13 and Table A11 in appendix A). For this reaction, cisplatin presents k = 4.39*10^{-5} s^{-1}, which is in excellent agreement with the experimental one (5.18*10^{-5} s^{-1}[4]) and is intermediate to the values calculated for isomer P and M. However, both PA and P for isomer P and M are less stable than PA and P obtained for cisplatin (Figure 13 and table A11 in appendix A).

In conclusion, phenanthriplatin shows activation barriers which are very similar to those obtained for the first hydrolysis reaction of cisplatin. The similarity could be related to its high cytotoxicity. In fact, low activation energy barriers and the consequent high

hydrolysis reaction rate seem to submit such complexes to fast degradation, causing potentially poor pharmacological activity.[76,99]

3.3.4.2 Reaction with bases

The interaction of the resulting *aqua*-activated phenanthriplatin with 9-methylguanine and 9-methyladenine is explored according to the general scheme depicted in Scheme 7. The latest experimental evidence[110] shows that phenanthriplatin forms bonds with N7 atom of 9-methylguanine (N7-Me-Gua), a behaviour observed also for cisplatin. However, phenanthriplatin forms bonds with N7 and N1 atoms of 9-methyladenine (N7-Me-Ade, N1-Me-Ade) too, and such a behaviour not observed for cisplatin. Unlike phenanthriplatin, cisplatin reacts with two guanine molecules, leading to the formation of intra and inter-molecular bonds with DNA.[10] The activation energy barrier for phenanthriplatin will then be compared to the one obtained for the first step (addition of one guanine molecule) of cisplatin.

In Figure 14 the optimized structures of R, RA, PA, P and TS at M06 level of theory are shown for both complexes of phenanthriplatin, while the structure of cisplatin is reported in Figure A5. Relevant bond distances and angles of optimized complexes are reported in Table A12-A18 in appendix A. The reaction G energy profiles are shown in Figure 15 (see also Table A19 in appendix A). The G energy profiles (Figure 15) for the reaction between N7-Me-Gua and phenanthriplatin show that the RA of isomer P and M lie under the reactant molecules, and that the RA of isomer P (-4.3 kcal mol^{-1}) seem to be more stable than those of isomer M (-3.0 kcal mol^{-1}, see Table A19 in appendix A). The formation of multiple H-bonds is observed in both isomers (Figure 14); the first H-bond is reported between the H atom of the coordinated water and the N7 atom of the guanine; the second one is observed between the other H atom of the coordinated water and the O atom of the guanine, and forms an additional H-bond with the H atom of the amino group of the Pt fragment.

The reaction with N7-Me-Ade and N1-Me-Ade, instead, shows a proton transfer from the coordinated water molecule to the N atom of adenine (see Figure 14). This behaviour was not observed for the reaction with guanine. However, similar proton transfer were reported in previous theoretical studies of platinum antitumor drugs interacting with adenine bases.[115]

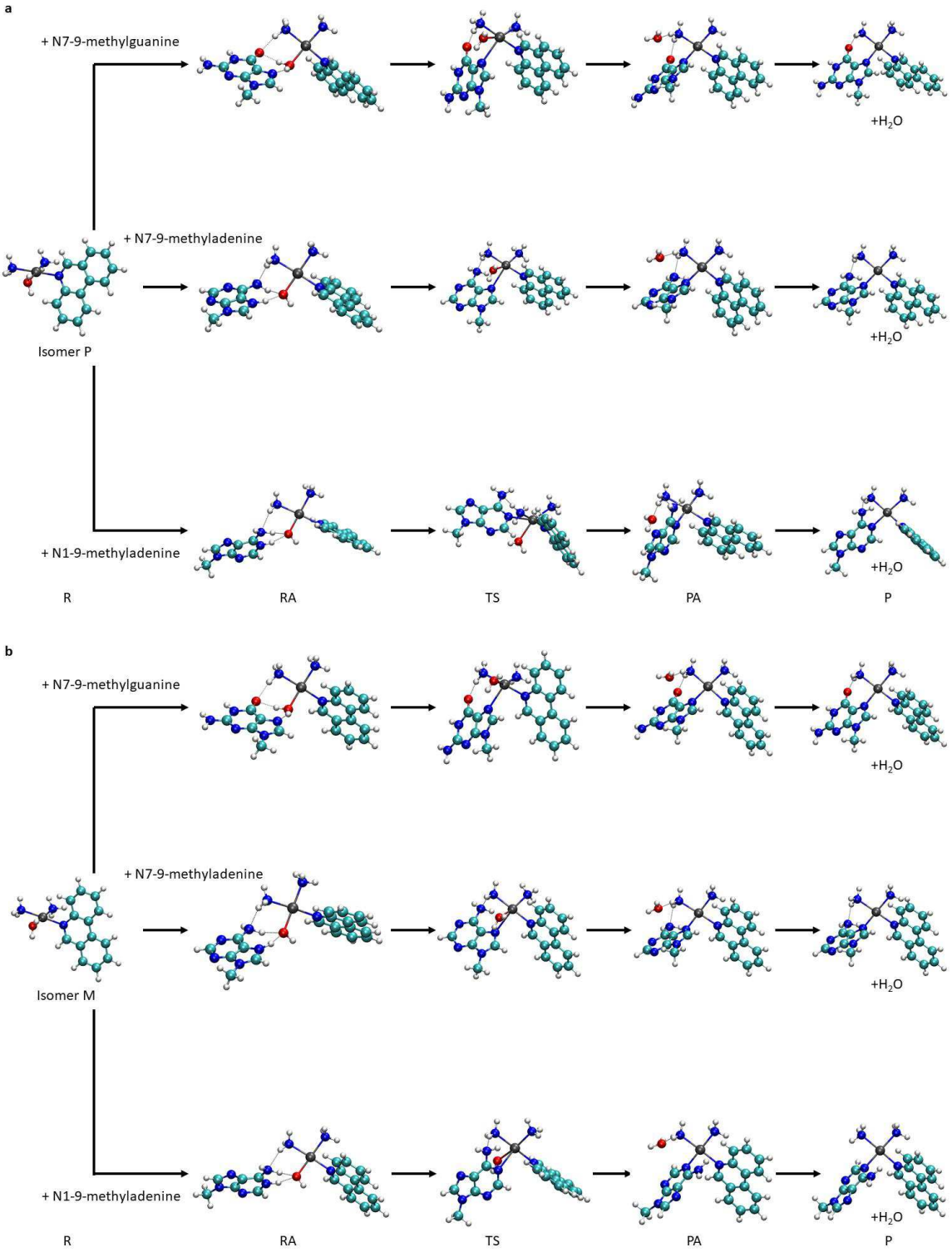

Figure 14 Optimized structures for the reaction between bases and isomer P (a) and isomer M (b) at M06 level of theory.

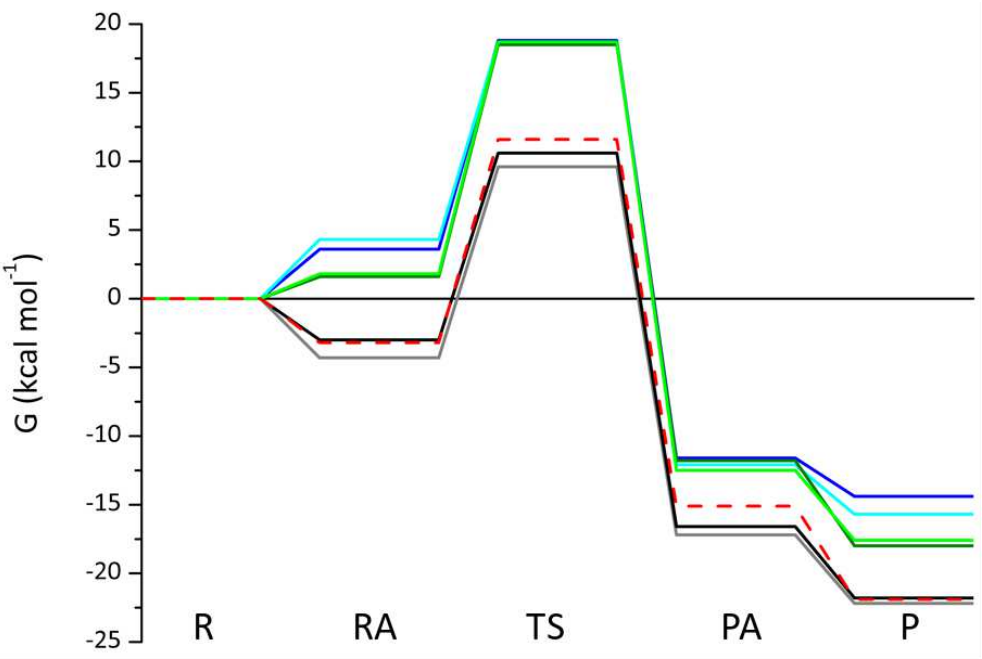

Figure 15 Activation Gibbs free energy profiles of isomer P (grey line) with N7-9-methylguanine, isomer M (black line) with N7-9-methylguanine, isomer P (blu line) with N7-9-methyladenine, isomer M (light blue line) with N7-9-methyladenine, isomer P (green line) with N1-9-methyladenine, isomer M (light green line) with N1-9-methyladenine, and first step (red dash line) of the reaction between N7-9-methylguanine and cisplatin in PCM water. At M06 level of theory.

Furthermore, the RAs for the reaction with N1-Me-Ade are more stable than those obtained for N7-Me-Ade, due to the different formation of H-bonds. As for N1-Me-Ade, the formation of three H-bonds is observed in isomer P and M. The O atom of the coordinated water molecule forms two H-bonds; the first with the H atom bond to N1 of the adenine and the second with the H atom of the N1-Me-Ade amino group (see Figure 14). The last H-bond is formed between the N atom of the amino group in N1-Me-Ade and the H atom of the amino group of the Pt fragment (see Figure 14). As for N7-Me-Ade, the RA of isomer P and M presents only two H-bonds; one between the H atom bond to N7 of adenine and the O atom of the coordinated water molecule and the second one between the N atom of the amino group of the adenine and the H atom of the amino group of the Pt fragment. In conclusion, the most stable RA was observed for N7-Me-Gua (see Figure 15 and Table A19 in appendix A), due to a greater interaction involve involving the O--H H-bond in respect to the N--H H-bond.

All transition states show a penta-coordinated structure; the imaginary frequencies, the G_a values and the relative calculated and experimental k are reported in Table 4. The

analysis of the vibrational modes clearly indicates the rupture of the bond between platinum and the water ligand (Pt-Ow) and the simultaneous formation of the metal-N bond of the N7-Me-Gua, N7-Me-Ade and N1-Me-Ade.

Table 4 Imaginary frequencies (i Freq, cm^{-1}), activation Gibbs free energy (G_a, kcal mol^{-1}), calculated (by eq1 at 298.15 K) and experimental rate constants k (s^{-1}) for the reaction between phenanthriplatin and N7-Me-Gua, N7 and N1-Me-Ade. At M06 level of theory.

	i Freq	G_a	k_{calc}	k_{exp}
Isomer-P + N7-Me-Gua	144.39	13.9	$4.03*10^{2}$	$3.6*10^{-5}$[110]
Isomer-M + N7-Me-Gua	144.64	13.6	$6.69*10^{2}$	$3.6*10^{-5}$[110]
Isomer-P + N7-Me-Ade	141.28	15.2	$4.49*10^{1}$	$4.2*10^{-6}$[110]
Isomer-M + N7-Me-Ade	149.96	14.4	$1.73*10^{2}$	$4.2*10^{-6}$[110]
Isomer-P + N1-Me-Ade	137.11	16.9	2.55	-
Isomer-M + N1-Me-Ade	129.47	16.9	2.55	-
Cisplatin + N7-Me-Gua	143.90	14.8	$8.82*10^{1}$	$3.20*10^{1}$[133]

Examining the data shown in Table 4, *aqua*-activated phenanthriplatin seems to react faster with N7-Me-Gua than N7-Me-Ade and N1-Me-Ade, while isomer M reacts slightly faster than isomer P. N7-Me-Ade, instead, seems to react faster than N1-Me-Ade; even in this case the M isomer seems to react slightly faster than the P isomer. As for N1-Me-Ade, isomers P and M show equal G_a values. The difference in reaction rates can be explained by observing the structures of the transition states (only for isomer M, where the reaction proceeds faster). All transition states have an H-bond between the H atom of the amino group of the Pt fragment and the O atom of guanine or N atom of the amino group adenine (see Figure 14). The distance between O and H is 1.756 Å for isomer M of N7-Me-Gua, 1.970 Å for isomer M of N7-Me-Ade and 2.030 Å for isomer M of N1-Me-Ade.

The reaction between *aqua*-activated phenanthriplatin and N7-Me-Gua leads to PA, which is more stable than RA (at M06 level of theory, see Figure 15), so the reaction is thermodynamically favoured in both complexes. Moreover, isomer P conduces to the most stable PA ($\Delta G_{PA} = G_{PA\text{-isomer P}} - G_{PA\text{-isomer M}} = -0.6$ kcal mol^{-1}, see Figure 15).

Such behaviour is also observed in the final products ($\Delta G_P = G_{P\text{-isomer P}} - G_{P\text{-isomer M}} = -0.4$ kcal mol^{-1}, see Figure 15, Table A19 in appendix A). The formation of H-bonds between the O atom of the guanine and H atom of the amine group is observed in both PA and P of both isomers, which are also more stable than those obtained for the reaction between phenanthriplatin and adenine.

Here too, the formation of H-bonds between the N atom of the adenine and the H atom of the amine group in Pt fragment is observed in PA and P. As for N7-Me-Ade, isomer M seems to conduce to the most stable PA (ΔG_{PA} = 0.5 kcal mol^{-1}), and the same behaviour was observed for N1-Me-Ade (ΔG_{PA} = 1.2 kcal mol^{-1}, see Table A19 in appendix A). In conclusion, the reaction between phenanthriplatin and N7-Me-Gua seems to be favoured from both a kinetic and thermodynamic point of view in respect to N7 and N1-Me-Ade, while the reaction with N1-Me-Ade seems to be thermodynamically favoured but kinetically least-favoured with respect to the reaction with N7-Me-Ade (see Table 4 and Table A19 in appendix A). According to these results, the release of water ligands and the consequent addition bases follow the order N7-Me-Gua > N7-Me-Ade > N1-Me-Ade. Such sequence is observed also experimentally[110], but the calculated reaction rates differ considerably (5-6 orders of magnitude) compared to the experimental ones (see Table 4). The inconsistency may depend on the different positions in which the bases can be found in RAs. In fact, a potential interaction between the bases and the phenanthridine rings via π-π has been observed. This type of structures were studied using M06, M06-D3 and B3LYP-D3 functionals (used for comparison). The M06-D3 and B3LYP-D3 functionals include the latest dispersion contribution correction (D3) of Grimme[130]. This contribution in simulations of weakly bonded (van der Waals, vdW) systems is indispensable to reach chemical accuracy and can influence the accuracy of thermodynamics. Such optimized structures, at M06 level of theory, are shown in Figure 16 for isomer M only, because the reaction takes place faster. Relevant bond distances and angles for optimized RA and TS are reported in Table A20 and A21 in appendix A.

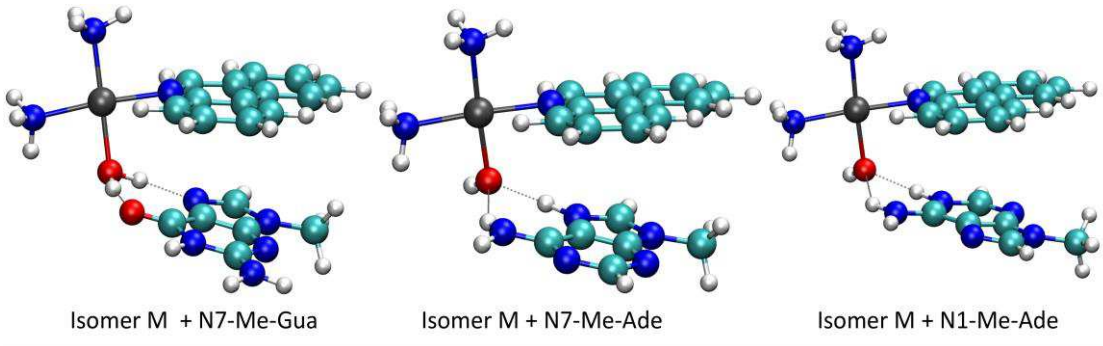

Figure 16 Optimized structures for the reagent adduct, π-π interaction between DNA bases and aromatic ligand of phenanthriplatin at M06 level of theory.

Here again, the results obtained at M06 level of theory show that the RA for the reaction with adenine has a proton transfer (see Figure 16), while no such behaviour was observed for guanine. Moreover, the formation of H-bonds is observed. The O atom of the coordinated water molecule forms two H-bonds; one with the entering N atom and one with the H atom of the amino group for N7 of adenine or the O atom of guanine (see Figure 16). Using these RAs and re-optimizing the transition states, G_a values are higher than in the previous case. The values are reported in Table 5 together with the energy difference between the RA in π-π ($RA_{\pi-\pi}$) configuration and RA ($\Delta G_{RA} = G_{RA\pi-\pi} - G_{RA}$) and relative k and imaginary frequencies.

Table 5 Energy difference between RA in π-π ($RA_{\pi-\pi}$) configuration and RA ($\Delta G_{RA} = G_{RA\pi-\pi} - G_{RA}$, kcal mol^{-1}), imaginary frequencies (i Freq, cm^{-1}), activation Gibbs free energy (G_a, kcal mol^{-1}) of theory and calculated (by eq1 at 298.15 K) and experimental rate constants k (s^{-1}). Calculation at M06, M06-D3 and B3LYP-D3 level of theory.

M06					
	ΔG_{RA}	i Freq	G_a	k_{calc}	k_{exp}
Isomer-M + N7-Me-Gua	-3.6	144.65	17.2	1.53	$3.6*10^{-5}$[110]
Isomer-M + N7-Me-Ade	-5.1	150.50	19.0	$7.36*10^{-2}$	$4.2*10^{-6}$[110]
Isomer-M + N1-Me-Ade	-4.4	128.20	22.1	$3.75*10^{-4}$	-
M06-D3					
	ΔG_{RA}	i Freq	G_a	k_{calc}	k_{exp}
Isomer-M + N7-Me-Gua	-7.2	-119.18	21.7	$7.36*10^{-4}$	$3.6*10^{-5}$[110]
Isomer-M + N7-Me-Ade	-8.5	-149.77	22.0	$4.29*10^{-4}$	$4.2*10^{-6}$[110]
Isomer-M + N1-Me-Ade	-8.1	-141.66	23.9	$1.88*10^{-5}$	-
Cisplatin + N7-Me-Gua	-	144.91	14.6	$1.32*10^{2}$	$3.20*10^{1}$[133]
B3LYP-D3					
	ΔG_{RA}	i Freq	G_a	k_{calc}	k_{exp}
Isomer-M + N7-Me-Gua	-1.6	161.81	19.3	$4.02*10^{-2}$	$3.6*10^{-5}$[110]
Isomer-M + N7-Me-Ade	-5.0	145.29	23.8	$2.39*10^{-5}$	$4.2*10^{-6}$[110]
Isomer-M + N1-Me-Ade	-6.4	135.40	25.8	$7.40*10^{-7}$	-
Cisplatin + N7-Me-Gua	-	148.65	15.3	$3.79*10^{1}$	$3.20*10^{1}$[133]

The RA structures shown in Figure 16 are more stable than those shown in the Figure 14. As a result, the formation of π-π interaction could be observed in solution. Moreover, a noticeable decrease in rate constants (Table 5) can be observed.[110] Similar results were obtained using M06-D3 and B3LYP-D3 functionals; here too, the RA for the reaction with adenine shows a proton transfer, while no such behaviour is observed for the reaction

with guanine; the same formation of H-bonds between bases and Pt-complex is observed. Again, the RAs interacting via π-π are more stable than the RAs that do not interact in this manner (see Table 5). However, the data reported in table 5 show that the introduction of the dispersion correction leads to values of the rate constants that are in better agreement with the experimental ones compared to the values calculated with pure M06 functional, highlighting the importance of such contribution. Moreover, the rate constants obtained with B3LYP-D3 functional result to be closer to the experimental ones compared to the constants obtained with M06-D3, indicating that B3LYP-D3 is better than M06-D3 for studying the reaction between phenanthriplatin and DNA bases. In fact, the G_a values are slightly higher than those calculated with M06-D3 functional. However, the rate constant for the reaction with the N7-Me-Gua, calculated with the M06-D3, is closer to the experimental one than that obtained with B3LYP-D3. Finally, the G_a values for cisplatin calculated with M06-D3 and B3LYP-D3 are similar to that calculated with M06, since in this case there is no π-π interaction.

Although this type of π-π interaction between bases and phenanthridine rings may be observed in solution, it does not occur when adding phenanthriplatin to DNA; indeed, the DNA structure makes this kind of interaction unlikely to form. In addition, the reaction rate follows the order N7-Me-Gua > N7-Me-Ade > N1-Me-Ade with all the used functionals. In conclusion, the addition of only one nitrogen base in complexes having aromatic ligands could provide constant rates not consistent with those obtained using DNA fragments. However, there is still a difference between the calculated and experimental rate constants, possibly due to the formation of H-bonds between bases and water, which decreases the possibility of a nucleophilic attack of the N atom to the Pt atom.

The comparison between the energies profiles (at M06 level of theory, see Figure 15, Table A19 in appendix A) of cisplatin and isomer P and isomer M for the reaction with guanine shows that the RA for cisplatin lie above the reactant molecules and presents a value which is similar to the values obtained for isomer M (see table A19 in appendix A). Moreover, cisplatin has a G_a value higher than both isomers. The k for the addition of N7-Me-Gua to cisplatin is one order of magnitude lower than phenanthriplatin and in good agreement with the experimental one (see table 4). The difference in reaction rates can be explained by observing the structures of the transition states in cisplatin and in isomer

M. In the transition states cisplatin presents two H-bond; the O atom of guanine forms one H-bond with the H atom of the coordinated water and the other one with the H atom of the amino group of the Pt fragment, where the distance is 1.955 Å and 1.932 Å respectively. Isomer M shows only one H-bond, but the distance between O and H is 1.756 Å. Furthermore, the PA for cisplatin is less stable than the PAs for isomer P and isomer M, while the final products have values that are similar to those obtained for isomer M (Figure 15 and table A19 in appendix A).

3.3.4.3 Rotation of the phenanthridine ligand in $[Pt(NH_3)_2(Ade)(phenanthridine)]^{2+}$

As reported in Riddell's work[110], the reaction products between *aqua*-activated phenanthriplatin and 9-methyladenine can potentially exist as a mixture of rotational diastereoisomers, or rotamers. Rotamers derive from the rotation of the adenine and phenanthridine ligands about their Pt-N bonds. Furthermore, an investigation of the rate and energetics of diastereomer interconversion was carried out, obtaining a G value for the interconversion of 16.1 kcal mol^{-1} for N7-Me-Ade adduct and 16.6 kcal mol^{-1} for N1-Me-Ade.

In our work, the interconversion from the isomer P to the isomer M due to the rotation of the phenanthridine ligand has been studied in water at M06 level of theory. The starting structure was obtained by fixing the N3-Pt-N2-C1 dihedral angel at an intermediate value between the values of isomers P and M (see Figure 17). From this point, additional structures were obtained by rotating the phenanthridine ligand in a clockwise and anticlockwise direction with 15° increments until the configuration of isomer P and M was obtained. In Figure 17 the optimized structures for the maximum (TS) obtained by the rotation of the phenanthridine ligand are reported together with the Gibbs free energy profile due to the rotation of the aromatic ligands. Relevant bond distances and angles of optimized TS are reported in Table A22 in appendix A.

The calculated activation G energy barriers for the interconversion are 16.0 kcal mol^{-1} for N7-Me-Ade adduct and 18.5 kcal mol^{-1} for N1-Me-Ade, in excellent agreement with the values obtained experimentally. However the values for N7-Me-Ade adduct (curve blue) are negative at about -45° which may be due to the fact that the complex has not been fully relaxed during the optimization; in fact, the value of N3-Pt-N2-C1 dihedral angle was fixed. Studying such interconversion is very important, because, experimentally,

phenanthriplatin could present two orientations of the phenanthridine ligands when binding to DNA, isomer P and M.[134] Isomer M seems to be the major configuration, while isomer P seems to be the minor configuration, which is also in good agreement with the values calculated in this work; in fact, isomer M forms faster than isomer P for the reaction with N7-Me-Gua and N7-Me-Ade.

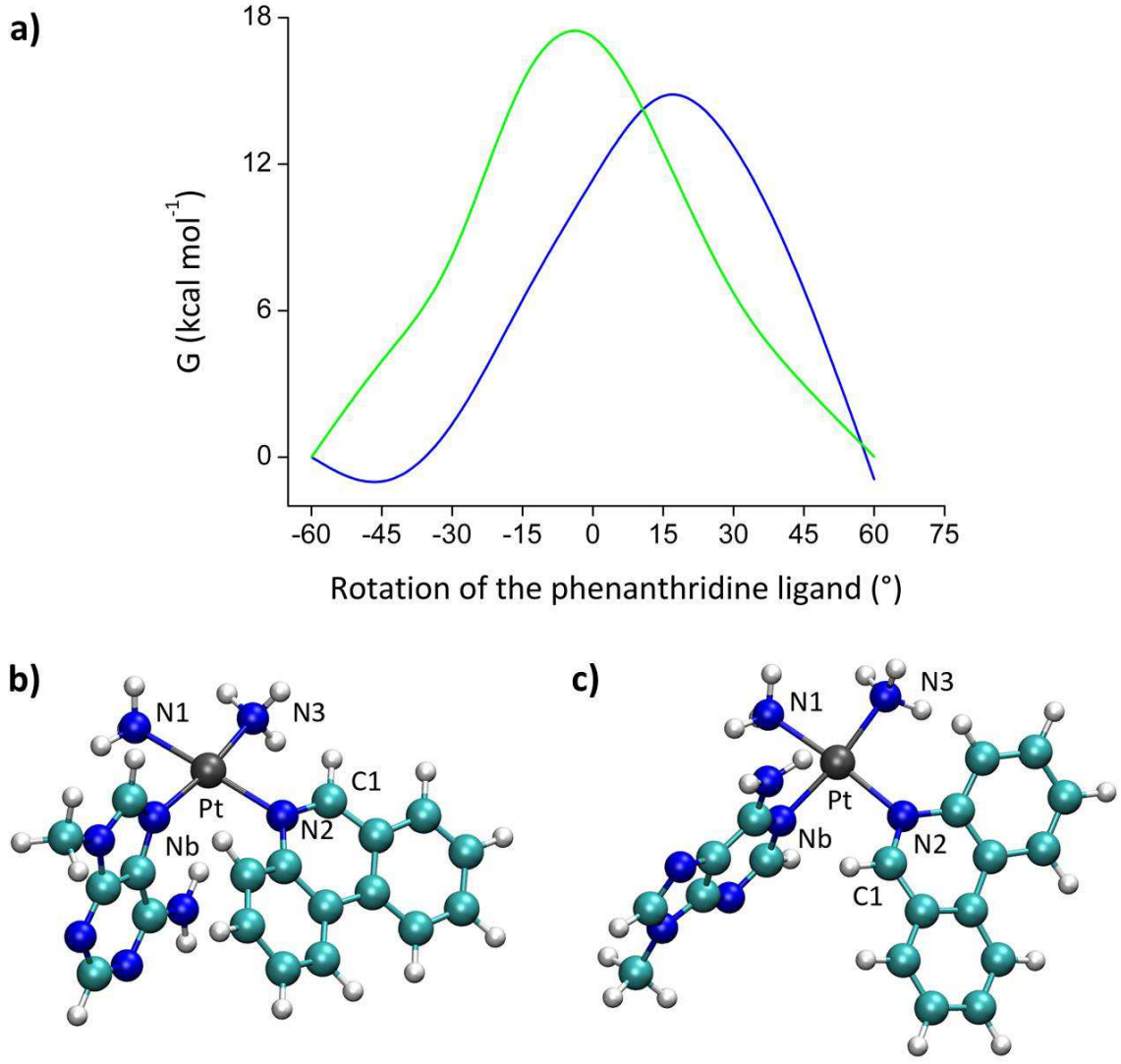

Figure 17 a) Gibbs free energy profile due to the rotation of the aromatic ligands for $[Pt(NH_3)_2$(N7-Me-Ade)(phenanthridine)$]^{2+}$ (blue line) and for $[Pt(NH_3)_2$(N1-Me-Ade)(phenanthridine)$]^{2+}$ (green line). Optimized structures for the maximum (TS) obtained by the rotation of the phenanthridine ligand in b) $[Pt(NH_3)_2$(N7-Me-Ade)(phenanthridine)$]^{2+}$ and in c) $[Pt(NH_3)_2$(N1-Me-Ade)(phenanthridine)$]^{2+}$.

3.3.4.4 Reaction with cysteine

Aqua-activated platinum complexes are very reactive species, which can react with molecules containing sulfur atoms such as MT, characterized by a high presence of the

cysteine amino acid, which eventually causes the inactivation of this drugs.[3] In this thesis the activation energies for reactions between cysteine and isomer P and M were been calculated at M06 Level of theory. In Figure 18 the optimized structures of R, RA, PA, P and TS are shown for both complexes of phenanthriplatin, while the structure of cisplatin is reported in Figure A6. Relevant bond distances and angles of optimized complexes and cisplatin are reported in Table A24-A25 in appendix A. The reaction G energy profiles are shown in Figure 19 (Table A26 in appendix A).

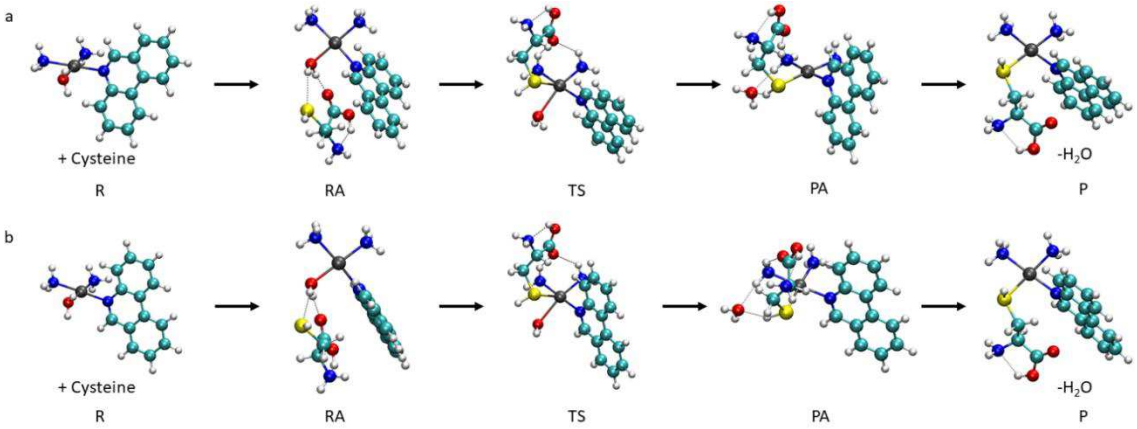

Figure 18 Optimized structures for the reaction between cysteine and isomer P (a) and isomer M (b) at M06 level of theory.

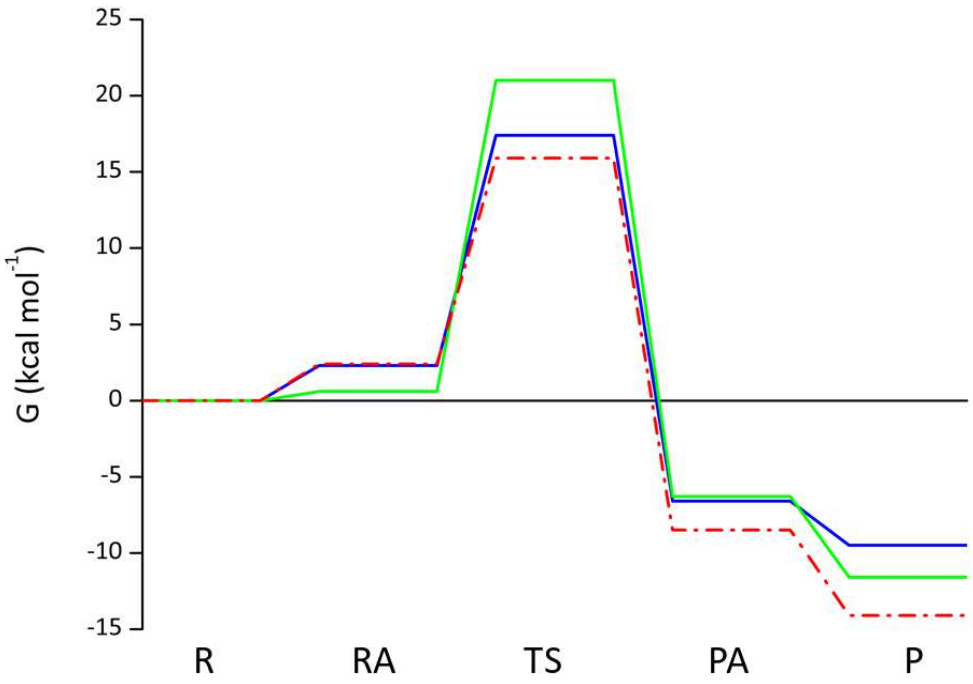

Figure 19 Activation Gibbs free energy profiles for the reaction between cysteine and isomer P (blue line), and between isomer M (green line) and cisplatin (red dot line) in PCM water. At M06 level of theory.

The G energy profiles (Figure 19) show that the RAs of isomers P and M of phenanthriplatin lie above the reactant molecules, and that the RA of isomer M (0.6 kcal mol^{-1}) seems to be more stable than the RA of isomer P (2.3 kcal mol^{-1}). In both cases, a proton transfer from the N atom of the amino group to the O atom of the carboxyl group of cysteine (transforming the amino acid from the zwitterionic form to the neutral form). Moreover, the H atom of the coordinated water form two H-bonds with the S atom and the O atom of the cysteine (Figure 18).

Transition states show a penta-coordinated structure. The imaginary frequencies observed are 133.46i cm^{-1} for isomer P and 127.32i cm^{-1} for isomer M. The analysis of the vibrational modes clearly indicates the rupture of the bond between platinum and the water ligand (Pt-Ow) and the simultaneous formation of the metal-sulfur (Pt-S) bond. The G_a value for isomer P is 15.1 kcal mol^{-1}, which corresponds to a k of $5.32*10^{1}$ s^{-1} at 298.15 K, whereas for isomer M a G_a 20.4 kcal mol^{-1} was obtained with a k of $6.94*10^{-2}$ s^{-1} at 298.15 K (see Table A26 in appendix A). Transition states present an H-bond between the O atom of the cysteine ligand and the H atom of the amino group in the Pt fragment (see Figure 18). The distance between O and H is 1.991 Å for isomer P, and is 2.002 Å for isomer M. Furthermore, the O atom of the cysteine seems to interact with a second H atom of the amino group in the Pt fragment. In fact, the distance between the two atoms is 2.218 Å for isomer P while is 2.237 Å in isomer M, this could explain the difference in G_a values. According to the results, the release of Cl^- ligands is kinetically preferred in isomer P.

Moreover, isomer P conduces to the most stable PA. An opposite behaviour is observed for the final products; isomer M is more stable than isomer P, but the reaction seems thermodynamically favoured in both cases.

The comparison between the energy profiles for the reaction between cysteine and cisplatin and the reaction of isomer P and isomer M shows that the RAs for cisplatin lie above the reactant molecules and are similar to those obtained for isomer P (see Table A26 in appendix A). G_a is 13.5 kcal mol^{-1}, which corresponds to a k of $7.92*10^{2}$ s^{-1}, in agreement with the experimental ones ($3.2*10^{3}$ s^{-1}[135]). The G_a value is lower than the values obtained for isomer P and M (ΔGa = = 1.6 kcal mol^{-1} for isomer P, ΔG_a = 6.9 kcal mol^{-1} for isomer M, see table A26 in appendix A). Moreover, both PA and P are more stable for cisplatin than for isomer P and M (Figure 20 and table A26 in appendix A). In

conclusion, phenanthriplatin shows higher activation barriers G_a than those obtained for cisplatin, a behaviour that could be related to the high cytotoxicity shown by such complex. Indeed, the reaction in phenanthriplatin seems disadvantageous compared to cisplatin, especially for the M isomer. Cisplatin seems to show a greater reactivity towards this class of molecules; indeed, the reaction in cisplatin seems to be favoured from a thermodynamic as well as a kinetic point of view.

3.3.5 Conclusions

In summary, the reactivity of the two phenanthriplatin diastereoisomers (isomer P and isomer M) was investigated using the DFT theory combined with the PCM method. In particular, the hydrolysis reaction, the reaction with bases such as 9-methylguanine and 9-methyladenine and the reaction with cysteine were studied. This work allowed us to make a direct comparison between the reactivity of phenanthriplatin and cisplatin, one of the most used chemotherapeutic agents.[44]

The study of the hydrolysis reaction, a key step for the activation of such species,[3] showed that phenanthriplatin has G_a (22.4 kcal mol^{-1} for isomer P and 23.9 kcal mol^{-1} for isomer M) close to those obtained for the first hydrolysis of cisplatin (23.4 kcal mol^{-1}). The high toxicity of phenanthriplatin may be partly due to the hydrolysis reaction, a low G_a, and the consequent high hydrolysis reaction rate, which might submit the complexes to fast degradation, causing potentially poor pharmacological activity.[76,99] Moreover, the hydrolysis process is the rate determining step (RDS) of the whole process.

Unlike cisplatin, phenanthriplatin reacts with both guanine and adenine; with the latter the formation of two products; N7 and N1, occurs. Guanine as a target for platination process is confirmed to be preferred over adenine for all the investigated compounds. In addition, the reaction rate follows the order N7-guanine > N7-adenine > N1-adenine. The dominating preference for guanine seems to be a hydrogen-bond-controlled process, confirming that H-bonds are important in imposing both structural and kinetic control on the purine platination processes. The comparison between the G_a of cisplatin and phenanthriplatin for the reaction with guanine shows that the reaction is kinetically favoured for phenanthriplatin. The calculated reaction rates differ considerably from the experimental ones, maybe due to the formation of a π-π interaction between the bases

and the phenanthridine ligand. Although this type of structure may be observed in solution, it cannot be observed in DNA. The addition of only one nitrogen base to complexes having aromatic ligands could provide constant rates not consistent with those obtained using DNA fragments. In addition, the reaction products between phenanthriplatin and adenine can potentially exist as a mixture of rotational diastereoisomers.[110] The calculated activation G energy barriers for the interconversion are in agreement with those obtained experimentally.

Finally, the study of the reaction between phenanthriplatin and cysteine has shown that such reaction is disadvantageous, both kinetically and thermodynamically, in phenanthriplatin in respect to cisplatin. In conclusion, phenanthriplatin seems to have hydrolysis rate comparable to cisplatin and to react faster with guanine than with sulfur molecules.

3.4 Nano-delivery of Cisplatin: Interactions with Graphene Prototypes

3.4.1 Introduction

In recent years, the nano-delivery of biologically active agents has been one of the most studied fields,[136] including different subjects such as material science, engineering, medicine and chemistry.

Nanoscale drug delivery is the administration of drugs using objects with dimensions in the nanometer regime for the transport of pharmacologically active agents. In the nano-delivery of anticancer agents, the main advantages of using nanoparticles relate to their ability to target tumour tissue in either an active or a passive manner.[137,138] These systems could be used as a possible solution to resolve the inconvenience of Pt-based drugs, being the nano-delivery able to reduce the systemic dose while increasing the amount of active molecule that reaches the target site.[136] Graphene-based nano-carries is a new class of compounds that are emerging as optimal candidates in the delivery of various active compounds.[139]

3.4.2 Graphene based materials

In 2004 Geim *et al.*[140] discovered graphene, the thinnest known material (see Figure 20), and won the Nobel Prize. The research on graphene has increased exponentially and finds applications in different sectors such as electronic and optoelectronic devices, photoconductive materials in solar cells, medical imaging, drug delivery and tissue engineering.[141]

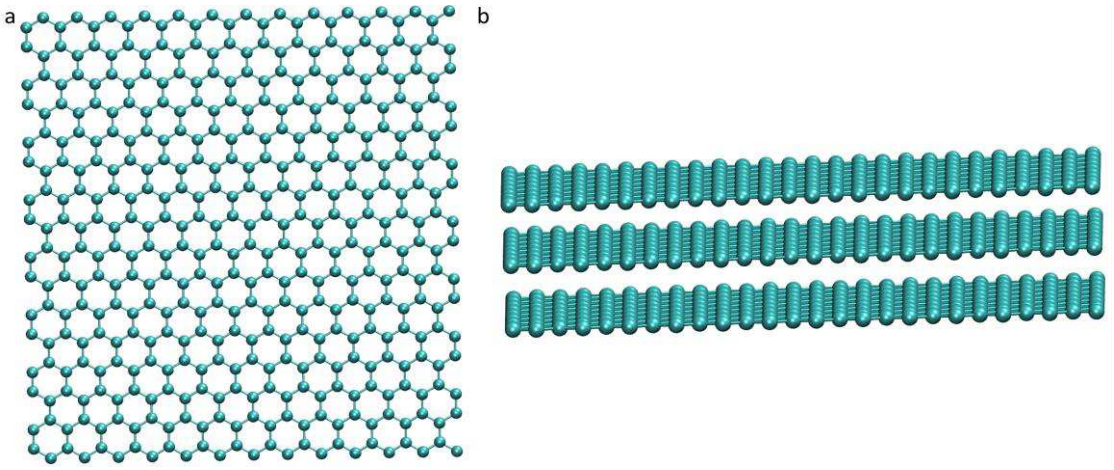

Figure 20 Structures of a) graphene and b) graphene multilayer.

Graphene-based materials are two-dimensional (2D) structures where each carbon is bound to other three carbons in the same plane in a sp2-hybridized flat structure. Their surfaces represent ideal adsorption platforms for a wide variety of molecules through covalent and non-covalent interactions, thanks to their high surface/volume ratio and ease of functionalization, which make them attractive as carriers for removal and delivery of bioactive agents.[142–145] The presence of strong carbon-carbon bonding, aromatic structure, reactive sites for surface reactions and free π electrons makes graphene a unique material with exceptional proprieties. Indeed, high electron density above and below the 2D graphene plane, provided by the π electron, could interact with the molecular orbitals of different compounds, thus facilitating reactions such as electrophilic substitution.[146] Moreover, the structure provides excellent thermal and electrical conductivity with a low coefficient of thermal expansion[147,148] and makes graphene one of the strongest tested materials; the breaking strength of single layer defect-free graphene is approximately 200 times higher than steel.[149]

Graphene-family nanomaterials are classified based on the number of layers in the sheet and chemical modification. The most used graphene systems are single-layer graphene, bi-layer graphene, multilayer graphene (see Figure 20), graphene oxide (GO) and reduced graphene oxide (rGO). Single-layer graphene is synthesized by repeated mechanical exfoliation[140] or extremely controlled growth on substrates like silicon carbide[150] via chemical vapor deposition (CVD).

Graphene oxide (GO) is a highly oxidized form of graphene, chemically modified with carboxylic acid, epoxide and hydroxyl groups in the plane. The carboxylate group provides colloidal stability and pH dependent negative surface charge,[151] while epoxide (-O-) and hydroxyl (-OH) can interact by hydrogen bonding.[152] GO is an amphiphilic sheet-like molecule, which can be used as a surfactant to stabilize hydrophobic molecules in a solution.[153,154] Reduced graphene oxide (rGO) can be obtained by thermal, chemical and UV treatment of GO under reducing conditions.[151] rGO is mainly produced to restore the electrical conductivity and optical absorbance in GO while reducing the oxygen content, surface charge, and hydrophilicity.[155]

One of the field in which graphene-based materials are used is biomedical applications,[141,156,157] because its unique properties make this material an excellent candidate for drug delivery.

3.4.3 Graphene-based materials as drug delivery systems

The main property of a delivery vehicle is the ability to carry drugs on the site of action and protect them from degradation, leading to a potential increase of efficacy.[158–162] In these respects, graphene-based nano-carriers have emerged as excellent candidates for drugs delivery because, as recent studied have demonstrated, they are less toxic compared to other carbon materials, and a proper functionalization of the surface can improve their biocompatibility in live organisms.[139] Different molecules can be transported by graphene-based materials[163–165] and different methods can be used to load the drugs (cargo) to graphene delivery systems. The cargo can interact directly with graphene sheets by hydrophobic interactions, π-π stacking, hydrogen bonding (if the graphene surface is functionalized with carboxylic acid, epoxide and hydroxyl groups) or by covalent bonding. After the drug loading, the cargo must be transported to its target

cell or target tissue and, generally, nano-carriers enter the cells by endocytosis. After entering the target cell, the cargo should be effectively released. Cargo release can be activated by a change in the local environmental conditions, such as the pH or the temperature, or through the recognition by a target receptor.[139]

Recently, cisplatin loading on graphene has been attempted through the formation of a covalent bond between the platform and cisplatin.[166,167] However, the square planar structure and the low solubility of cisplatin suggests that this species may have a certain affinity with the graphene surface; therefore, a favourable adsorption of cisplatin on graphene can be predicted. Even from a theoretical point of view, the study of non-covalent interactions between cisplatin and graphene is rather poor. However, Cuevas-Flores *et al.*[168] did study the interaction between cisplatin and graphene prototypes in gas-phase. They chose the cisplatin-pyrene complex as graphene prototype and considered different orientations of cisplatin. They performed scan at MP2C level of theory, finding that parallel geometries show the largest attraction. The calculations were used as reference data to validate selected DFT levels, in particular, the best DFT functional reproducing MP2C energy is PBE-D3(BJ). This functional was finally used to study the interaction between cisplatin and larger graphene prototypes; the best prototypes seem to be ovalene ($C_{32}H_{14}$), because it represents the best compromise between computational cost and accuracy.

3.4.4 Aim of this work

The purpose of this work is to provide more details about the interactions between cisplatin and graphene by means of MP2 and DFT calculation and to introduce the solvent effect, since no works considering the solvent effect can be found in literature.

3.4.5 Computational details

Circumcoronene ($C_{54}H_{18}$) was chosen as the representative model of graphene, as Cuevas-Flores[168] observed that the change in the interaction energy for large surfaces of circumcoronene is small. In this work, different orientations of cisplatin were taken into account, four to be precise (Figure 21): one parallel (P) and three perpendicular (N, Cl, N-Cl) geometries. The interaction between cisplatin and graphene was studied by

performing scans as a function of the distance (r) between the Pt atom and the centre of mass (COM) of circumcoronene. The r coordinate varied from 2.6 Å to 10.5 Å for P orientation, from 3.8 Å to 10.5 Å for N orientation and from 4 Å to 10.5 Å for Cl and N-Cl orientation. The interaction energy (E_{int}) was calculated following this equation:

$$E_{int} = E_{tot} - (E_{circum} + E_{cis}) \quad \text{(eq2)}$$

where E_{tot} is the potential energy for the cisplatin-circumcoronene dimer, E_{circum} is the potential energy of circumcoronene at infinitive distance, and E_{cis} is the potential energy of cisplatin at infinitive distance. All E_{int} were corrected for the basis set superposition error (BSSE) by the counterpoise method of Boys and Bernardi.[168]

Quantum-mechanical calculations were carried out at MP2 and DFT level of theory. Geometry optimizations of isolated molecules were carried out at MP2 level of theory in vacuum with a 6-31+G(d,p) basis set for all atoms except the platinum atom, which was described by the quasi-relativistic Stuttgart-Dresden pseudopotential (SDD). Improved energies for the cisplatin-circumcoronene dimer were obtained by single-point calculations using a 6-311+G(d,p) basis sets for all elements, while platinum was described by the Stuttgart-Dresden pseudopotential. Several DFT functionals were considered for the E_{int} calculation, from standard GGA functional such as BPBE and BP86[169] to hybrid-GGA functional such as B97[169] (19.4% Hartree Fock (HF) exchange), B3PW91[170,171] (20% HF exchange), PBE1PBE[172] (25% HF exchange), BMK[173] (42% HF exchange), M062X[121,122] (54% HF exchange) and M06HF[121,122] (100% HF exchange). Moreover, the range-separated hybrid GGAs functionals such as CAM-B3LYP[174] and LC-wPBE[174] were also tested. In such functionals, the fraction of exact exchange varies as a function of the interelectronic distance, by partitioning the Coulomb operator. All DFT functionals include the latest dispersion contribution correction (D3) of Grimme,[130] and the damped dispersion scheme of Becke-Johnson (BJ)[175], as it has been observed that the inclusion of the dispersion correction allows to obtain a better agreement with the reference MP2 energy.[168] The solvent effect was taken into account using the method reported in the work of Melchior and collaborators,[176] and water was chosen as a solvent, considering that the drugs are administered in aqueous solutions.[177] All calculations were performed using the Gaussian 16 program.[178]

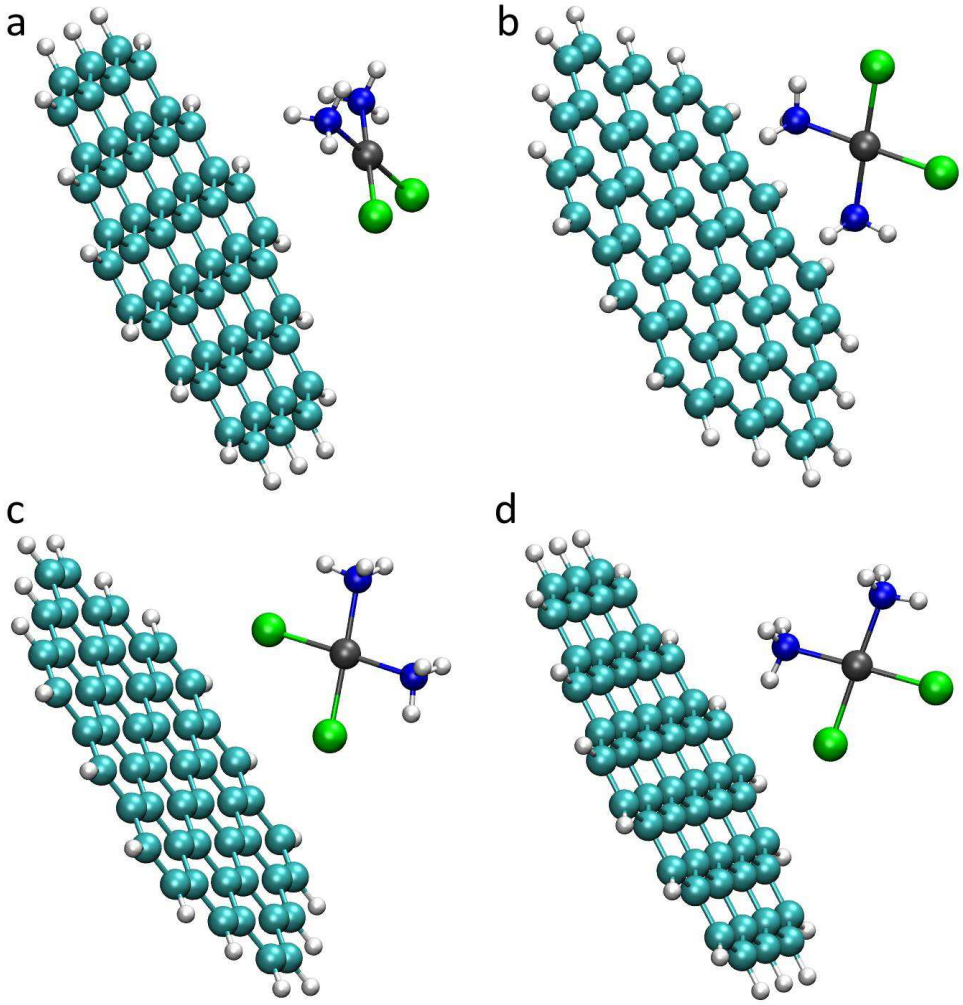

Figure 21 Orientation of cisplatin studied in this work: a) parallel P b) perpendicular N, c) perpendicular Cl d) perpendicular N-Cl.

3.4.6 Results and Discussion

3.4.6.1 Comparison between MP2 and DFT in the calculation on E_{int}

The work started by evaluating which DFT functional best reproduces MP2 E_{int}. The MP2 method can properly describe non-covalent interactions such as dispersion forces, but it implies an overestimation of π-π stacking interactions in complexes such as the benzene dimer and has a higher computational cost.[179–182] For this reason, only 3 point were calculated at the MP2 level, where cisplatin is parallel to the surface (Figure 21a) and in proximity of the minimum (an idea of the minimum position was obtained from MP2 calculations on coronene ($C_{24}H_{12}$) cisplatin dimer, not reported in this thesis). Table 6

shows the comparison between the E_{int} calculated at MP2 level and the E_{int} calculated with the selected DFT functionals.

Table 6 Comparison between MP2 and DFT; E_{int} (kcal mol^{-1}), r (Å) is the distance between the Pt atom and the COM of circumcoronene.

	E_{int}		
Functional	r 2.8	r 3.2	r 3.6
MP2	1.8	-17.2	-15.1
BPBE-D3	-11.5	-28.8	-23.1
BPBE-D3(BJ)	-13.5	-27.9	-24.1
BP86-D3	-7.9	-26.3	-21.9
B97-D3	0.9	-19.8	-17.6
B3PW91-D3	-7.1	-25.9	-21.8
B3PW91-D3(BJ)	-8.2	-24.4	-21.6
PBE1PBE-D3(BJ)	2.1	-17.0	-17.1
BMK-D3	-8.9	-29.3	-22.1
M062X-D3	3.5	-17.5	-16.6
M06HF-D3	-4.9	-20.7	-18.1
CAM-B3LYP-D3	4.4	-18.2	-17.4
LC-wPBE-D3(BJ)	-3.6	-21.3	-19.8

On the one hand, standard GGA functionals, BPBE-D3, BPBE-D3(BJ) and BP86, together with hybrid-GGA functional, BMK-D3, are the worst at reproducing MP2 E_{int}, because they overestimate the E_{int} from 7.1 to 12.1 kcal mol^{-1}; on the other hand, the best DFT functionals are the hybrid-GGA M062X-D3 and the range-separated hybrid GGAs CAM-B3LYP-D3. The difference between the MP2 and DFT energy (ΔE_{int}) calculated according to this equation:

$$\Delta E_{int} = E_{int(MP2)} - E_{int(DFT)} \qquad \text{(eq3)}$$

shows that M062X-D3 reproduces the E_{int} better than CAM-B3LYP-D3: ΔE_{int} for M062X-D3 functional is -1.7 kcal mol^{-1} at 2.8 Å, 0.3 kcal mol^{-1} at 3.2 Å, 1.5 kcal mol^{-1} at 3.6 Å, ΔE_{int} for CAM-B3LYP-D3 functional is -2.6 kcal mol^{-1} at 2.8 Å, 1.0 kcal mol^{-1} at 3.2 Å, 2.3 kcal mol^{-1} at 3.6 Å. In both cases, there are more marked deviations in the repulsive part of the E_{int} profile (where the E_{int} is positive) compared to MP2 energies. It is interesting to note that even the E_{int} values of PBE1PBE-D3(BJ) functional are very close to MP2 energy, although a slight increase in such energy, going from 3.2 Å to 3.6 Å, is observed; hence, comparing

the E_{int} on more than one point is very important. In conclusion, M062X-D3 is the functional that provides the best agreement with MP2 energy, so it was used to obtain complete scans for all the studied orientations.

3.4.6.2 Cisplatin interaction with circumcoronene

The E_{int} profiles, represented as a function of the r of the Pt atom from the COM of circumcoronene, obtained at the M062X-D3 level of theory in vacuum and in water, are reported in Figure 22, together with points calculated at an MP2 level of theory.

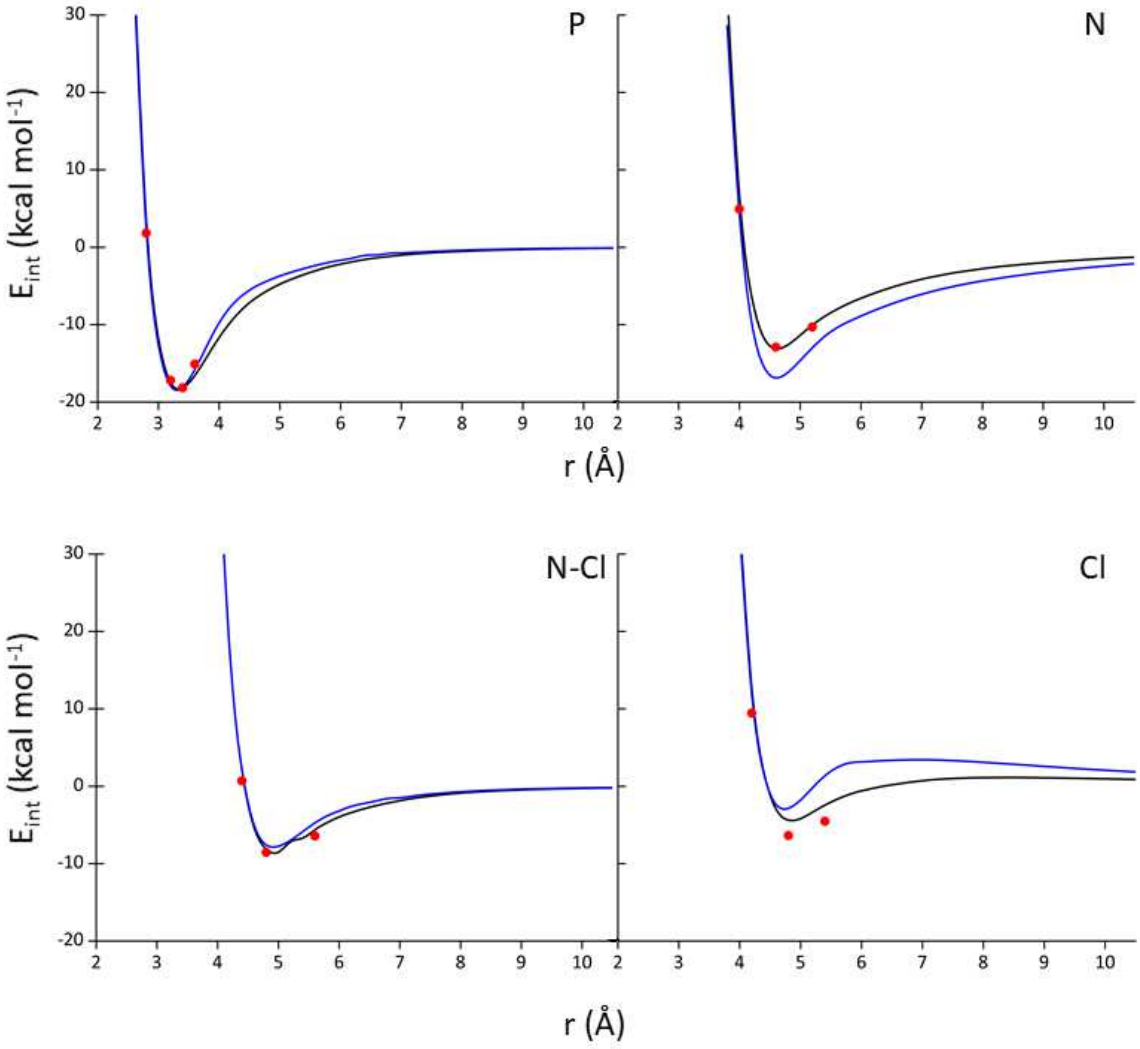

Figure 22 E_{int} as a function of the r (Å) obtained at the M062X-D3 level for the different configurations of the cisplatin circumcoronene dimer. The black curve is the E_{int} in vacuum, the blue curve is E_{int} in water and the red dot is E_{int} at MP2 level in gas phase.

The E_{int} calculated at an MP2 level of theory in vacuum, reported in table 7, are in good agreement with the energy calculated at M62X-D3 for P, N, and N-Cl orientations. Marked differences are observed in the repulsive part of the E_{int} profile, while the energies are in good agreement in proximity to the minimum, confirming the reliability of the DFT computational protocol used. However, more marked deviations between MP2 and M062X-D3 energies are observed for Cl orientation (see Figure 22, table 7).

Table 7 Comparison between MP2 and M062X-D3 E_{int} (kcal mol^{-1}) in gas phase.

		E_{int}	
Orientation	r (Å)	M062X-D3	MP2
P	2.8	3.5	1.8
	3.2	-17.5	-17.2
	3.4	-18.2	-18.1
	3.6	-16.6	-15.1
N	4	6.8	4.9
	4.6	-13.1	-12.9
	5.2	-10.8	-10.3
N	4.4	2.0	0.7
	4.8	-8.1	-8.5
	5.6	-5.6	-6.4
Cl	4.2	12.6	9.4
	4.8	-4.4	-6.4
	5.4	-2.4	-4.5

The largest E_{int} in vacuum was observed when cisplatin is parallel to the surface of the circumcoronene (Figure 21a); the minimum is located at about 3.4 Å and E_{int} is -18.2 kcal mol^{-1}. The values are similar to those obtained by Cuevas-Flores,[168] who reported an E_{int} value of -16.5 kcal mol^{-1} at a distance of 3.5 Å. Among the perpendicular orientations, the most negative E_{int} was observed when the NH_3 groups of cisplatin are oriented towards the circumcoronene plane (Figure 21b). The minimum is located at about 4.6 Å and the E_{int} is -13.1 kcal mol^{-1}; a shift of the energy minimum of 1.2 Å and an E_{int} reduction of 5.1 kcal mol^{-1} compared to the parallel orientation can be observed. Again, the values are similar to those reported by Cuevas-Flores (12.4 kcal mol^{-1} at 4.7 Å).[168] The results for the N-Cl and Cl perpendicular configurations show that the minima of the energy profiles are located an even wider distances (around 5.0 Å and 4.8 Å respectively); furthermore, the E_{int} are smaller than the other two configurations (-8.5 kcal mol^{-1} and -4.4 kcal mol^{-1}

respectively). It is interesting to note that the E_{int} profiles obtained for Cl orientation are different compared to all other cases; in fact, at a distance of 6.4 Å, E_{int} starts to assume positive values, with a maximum localized at 8.5 Å where the E_{int} is 1.1 kcal mol^{-1}; the same behaviour was observed in Cuevas-Flores work.[168]

With the aim of further understanding of the interaction properties of cisplatin on circumcoronene, the total electronic density of states (DOS) for the cisplatin circumcoronene dimer, circumcoronene and cisplatin, together with the partial DOS (PDOS) for adsorbed cisplatin molecule and for circumcoronene (red curve) were calculated at the minimum of the E_{int} in vacuum and are reported in Figure 23.

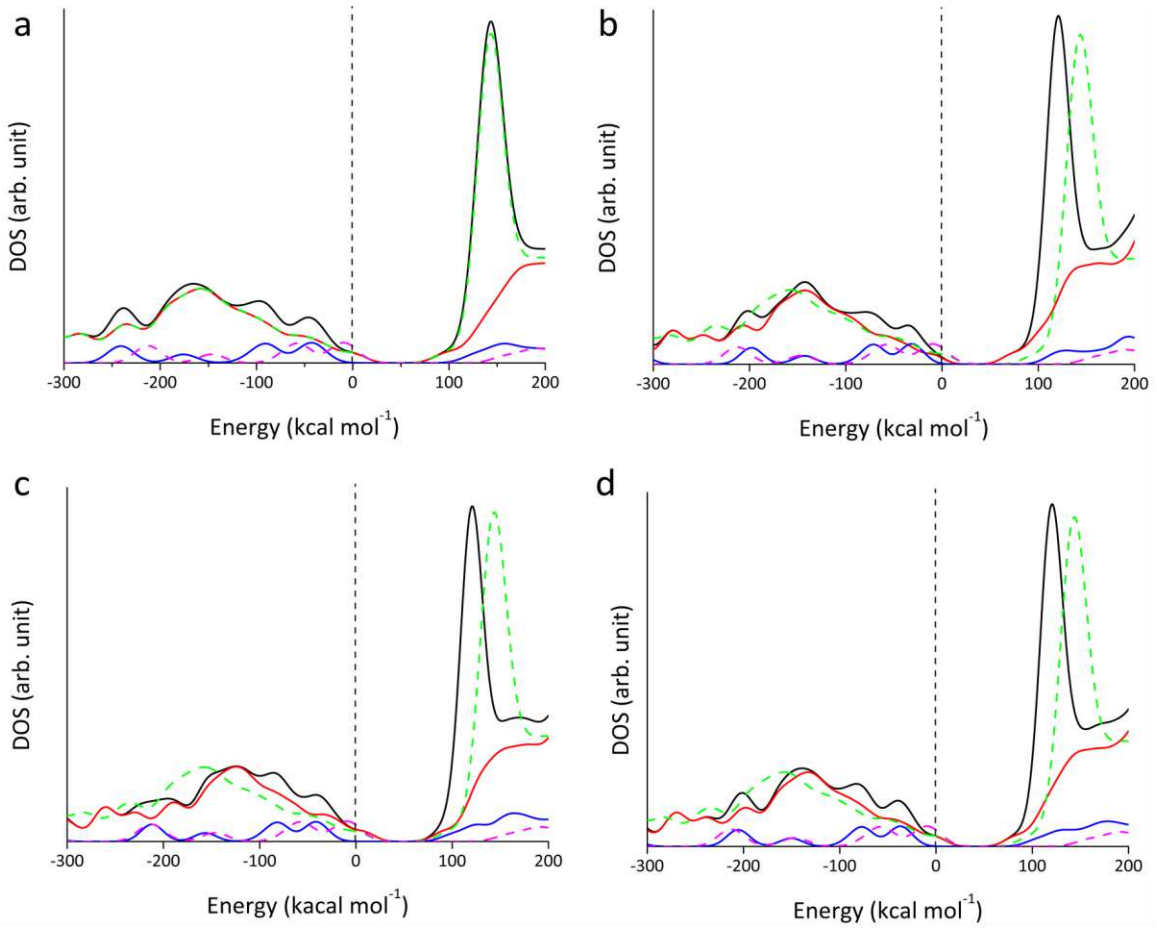

Figure 23 DOS for the cisplatin circumcoronene dimer (black curves), DOS for circumcoronene (green dash curve) and the DOS for cisplatin (magenta dash curve), PDOS for adsorbed cisplatin molecule (blue curves), PDOS for circumcoronene (red curve), for the different orientation of cisplatin. The Fermi level, indicated with a dash line, was set as zero.

In comparison with the DOS of the non-adsorbed cisplatin molecule (magenta dash curve), the DOS of the adsorbed cisplatin (blue curve) moved left. The electrons for adsorbed cisplatin comprised between 0 and -100 kcal mol^{-1} shifted by about -32 kcal mol^{-1} below the Fermi level, which implied that the adsorption state favoured the stability of the electronic structure of cisplatin. Furthermore, when cisplatin was parallel to the surface of the circumcoronene electrons between -200 and -300 kcal mol^{-1} shifted by about -29 kcal mol^{-1} below the Fermi level, while in other cases such behaviour was not observed. The observations are in agreement with the trend of E_{int}, as the parallel orientation of cisplatin appears to be the most stable orientation. No difference was observed in the DOS of circumcoronene after cisplatin adsorption when it was parallel to the surface. However, In comparison to the DOS of the circumcoronene without cisplatin (green dash line in Fugure 23), the DOS of the circumcoronene with cisplatin (red curve) moved right; the electrons for free circumcoronene comprised between -100 and -200 kcal mol^{-1} are shifted by about 13 kcal mol^{-1} for N orientation, about 25 kcal mol^{-1} for N-Cl orientation and about 32 kcal mol^{-1} for Cl orientation, implying that, when cisplatin is adsorbed with such orientations, a destabilization of the circumcoronene electronic structure occurs. Moreover, such behaviour is also in good agreement with the trend of interaction energies that follow the order P > N > N-Cl > Cl, and is further confirmed by the calculation of the electron density overlap reported in Figure 24, where the electron density of the two monomers overlap with each other evidently. From the Figure 24 we can observe that the electron density overlaps are always distributed below the cisplatin molecule; furthermore, the configuration P seems to have the highest electron density.

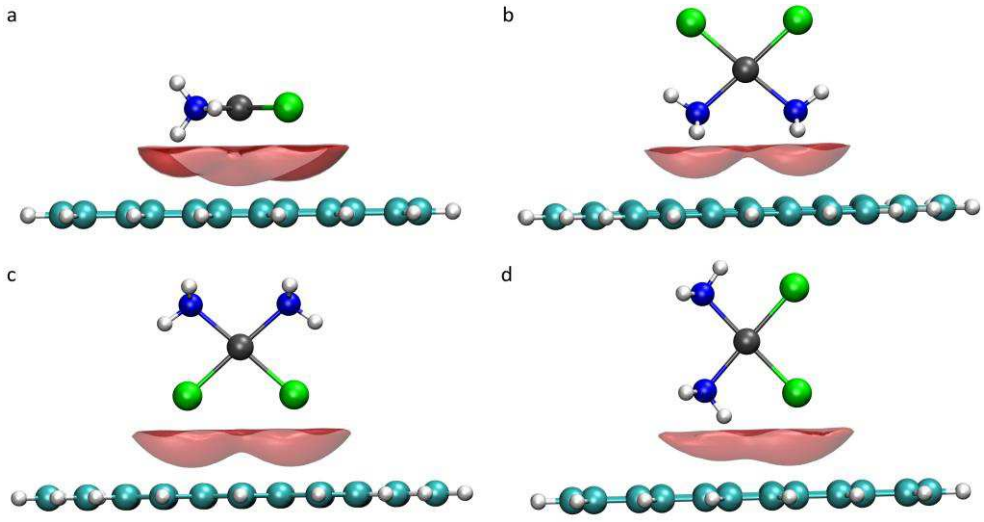

Figure 24 Electron density (in red) overlap between circumcoronene and cisplatin. Isovalue 0.0006 a.u.

Even with the introduction of the solvent (see Figure 22, blue curve) the largest E_{int} was observed when cisplatin was parallel to the graphene surface. However, E_{int} value is -18.1 kcal mol^{-1}, similar to what was calculated in vacuum, and no variation in the minimum point is observed. Even in this case, the N orientation is the most favoured among perpendicular orientations, no variation in the minimum point is observed, although a descries in E_{int} of -4 kcal mol^{-1} is observed (from -13.1 kcal mol^{-1} in vacuum to -17.2 kcal mol^{-1} in water). The results for the N-Cl and Cl perpendicular configurations show that the minima of the energy profiles do not change in comparison to vacuum calculation, and in both cases an increase in E_{int} is observed (from -8.5 to -7.7 kcal mol^{-1} for N-Cl orientation and from -4.4 to -2.8 kcal mol^{-1} for Cl orientation). Also in this case, the E_{int} for Cl orientation starts to assume positive values at the distance of 5.4 Å, and the maximum is localized at 7.0 Å where E_{int} is 3.4 kcal mol^{-1}. In conclusion, the introduction of the solvent does not drastically change the E_{int} profiles between cisplatin and circumcoronene. However, there is a decrease in E_{int} for N orientation, which is now similar to the E_{int} calculated for P orientation.

3.4.7 Conclusions

In summary, the interaction energy profiles between cisplatin and circumcoronene were carried out at DFT level in vacuum and with the introduction of the solvent (water). Different orientations of cisplatin in respect to circumcoronene were taken into account. Different DFT functional, from standard GGA functional to hybrid-GGA, were tested and compared with the interaction energy obtained from MP2 calculations. The functional that best reproduces MP2 energies is M62X-D3, which was used to obtain the energy profiles. The E_{int} in vacuum followed the order P > N > N-Cl > Cl. The density of states analysis showed that when cisplatin is adsorbed with perpendicular orientations (N, N-Cl, Cl), a destabilization of the circumcoronene electronic structure occurs. Finally, the introduction of the solvent does not drastically change the E_{int} profiles between cisplatin and circumcoronene; the E_{int} in water followed the order P > N > N-Cl > Cl. However, a decrease in E_{int} was observed for N orientation, which is now similar to the one calculated for P orientation.

3.5 References

[1] B. Rosenberg, L. Van Camp, T. Krigas, *Nature* **1965**, *205*, 698–699.

[2] B. Rosenberg, L. Van Camp, J. E. Trosko, V. H. Mansout, *Nature* **1969**, *222*, 385–386.

[3] L. Kelland, *Nat. Rev. Cancer* **2007**, *7*, 573–584.

[4] S. J. Berners-price, T. G. Appleton, in *Cancer Drug Discov. Dev.* (Eds.: L.R. Kelland, N.P. Farrel), Humana Press, Totowa, **2000**, pp. 3–35.

[5] P. C. A. Bruijnincx, P. J. Sadler, *Curr. Opin. Chem. Biol.* **2008**, *12*, 197–206.

[6] C. G. Hartinger, N. Metzler-nolte, P. J. Dyson, *Organometallics* **2012**, *31*, 5677–5685.

[7] T. C. Johnstone, K. Suntharalingam, S. J. Lippard, *Chem. Rev.* **2016**, *116*, 3436–3486.

[8] S. Dasari, B. P. Tchounwou, *Eur. J. Pharmacol.* **2014**, *740*, 364–378.

[9] *U.S. Natl. Libr. Med. Cisplatin Inject. Accessed 2015; http//www.nlm.nih.gov/medlineplus/druginfo/meds/a684036. html.* **n.d.**

[10] Y. Jung, S. J. Lippard, *Chem Rev* **2007**, *107*, 1387–1407.

[11] T. C. Johnstone, S. J. Lippard, *Phil.Trans.R.Soc.A* **2015**, *373*, 1–12.

[12] D. P. Gately, S. B. Howell, *Br. J. Cancer* **1993**, *67*, 1171–1176.

[13] M. D. Hall, M. Okabe, D. Shen, X. Liang, M. M. Gottesman, *Annu. Rev. Pharmacol. Toxicol.* **2008**, *48*, 495–535.

[14] S. Ishida, J. Lee, D. J. Thiele, I. Herskowitz, *Proc Natl Acad Sci* **2012**, *99*, 14298–14302.

[15] K. D. Ivy, J. H. Kaplan, *Mol. Pharmacol.* **2013**, *83*, 1237–1246.

[16] S. E. Miller, A. House, *Inorganica Chim. Acta* **1989**, *161*, 131–137.

[17] J. Reishus, D. S. Martin Jr., *J. Am. Chem. Soc.* **1961**, *83*, 2457–2462.

[18] A. Eastman, *Pharmacol. Ther.* **1987**, *34*, 155–166.

[19] Y. Sedletska, M.-J. Giraud-Panis, J. Malinge, *Curr. Med. Chem. - Anti-Cancer Agents* **2005**, *5*, 251–265.

[20] D. J. Beck, R. R. Brubaker, *J. Bacteriol.* **1973**, *116*, 1247–1252.

[21] H. N. A. Fraval, C. J. Rawlings, J. J. Roberts, *Mutat. Res.* **1978**, *51*, 121–132.

[22] A. Casini, J. ReediJk, *Chem. Sci.* **2012**, *3*, 3135–3144.

[23] M. F. Osborn, J. D. White, M. M. Haley, V. J. DeRose, *ACS Chem. Biol.,* **2014**, *9*, 2404–2411.

[24] R. Mezencev, *Curr. Cancer Drug Targets* **2014**, *14*, 794–816.

[25] E. R. Jamieson, S. J. Lippard, *Chem. Rev.* **1999**, *99*, 2467–2498.

[26] V. Brabec, *Prog. Nucleic Acid Res. Mol. Biol.* **2002**, *71*, 1–68.

[27] E. Wexselblatt, E. Yavin, D. Gibson, *Inorganica Chim. Acta* **2012**, *393*, 75–83.

[28] G. L. Cohen, W. R. Bauer, J. K. Barton, S. J. Lippard, *Science* **1979**, *203*, 1014–1016.

[29] A. M. J. Fichtinger-Schepman, J. L. van der Veer, J. H. J. Den Hartog, P. H. M. Lohman, J. Reedijk, *Biochemistry* **1985**, *24*, 707–713.

[30] M. Kartalou, J. M. Essigmann, *Mutat. Res.* **2001**, *478*, 1–21.

[31] R. C. Todd, S. J. Lippard, *Metallomics* **2009**, *1*, 280–291.

[32] Y. Jung, S. J. Lippard, *J. Biol. Chem.* **2006**, *281*, 1361–1370.

[33] C. A. Rabik, M. E. Dolan, *Cancer Treat. Rev.* **2007**, *33*, 9–23.

[34] N. Graf, W. H. Ang, G. Zhu, M. Myint, S. J. Lippard, *ChemBioChem* **2011**, *12*, 1115–1123.

[35] M. E. Bianchi, M. Beltrame, G. Paonessa, *Science* **1989**, *243*, 1056–1059.

[36] J. O. Thomas, A. A. Travers, *TRENDS Bioc hemical Sci.* **2001**, *26*, 167–174.

[37] P. M. Pil, S. J. Lippard, *Science* **1992**, *256*, 234–237.

[38] S. Park, S. J. Lippard, *Biochemistry* **2011**, *50*, 2567–2574.

[39] D. Wang, S. J. Lippard, *Nat. Rev.* **2005**, *4*, 307–320.

[40] T. C. Johnstone, J. J. Wilson, S. J. Lippard, *Inorg. Chem.* **2013**, *52*, 12234–12249.

[41] B. P. Esposito, R. Najjar, *Coord. Chem. Rev. 232* **2002**, *232*, 137–149.

[42] A. I. Ivanov, J. Christodoulou, J. A. Parkison, K. J. Barnham, A. Tucker, J. Woodrow, P. J. Sadler, *J. Biol. Chem.* **1998**, *273*, 14721–14730.

[43] M. J. Cleare, J. D. Hoeschele, *Bioinorg. Chem.* **1973**, *2*, 187–210.

[44] N. J. Wheate, S. Walker, G. E. Craig, R. Oun, *Dalt. Trans.* **2010**, *39*, 8113–8127.

[45] M. G. Apps, E. H. Y. Choi, N. J. Wheate, *Endocr. Relat. Cancer* **2015**, *22*, R219–R233.

[46] R. S. Go, A. A. Adjei, *our nal Clin. Oncol.* **1999**, *17*, 409–422.

[47] S. Neidle, I. M. Ismail, P. J. Sadler, *J. Inorg. Biochem.* **1980**, *13*, 205–212.

[48] U. Frey, J. D. Ranford, P. J. Sadler, *Inorg. Chem.* **1993**, *32*, 1333–1340.

[49] T. Boulikas, M. Vougiouka, *Oncol. Rep.* **2003**, *10*, 1663–1682.

[50] J. Kasparkova, M. Vojtiskova, G. Natile, V. Brabec, *Chem. - A Eur. J.* **2008**, *14*, 1330–1341.

[51] C. A. Puckett, R. J. Ernst, J. K. Barton, *Dalt. Trans.* **2010**, *39*, 1159–1170.

[52] A. Kuwahara, M. Yamamori, K. Nishiguchi, T. Okuno, N. Chayahara, *Int. J. Med. Sci.* **2009**, *6*, 305–311.

[53] M. E. Alberto, M. F. A. Lucas, M. Pavelka, N. Russo, *J. Phys. Chem. B* **2009**, *113*, 14473–14479.

[54] Y. Kawai, S. Taniuchi, S. Okahara, M. Nakamura, M. Gemba, *Biol. Pharm. Bull.* **2005**, *28*, 1385–1388.

[55] T. Kodaira, N. Fuwa, T. H., S. Hidano, *Anticancer Res.* **2006**, *26*, 2265–2268.

[56] D. Kim, G. Kim, J. Gam, Y. Cho, H. Kim, J. H. Tai, K. H. Kim, W. Hong, J. Park, *J. Med. Chem.* **1994**, *37*, 1471–1485.

[57] D. Kim, H. Kim, Y. Cho, J. H. Tai, J. S. Ahn, T. Kim, K. H. Kim, W. Hong, *Cancer Chemother Pharm.* **1995**, *35*, 441–445.

[58] D. Kim, H. Kim, J. H. Tai, Y. Cho, T. Kim, K. H. Kim, J. Park, W. Hong, *Cancer Chemother Pharmacol* **1995**, *37*, 1–6.

[59] M. Degardin, J. P. Armand, B. Chevallier, P. Cappelaere, M. Lentz, M. David, H. Roché, *Invest. New Drugs* **1995**, *13*, 253–255.

[60] G. Di Carlo, N. Mascolo, A. A. Izzo, F. Capasso, *Life Sci.* **1999**, *65*, 337–353.

[61] J. B. Harborne, C. A. Williams, *Phytochemistry* **2000**, *55*, 481–504.

[62] R. F. V de Souza, W. F. De Giovani, *Redox Rep.* **2014**, *9*, 97–104.

[63] H. Sakagami, Y. Jiang, K. Kusama, T. Atsumi, T. Ueha, M. Toguchi, I. Iwakura, K. Satoh, T. Fukai, T. Nomura, *Anticancer Res.* **2000**, *20*, 271—277.

[64] C. Kanadaswami, L. Lee, P. H. Lee, J. Hwang, F. Ke, Y. Huang, M. Lee, *In Vivo (Brooklyn).* **2005**, *910*, 895–910.

[65] C. D. Kanakis, P. A. Tarantilis, M. G. Polissiou, S. Diamantoglou, H. A. Tajmir-Riahi, *Cell Biochem Biophys* **2007**, *49*, 29–36.

[66] N. K. Janjua, A. Siddiqa, A. Yaqub, S. Sabahat, R. Quereshi, S. ul Haque, *Spectrochim. Acta Part A* **2009**, *74*, 1135–1137.

[67] K. C. Bible, J. L. Lensing, S. A. Nelson, Y. K. Lee, J. M. Reid, M. M. Ames, C. R. Isham, J. Piens, S. L. Rubin, J. Rubin, et al., *Clin. Cancer Res.* **2005**, *11*, 5935–5941.

[68] Y. Wang, A. Han, E. Chen, R. K. Singh, C. O. Chichester, R. G. Moore, A. P. Singh, N. Vorsa, *Int. J. Oncol.* **2015**, *46*, 1924–1934.

[69] T. J. Zwang, K. Singh, M. S. Johal, C. R. Selassie, *J. Med. Chem.* **2013**, *56*, 1491–1498.

[70] S. Mohan, K. Thiagarajan, R. Chandrasekaran, *Nat. Prod. Res.* **2014**, *29*, 366–369.

[71] H. Cui, J. Yuan, X. Du, M. Wang, L. Yue, J. Liu, *Oncol. Rep.* **2015**, *33*, 1284–1290.

[72] A. Medrano, S. M. Dennis, A. Alvarez-Valés, J. Perles, T. McGregor Mason, A. G. Quiroga, *Dalt. Trans.* **2015**, *44*, 3557–3562.

[73] P. Bergamini, V. Bertolasi, L. Marvelli, A. Canella, R. Gavioli, N. Mantovani, S. Manas, A. Romerosa, *Inorg. Chem.* **2007**, *46*, 17–23.

[74] A. Romerosa, P. Bergamini, V. Bertolasi, A. Canella, M. Cattabriga, R. Gavioli, S. Manas, N. Mantovani, L. Pellecani, *Inorg. Chem.* **2004**, *43*, 905–913.

[75] D. Montagner, E. Zangrando, B. Longato, *Inorg. Chem.* **2008**, *47*, 2688–2695.

[76] M. M. Dell'Anna, V. Censi, B. Carrozzini, R. Caliandro, N. Denora, M. Franco, D. Veclani, A. Melchior, M. Tolazzi, P. Mastrorilli, *J. Inorg. Biochem.* **2016**, *163*, 346–361.

[77] Z. Chval, M. Sip, *J. Mol. Struct. THEOCHEM* **2000**, *532*, 59–68.

[78] J. V. Burda, M. Zeizinger, J. Leszczynski, *J. Comput. Chem.* **2005**, *26*, 907–914.

[79] C. Zhu, J. Raber, L. A. Eriksson, *J. Phys. Chem. B* **2005**, *109*, 12195–12205.

[80] D. V. Deubel, *J. Am. Chem. Soc.* **2006**, *128*, 1654–1663.

[81] J. K. C. Lau, D. V. Deubel, *J. Chem. Theory Comput.* **2006**, *2*, 103–106.

[82] M. F. A. Lucas, M. Pavelka, M. E. Alberto, N. Russo, *J. Phys. Chem. B* **2009**, *113*, 831–838.

[83] A. Melchior, E. Sánchez Marcos, R. R. Pappalardo, J. M. Martínez, *Theor. Chem. Acc.* **2011**, *128*, 627–638.

[84] M. E. Alberto, C. Cosentino, N. Russo, *Struct Chem* **2012**, *23*, 831–839.

[85] V. Graziani, C. Coletti, A. Marrone, N. Re, *J. Phys. Chem. A* **2016**, *120*, 5175–5186.

[86] V. P. Reddy, I. Mitra, S. Mukherjee, P. S. Sengupta, R. Dodda, S. C. Moi, *Chem. Phys. Lett.* **2016**, *657*, 148–155.

[87] I. Mitra, V. P. B. Reddy, S. Mukherjee, W. Linert, S. C. Moi, *Chem. Phys. Lett.* **2017**, *678*, 250–258.

[88] S. Mukherjee, V. P. R. B, I. Mitra, W. Linert, S. C. Moi, *Chem. Phys. Lett.* **2017**, *678*, 241–249.

[89] D. Andrae, U. Häußermann, M. Dolg, H. Stoll, H. Preuß, *Theor. Chim. Acta* **1990**, *77*, 123–141.

[90] P. Di Bernardo, P. L. Zanonato, F. Benetollo, A. Melchior, M. Tolazzi, L. Rao, *Inorg. Chem.* **2012**, *51*, 9045–9055.

[91] A. Melchior, E. Peralta, M. Valiente, C. Tavagnacco, F. Endrizzi, M. Tolazzi, *Dalt. Trans.* **2013**, *42*, 6074–6082.

[92] F. Endrizzi, A. Melchior, M. Tolazzi, L. Rao, *Dalt. Trans.* **2015**, *44*, 13835–13844.

[93] J. Tomasi, B. Mennucci, R. Cammi, *Chem. Rev.* **2005**, *105*, 2999–3093.

[94] M. J. Frisch, G. W. Trucks, H. B. Schlegel, G. E. Scuseria, M. A. Robb, J. R. Cheeseman, G. Scalmani, V. Barone, B. Mennucci, G. A. Petersson, et al., *Gaussian, Inc., Wallingford CT,* **2009**.

[95] J. Kreutzer, P. Blaha, U. Schubert, *Comput. Theor. Chem.* **2016**, *1084*, 162–168.

[96] M. Pavelka, M. F. a Lucas, N. Russo, *Chem. - A Eur. J.* **2007**, *13*, 10108–10116.

[97] G. Lamm, G. R. Pack, *Proc. Natl. Acad. Sci. U.S.A* **1990**, *87*, 9033–9036.

[98] J. Vinje, E. Sletten, J. Kozelka, *Chem. - A Eur. J.* **2005**, *11*, 3863–3871.

[99] M. E. Alberto, V. Butera, N. Russo, *Inorg. Chem.* **2011**, *50*, 6965–6971.

[100] L. P. Martin, T. C. Hamilton, R. J. Schilder, *Mol. Pathw.* **2008**, *14*, 1291–1296.

[101] M. D. Hall, T. W. Hambley, *Coord. Chem. Rev.* **2002**, *232*, 49–67.

[102] T. C. Johnstone, G. A. Y. Park, S. J. Lippard, **2014**, *476*, 471–476.

[103] K. S. Lovejoy, R. C. Todd, S. Zhang, M. S. Mccormick, J. A. D'Aquino, J. T. Reardon, A. Sancar, K. M. Giacomini, S. J. Lippard, *Proc Natl Acad Sci* **2008**, *105*, 8902–8907.

[104] G. Zhu, M. Myint, W. H. Ang, L. Song, S. J. Lippard, *Cancer Res.* **2012**, *72*, 790–800.

[105] D. Wang, G. Zhu, X. Huang, S. J. Lippard, *Proc Natl Acad Sci* **2010**, *107*, 9584–9589.

[106] G. E. Damsma, A. Alt, F. Brueckner, T. Carell, P. Cramer, *Nat. Struct. Mol. Biol.* **2007**, *14*, 1127–1133.

[107] K. S. Lovejoy, M. Serova, I. Bieche, S. Emami, M. D. Incalci, M. Broggini, E. Erba, C. Gespach, E. Cvitkovic, S. Faivre, et al., *Mol. Cancer Ther.* **2011**, *10*, 1709–1720.

[108] G. Y. Park, J. J. Wilson, Y. Song, S. J. Lippard, *Proc Natl Acad Sci* **2012**, *109*, 11987–11992.

[109] R. H. Shoemaker, *Nat. Rev. Cancer* **2006**, *6*, 813–823.

[110] I. A. Riddell, T. C. Johnstone, G. Y. Park, S. J. Lippard, *Chem. - A Eur. J.* **2016**, *22*, 7574–7581.

[111] M. H. Baik, R. a. Friesner, S. J. Lippard, *J. Am. Chem. Soc.* **2003**, *125*, 14082–14092.

[112] J. Raber, C. B. Zhu, L. A. Eriksson, *J. Phys. Chem. B* **2005**, *109*, 11006–11015.

[113] L. A. Costa, T. W. Hambley, W. R. Rocha, W. B. De Almeida, H. F. Dos Santos, *Int. J. Quantum Chem.* **2006**, *106*, 2129–2144.

[114] Y. Gao, L. Zhou, *Theor. Chem. Acc.* **2009**, *123*, 455–468.

[115] Z. Xu, L. Zhou, *Int. J. Quantum Chem.* **2010**, *111*, 1907–1920.

[116] D. Zhang, L. Zhou, *Comput. Theor. Chem.* **2011**, *967*, 102–112.

[117] F. Šebesta, J. V Burda, *J. Inorg. Biochem.* **2017**, *172*, 100–109.

[118] T. Zimmermann, J. V. Burda, *Interdiscip. Sci. Comput. Life Sci.* **2010**, *2*, 98–114.

[119] B. Chen, L. Zhou, *Comput. Theor. Chem.* **2015**, *1074*, 36–49.

[120] T. C. Johnstone, S. J. Lippard, *J. Am. Chem. Soc.* **2014**, *136*, 2126–2134.

[121] Y. Zhao, D. G. Truhlar, *Theor. Chem. Acc.* **2008**, *120*, 215–241.

[122] Y. Zhao, D. G. Truhlar, *Accounts Chem. reserch* **2008**, *41*, 157–167.

[123] N. Takagi, S. Sakaki, *J. Am. Chem. Soc.* **2012**, *134*, 11749–11759.

[124] Y. Liu, J. Zhao, F. Li, Z. Chen, *J. Comput. Chem.* **2013**, *34*, 121–131.

[125] M. Malik, D. Michalska, *Spectrochim. Acta. A. Mol. Biomol. Spectrosc.* **2014**, *125*, 431–9.

[126] H.-Y. Chen, H.-F. Chen, C.-L. Kao, P.-Y. Yang, S. C. N. Hsu, *Phys. Chem. Chem. Phys.* **2014**, *16*, 19290–19297.

[127] H. Wang, J. W. Bozzelli, *ChemPhysChem* **2016**, 1983–1992.

[128] H. S. Yu, X. He, S. L. Li, D. G. Truhlar, *Chem. Sci.* **2016**, *7*, 5032–5051.

[129] P. J. Stephens, F. J. Devlin, C. F. Chabalowski, M. J. Frisch, *J. Phys. Chem.* **1994**, *98*, 11623–11627.

[130] S. Grimme, S. Ehrlich, L. Goerigk, *J. Comput. Chem.* **2011**, *32*, 1456–1465.

[131] M. Mikola, K. D. Klika, A. Hakala, J. Arpalahti, *Transition* **1999**, *38*, 571–578.

[132] J. Jestin, J. Chottard, U. Frey, G. Laurenczy, A. E. Merbach, *Inorg. Chem.* **1994**, *33*, 4277–4282.

[133] V. Monjardet-Bas, J. C. Chottard, J. Kozelka, *Chem. - A Eur. J.* **2002**, *8*, 1144–1150.

[134] M. T. Gregory, G. Y. Park, T. C. Johnstone, Y.-S. Lee, W. Yang, S. J. Lippard, *Proc. Natl. Acad. Sci.* **2014**, *111*, 9133–9138.

[135] R. N. Bose, S. K. Ghosh, S. Moghaddas, *J. Inorg. Biochem.* **1997**, *65*, 199–205.

[136] C. Demetzos, N. Pippa, *Drug Deliv.* **2014**, *21*, 250–257.

[137] D. Peer, J. M. Karp, S. Hong, O. C. Farokhzad, R. Margalit, R. Langer, *Nat. Nanotechnol.* **2007**, *2*, 751–760.

[138] E. Ruoslahti, S. N. Bhatia, M. J. Sailor, *J. Cell Biol.* **2010**, *188*, 759–768.

[139] C. McCallion, J. Burthem, K. Rees-Unwin, A. Golovanov, A. Pluen, *Eur. J. Pharm. Biopharm.* **2016**, *104*, 235–250.

[140] K. S. Novoselov, A. K. Geim, S. V. Morozov, D. Jing, Y. Zhang, S. V. Dubonos, I. V. Grigorieva, A. A. Firsov, *Science* **2004**, *306*, 666–669.

[141] S. Goenka, V. Sant, S. Sant, *J. Control. Release* **2014**, *173*, 75–88.

[142] H. Wang, X. Yuan, Y. Wu, H. Huang, X. Peng, G. Zeng, H. Zhong, J. Liang, M. M. Ren, *Adv. Colloid Interface Sci.* **2013**, *195–196*, 19–40.

[143] J. Zhao, Z. Wang, J. C. White, B. Xing, *Environ. Sci. Technol.* **2014**, *48*, 9995–10009.

[144] R. Balasubramanian, S. Chowdhury, *J. Mater. Chem. A* **2015**, *3*, 21968–21989.

[145] J. G. Yu, L. Y. Yu, H. Yang, Q. Liu, X. H. Chen, X. Y. Jiang, X. Q. Chen, F. P. Jiao, *Sci. Total Environ.* **2015**, *502*, 70–79.

[146] K. P. Loh, Q. Bao, P. K. Ang, J. Yang, *J. Mater. Chem.* **2010**, *20*, 2277–2289.

[147] T. Schwamb, B. R. Burg, N. C. Schirmer, D. Poulikakos, *Nanotechnology* **2009**, *20*, 405704.

[148] N. K. Mahanta, A. R. Abramson, *2012 13th IEEE Intersoc. Conf.* **2012**, 1–6.

[149] T. Kuila, S. Bose, A. K. Mishra, P. Khanra, N. H. Kim, J. H. Lee, *Prog. Mater. Sci.* **2012**, *57*, 1061–1105.

[150] M. Sprinkle, M. Ruan, Y. Hu, J. Hankinson, M. Rubio-Roy, B. Zhang, X. Wu, C. Berger, W. A. de Heer, *Nat. Nanotechnol.* **2010**, *5*, 727–731.

[151] S. Park, J. An, I. Jung, R. D. Piner, S. J. An, X. Li, A. Velamakanni, R. S. Ruoff, *Nano Lett.* **2009**, *9*, 1593–1597.

[152] J. Kim, L. J. Cote, F. Kim, W. Yuan, K. R. Shull, J. Huang, *J. Am. Chem. Soc.* **2010**, *132*, 8180–8186.

[153] F. Kim, L. J. Cote, J. Huang, *Adv. Mater.* **2010**, *22*, 1954–1958.

[154] F. Guo, F. Kim, T. H. Han, V. B. Shenoy, J. Huang, R. H. Hurt, *ACS Nano* **2011**, *5*, 8019–8025.

[155] A. Bagri, C. Mattevi, M. Acik, Y. J. Chabal, M. Chhowalla, V. B. Shenoy, *Nat. Chem.* **2010**, *2*, 581–587.

[156] L. Feng, L. Wu, X. Qu, *Adv. Mater.* **2013**, *25*, 168–186.

[157] K. Yang, L. Feng, Z. Liu, *Adv. Drug Deliv. Rev.* **2016**, *105*, 228–241.

[158] E. Mastrobattista, M. A. E. M. van der Aa, W. E. Hennink, D. J. A. Crommelin, *Nat. Rev. Drug Discov.* **2006**, *5*, 115–121.

[159] A. Hatefi, B. F. Canine, *Gene Ther. Mol. Biol.* **2009**, *13(A)*, 15–19.

[160] A. P. Lam, D. A. Dean, *Gene Ther.* **2010**, *17*, 439–447.

[161] J. V. Natarajan, C. Nugraha, X. W. Ng, S. Venkatraman, *J. Control. Release* **2014**, *193*, 122–138.

[162] D. Arora, S. Jaglan, *Trends Food Sci. Technol.* **2016**, *54*, 114–126.

[163] X. Z. Xiaoying Yang Zunfeng Liu, Yanfeng Ma, Yi Huang,and, Y. Chen, *J Phys Chem C* **2008**, *112*, 17554.

[164] Z. Liu, J. T. Robinson, X. Sun, H. Dai, *J Am Chem Soc* **2008**, *130*, 10876–10877.

[165] Z. Liu, L. Zhao, Z. Zhou, T. Sun, Y. Zu, *Scanning* **2012**, *34*, 302–308.

[166] L. Tian, X. Pei, Y. Zeng, R. He, Z. Li, J. Wang, Q. Wan, X. Li, *J. Nanoparticle Res.* **2014**, *16*, 2709.

[167] G. Y. Chen, C. Le Meng, K. C. Lin, H. Y. Tuan, H. J. Yang, C. L. Chen, K. C. Li, C. S. Chiang, Y. C. Hu, *Biomaterials* **2015**, *40*, 12–22.

[168] M. del R. Cuevas-Flores, M. A. Garcia-Revilla, M. Bartolomei, *J. Comput. Chem.* **2017**, 1–10.

[169] A. D. Becke, *Phys. Rev. A* **1988**, *38*, 3098–3100.

[170] A. D. Becke, *J. Chem. Phys.* **1993**, *98*, 1372–1377.

[171] A. D. Becke, *J. Chem. Phys.* **1993**, *98*, 5648–5652.

[172] C. Adamo, V. Barone, *J. Chem. Phys.* **1999**, *110*, 6158–6170.

[173] A. D. Boese, J. M. L. Martin, *J. Chem. Phys.* **2004**, *121*, 3405–3416.

[174] O. A. Vydrov, J. Heyd, A. V. Krukau, G. E. Scuseria, *J. Chem. Phys.* **2006**, *125*, 074106:1-9.

[175] E. R. Johnson, A. D. Becke, *J. Chem. Phys.* **2006**, *124*, 174104.

[176] A. Melchior, J. M. Martínez, R. R. Pappalardo, E. Sánchez Marcos, *J. Chem. Theory Comput.* **2013**, *9*, 4562–4573.

[177] M. E. Cooley, L. E. Davis, M. DeStefano, J. Abrahm, *Cancer Nurs.* **1994**, *17*, 173–184.

[178] M. J. Frisch, G. W. Trucks, H. B. Schlegel, G. E. Scuseria, M. A. Robb, J. R. Cheeseman, G. Scalmani, V. Barone, G. A. Petersson, H. Nakatsuji, et al., *Gaussian 16 Revis. A 03* **2016**.

[179] M. O. Sinnokrot, E. F. Valeev, C. D. Sherrill, *J. Am. Chem. Soc.* **2002**, *124*, 10887–10893.

[180] M. B. Goldey, B. Belzunces, M. Head-Gordon, *J. Chem. Theory Comput.* **2015**, *11*, 4159–4168.

[181] P. Jurečka, J. Šponer, J. Černý, P. Hobza, *Phys. Chem. Chem. Phys.* **2006**, *8*, 1985–1993.

[182] K. E. Riley, M. Pitonak, P. Jurečka, P. Hobza, *Chem. Rev.* **2010**, *110*, 5023–5063.

Chapter 4

Fluoroquinolones: Study of the Chemical Properties and the Adsorption Mechanism on Carbon Nano Tube

One sometimes finds what one is not looking for.
When I woke up just after dawn on Sept. 28, 1928,
I certainly didn't plan to revolutionize all medicine
by discovering the world's first antibiotic.
But I guess that was exactly what I did.
Cit. "Alexander Fleming"

4.1 Introduction

4.1.1 A brief history of the quinolones

The history of quinolone antibacterial compounds started in 1962 with nalidixic acid. The compound showed a modest Gram-negative activity and a low oral absorption, therefore it was not a good candidate for the treatment of systemic infections. Its urinary concentrations, however, were found to be high, so the compound was (and continues to be) used for the treatment of urinary tract infections, although after its introduction into clinical use a number of organisms were found to possibly develop resistance.[1] The compound was used as a starting model to obtain new drugs that would improve the unsatisfactory tolerance and increase the activity spectrum.[2] Structure-activity studies have shown that the 1,4-dihydro-4-oxo-3-pyridinecarboxylic acid moiety is essential for antibacterial activity, and that such system must be bound with an aromatic ring; the structure is called "4-quinolone" skeleton (Scheme 1).[1]

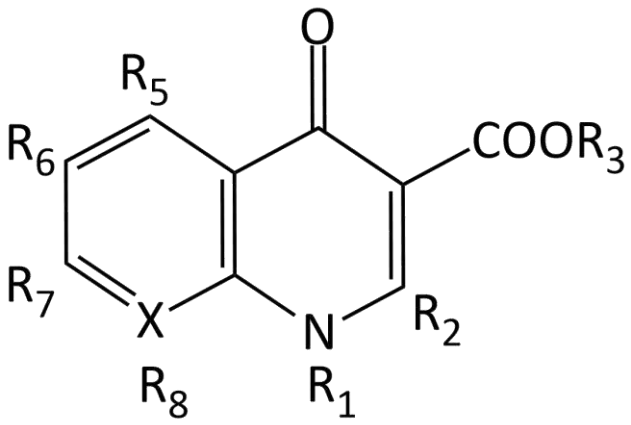

Scheme 1 4-quinolone' skeleton (4-oxo-1,4 dihydroquinolone).

Marginal structural modifications were initially made in order to develop some of the early second-generation compounds such as oxolinic acid and cinoxacin. More substantial structural changes were obtained by adding the piperazine ring to position R_7 (see Scheme 1), thereby leading to the development of the pipemidic acid, which showed an increase in the activity against Gram-negative bacteria. Third-generation quinolones were marked by fluorination at the R_6 position (see Scheme 1), giving rise to the classification of future compounds, such as fluoroquinolones (FQs). Carbon for nitrogen substitution at the X

position and alkyl substitution at the R_1 position (see Scheme 1) is essential for activity, with lower alkyl (methyl, ethyl, cyclopropyl) compounds generally having progressively greater potency. Norfloxacin was the first quinolone to be used in the treatment of ocular infectious diseases, because it demonstrated activity against Gram-negative and Gram-positive bacilli. The addition of a cyclopropryl ring at the R_1 position (see Scheme 1) led to the development of ciprofloxacin, while the addition of a six-member (pyridobenzoxazine) ring between the R_1 and R_8 positions led to the development of ofloxacin. Levofloxacin, created by means of isolation of the active enantiomer of ofloxacin, further improved susceptibility against Gram-positive bacteria. Emerging resistance among Gram-positive organisms led to the development of newer agents. The addition of a methoxy sidechain at the R_8 position (see Scheme 1) led to the development of fourth-generation compounds, including moxifloxacin. FQs now exhibit an extended spectrum of activity, including effectiveness against additional Gram-negative pathogens (e.g., *P. aeruginosa*, *H. influenzae*, *N. gonorrhoeae*), Gram-positive cocci (e.g., *S. aureus*) and some streptococci, and they are by far the most frequently used antibacterial quinolones. [2–6] Nowadays, numerous representatives are used in both human (Scheme 2) and veterinary (Scheme 3) medicine.[6]

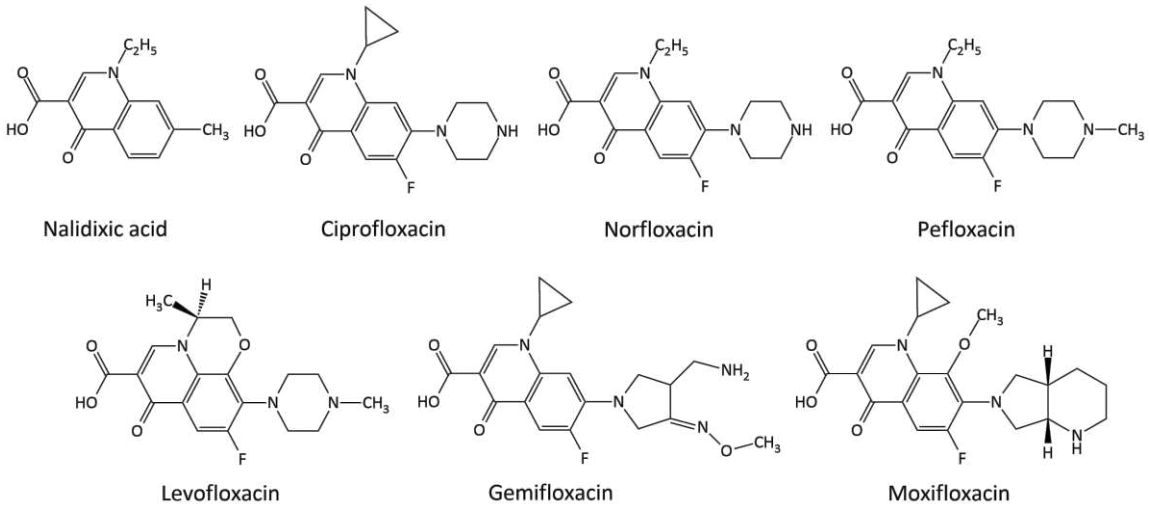

Scheme 2 Antibacterial quinolone derivatives commonly used in human medicine.

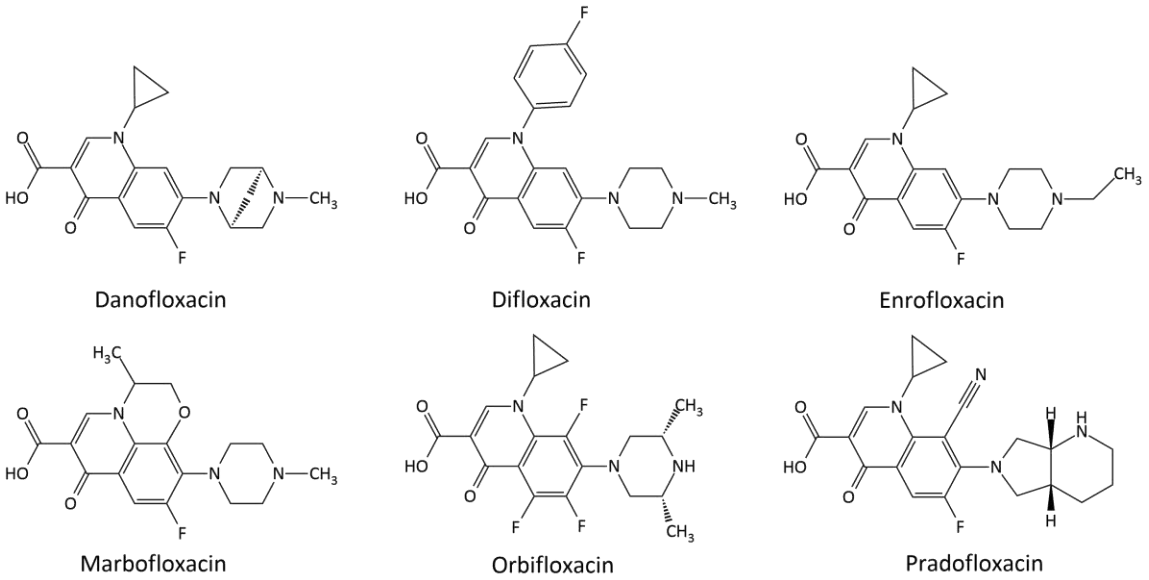

Scheme 3 Antibacterial quinolone derivatives commonly used in veterinary medicine.

4.1.2 Mechanism of action and resistance

FQs act by inhibiting two type of topoisomerases enzymes that human cells lack, DNA gyrase and topoisomerase IV (Topo IV), essential for bacterial DNA replication, thereby enabling these agents to be both specific and bactericidal.[7,8] DNA gyrase introduces negative superhelical twists in the bacterial DNA double helix ahead of the replication fork, thereby catalysing the separation of daughter chromosomes. Such activity is essential for the initiation of DNA replication and allows the binding of initiation proteins. DNA gyrase is an excellent target for FQs, because it is not present in eukaryotic cells and it is essential for bacterial growth.[9–11] Topo IV has two functions in the cell: firstly, it serves as a decatenating enzyme that resolves interlinked daughter chromosomes after DNA replication (Topo IV is required at the terminal stages of DNA replication to unlink newly replicated daughter chromosomes); secondly, it relaxes positive supercoils (a function shared with the DNA gyrase).[9–13] The mechanism of quinolone inhibition occurs via formation of a ternary cleavage complex with the topoisomerase enzyme and DNA (see Figure 1). FQs bind in a noncovalent manner to the enzyme−DNA interface in the cleavage−ligation active site. Drugs interact with the protein and intercalate into the DNA at both cleaved scissile bonds. As a result of their intercalation, FQs increase the steady-state concentration of cleavage complexes by acting on ligation as physical blocks. When replication forks, transcription complexes or other DNA tracking systems collide with

drug-stabilized gyrase or Topo IV−DNA cleavage complexes, which are converted to permanent chromosomal breaks. In turn, the generation of DNA breaks triggers the SOS response and other DNA repair pathways. If the strand breaks overwhelm such processes, they can lead to cell death.[14–17]

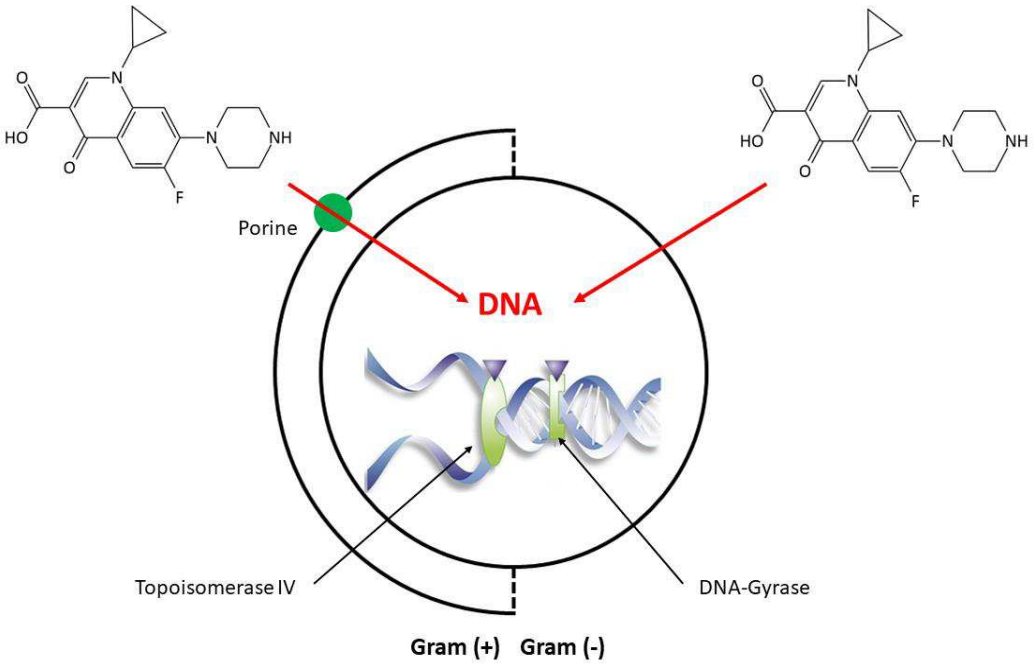

Figure 1 Schematic representation of mechanism of action for FQs.

In general, bacterial resistance to antibiotics occurs in two ways. The first way is known as the ‘‘natural’’ way, when all the strains of the same bacterial species are resistant to a particular drug. This type of antibiotic resistance is known as intrinsic resistance. The second way is ‘‘acquired’’, and occurs when resistant strains have evolved from susceptible ones through a selection after mutation or lateral genetic transfer events. FQs have been extensively used in medicine and in the livestock production units,[6] even though the prescribing guidelines suggest limiting the use of FQs, since the resistance continues to rise and becomes a major problem in the clinical setting.[18] Resistance to the fluoroquinolones can occur via a range of mechanisms (see Figure 2). The most common mechanism of FQs resistance is due to a mutation of the genes that encode the primary and secondary targets of these drugs, the DNA gyrase and Topo IV. The region where mutations arise in the genes that encode fluoroquinolone resistance is a short DNA sequence, the quinolone resistance-determining region (QRDR). Mutations in the QRDR

region, resulting in amino acid substitutions, alter the structure of the target protein and subsequently the FQs binding affinity of the enzyme, leading to drug resistance. Other resistance mechanisms can be: transmissible quinolone-resistance mechanisms due to plasmid-mediated quinolone resistance (PMQR) genes, changes in the permeability of the cell membrane, efflux of FQs due to chromosomal multidrug efflux pumps, capable of actively removing FQs from the bacterial cell.[3,7,8,19]

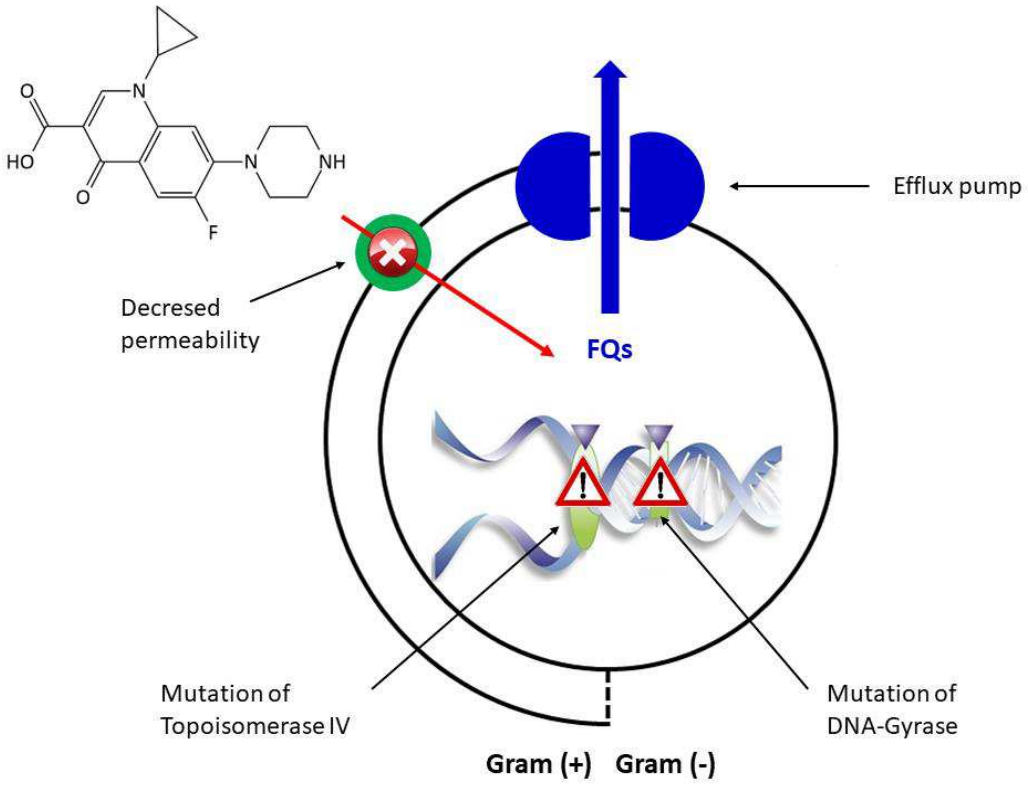

Figure 2 Schematic representation of mechanisms of resistance for FQs.

4.2 Chemical Properties: Inside the Acidity of Fluoroquinolone Antibacterials

4.2.1 Acid base proprieties

pH plays an extremely important role on both the activity and the pharmacokinetics of a drug and is well known mainly for its acid-base properties. In particular, the activity of FQs is reported to be pH-dependent; the binding of the bacterial DNA gyrase and Topo IV enzyme is therefore assumed to be dependent on the protonation states of FQs.[20,21] The study of the protonation equilibria of FQs has been extensively developed over the last

twenty years, and various techniques have been used to obtain both equilibrium constants and proton coordination sites.[22–27] Fluoroquinolones (FQs) are ampholyte compounds presenting multiple sites that could be protonated depending on pH. However, the reported acid–base properties of FQs are highly controversial, particularly as regards the values of protonation constants and even the number of basic sites.[26] FQs can exist in five different pH-dependent protonation species, namely: di-cation, (H_3FQ^{2+}), cation (H_2FQ^{+}), zwitterions (zHFQ), neutral (nHFQ) species and anion (FQ^{-}). A scheme of the equilibria involving such species is reported in scheme 4.

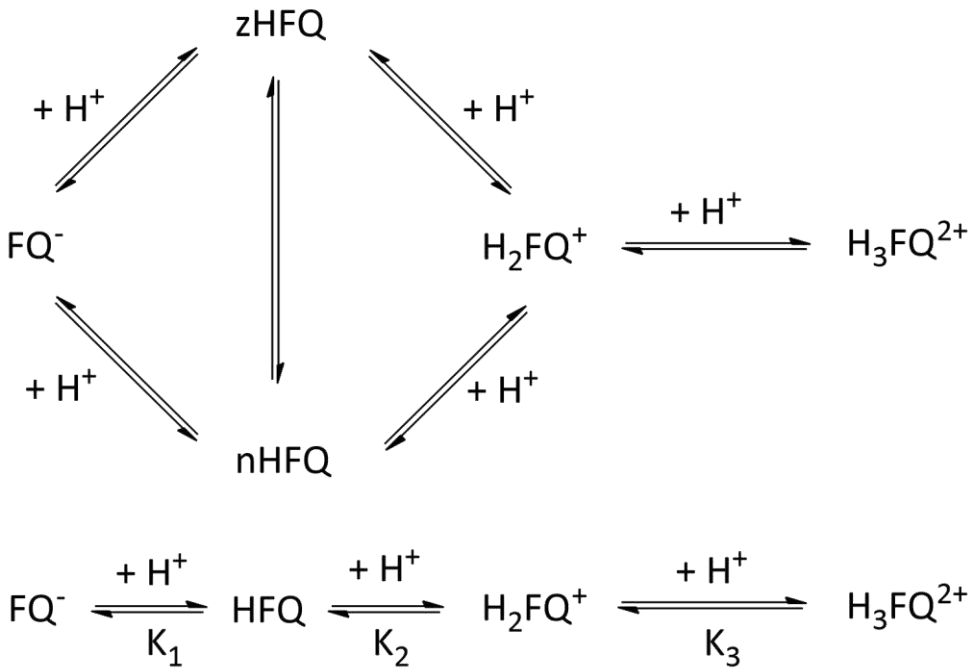

Scheme 4 Protonation equilibria involving micro-species and protonation equilibria taking into account only the macro-species.

The mole fractions of zHFQ and nHFQ species reach their maximum values at the isoelectric point (pH 7), in water. From an experimental point of view, zHFQ seems to be the most stable species,[22,23,26,27] although according to some theoretical works employing the polarizable continuum model (PCM)[28] to simulate the solvent the most stable species should be nHFQ.[25,29] The inconsistency could be related to the fact that the PCM model does not take into account the structure of the solvent. Therefore, important interactions (hydrogen bond) between the solute and the solvent that could stabilize zHFQ form in water can be missed, thereby leading to wrong conclusions.[30,31]

The problem could be solved using the discrete-continuum approach, according to which some water molecules are placed around the solute to capture strong interactions, and the entire system is then immersed in the continuum cavity. In 2007 Lamber *et al.*[32] investigated the relative stability of zHFQ and nHFQ forms of levofloxacin by means of DFT calculations, using both the PCM model and the discrete-continuum approach. In their work the discrete-continuum approach was performed by placing 5 molecules of water near the ionizable groups. Four water molecules were used to stabilize the carboxylate (COO^-) group, since preliminary calculations with one or two water molecules did not show any significant changes with respect to the continuum model results. The fifth molecule is necessary to stabilize the N atom of the piperazine ring. Thanks to the use of this approach, the authors revealed that zCFX is slightly more stable than the nCFX form in water, and hydrogen bonds were shown to play a key role.

The H_3FQ^{2+} species (available only in extremely acidic pH) presents another incongruity: the protonation may take place at both the piperazine[26,33] ring and the carbonyl oxygen.[34,35]

4.2.2 Aim of this work

In the present thesis Ciprofloxacin (CFX) (scheme 5) has been chosen as a representative model, because it is the most prescripted FQ in the world.[6] CFX was patented in 1983 by Bayer A.G. and subsequently approved by the United States Food and Drug Administration (US FDA) for use in the United States in 1987.[36] CFX is on the World Health Organization's List of Essential Medicines, the most effective and safe medicines needed in a health system, and[37] has been a very successful drug for Bayer A.G., generating billions of dollars in revenue.[36] Ciprofloxacin is the most potent FQ, used for the treatment of bacterial gastroenteritis caused by Gram-negative bacilli. It is also used for the treatment of respiratory tract infections and it is particularly effective for controlling bronchitis and pneumonia and for combating infections of the skin, soft tissues, bones, joints, urinary tract infections. It is particularly convenient for the control of chronic infections characterized by renal tissue involvement.[5] CFX has also attracted significant interest among the scientific community, due to its antiproliferative and apoptotic activities in several cancer cell lines; CFX was observed to induce time- and dose-dependent growth

inhibition and apoptosis of various carcinoma, osteosarcoma and leukemia cell lines by blocking mitochondrial DNA synthesis.[38–41]

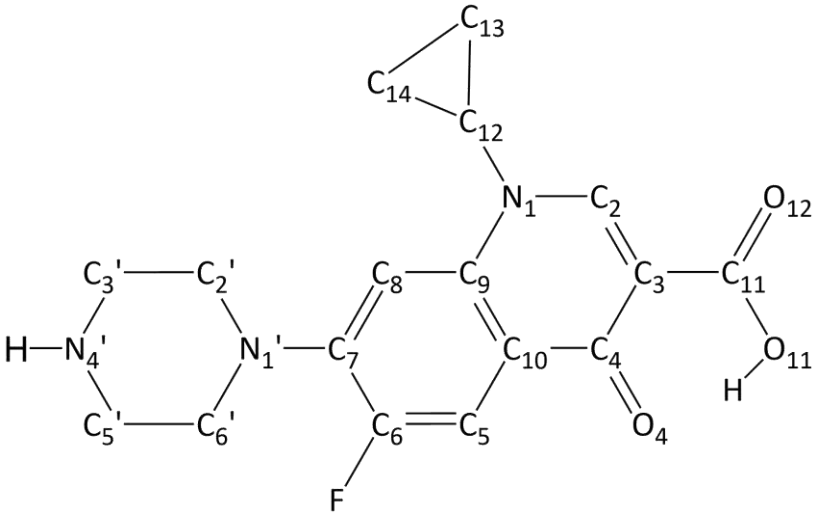

Scheme 5 Schematic representation of ciprofloxacin (CFX, neutral form).

In our work, DFT calculations were run to provide geometries, relative stability and photochemical behaviour of the different protonation states of CFX in gas phase and polarized continuum medium (PCM). A discrete-continuum approach was also introduced in order to overcome the limit of the PCM method discussed above. To understand how many water molecules surround zCFX-N4' and nCFX molecules, a molecular dynamics simulations were performed in order to build a good cluster to be used for the discrete-continuum approach. Furthermore, calculated UV-Vis absorbance spectra were carried out for CFX^-, zCFX, nCFX, H_2CFX^+ and H_3CFX^{2+} species in the various possible tautomeric forms, in order to provide detailed information on the effect of protonation on such spectra.

4.2.3 Computational details

4.2.3.1 Molecular dynamics simulation

The GROMACS 5.1.4 package[42] was used to perform MD simulations in water on systems containing nCFX, zCFX, and 1000 water molecules. The united atom GROMOS 54A7 force field (G54A7)[43] , used to represent all bonded and non-bonded interactions, has been so far one of the most successful; it was developed primarily for the simulation of large

organic molecules and has been thoroughly tested.[44] The cross-term Lennard-Jones (12, 6) parameters were obtained using the Lorenz-Berthelot combination rules. Water was described by the SPCE model.[45] United atom (UA) topologies for nCFX and zCFX were obtained from ATB (Automated topology builder).[46] The particle-mesh Ewald method was used to calculate long-range electrostatic interactions[47,48], whereas vdW interactions were treated with smooth cut-off at a distance of 12 Å. Periodic boundary conditions were applied in all directions, the LINear Constraint Solver (LINCS) algorithm[49] was applied to constrain all hydrogen bonds. After energy minimization, the systems were pre-equilibrated by MD simulations in NVT canonical ensemble and in NPT isothermal-isobaric ensemble at 1 atm and 298.15 K for 1 ns at the temperature of 298.15 K and 1 atm with Berendsen coupling methods.[50] The simulation was run with NPT ensemble at 1 atm and 298.15 K for 10 ns with a time step of 2 fs. The V-rescale[51] algorithm was used as temperature coupling method, while the Parrinello-Rahman algorithm[52] was chosen as pressure coupling method. Hydrogen bonds were detected by analysing the trajectories with the program g_hbond of the GROMACS software. A proton-acceptor distance cut-off of 0.35 nm and a hydrogen-acceptor-donor angle cut-off of 30° degrees were used for defining the hydrogen bonds.

4.2.3.2 Quantum mechanics calculations

DFT calculations were performed with the Gaussian 09 program[53] using the B3LYP functional.[54] The B3LYP hybrid functional was very successful in the thermochemistry of atoms and molecules. The B3LYP hybrid functional has become a standard method used to study organic chemistry.[55] All geometries of CFX in different protonation states were carried out in vacuum with a 6-311G(d,p) basis set for all atoms. Solvent effects were taken into account in two alternative ways: (1) implicit solvent introduced by the PCM method[28] using the universal force field (UFF)[56] radius for the spheres centred on each atom; (2) discrete-continuum approach, obtained by placing 10 water molecules around the protonated groups of the solute to capture the strong interactions and immerse the entire system in the continuum cavity. In the latter case, water molecules have been selected on the basis of the average number of waters that form hydrogen bonds with the ionizable groups, determined by preliminary molecular dynamics simulations. The cluster of 10 water molecules was constructed by taking some representative snapshots,

obtained by means of molecular dynamics simulations, and by optimizing the system at B3LYP/6-311G(d, p)/H_2O/methanol level of theory.

In order to confirm that stationary points were true minima, an analytical calculation of second derivatives of the energy and a vibrational frequency analysis were carried out. The same techniques were also used to extract zero-point vibrational energies (ZPVE) and thermal corrections to the electronic energy (E), Gibbs free energies (G) at 298 K. Excitation spectra of CFX^-, zCFX, nCFX, H_2CFX^+, H_3CFX^{2+} were calculated using the time-dependent formalism (TD-DFT)[57] at the same level of theory (B3LYP/6-311gG (d, p)/H_2O).

4.2.4 Results and discussion

4.2.4.1 Molecular dynamics simulation

Molecular dynamics simulations were performed to understand the amount of hydrogen bonds (H-bons) formed between water, zCFX-N4' and nCFX (see Scheme 6). The aim is understanding how many water molecules interact with zCFX-N4' and nCFX, in order to build a good cluster formed by z-nCFX and water molecules to be used for the discrete-continuum approach in the quantum mechanics calculations part. Indeed, constructing a cluster of water molecules by randomly inserting them could lead to an inefficient arrangement of the molecules and, consequently, of the hydrogen bonds, which could affect the relative stability of zCFX-N4' and nCFX molecules.

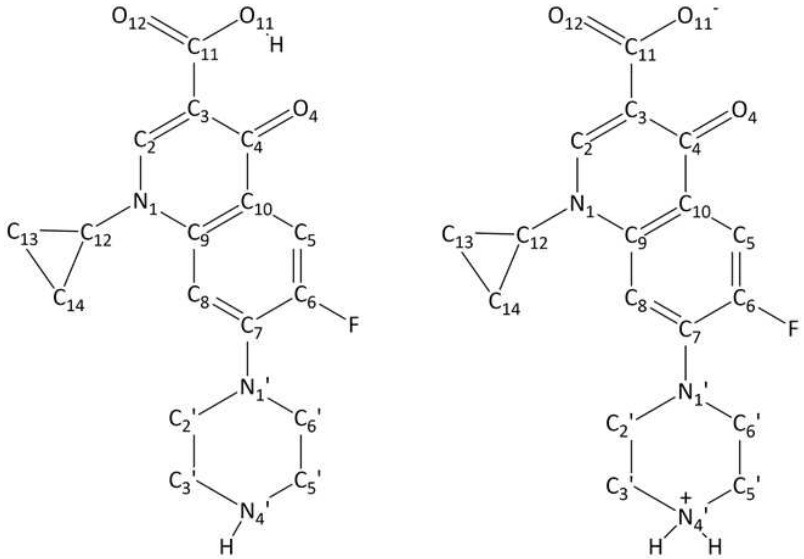

Scheme 6 Schematic representation of neutral and zwitterion form of CFX.

The time evolution of the H-bonds formed between water and zCFX-N4’ or nCFX is reported in Figure 3, along with the time evolution of the H-bonds formed between water and the inonizable groups presents in CFX.

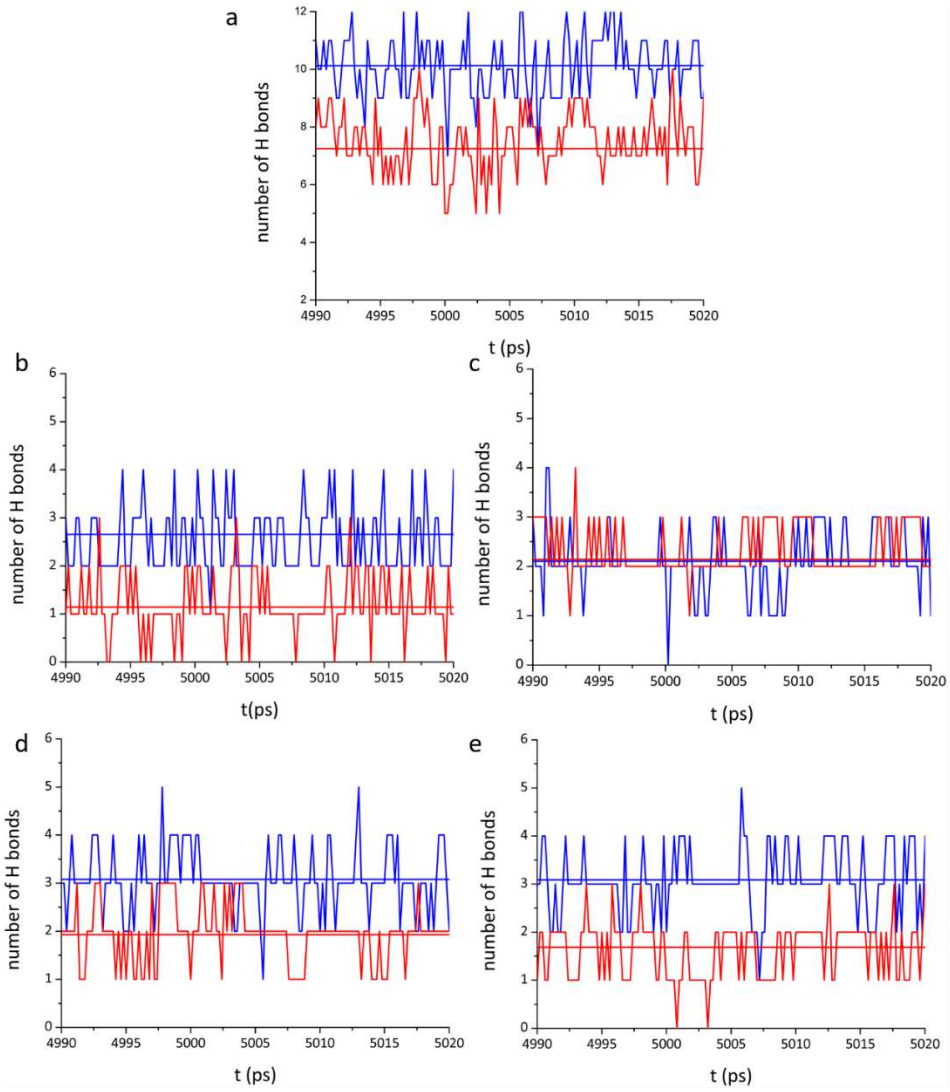

Figure 3 Time evolution (from 4990 to 5020 ps) of the H-bonds formed between water and a) CFX, b) N4’ c) O4, d) O11, e) O12. The blue curve represents zCFX-N4’ and the red curve represents nCFX. The straight line represents the average of the number of hydrogen bonds calculated throughout the trajectory.

The analysis of the number of H-bonds revealed that zCFX-N4’ and nCFX form on average 10.1 and 7.3 hydrogen bonds respectively. A more detailed observation reveals that N4’ amino group forms 2.6 H-bonds in zCFX-N4’ and 1.1 in nCFX. The difference can be explained by observing that N4' is bound to two H atoms in zCFX-N4’ and has a positive charge, while in nCFX it is bound to a single H atom and has no charge. Thanks to its

positive charge, the N4 'atom of zCFX-N4' interacts more effectively with the O atoms of water compared to the N4' atom of nCFX. For O4, the number of H-bonds for zCFX-N4' is very close to the number obtained for nCFX (2.1 and 2.2 respectively). Marked differences have been observed in O11 and O12 atoms. For zCFX-N4', O11 forms 3.1 H-bonds while nCFX forms 1.9; similar behaviors are reported for O12, where zCFX-N4' forms 3.1 H-bonds and nCFX 1.6. Such behavior can be explained by observing that the carboxyl group has a delocalized negative charge in zCFX-N4', while it is neutral in nCFX; therefore, COO^- in zCFX-N4' interacts more strongly with water compared to nCFX. H-bonds for other ionizable groups, N1, N1' and F, are not observed. Such trend is confirmed by the radial distribution function (RDF) calculated between the ionizable groups of CFX and H or O atoms of water molecules (Figure 4).

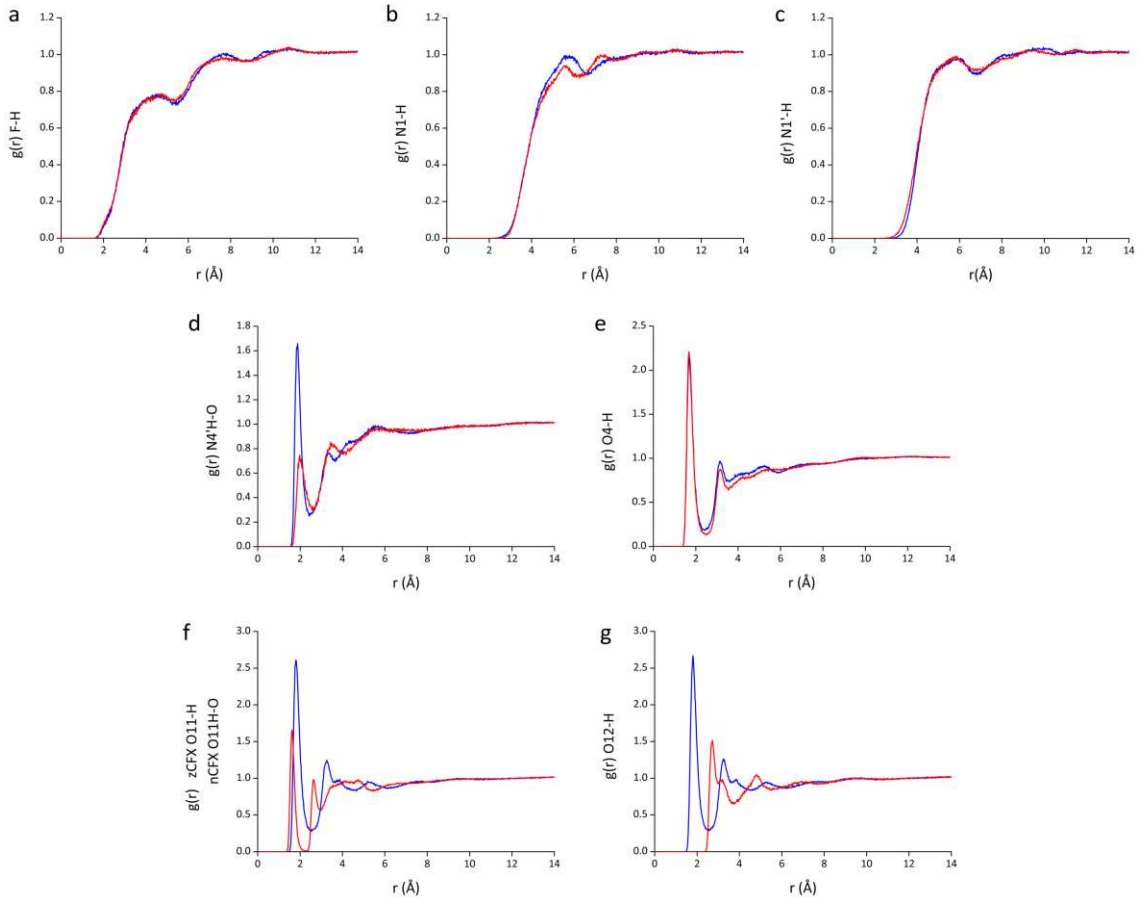

Figure 4 Simulated RDFs relative to a) F atom of z-nCFX and H atoms of water molecules; b) N1 atom of z-nCFX and H atoms of water molecules; c) N1' atom of z-nCFX and H atoms of water molecules; d) N4'-H atom of z-nCFX and O atoms of water molecules; e) O4 atom of z-nCFX and H atoms of water molecules; f) O11 atom of zCFX and H atoms of water molecules and O11-H atom of nCFX and O atoms of water molecules; g) O12 atom of z-nCFX H atoms of water molecules. The blue curve represents zCFX, the red curve represents nCFX.

RDF curve shows a notable peak, which indicates the most probable distance between the ionizable group of z-nCFX and the O or H atom of waters. For F, N1 and N1', RDF presents a flat curve (see Figure 4a, 4b, 4c), indicating a weak interaction between these groups and the O or H atoms of the water molecules. The RDF curves are in good agreement with the results of the analysis of the number of hydrogen bonds. For N4' ammine group, RDF shows a sharp peak at 1.9 Å for both zCFX-N4' and nCFX, indicating the most probable distance between N4'-H and the O atom of waters. The intensity of the peak in zCFX-N4' is more than twice than intensity of nCFX and the magnitude of RDF peak is directly proportional to the relative density of O atoms in water, indicating that the density of O atoms in zCFX-N4' is double the density in nCFX. A similar behaviour has been observed also for O11 and O12. The peak positions for O11 in zCFX-N4' are located at 1.8 Å and 1.6 Å in nCFX, while for O12 the peak is located at 1.8 Å in zCFX-N4' and at 2.7 in nCFX. On the contrary, O4 RDF curves show a similar pattern. The intensity of the peak in zCFX-N4' is equal to the one reported for nCFX, and the peak is located at 1.7 Å for both zCFX-N4' and nCFX. Such behavior has also been confirmed by the calculation of spatial distribution functions (SDF, see Figure 5) of O and H atoms of waters.

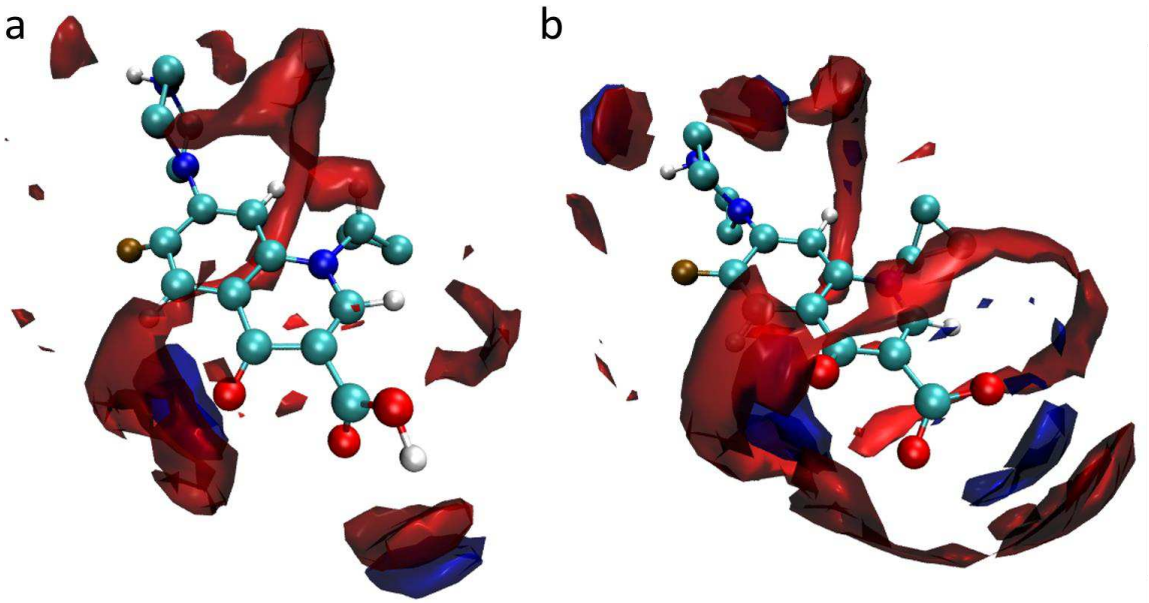

Figure 5 Spatial distribution functions for a) nCFX and b) zCFX-N4' at isovalue 13.5. SDF of O atoms of waters in red, SDF of H atoms of waters in blue.

Figure 5 shows that the density of O atoms around the amino group N4 ' is greater in zCFX-N4' than in nCFX. A similar pattern has been observed for the carboxy group. It is interesting to note that, in nCFX, O12 does not seem to greatly interact with the H atoms of the waters.

In conclusion, zCFX-N4' appears to form a higher number of hydrogen bonds compared to nCFX (10 and 7 respectively). In addition, the differences in the solution properties in zCFX-N4' and nCFX seem to be due to the presence of the carboxyl group and the N4 'amine group, which present a negative and a positive charge in zCFX-N4' and a neutral charge in nCFX. Dynamic simulations have been useful to understand how many molecules of water interact with CFX. This information has served us to get a representative cluster of water molecules and CFX to be used for the discrete-continuum approach. In our work we chose to use a cluster of 10 water molecules and CFX, obtained from a snapshot of the molecular dynamics simulations.

4.2.4.1 Quantum mechanics calculations

First Protonation

This part of the work started by analyzing the relative stability of zCFX and nCFX species in gas phase, implicit water and with discrete-continuum approach. The experimental data show that nCFX (protonation of O11 oxygen) and zCFX (protonation of N4' nitrogen, zCFX-N4') species (Scheme 7) is formed, and that zCFX-N4' is the most stable species in water.[22,23,26,27]

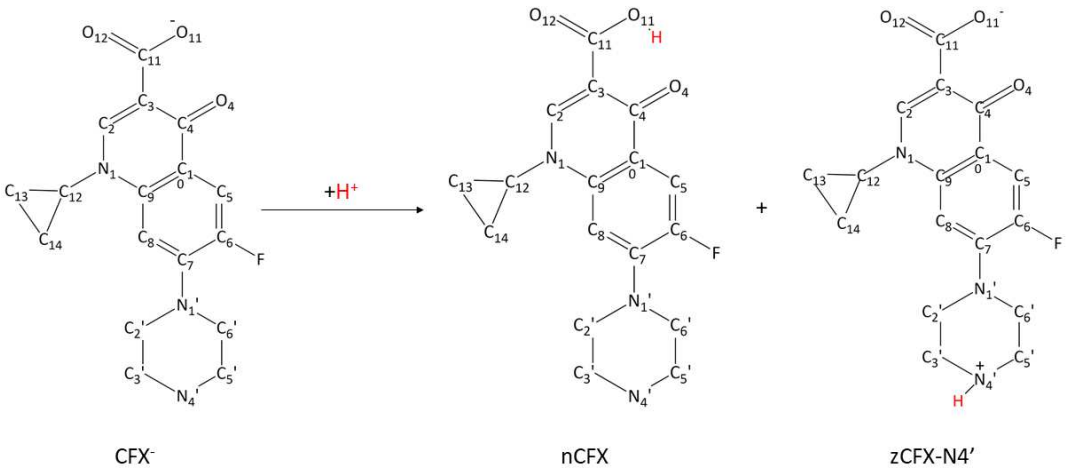

Scheme 7 CFX^- nCFX and zCFX-N4' species of CFX reported in literature. For simplicity, the proton of the first protonation reaction is indicated in red.

The optimized structures of the different species in implicit water are displayed in Figure 6. Overall, there are small structural changes in bond lengths and angles values, (see Table A1 in appendix B) between CFX^- and nCFX, zCFX-N4' species.

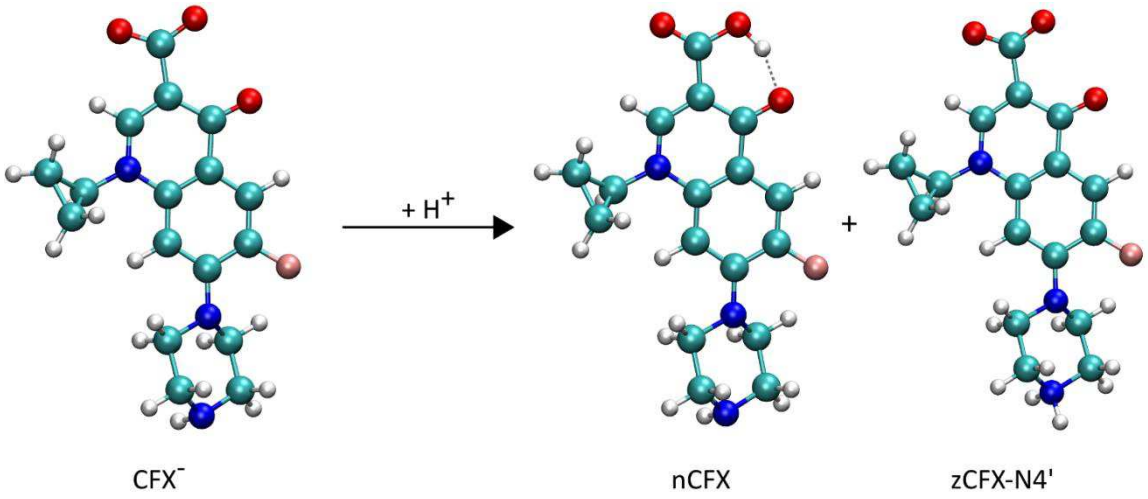

Figure 6 Optimized structures of CFX^-, nCFX and zCFX-N4' species in implicit water.

nCFX exhibits an increase of the distance C11-O11 (1.251 Å to 1.336 Å) and a slight decrease of the distance C11-O12 (1.261 Å to 1.216 Å); moreover, the formation of a hydrogen bond between O11-H and O4 (Figure 6) can be observed. The major change in zCFX-N4' occurred on the piperazine ring, where an increase of the distances C3'-N4' (1.468 Å to 1.509 Å) and C5'-N4' (1.467 Å to 1.510 Å) has been registered. For this species, X-Ray diffraction has been obtained. Table 1 shows the most significant atomic distances of zCFX-N4' from X-ray[58] (with relative esd) and optimized structures in PCM. The calculated bond lengths and angles are in excellent agreement with the experimental ones, confirming the reliability of the computational protocol used (as can be seen from MAE and RMSD index[59] calculated on bond lengths, measuring 0.008 Å and 0.014 Å respectively).

The computed Gibbs free energies in gas phase show that nCFX is more stable than zCFX-N4' form $\Delta G = 90.9$ kcal mol^{-1} ($\Delta G = G_{zHFQ\text{-}4'} - G_{nCFX}$). Such behavior does not change when introducing the implicit water: nCFX remains the most stable ($\Delta G = 24.7$ kcal mol^{-1}).

This result is in agreement with other similar computational works[25,29] but in contrast with experimental data.[22,23,26,27] Therefore, the effect of the presence of explicit water molecules solvating the ionisable groups was considered. Water molecules were

introduced to obtain a cluster composed by CFX and 10 water molecules. The number of water molecules added to CFX was calculated on the basis of the average number of waters solvating the MD simulations (see MD parts in results and discussion). The obtained cluster was then optimized in PCM water to produce stable final structures (Figure 7).

Table 1 Most significant bond lengths (Å) in zCFX-N4' form from x-Ray[58] (esd are reported in parentheses) and optimized structures in implicit water.

	zCFX-N4'	
Distance	Exp.[58]	Calc.
C11-O12	1.251(3)	1.261
C11-O11	1.254(3)	1.250
C11-C3	1.504(3)	1.547
C4-O4	1.251(3)	1.238
N1'-C2'	1.479(3)	1.460
C2'-C3'	1.501(3)	1.523
C3'-N4'	1.484(3)	1.509
N4'-C5'	1.489(3)	1.510
C5'-C6'	1.518(3)	1.520
C6'-N1'	1.462(3)	1.470

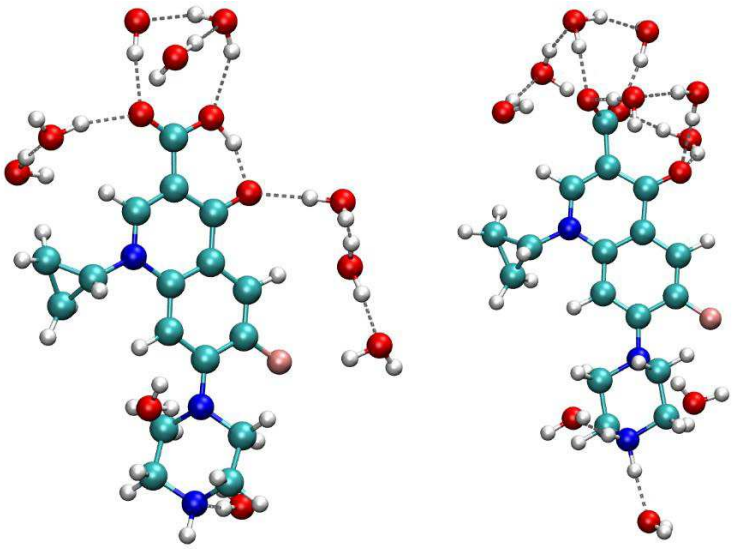

nCFX zCFX-N4'

Figure 7 Optimized cluster structures of a) nCFX and b) zCFX-N4' species in implicit water (discrete-continuum approach).

After the introduction of this method, zCFX-N4' species is now predicted to be slightly more stable than the nCFX form with ΔG = -2.1 kcal mol^{-1} , in nice agreement with experimental literature.[22,23,26,27]

The driving force in the stabilization of zCFX-N4' species could be related to the energy contribution of hydrogen bonds. The hypothesis was verified by calculating the cluster energies formation without CFX ($\Delta X = X_{cluster10w} - X_{10w}$ where X is E or G) and the cluster energies formation with CFX ($\Delta X = X_{cluser10w-CFX} - X_{cluster10w+CFX}$ where X is E or G) for nCFX and zCFX-N4'; results are reported in Table 2.

Table 2 Cluster energy formation (kcal mol^{-1}).

	ΔE	ΔG
$10H_2O$ → Cluster10w (nCFX)	-18.6	53.6
$10H_2O$ → Cluster10w (zCFX-N4')	-14.4	63
nCFX+cluster10w → cluster10w-nCFX	-31.7	34.9
zCFX+cluster10w → cluster10w-zCFX	-66.7	8.1

The results show that ΔE cluster formation energy without CFX is negative in both cases, but the ΔE of nCFX is about 4 kcal lower than the ΔE of zCFX-N4'. The difference could be due to the reduced formation of water-water hydrogen bonds in the case of zHFQ-N4'. In fact, we can observe that the ΔE cluster formation energy with CFX (measure of the interaction energy between CFX and waters cluster) remains negative, but presents a trend that is opposite to the previous case. ΔE for zCFX-N4' is much more negative compared to nCFX (about 35 $kcamol^{-1}$), possibly due to a greater formation (and thus stabilization) of hydrogen bonds between water and zCFX-N4' compared to nCFX. ΔG values, instead, are positive, due to the loss of entropy. In any case, ΔG values confirm those reported above.

Finally, the clusters shown in Figure 7 have been optimized using methanol as implicit solvent, in order to understand how the solvent affects the relative stability of the two species. The computed energies show that zCFX-N4' is slightly more stable than nCFX (ΔG = -1.6 kcal mol^{-1}). A decrease of 0.5 kcal mol^{-1} was observed, due to lower polarity of methanol in relation to water.

Other possible zCFX forms (scheme 8) could be present; in fact, the protonation could take place also in N1 (zCFX -N1) and N1' (zCFX-N1') nitrogen, as well as in O4 oxygen (zCFX – O4).

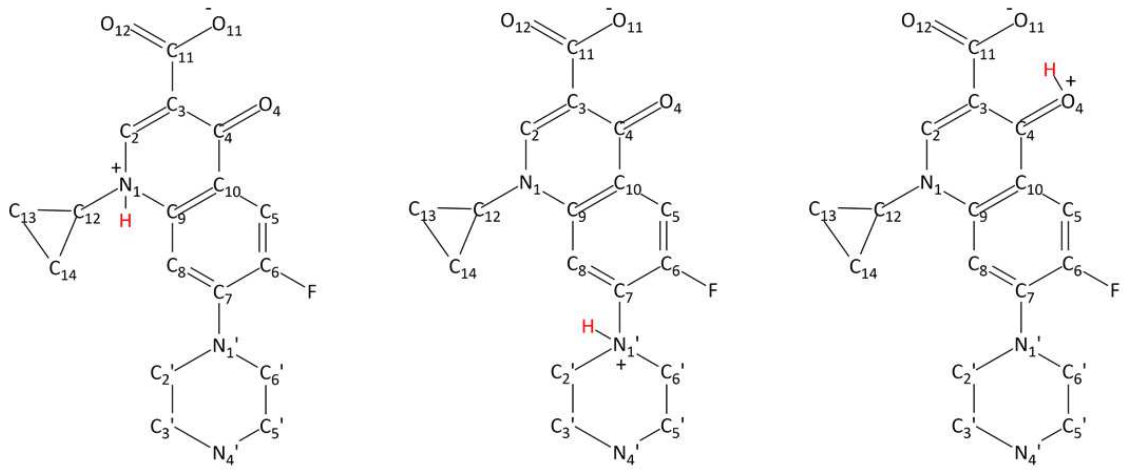

Scheme 8 Other possible zCFX forms studied in this work. For simplicity, the proton of the first protonation reaction is indicated in red.

Such zCFX forms were analyzed in our work, and their optimized geometries in implicit water are shown in Figure 8.

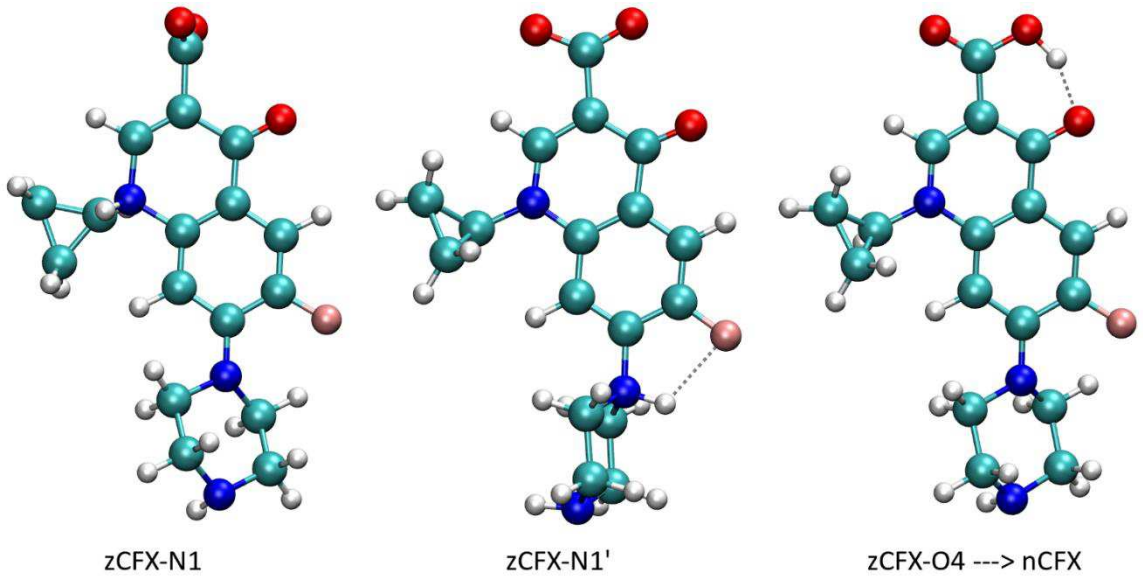

Figure 8 Optimized structures of different zCFX forms in implicit water.

There are small changes in bond lengths and angles between zCFX-N4' and other zCFX forms (see Table 4). The most significant atomic distances and angles of zCFX-N1 and zCFX-N1' are reported in Table A2 in appendix B, in comparison with those obtained for zCFX-N4'. The largest change in zCFX-N1 form was observed in the quinolone ring, with an increase of the distances C2-N1 (1.362 A to 1.486 A) and C9-N1 (1.393 A to 1.486 A); furthermore, a reduction of the angles C2-N1-C12 (119.9° to 108.7°) and C9-N1-C12 (120.7° to 111.5°) can be observed. Finally, the carboxyl group is rotated approximately 90 ° (Figure 8). The major change in zCFX-N1' form was observed on the piperazine ring, where an increase of the distances N1'-C2' (1.460 A to 1.525 A) and C6'-N1' (1.470 A to 1.570 A) and the formation of a hydrogen bond between N1'-H and F (Figure 8) are observed. zCFX-O4 form showed a proton transfer from O4 to O11 with reformation of nCFX form (Figure 8).

The relative stability of these forms is summarized in Table 3. ΔG values were calculated as difference between zCFX-N4' (taken as reference) and other zCFX forms ($\Delta G = G_{zCFX\text{-}n} - G_{zHFQ\text{-}N4'}$ where zCFX-n is zCFX-N1, N1', O4).

Table 3 Relative stability (kcal mol^{-1}) of different zCFX forms in gas-phase, implicit water (PCM).

	ΔG Gas-phase	ΔG PCM
zCFX-N4' → zCFX-N1	-6.8	34.8
zCFX-N4' → zCFX-N1'	-11.2	9.3

The results show that, in gas phase, both zCFX-N1 and ZCFX-N1' forms are more stable than zCFX-N4' form, with zCFx-N1' being the most stable species. The introduction of implicit water leads to a change of this trend, and the more stable species appears to be zCFX-N4'. In conclusion, the most stable form appears to be zCFX-N4', a result in nice agreement with experimental literature.[22,23,26,27]

Second protonation

Experimental data[22,23,26,27] argue that, in the second protonation reaction, the formation of the H_2CFX^+ species (protonation of O11 oxygen, H_2CFX^+-O11) reported in Scheme 9a occurs. However, there may be additional H_2FQ^+ forms (Scheme 9b), and the protonation could also take place in N1 (H_2CFX^+-N1) and N1' nitrogen (H_2CFX^+-N1'), as well as in O4

oxygen (H_2CFX^+-O4). The optimized structures of different species in water are displayed in Figures 9. Overall, there are small changes in bond lengths and angles between zCFX-N4' and H_2CFX^+ species (see Table A3 in appendix B).

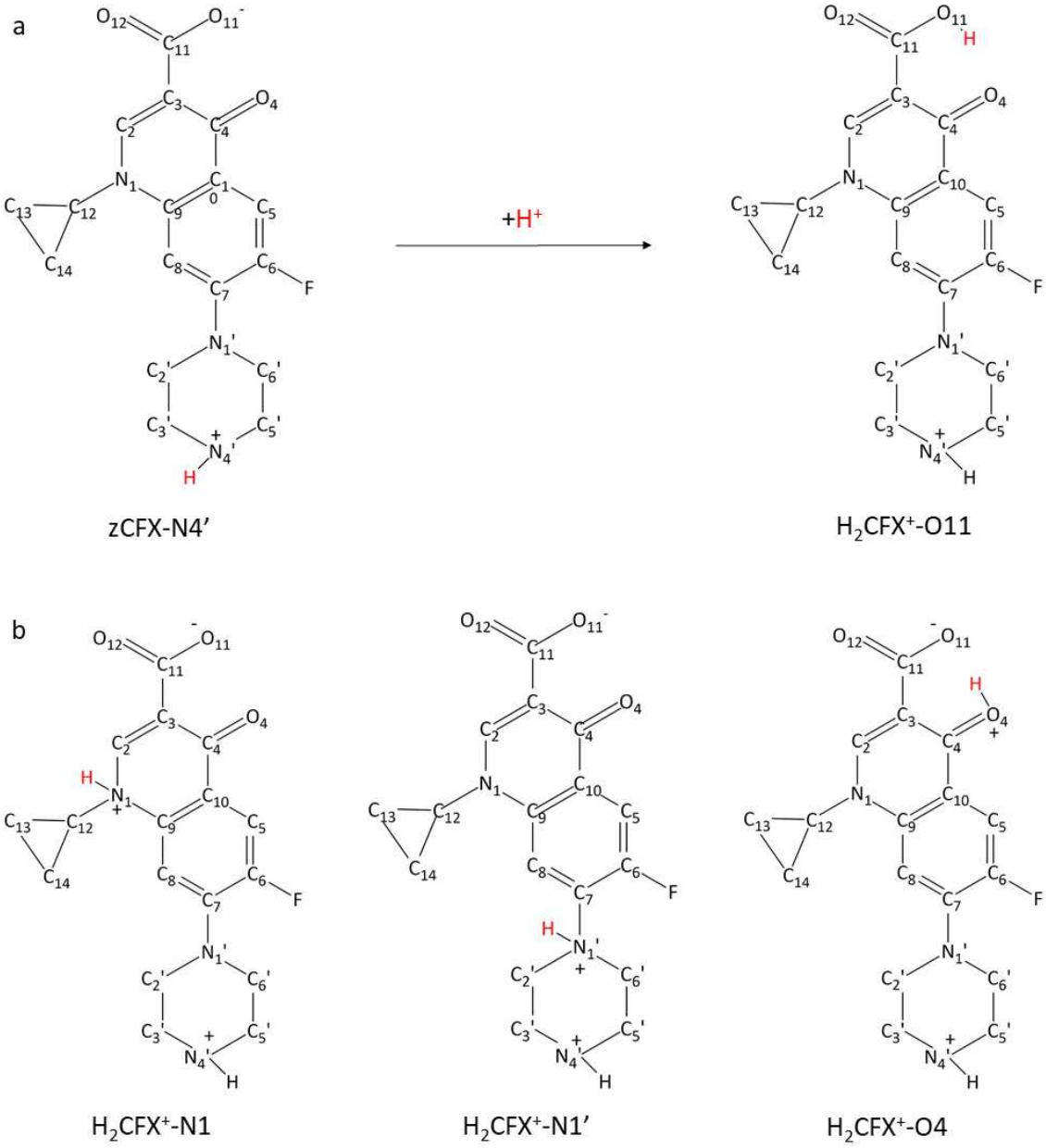

Scheme 9 a) zCFX-N4' and H_2CFX^+-O11 b) Other possible H_2CFX^+ forms studied in this work. For simplicity, the proton of the second protonation reaction is indicated in red.

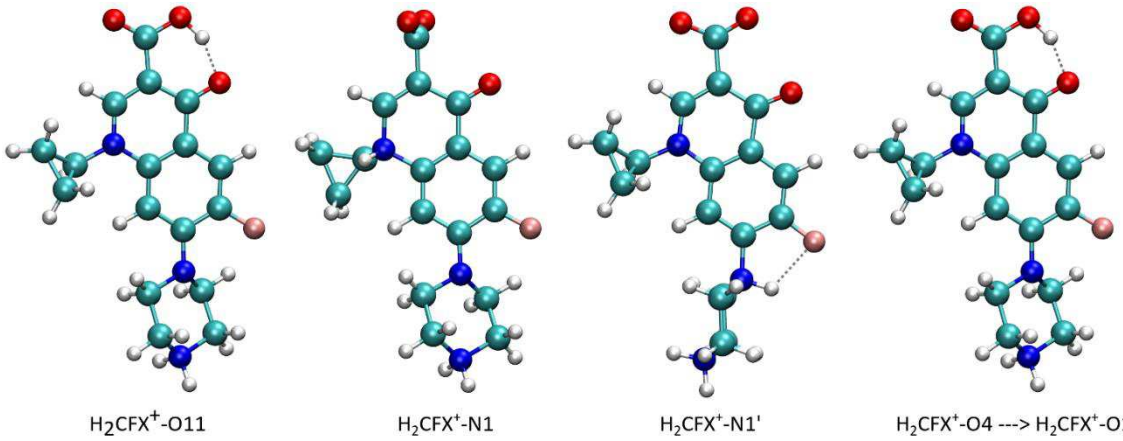

Figure 9 Optimized structures of H_2CFX^+-O11 H_2CFX^+-N1, H_2CFX^+-N1' and H_2CFX^+-O4 forms in implicit water.

In the case of H_2CFX^+-O11, an increase of the distance C11-O11 (1.250 A to 1.336 A), and a slight decrease of the distance C11-O12 (1.261 A to 1.216 A) was observed; the formation of a hydrogen bond between O11-H and O4 (Figure 9) occurred. H_2CFX^+-O11 form was characterized by X-Ray.[60] Table 4 shows the most significant atomic distances in H_2CFX-O11 from X-Ray (with relative esd) and optimized structures in PCM.

Table 4 Most significant bond lengths (Å) in H_2CFX^+-O11 form from x-Ray[60] (esd are reported in parentheses) and optimized structures in implicit water.

	H_2CFX^+-O11	
Distance	Exp.[60]	Calc.
C11-O11	1.213(6)	1.216
C11-O12	1.319(6)	1.336
C11-C3	1.477(7)	1.489
C4-O4	1.265(6)	1.255
O11-O4 H-bond	2.535(5)	2.563

The calculated bonding distances reported in the table 7 are in excellent agreement with the experimental ones; the MAE and RMSD index is of 0.007 Å and 0.001 Å respectively. The biggest change in H_2CFX^+-N1 was observed in the quinolone ring (see Table A3 in appendix B), with an increase of the distances C2-N1 (1.362 A to 1.486 A) and C9-N1 (1.393 A to 1.484 A); furthermore, a reduction of the angles C2-N1-C12 (119.9° to 108.8°) and C9-N1-C12 (120.7° to 111.6°) was registered. Finally, carboxyl group rotated approximately 90 ° (Figure 9). The major change in H_2CFX^+-N1' was observed on the

piperazine ring, with an increase of the distances C2'-N1' (1.470 A to 1.521 A) and C6'-N1' (1.460 A to 1.519 A); we also observed the formation of a hydrogen bond between N1'-H and F (Figure 9). H_2CFX^+-O4 form showed a proton transfer from O4 to O11, with reformation of H_2CFX^+-O11 form (Figure 9).

The relative stability of the forms is summarized in Table 5. ΔG values were calculated as difference between H_2CFX^+-O11 (taken as reference) and the other H_2CFX^+ forms ($\Delta G = G_{H2CFX^+-n} - G_{H2CFX^+-O11}$, where H_2CFX^+-n is H_2CFX^+-N1, N1').

Table 5 Relative stability (kcal mol^{-1}) of the different H_2FQ^+ forms in gas-phase and implicit water.

	ΔG Gas-phase	ΔG PCM
H_2CFX^+-O11 → H_2CFX^+-N1	92.4	59.9
H_2CFX^+-O2 → H_2CFX^+-N1'	119.8	45.4

The results in gas-phase and in implicit water show that H_2CFX^+-O11 is always much more stable than the other possible forms. The most stable form between H_2CFX^+-N1 and H_2CFX^+-N1' in gas phase results to be the first one. A different behavior occurs with the introduction of implicit water; in fact, H_2CFX^+-N1' becomes the most stable form. Such behavior could be explained by assuming that the piperazine ring is more exposed to the solvent than N1 nitrogen, leading to a stabilization of the system. In this case we did not use the discrete-continuum approach, considering that the data in gas-phase and in PCM confirm what is reported in literature.[22,23,26,27]

UV-VIS Spectra for first and second protonation

The UV-vis spectra were simulated to have a comparison with the experimental ones.[61] The characteristic absorption bands of CFX in different protonation states were found in the range of 280-290 nm and 320-360 nm. Calculated absorption spectra are showed in Figure 10. The main absorption peak of these species is located in the UV region of the spectrum, at 260-280 nm. All species also display a weaker absorption in the 300-400 nm range, extending toward the visible region; more bands are obtained at wavelengths of less than 250 nm for all species. The findings are in good agreement with experimental spectra[61] and previous computational works.[25] Musa *et al.*[25] calculated the absorption spectra for different species of norfloxacin (NOR) at the TD-B3LYP/6-31G(d,p) level of

theory, finding that the main absorption peak of such species is located in the 260-280 nm wavelength range.

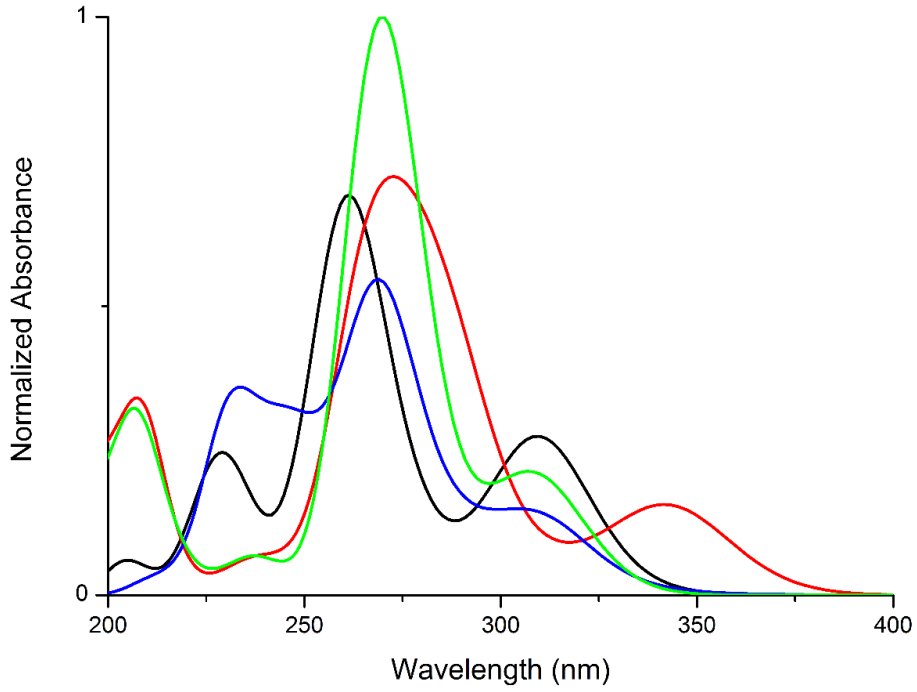

Figure 10 Computed UV-VIS spectra in implicit water of CFX^- (black line), nCFX (red line), zCFX-N4' (blue line) and H_2CFX^+-O11 (green line) species.

The major variations in experimental spectra, going from the CFX^- to the H_2CFX^+-O11 species (decreasing the pH), are the increase of the intensity of the principal band at 280-290 nm, accompanied by its shift to higher wavelengths, and the decrease of the intensity of the bands between 320 and 360 nm. To understand the effect of the protonation site on the absorption spectra, the relevant frontier molecular orbitals, which play a dominant role in electronic transitions of FQs, have been reported in Figure 11; the main transitions are reported in Table 6.

Table 6 Wavelengths (λ) in nm, molecular orbitals and relative percentage contribution (%), oscillator strength (f(osc)) of FQ^-, nHFQ, zHFQ-N4' and H_2FQ^+-O11 species.

Species	λ	Orbital	%	f(osc)	λ	Orbital	%	f(osc)
CFX^-	260	HOMO-5 → LUMO	41	0.5156	311	HOMO →LUMO+1	55	0.1144
nCFX	275	HOMO-1 → LUMO+1	46	0.4026	342	HOMO → LUMO	95	0.1389
zCFX-N4'	268	HOMO-2 → LUMO+1	46	0.4704	310	HOMO→ LUMO	54	0.0877
H_2CFX^+-O11	268	HOMO-1 →LUMO+1	52	0.778	309	HOMO → LUMO	81	0.1637

With the first protonation step (CFX^- → nCFX + zCFX-N4'), a shift of the main maximum towards higher wavelengths is observed (+15 nm in the case of nCFX, +8 nm for zCFX-N4' and H_2CFX^+-O11), in agreement with the experimental trend. According to Figure 10, an absorption peak relative to nCFX should be obtained in the high wavelength range by lowering the pH. On the contrary, the experimental spectra[61] only show a weak shoulder in the 360-400nm range: therefore, nCFX species is argued to form only in small amounts. The formation of a small shoulder in the low wavelength range (~210 nm)[61] is compatible with the formation of H_2CFX^+-O11 species (green line in Figure 10). It is interesting to note that the bands placed at a higher wavelength, corresponding to the HOMO → LUMO excitation, are useful to distinguish zCFX (λ = 310 nm) from nCFX (λ = 342 nm); an explanation can be provided by observing the structure of the orbital (Figure 11).

HOMO and HOMO-1, orbitals of CFX^- and zCFX-N4' localized on the carboxyl group, are very similar. HOMO-2 in CFX^- form is slightly different, because a localization is observed on the piperazine ring, while in zCFX-N4' form the orbital is localized on the carbonyl group. In both species LOMO is localized on the quinolone ring. LUMO+1 orbital has minor components on the N1' atom of the piperazinyl ring and on the carboxyl group too.

For nCFX, HOMO, HOMO-1 and HOMO-2 are localized on the quinolone ring and on the piperazinyl ring. LUMO and LUMO + 1 are very similar to those obtained for CFX^- and zCFX-N4' species, which could explain the difference in λ in nCFX and zCFX-N4'.

Finally, HOMO and HOMO-1 of H_2CFX^+-O11 are localized on the quinolone ring, while HOMO-2 is localized on the carbonyl and carboxyl group. LUMO and LUMO+1 are very similar to those obtained for CFX^- and zCFX-N4' species. On the basis of the orbital structures, we can hence assume that the photochemical behavior between nCFX and zCFX-N4' species is governed by HOMO -> LUMO excitation. The difference in the photochemical behavior can be explained considering that, for this species, the HOMO orbitals are localized in different parts of the molecule.

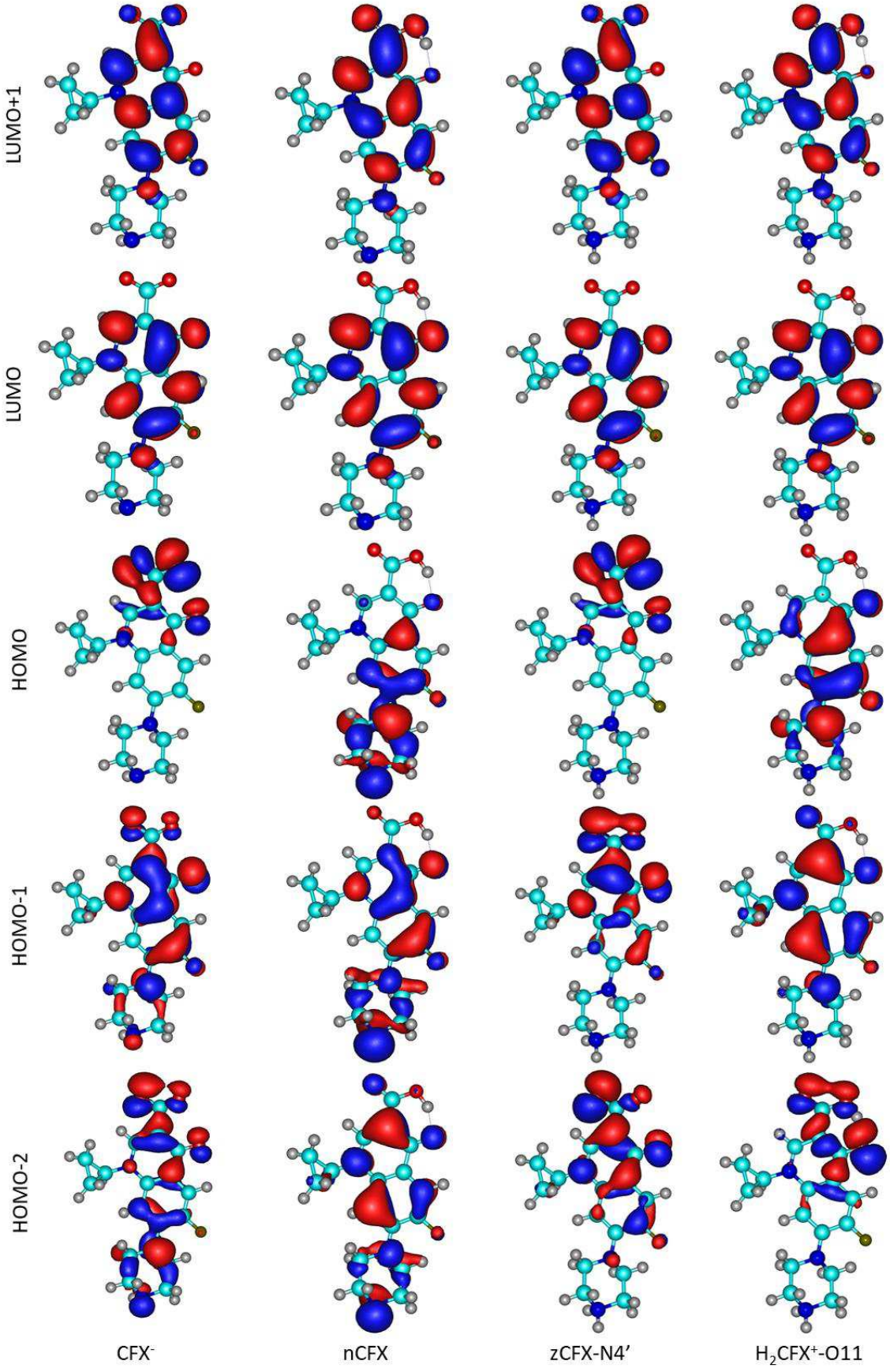

Figure 11 Ground-state orbitals of CFX^-, nCFX, zCFX-N4' and H_2CFX^+-O11 species (isovalue=0.03).

Third protonation and relative UV-Vis spectra.

The experimental data suggest that the formation of the H_3CFX^{2+} species occurs only in extremely acidic conditions.[26] However, the literature is not unanimous: this last protonation, in fact, could take place either in N1' nitrogen of the piperazine ring (H_3FQ^{2+}-N1')[26,33] or in carbonyl oxygen (H_3FQ^{2+}-O4).[34,35] Moreover, there may be an additional H_3CFX^{2+} form, and the protonation could take place also in N1 nitrogen (H_3CFX^{2+}-N1). The forms are reported in Scheme 10.

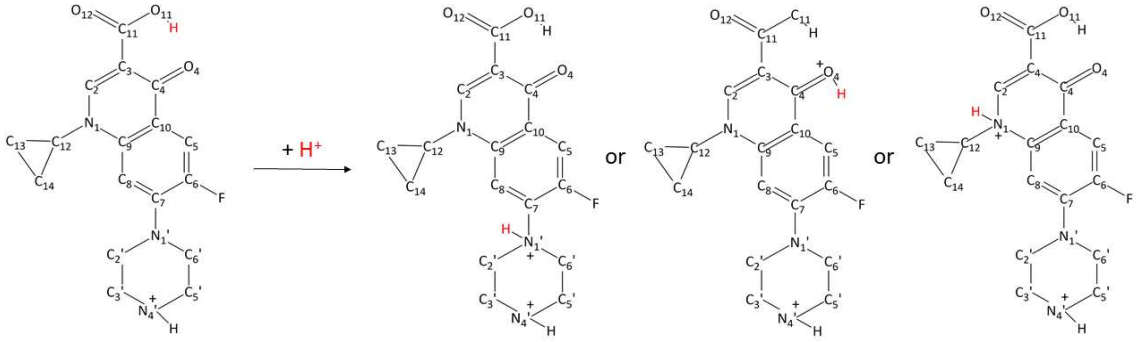

Scheme 10 Possible H_3CFX^{2+} form. For simplicity, the proton of the third protonation reaction is indicated in red.

The optimized structures of the different species are displayed in Figure 12. Overall, there are small changes in bond lengths and angles between H_2CFX^+ and H_3CFX^{2+} species (Table A4 in appendix B).

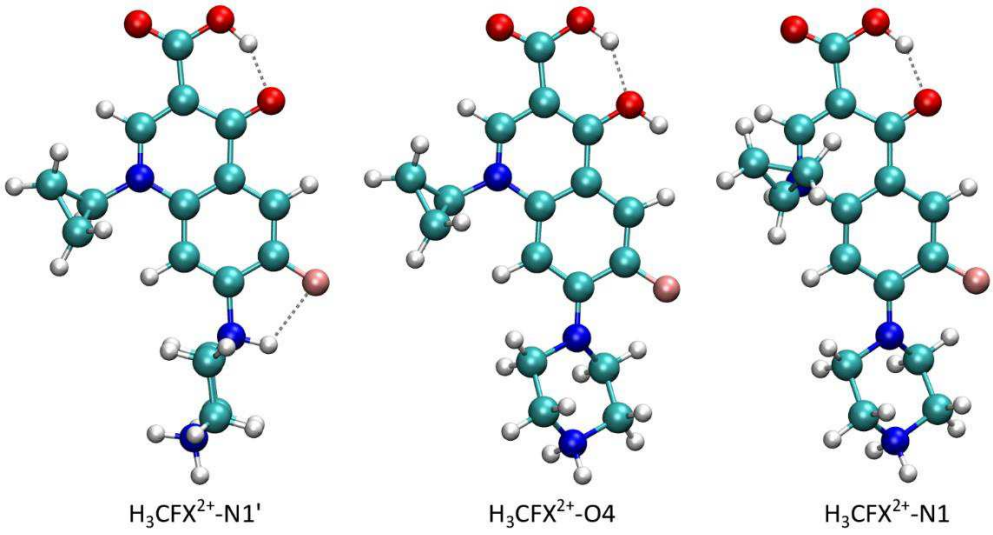

Figure 12 Optimized structures of H_3CFX^{2+} forms in implicit water.

The major change for H_3CFX^{2+}-N1' form was observed on the piperazine ring, with an increase of the distances N1'-C2' (1.461 A to 1.521 A) and C6'-N1' (1.471 A to 1.523 A); the formation of a hydrogen bond between N1'-H and F (Figure 12) was also observed. For H_3FQ^{2+}-O4 form, an increase of the distance C4-O4 (1.255 A to 1.334 A) and the formation of a hydrogen bond between O11-H and O4 (Figure 12) were observed. The X-Ray structure for di-cationic form of NOR (H_3NOR^{2+}-O4) was obtained.[34] Table 7 show the most significant atomic distances of NOR from X-ray with relative esd and CFX optimized structures.

Table 7 Most significant bond lengths (Å) in H_3NOR^{2+}-O4 form from X-ray[34] (esd are reported in parentheses) and H_3CFX^{2+}-O4 optimized structures in implicit water.

	H_3FQ^{2+}-O4	
	NOR	CFX
Distance (A)	Exp.[34]	Calc.
C11-O12	1.226(2)	1.208
C11-O11	1.313(2)	1.336
C11-C3	1.479(3)	1.505
C4-O4	1.319(2)	1.334

The calculated bonding distances reported in the table 7 are in excellent agreement with the experimental data; the MAE and RMSD index are of 0.001 Å and 0.015 Å respectively. The largest change in H_3CFX^{2+}-N1 form was observed on the quinolone ring, with an increase of the distances C2-N1 (1.346 A to 1.462 A) and C9-N1 (1.402 A to 1.486 A), accompanied by a reduction of the angles C2-N1-C12 (119.7° to 112.3°) and C9-N1-C12 (120.4° to 109.6°).

ΔG values, calculated as difference between the H_3CFX^{2+}-O4 (taken as reference) and other H_3CFX^{2+} forms ($\Delta G = G_{H3CFX2^+\text{-}n} - G_{H3CFX2^+\text{-}O4}$ where H_2CFX^{2+}-n is H_3CFX^{2+}-N1 and N1'), are reported in Table 8.

Table 8 Relative stability (kcal mol^{-1}) of the different H_3CFX^{2+} forms in gas-phase and implicit water.

Form	ΔG gas-phase	ΔG PCM
H_3FQ^{2+}-N1	39.5	33.2
H_3FQ^{2+}-N1'	41.0	3.7

The results show that the H_3CFX^{2+}-O4 form is always more stable than the other possible forms. As already observed for the second protonation reaction, the most stable form between H_3CFX^{2+}-N1 and H_3CFX^{2+}-N1' in gas phase is the former; conversely, the most stable form with implicit solvent is the latter. In order to evaluate the electronic transitions of CFX in different protonation H_3CFX^{2+} form, UV-vis spectra were simulated (Figure 13). The main absorption maxima wavelengths, the orbitals involved, the relative percentage contribution and the oscillator strength are reported in Table 9. The molecular orbitals involved in the electronic transitions are shown in Figure 14.

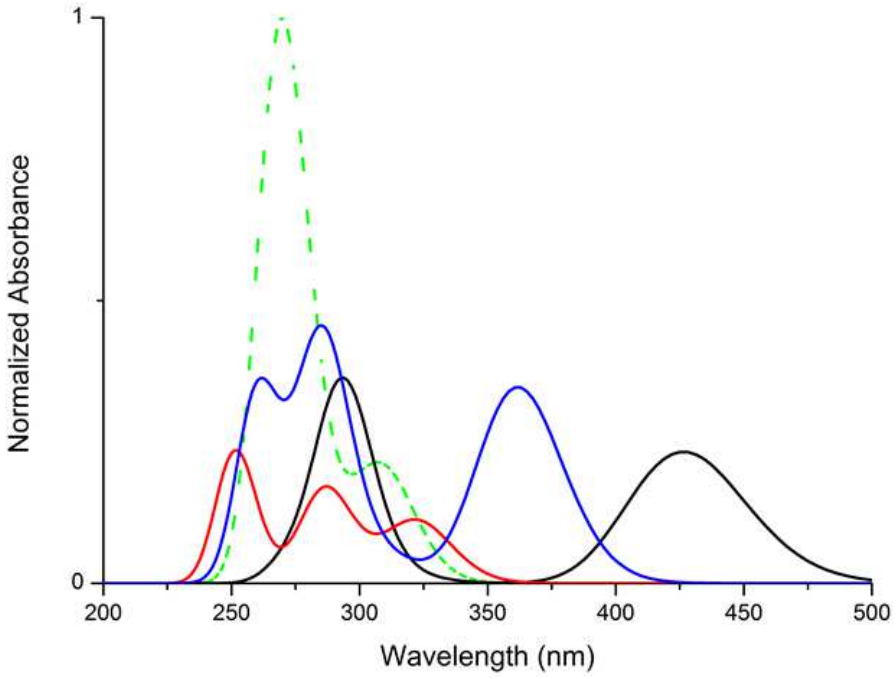

Figure 13 Computed UV-VIS spectra in implicit water of H_3CFX^{2+}-N1 (black line), H_3CFX^{2+}-N1' (red line), H_3CFX^{2+}-O4 (blue line), H_2CFX^{+}-O11 (green dot line, for comparison) forms.

Table 9 Wavelengths (λ) in nm, orbitals and relative percentage contribution (%), oscillator strength (f(osc)) of possible H_3CFX^{2+} form.

Form	λ	Orbital	%	f(osc)	λ (nm)	Orbital	%	f(osc)
H_3CFX^{2+}-N1	293	HOMO → LUMO+1	95	0.3279	426	HOMO → LUMO	98	0.2151
H_3CFX^{2+}-N1'	251	HOMO-3 → LUMO	82	0.2178	321	HOMO → LUMO	96	0.1024
H_3CFX^{2+}-O4	285	HOMO → LUMO+1	50	0.4092	361	HOMO → LUMO	93	0.3207

The main experimental absorption peak[61] of these species is located in the 250-290 nm spectral range. The major variation in experimental spectra, going from H_2CFX^{+} to H_3CFX^{2+}

species (decreasing the pH), is the appearance of the band at 360-400 nm, accompanied by a decrease of the intensity of the other bands. The computed spectrum that best reproduces such trend seems to be H_3CFX^{2+}-O4 form (Figure 13, Table 9), in which a decrease of the intensity of the principal bands and the appearance of the band at 361 nm are observed. Moreover, in this region H_3CFX^{2+}-O4 has a higher probability (oscillator strength) of absorption in respect to H_3CFX^{2+}-N1' and H_3CFX^{2+}-N1. The computed spectra for H_3CFX^{2+}-N1 and H_3CFX^{2+}-N1' are very different from the experimental spectra. In order to understand the effect of the protonation on the absorption spectra, it is useful to examine the relevant frontier molecular orbitals (Table 9).

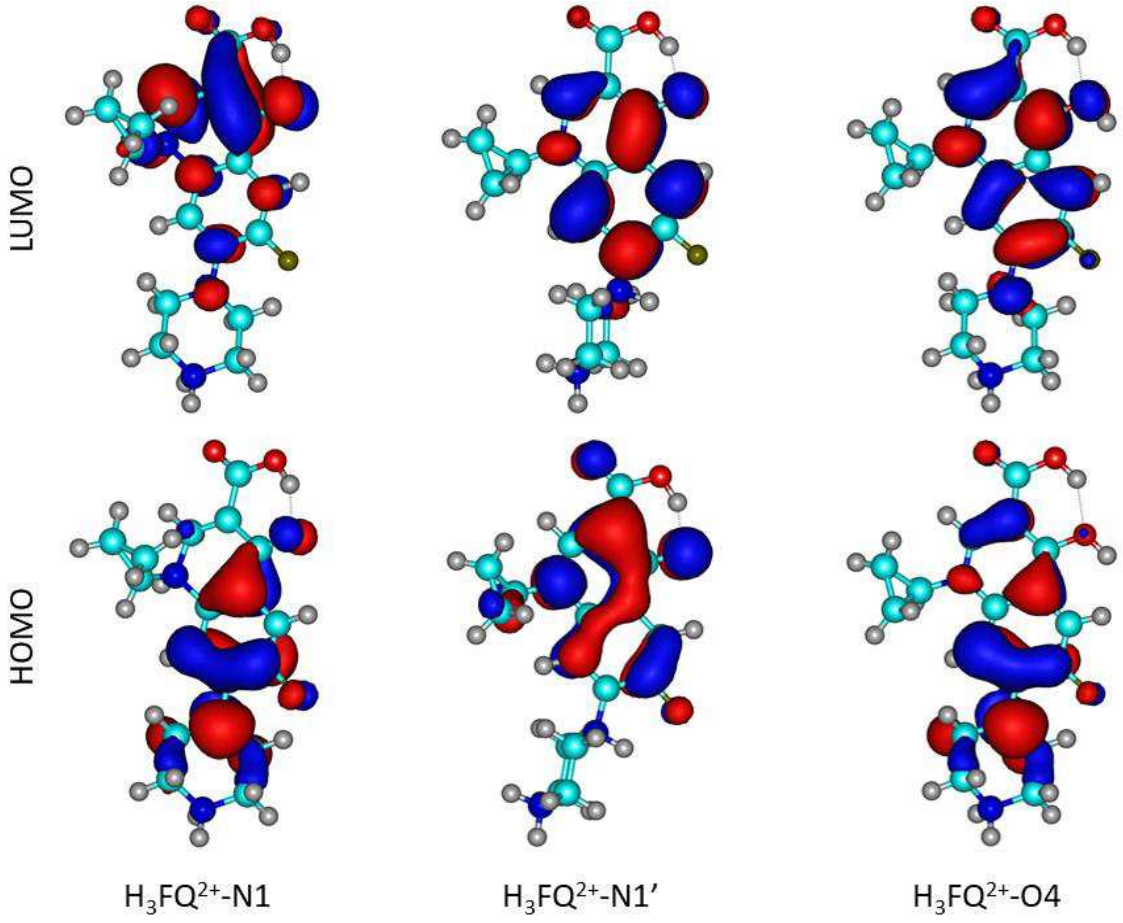

Figure 14 Ground-state orbitals of possible H_3CFX^{2+} form (isovalue=0.03).

For H_3CFX^{2+}-N1 and H_3CFX^{2+}-O4 forms, HOMO is very similar and localized on the quinolone ring and to less extent on N1' of the piperazinyl ring, while for the H_3CFX^{2+}-N1' form the orbital is localized only on the quinolone ring. LUMO is localized on the carboxyl

group for H_3CFX^{2+}-N1 form and on quinolone ring for H_3CFX^{2+}-N1' form. For H_3CFx^{2+}-O4, LUMO is localized on the quinolone ring and on the carbonyl group.

4.2.6 Conclusions

In our work, the relative stability of the possible forms of CFX was studied from a theoretical point of view. Molecular dynamics simulations were conducted to obtain information on the amount of H-bonds formed between water, zCFX-N4' and nCFX. The results showed that zCFX-N4' forms on average 10 H-bonds, while the H-bonds formed by nCFX are on average 7. The amino group N4' and the carboxy group are responsible for the various properties of zCFX-N4' and nCFX. This information has been used to build a representative cluster formed by z-nCFX and 10 water molecules. The cluster has been used for the discrete-continuum approach in the quantum mechanics calculations. In the second part of our work, the geometries, relative stability and photochemical behaviour of the different protonation states of the antibiotic compound ciprofloxacin have been studied by DFT calculation. Our computations confirm the predominance of the zCFX-N4' form in water, thanks to the introduction of a discrete-continuum approach; the result was further confirmed through calculated absorption UV-Vis spectra. A slight decrease of stability of the zCFX-N4' species with respect to nCFX was observed by using from water instead of methanol as implicit solvent, due to lower polarity of such solvent. The protonation sequence N4'→O11→O4 was firstly confirmed through the comparison with crystalline structures present in the literature; secondly, by means of the calculation of the relative stability for such species; thirdly, through calculated absorption UV-Vis spectra.

4.3 Antibacterial Fluoroquinolones as Pollutants: Adsorption on Carbon Nano-tube, a Molecular Dynamics Simulation Study

4.3.1 FQs pollution

In addition to being used in human and veterinary medicine, FQs are also used in agriculture and aquaculture. The unreasonable use of such antibiotics has led to the emergence of a global environmental pollution problem, namely the environmental pollution with FQs.[62] This class of compounds was known to have a low antimicrobial

resistance. In recent years, however, an increase in the antimicrobial resistance has alerted the international authorities;[63] the presence of such phenomenon has already been demonstrated and is known to be gradually increasing. To understand the problem, we need to know how FQs can enter the environment (Figure 15).

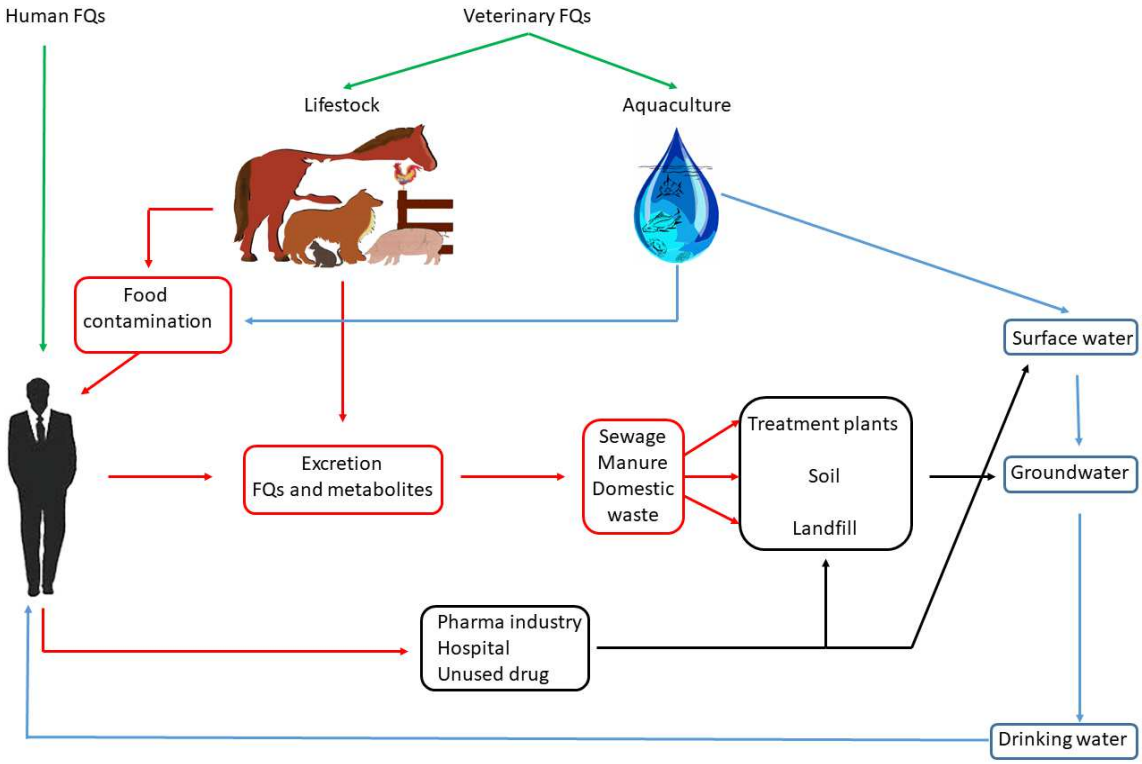

Figure 15 Pollution with FQs. The FQs and their metabolites end up in the sewage, manure and domestic waste, then in soil and waters. In addition, the presence of fluoroquinolones residues in food of animal origin causes the emergence of bacterial resistance.

The excretion of FQs by animals and humans through faeces and urine is the principal pathway by which they can enter the environment. FQs can be excreted unchanged or as the product of conjugation, oxidation, hydroxylation, dealkylation, or decarboxylation processes.[62] Original compound residues are defined as the amount of antibiotic not absorbed by a human or animal digestive system and excreted through faeces into the external environment, or the detectable level of antibiotics remaining in the muscle fibres of animals.[64–66] In turn, the amount of antibiotic residue has implications on the bacterial ecology, as well as on the invertebrate and vertebrate ecology in soil matrices and surrounding surface water. Moreover, the formation of metabolites is also possible. Metabolites are molecules transformed from a parent compound through a biochemical

transformation process. The transformation can occur within the body, or in sewage, manure, soil, and the environment.[67] In addition, the degradation of FQs can lead to the formation of metabolites resembling other FQ drugs; for example, a metabolite of enrofloxacin, a FQ used only in veterinary medicine, closely resembles CFX, which is used only in human medicine, so the enrofloxacin metabolite has to be distinguished from true CFX.[68] Another possible pathway through which FQs enter the environment is photochemical degradation.[69–71] The studies on products resulting from photochemical degradation are limited, and both the presence of antibacterial activity in such products and their potential threat to the environment and human health remain to be determined. Chemical changes occur in the structure by irradiation, but usually the quinolone ring remains intact and the antibacterial activity of the compounds is generally high.

4.3.2 Water pollution with FQs and remediation

Surface water plays an important role in the emergence and spread of antibiotic resistance, so the development of strategies to improve water quality has become a permanent necessity. Pharmaceutical industry waste, hospital waste and therapeutic drugs contribute to the excretion of unchanged fluoroquinolones and their metabolites in the domestic wastewater.[72] Considering their serious threat to the environment and their inherent health threat to human beings, the development of efficient removal techniques is becoming an urgent matter to be addressed. Accordingly, it is necessary to implement techniques to effectively remove FQs in aquatic environments. Thus, different treatment techniques including adsorption,[73] advanced oxidation process and bioremediation[74] were investigated. Among those techniques, adsorption seems to have interesting potentialities for emerging organic pollutants remediation, considering its versatility and removal efficiency.[73] Adsorption may be defined as an accumulation of compounds (adsorbate) on the surface provided by solid materials (adsorbent), and it is widely used to remove substances from fluid phases.[75,76] Due to their high specific surface area, nano-adsorbents show a rate of adsorption for organic compounds which is considerably high compared with macroscopic adsorbents systems. They have a great potential for novel, more efficient, and faster decontamination processes aimed at removing organic and

inorganic pollutants like heavy metals and micropollutants. Current research activities mainly focus on the following types of nano-adsorbents:[73]

- Carbon nanotubes (CNTs)
- Metal-based nanoadsorbents
- Polymeric nanoadsorbents
- Zeolites.

4.3.3 Carbon nanotubes

In this thesis, I will focus my attention on carbon nano-tubes (CNTs). CNTs were originally discovered and fully described by Sumio Iijima in his TEM observation,[77] even though some scientists believe that the discovery was made earlier by Bacon.[78] CNTs, like graphene (see chapter 3), are allotropes of carbon with a cylindrical three-dimensional (3D) structure where carbon is bound to other three carbons in a sp2 bond formed by rolling single or multiple layers of graphene sheets into seamless cylinders.[79] These cylindrical structures have two forms: single-walled CNTs (SW-CNTs) and multi-walled CNTs (MW-CNTs) reported in Figure 16.

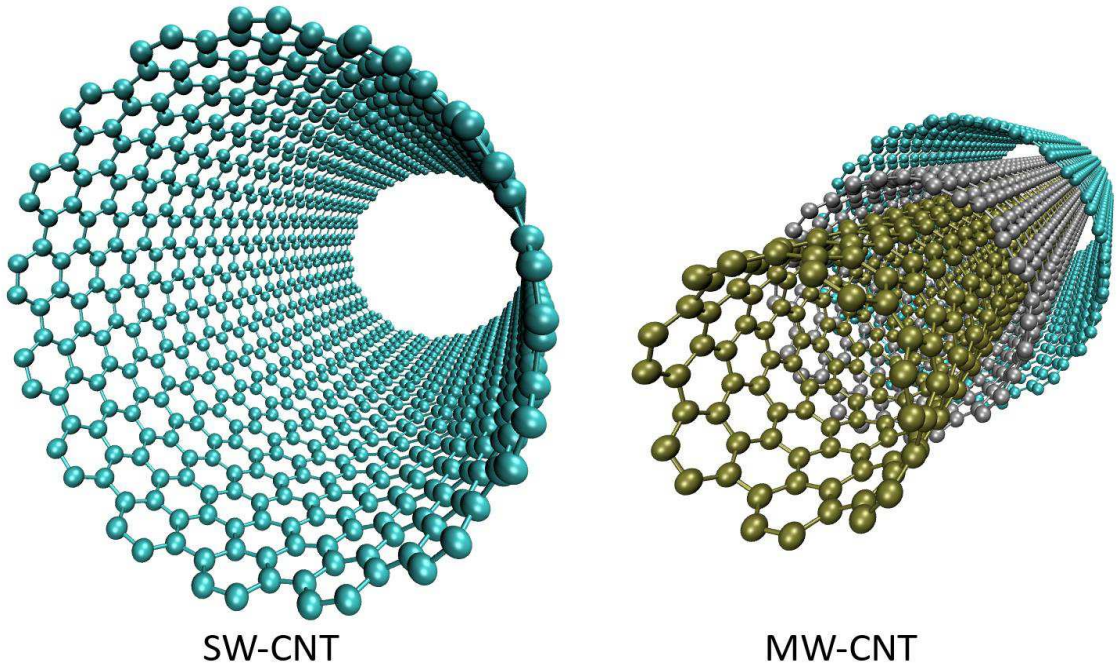

Figure 16 Structures of single-walled CNTs (SW-CNTs) and multi-walled CNTs (MW-CNTs).

SW-CNTs are composed of a single cylindrical graphene layer, while MW-CNTs comprise several concentric cylinders of graphitic shells, each forming a SW-CNT. Moreover, MW-CNTs generally have a larger outer diameter (2.5 - 100 nm) compared to SW-CNTs (0.6 - 2.4 nm).[80] As observed for graphene (see chapter 3), the sp2 structure, which is stronger than the sp3 bond found in diamonds, gives the CNTs unique properties, such as high tensile strength, ultra-light weight and excellent chemical and thermal stability. Another amazing property of CNTs is elasticity: when a high pressure is exercised, it can bend, twist, kink, and in the end the nanotube will return to its original structure. However, its elasticity presents a limit and, under very physically powerful forces, the shape of a CNT can be temporarily deformed. Moreover, some of the structure defects can weaken CNTs strength.[81] Several techniques have been developed to synthetizing CNTs; the most commonly procedure are: arc-discharge technique,[82,83] laser-ablation technique[84] and catalytic chemical vapor deposition (CVD) technique.[85,86]

CNTs can be functionalized in different ways, and various functional groups can easily be attached on the surface of CNTs by chemical modification, which enhances its aqueous solubility with reduced tendency of agglomeration. Chemical modification can be accomplished by adsorption and other interactions (electrostatic, hydrophobic, or covalent and non-covalent bonding). As observed for graphene based materials, the unique structure of CNTs is characterized by highly assessable adsorption sites, adjustable surface chemistry and the presence of delocalized π electrons, rendering this material an excellent candidate for environmental remediation. However, their use on an industrial scale for large municipal water and wastewater treatment plants is not expected in the midterm, because of high production costs.[87] Point-of-use applications that require small quantities of CNTs are more competitive; for example, the elimination of heavily degradable contaminants such as many antibiotics and pharmaceuticals.[73]

4.3.4 CNTs as adsorbents system in wastewater treatment

The adsorption of synthetic organic compound by CNTs has been rapidly growing.[77,88,89] The studies included the adsorption of a multitude of organic contaminants such as polycyclic aromatic hydrocarbons (PAHs), benzene derivatives, phenolic compounds,

pharmaceuticals, polychlorinated biphenyls, proteins, insecticides, herbicides, organic dyes, and dioxin by CNTs.[90]

Moreover, CNTs have demonstrated potential as adsorbent systems applied in water and wastewater treatment for the removal of FQs.

Several experimental studies of adsorption of FQs on CNTs are reported in the literature. For example, Li *et al.*,[91] found that the adsorption of CFX on SW and MW-CNTs was greatly affected by pH and proposed that hydrophobic interactions controlled sorption for neutral and zwitterionic CFX, while electrostatic interactions were the dominant mechanism for ionic CFX sorption.

The CFX sorption was thermodynamically favourable for all CNTs used, although in the case of SW-CNTs the sorption process is an entropy driven process (*i.e.* positive ΔH of adsorption), while the opposite behaviour was observed for CFX sorption on MW-CNTs. SW-CNTs present the highest sorption for CFX, due to the fact that they have the largest surface area among all CNTs.[91] The adsorption of the FQs Norfloxacin (NOR) and Ofloxacin (OFL) on CNTs has been studied by Peng *et al.*[92] to evaluate the role of structural and hydrophobic properties in regulating their adsorption. They concluded that, even though OFL and NOR showed one order of magnitude difference in their solubilities, their adsorption coefficients were similar. The major difference between the hydrophobicities of NOR and OFL did not result in their difference regarding adsorption on CNTs. The similar structures of OFL and NOR indicated that their adsorption on CNTs was also a structural-controlled process.

In 2015 Ncibi *et al.*[93] conducted some experiments to investigate the use of SW-CNTs, double-walled (DW-CNTs) and MW-CNTs agglomerates for the removal of two antibiotics, Oxytetracycline (OXY) and CFX, from aqueous solution by means of UV-Vis spectrophotometry. The experimental results revealed that a moderate increase in adsorption between pH 3 and 7 for both antibiotics. The highest removal capacities were registered using SW-CNTs for both antibiotics.

In recent years, the interaction between drugs and CNT has been studied by means of MD simulations, allowing to have a detailed picture of the adsorption/release mechanisms and thermodynamics thanks to the calculation of the binding free energy, obtained through the combination of the potential of mean force (PMF) with umbrella sampling (US) technique.[94–105]

While numerous experimental studies have been conducted on the adsorption of CFX to CNT,[91,93,106–111] only one computational work related to the interactions between CFX and CNT is present in the literature.[112] In that work, the heat-driven release of CFX from CNT was studied by means of molecular dynamics (MD) simulations[112], although only neutral CFX was considered and no free energy data the CFX adsorption were obtained.

4.3.5 Aim of this work

In this work, MD simulations have been used to study the adsorption of both neutral and zwitterionic forms of CFX (see Scheme 6) on SW-CNT in vacuum and in water. Furthermore, we determined the free energy profile of CFX for the adsorption using the Umbrella sampling technique (US)[113], and we used it to discuss the difference between neutral and zwitterionic form. US technique is a useful method to analyse the macromolecular interaction. The understanding of adsorption mechanisms at a molecular level can help to improve the efficiency of CNTs as adsorbent systems in wastewater treatment.

4.3.6 Computational details

4.3.6.1 Force fields and models

The GROMACS 5.1.4 program[42] was used to perform MD simulations in vacuum and in presence of water on several systems containing nCFX, zCFX, SWCNT and water. The united atom GROMOS 54A7 force field (G54A7)[43] was used to represent all the bonded and non-bonded interactions. The cross-term Lennard-Jones (12,6) parameters were obtained using the Lorenz-Berthelot combination rules. Water was described by the SPCE model.[45] LINCS algorithm[49] was applied to constrain all hydrogen bonds. The (14,14) armchair SW-CNT, with terminal hydrogen atoms, was created using VMD.[114] The CNT diameters has been set to 1.9 nm and the length to 6 nm. The diameter is typical of CNTs used experimentally, indeed, the typically diameters are from 0.6 to 2 nm [87] while the lengths range is from less than 100 nm to several centimeters, thereby bridging molecular and macroscopic scales.[87] United atom (UA) topologies for nCFX, zCFX and SW-CNT, obtained from ATB (Automated topology bulider),[46] were used. MK charges[115]

calculated at B3LYP/6-31G level of theory (reported in Table A5 in appendix B) has been used for nCFX and zCFX, instead, for SW-CNT the charges have been set to zero.

4.3.6.2 MD simulations in vacuum

The simulated systems consisted of a SW-CNT located in the center of the MD simulation cell (X = 10.0 nm, Y = 10.0 nm and Z = 10.0 nm) and 1, 2, 4 and 8 CFX molecules were located to the outer surface and in the inner surface of the SW-CNT. The simulations were conducted in microcanonical (NVE) ensemble. The total length for each simulation was 5 ns and the time step was 2 fs. Periodic boundary conditions, non-bonded interaction cutoffs, temperature coupling and pressure coupling were all turned off. The interaction energy (E_{int}) was calculated by following equation:

$$E_{int} = E_{tot} - (E_{SW-CNT} + E_{z-nCFX}) \quad \text{(eq1)}$$

where E_{tot} is the potential energy for the SW-CNT-z-nCFX system minimum geometry configuration, $E_{z\text{-}nCFX}$ is the potential energy of the adsorbed zCFX or nCFX in a vacuum with the geometry unchanged, and $E_{SW\text{-}CNT}$ is the potential energy of the surface.[116] Moreover, the relaxed interaction energy ($E_{int\text{-}relax}$) was calculated taking into account the relaxation (minimum geometry configuration) of CFX and SW-CNT.

4.3.6.3 MD simulations in water

The simulated systems consisted of a SW-CNT located in the center of the MD simulation cell, 1, 2, 4 and 8 CFX molecules were located to the outer and inner surface of the SW-CNT with 11100 water molecules.

The particle-mesh Ewald method was used to calculate the long-range electrostatic interactions[47,48], whereas the van der Waals interactions were treated with smooth cut-off at a distance of 12 Å. Periodic boundary conditions have been applied in all directions. After energy minimization, the systems were pre-equilibrated by MD simulations in NVT ensemble at the temperature of 298.15 K and in NPT ensemble at 1 atm and 298.15 K for 1 ns with Berendsen coupling method.[50] The simulation was run with NPT ensemble at 1 atm and 298.15 K for 5 ns with a time step of 2 fs where the V-rescale[51] algorithm was

used as temperature coupling method, while, the Parrinello-Rahman barostat was employed.[52]

Simulations of zCFX and nCFX in water, without SW-CNT, have been conducted to obtain the hydration energy (E_{hyd}) of CFX. The simulated systems consisted of one CFX molecule and 1000 waters molecules. The system was simulated for 5 ns in NPT ensemble at 1 atm and 298.15 K. E_{hyd} was calculated according to the following equation:

$$E_{hyd} = E_{CFX-H_2O} - (E_{CFX} + E_{H_2O}) \quad \text{(eq2)}$$

where $E_{CFX\text{-}H2O}$ is the potential energy of the CFX immersed in a box of water, E_{CFX} is the potential energy of CFX in vacuum (in NPT ensemble) and E_{H2O} is the potential energy of the box of water without the CFX molecules.

4.3.6.4 Free energy calculation

Free energy calculations were carried out using the umbrella sampling technique.[113] This technique requires the prior generation of initial configurations along a reaction coordinate (ξ), between two interacting species. The position of one of these species is kept constant in order to have a reference point, while the other group is placed at increasing center-of-mass (COM) distance from the reference with its position maintained by an 'umbrella' potential. These COM distances represent "sampling windows" wherein independent simulations are conducted to generate a set of structures along the reaction coordinate. The values of the potential of mean force (PMF) can be calculated from of these windows. To assemble a PMF curve as a function of the entire reaction coordinate, energy values in adjacent windows are reassembled such that they produce a continuous function.[113]

The free energy profiles have been calculated for the adsorption of nCFX and zCFX to the outer and inner surface of SW-CNT. To generate equilibrated starting structures for the pulling simulations, one molecule of nCFX or zCFX were placed respectively 2.5 Å out of the external surface and in the middle of the inner surface of SW-CNT. The rectangular box size for the adsorption on the outer surface was X = 8.0 nm, Y = 13.6 nm and Z = 8.0 nm with 28050 water molecules. Instead, for the adsorption on the inner surface the box size was X = 5.0 nm, Y = 6.0 nm and Z = 20.0 nm with 19050 water molecules.

As regards the non-bonded interactions, periodic boundary conditions, constraint algorithm and simulation protocol, the same conditions of the simulations in water have been used. The position restraint algorithm was employed to restrain the position of SW-CNT in order to obtain an immobile reference. The starting configurations were obtained by pulling the CFX molecule from the outer/inner surface of SW-CNT to the bulk water phase with an umbrella potential,[117] along the Y axis for the adsorption on the outer surface and along the Z axis for the adsorption on the inner surface (see Figure 17). 16 configurations have been selected as umbrella sampling windows for the adsorption on the outer surface, while 22 configurations have been selected as windows for the adsorption on the inner surface, with a spacing of 0.2 nm. After a short equilibration (0.5 ns) each window was simulated for 10 ns in NPT ensemble at 1 atm and 298.15 K where the V-rescale algorithm[118] was used as temperature coupling method, while the Parrinello-Rahman algorithm[52] was chosen as pressure coupling method. During this simulation an Umbrella potential has been applied between nCFX or zCFX and SW-CNT, with a force constant of 1000 kJ mol^{-1} nm^{-2}. The value of the force experienced by zCFX and nCFX was saved every 4 ps. To determine the PMF for the systems studied, we processed the results from all windows of the restrained MD simulations for each system using the Weighted Histogram Analysis Method (WHAM).[119]

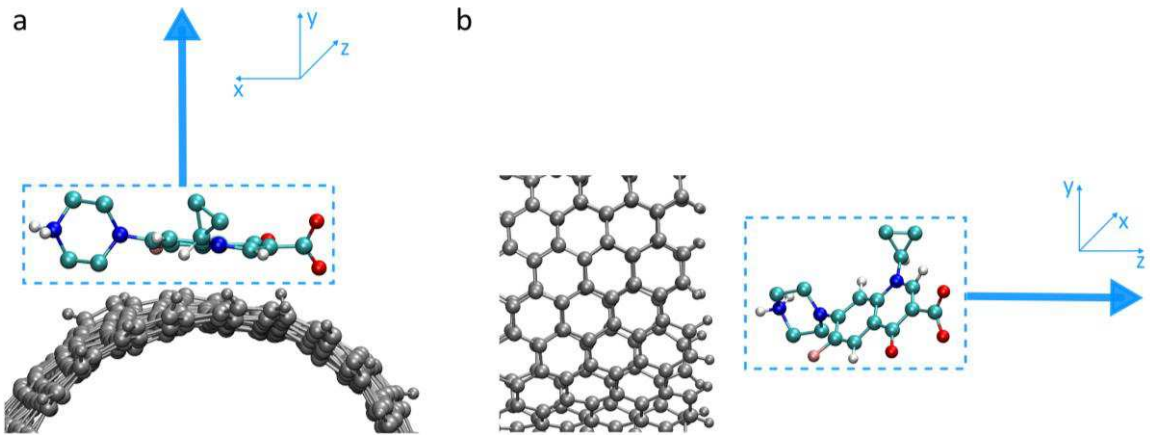

Figure 17 Pulling direction of CFX molecules.

4.3.7 Results and discussion

4.3.7.1 MD simulation in vacuum

In the first simulations, 1, 2, 4, 8 CFXs molecules were placed close to the surface of SW-CNT. CFX molecules remain adsorbed to the SW-CNT surface by π-π interactions in all cases.[112] Both nCFX and zCFX show similar structures as regards the adsorption of one molecule on the outer surface of SW-CNT. The minimum geometry configuration of SW-CNT-CFX systems for the adsorption of one molecule in vacuum are reported in Figure 18. As regards the adsorption on the inner surface, zCFX assumes a cyclic conformation due to the formation of an intramolecular hydrogen bond between the carbonyl group and the amino group of the piperazine ring, while the minimum geometry of nCFX is parallel to the SW-CNT surface (Figure 18c and 18d). The formation of hydrogen bonds (H-bonds) between the carbonyl group or carboxylic acid group and the amino group of the piperazine ring (see Figure 19-22) is observed when multiple CFX molecules (2, 4 and 8) are adsorbed to the SW-CNT surface.

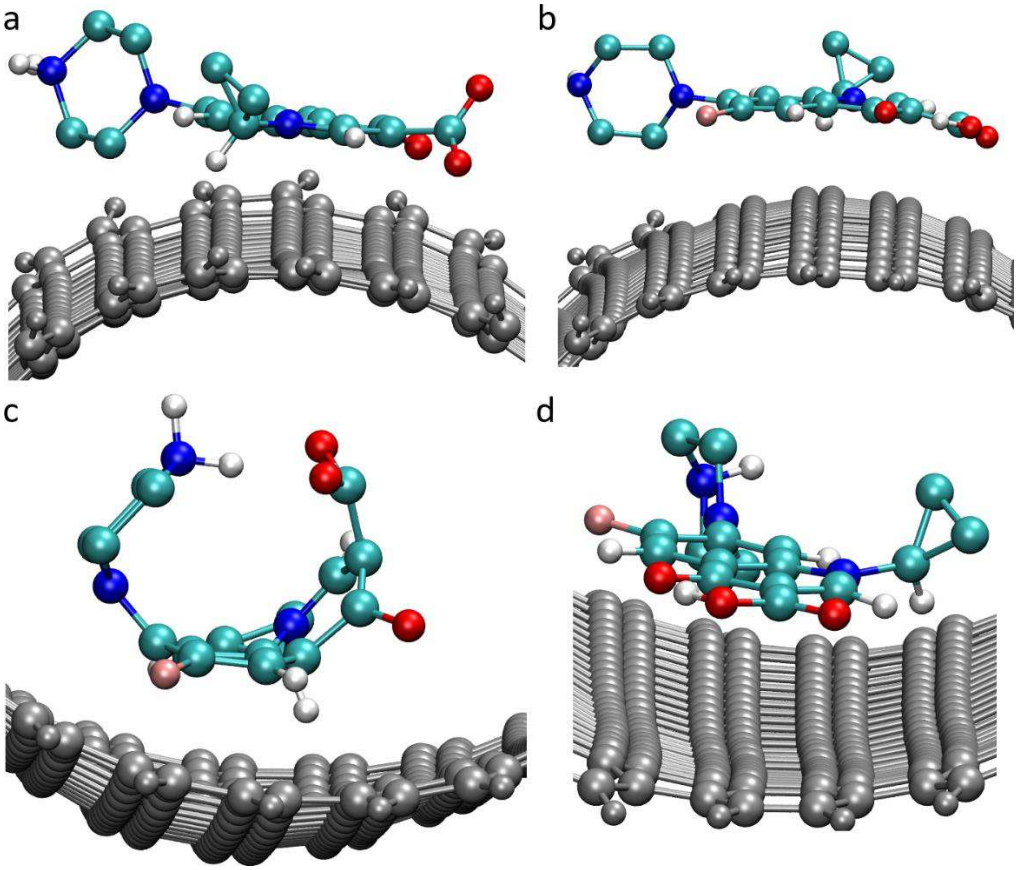

Figure 18 Minimum geometry configuration of a) zCFX and b) nCFX adsorbed on the outer surface of SW-CNT in vacuum, and c) zCFX, d) nCFX adsorbed on the inner surface of SW-CNT in vacuum.

To better understand this phenomenon, an analysis of the H-bonds between CFX molecules has been performed. The average number of H-bonds between CFX and CFX, calculated over the duration of the simulation, is shown in the Table 10.

Table 10 Average number of H-bonds between CFX molecules for the adsorption of 2, 4 and 8 CFX molecules, where n_{ads} is the number of CFX molecules adsorbed.

	Average of H-bond			
n_{ads} CFX	zCFX out	nCFX out	zCFX in	nCFx in
2	2.5	2.6	2.1	3.0
4	7.4	6.3	5.8	5.8
8	14.0	13.1	12.7	12.0

The data in Table 10 show that the number of H-bonds increases with the increase in the number of adsorbed molecules. The average number of H-bonds for adsorption on the inner and outer surface is comparable to zCFX and nCFX; when four and eight CFX molecules are adsorbed they tend to form more H-bonds if located on the outer surface, while for the adsorption of two molecules the number of H-bonds on the inner and outer surface is comparable. H-bonds influence the adsorption geometry of CFX molecules on the SW-CNT surface.

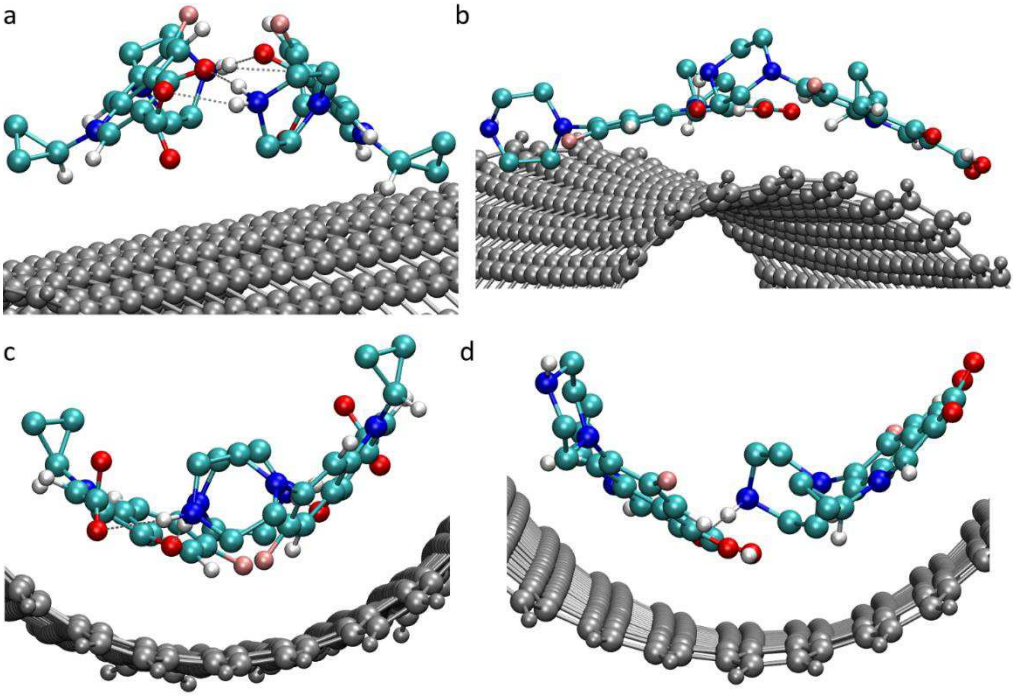

Figure 19 Minimum geometry configuration of a) two zCFXs and b) two nCFXs adsorbed on the outer surface of SW-CNT and c) two zCFXs, d) two nCFXs adsorbed on the inner surface of SW-CNT in vacuum.

Indeed, the adsorptions of two zCFX molecules are not perfectly parallel to outer surface, as reported in Figure 19a. However, the two nCFX molecules are parallel to the SW-CNT surface (see Figure 19b), and the same behaviour is observed for both zCFX and nCFX for adsorption to the inner surface (Figure 19c and 19d). The adsorption of four CFX molecules to the outer surface highlights the fact that they remain parallel to the CNT surface for both zCFX and nCFX (see Figure 20a and 20b) the same behaviour is reported for nCFX, adsorbed to the inner surface (see Figure 20d). For the adsorption on the inner surface, the four zCFXs present a "sandwich" configuration (Figure 20c), where CFX molecules interact with each other via π-π through their own aromatic rings.

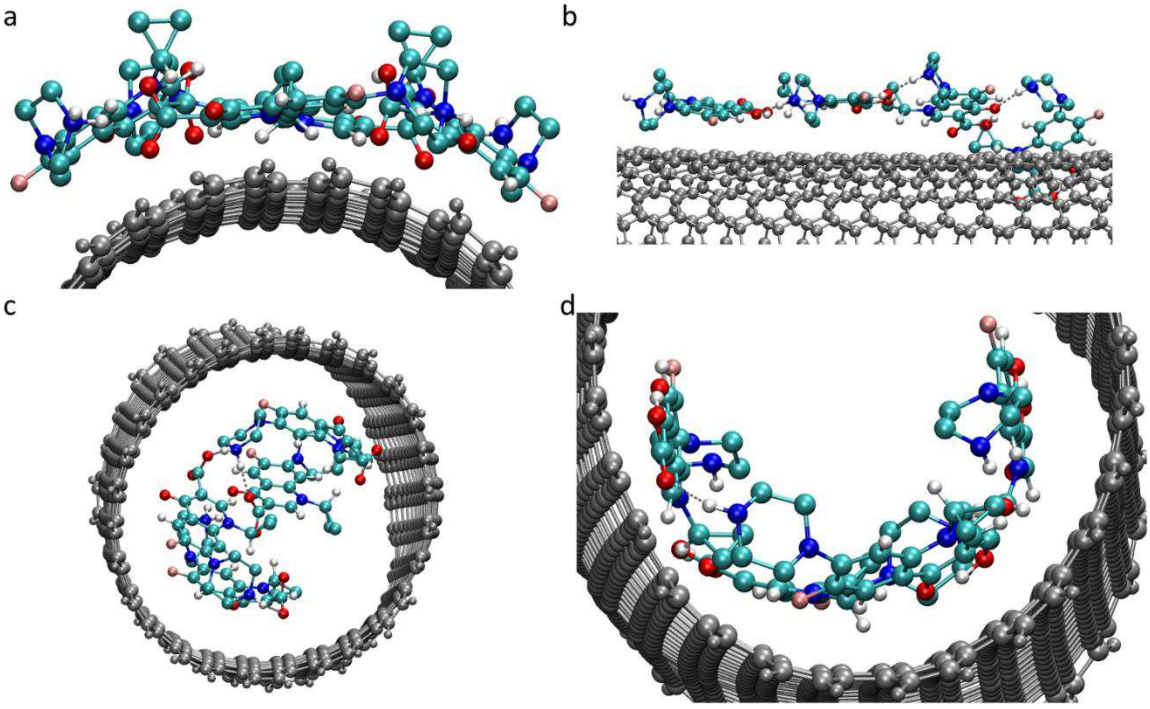

Figure 20 Minimum geometry configuration of a) four zCFXs and b) four nCFXs adsorbed on the outer surface of SW-CNT, and c) four zCFXs, d) four nCFXs adsorbed on the inner surface of SW-CNT.

Such type of conformation, reported in detail in Figure 21, can lead to a decrease in the interaction between the aromatic ring of SW-CNT and the quinolone ring of zCFX. The "sandwich" configuration, however, has already been reported in literature for the interaction between both forms of CFX and lipid membranes.[120]

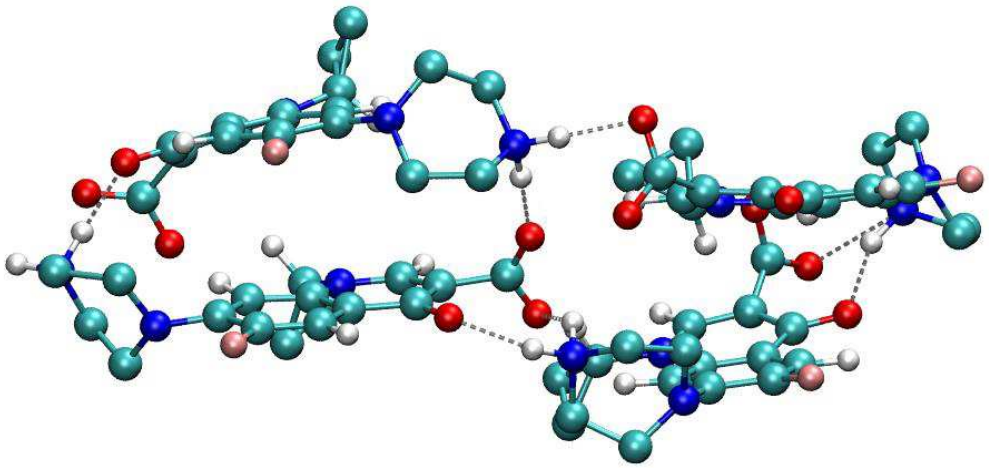

Figure 21 Detailed structure of four zCFX molecules adsorbed on inner surface.

The same type of configuration is also observed for the adsorption of eight z and nCFX to the inner surface (figures 22c and 22d). Finally, the adsorption of eight zCFX molecules to the outer surface shows that some molecules are not parallel to the surface due to the intricate H-bonding network that they form (Figure 22a). On the contrary, the eight nCFX molecules are all parallel to the surface.

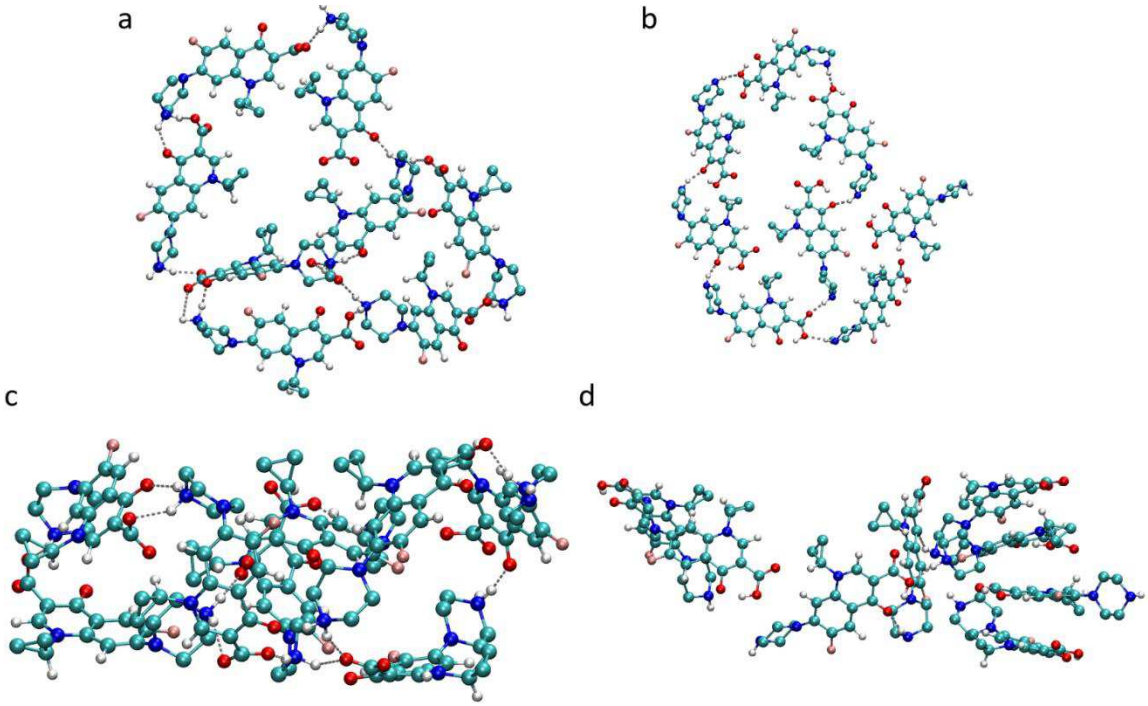

Figure 22 Minimum geometry configuration of a) eight zCFXs and b) eight nCFXs adsorbed on the outer surface of SW-CNT in vaccum, and c) eight zCFXs, d) eight nCFXs adsorbed on the inner surface of SW-CNT in vacuum. For clarity, the structure of SW-CNT has not been reported.

In order to better understand the interaction between SW-CNT and CFX the minimum distances (r_m) calculated between any pair of atoms closest to the two molecules as a function of time (r_m *vs.* time) have been carry out. The average of r_m ($\overline{r_m}$) calculated from the graph of r_m *vs.* time for each CFX molecule are between 2.64 ± 0.01 Å and 3.22 ± 0.01 Å, indicating that these are the minimum distances between CFX and SW-CNT. The analysis of r_m curves *vs.* time indicates that CFX stayed in contact with the surface for the entire trajectory in all cases.

The $\overline{r_m}$ values for the absorption of one CFX molecule on the outer SW-CNT surface are similar, however zCFX seems to be closer to the surface than nCFX (2.84 ± 0.01 Å and 2.90 ± 0.01 Å respectively); the same behaviour is observed for the adsorption to the inner surface (2.78 ± 0.01 Å for zCFX 2.86 ± 0.01 Å for nCFX). The graph r_m *vs.* time relative to the adsorption of one CFX molecule shows an approximately constant value, however, for adsorption of zCFX on the inner surface, a decrease in the r_m value from 3.00 ± 0.01 Å to 2.70 ± 0.01 Å (Figure 23a) is registered around 1.8 ns, together with a decrease in the fluctuation of the r_m value where a step-trend is observed. This is related to the cyclic conformation assumed by zCFX (Figure 18c), observed until the end of the simulation. The $\overline{r_m}$ values for the absorption of two CFXs molecules are between 2.64 ± 0.01 Å and 2.95 ± 0.01 Å and the graphs r_m *vs.* time show an approximately constant value. The $\overline{r_m}$ values for adsorption on the outer surface of four zCFX molecules are between 2.86 ± 0.01 Å and 3.13 ± 0.01 Å, while for nCFX the $\overline{r_m}$ values are similar, between 2.86 ± 0.01 Å and 2.97 ± 0.01 Å. For adsorption to the internal surface, nCFX presents $\overline{r_m}$ values ranging from 2.89 ± 0.01 Å to 2.96 ± 0.01 Å. In these cases, the graph r_m *vs.* time shows an approximately constant value. For four zCFX molecules adsorbed to the inner surface, the $\overline{r_m}$ values are between 2.92 ± 0.01 Å to 3.22 ± 0.01 Å, although the graphs r_m *vs.* time show an increase in r_m values for CFX 1 and CFX 3 after 1ns (Figure 23b and 23c) from the beginning of the simulation. Trajectory analysis shows that, at the beginning of the simulation, the four zCFX molecules were in a linear structure (Figure 24) but, after about 1ns, where a step-trend in the value of r_m is observed, the structure changed completely; in fact, molecules presents a “sandwich” configuration (see Figure 21). This structure was conserved until the end of the simulation (Figure 20c). It is interesting to note that after about 1 ns zCFX3 has a high fluctuation in the values of r_m (from 2.25 Å to 4.00 Å), due to the fluctuation of the sandwich structure; moreover, zCFX3 presents the highest value of $\overline{r_m}$ (3.22 Å).

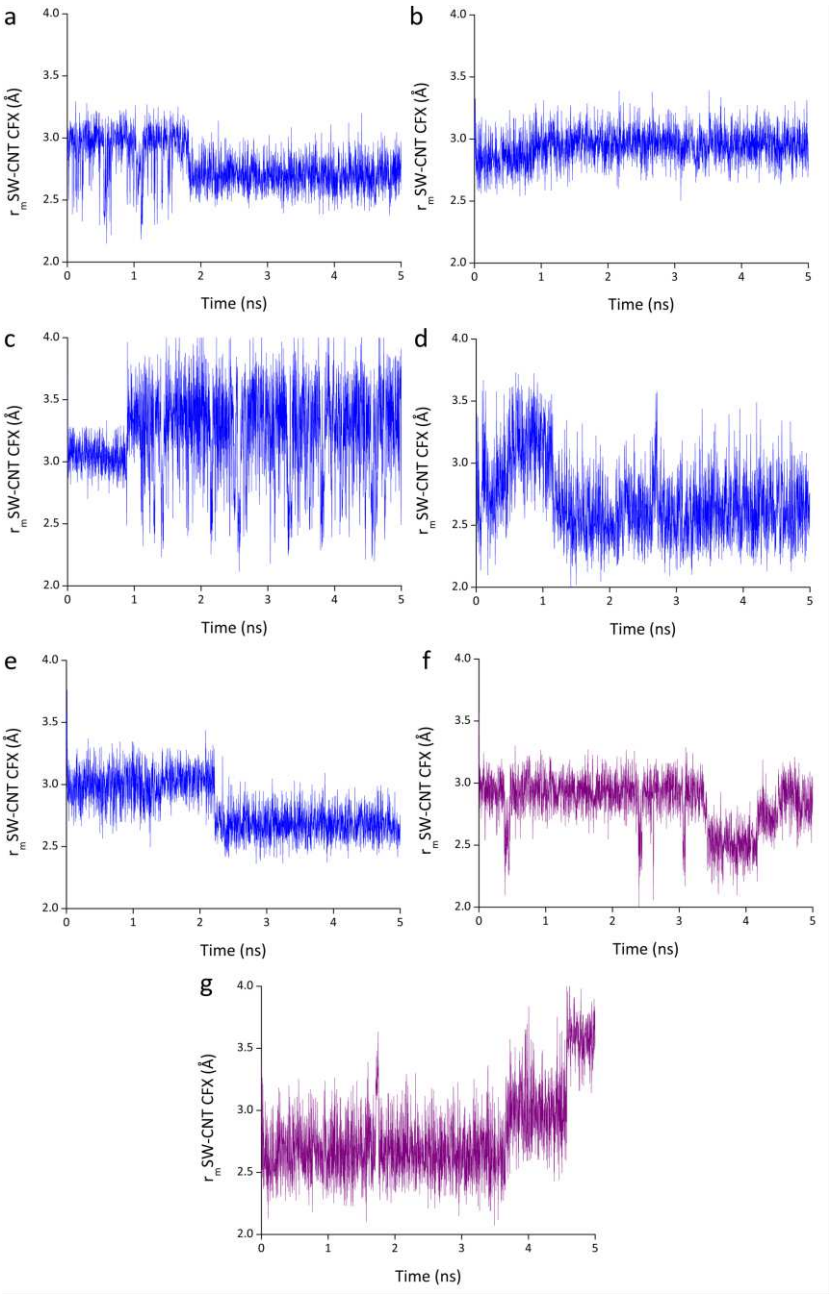

Figure 23 r_m *vs.* time for: a) zCFX adsorbed on the inner surface, b) zCFX1 and c) zCFX3 for the adsorption of 4CFX molecules on the inner surface, d) zCFX7 and e) zCFX8 for the adsorption of 8CFX molecules on the inner surface, f) nCFX1 g) nCFX2 for the adsorption of 8CFX molecules on the inner surface.

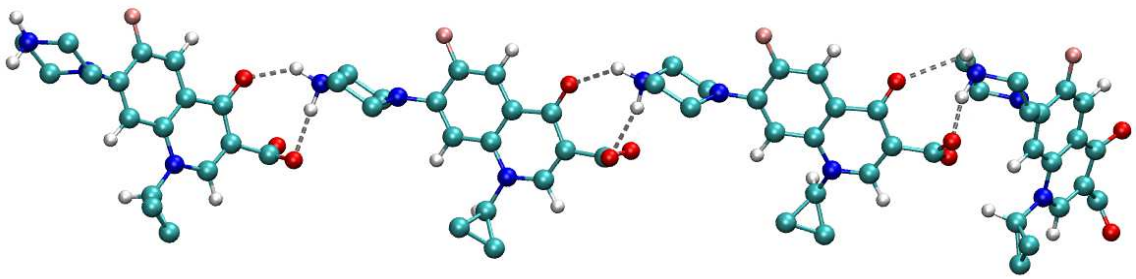

Figure 24 Snapshot of the initial configuration of four zCFX molecules (t = 0 ns). For clarity, the structure of SW-CNT has not been reported.

The $\overline{r_m}$ values for the adsorption of eight molecules of zCFX and nCFX on outer surface are similar, ranging between 2.807 ± 0.01 Å and 3.063 ± 0.01 Å for zCFX and between 2.930 ± 0.01 Å and 3.068 ± 0.02 Å for nCFX; the graph r_m *vs.* time shows an approximately constant value. For zCFX molecules absorbed to the inner surface, $\overline{r_m}$ values are between 2.93 ± 0.01 Å and 3.16 ± 0.01 Å, while for nCFX molecules they are between 2.81 ± 0.01 Å and 3.17 ± 0.01 Å. Moreover, the graph r_m *vs.* time does not show a constant value. For zCFX, the molecules exhibiting nonlinear trends are CFX7 and CFX8 (Figure 23d and 23e). In addition, the trajectory analysis shows that, at the beginning of the simulation, the eight zCFX molecules were in a linear structure and CFX7 and CFX8 present cyclic conformations (Figure 25a, CFX7 and CFX8 highlighted in red), but after about 1.2 ns the structure changed completely, so CFX molecules present a "sandwich" configuration (see Figure 22c). In the case of nCFX, the molecules that do not have a constant value are CFX1 and CFX2 (see Figure 23f and 23g) due to the change occurred in their conformation (highlighted in red in Figure 25b and 25c). Also in this case zCFX7 and nCFX8 present a high fluctuation in the values of r_m (from 2.11 Å to 3.56 Å for zCFX7 and from 2.08 Å to 4.61 Å for nCFX2), due to the fluctuation of the complex structure that the eight molecules form.

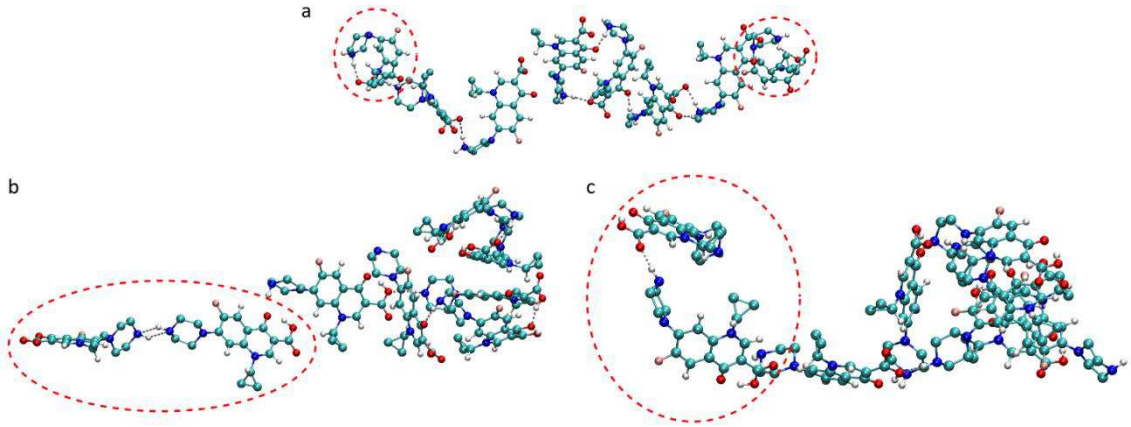

Figure 25 Snapshot from the eight zCFX molecules at the beginning of the simulation (a); snapshot taken from the eight nCFX molecules after 3ns of beginning of the simulation (b), and at the end of simulation (c). For clarity, the structure of the SW-CNT has not been reported.

Finally, radial distribution function curves (RDF), calculated between any pair of atoms of SW-CNT and CFX using Gromacs g_rdf tool, are reported in Figure 26.

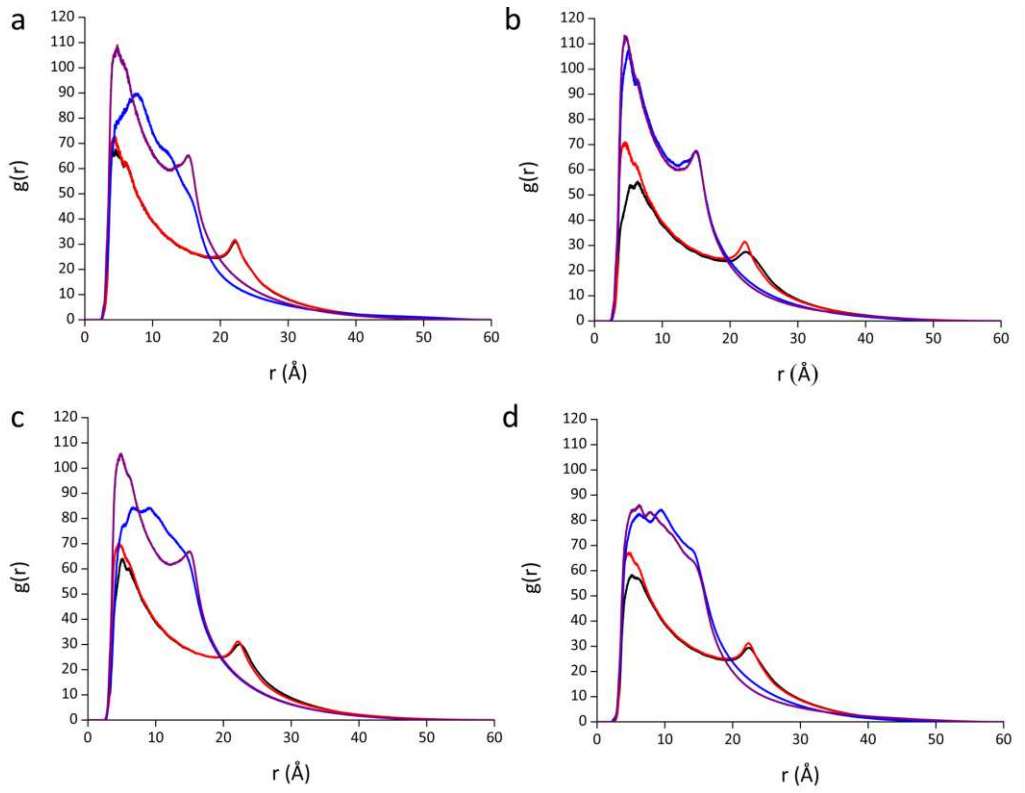

Figure 26 RDFs Calculated between the SW-CNT surface and the centre of mass (COM) of CFX in vacuum for a) 1, b) 2, c) 4, d) 8 CFX molecules. Black: zCFX adsorbed on the outer surface of SW-CNT, blue: zCFX adsorbed on the inner surface of SW-CNT, red: nCFX adsorbed on the outer of SW-CNT, purple: nCFX adsorbed on the inner surface of SW-CNT.

The curves show a notable peak, which indicates the most probable distance between CFX and the SW-CNT surface. The peak positions for such curves occur in the range from 4.3 Å to 9.4 Å, implying the position of the first adsorption layer for CFX. Furthermore, the presence of a second peak has been observed, and the peak positions occur in the range from 22.1 Å to 22.3 Å for the adsorption on the outer surface and from 14.9 Å to 15.3 Å for the adsorption on the inner surface, due to the CNT carbon atoms on the opposite side of the surface. The RDF curves for the adsorption of one CFX molecule on the outer surface show a similar behaviour for both nCFX and zCFX, although the RDF curves for zCFX, adsorbed to the inner surface, are wider that nCFX, indicating that the adsorption of zCFX is less close around SW-CNT due to the cyclic conformation assumed by it (Figure 18c). The RDF curve for the adsorption of two zCFX molecules to the outer surface shows a decrease in intensity in the first peak in respect to nCFX, indicating that the adsorption is less compact around the outer surface of SW-CNT and could be related to the conformation assumed by the two molecules of zCFX (see Figure 19a). For four CFX

molecules, the RDF curve shows that the adsorption of zCFX is less compact around the inner surface of SW-CNT, which can be explained by observing that the CFX molecules present a "sandwich" configuration (figure 20c and 21). Finally, the RDF curves for the adsorption of eight CFX molecules show that the most compact adsorption is observed when CFXs are adsorbed to the outer surface. A widening of the RDF curve has been observed for the adsorption on the inner surface, due to the formation of sandwich configurations (see Figures 22c and 22d). In conclusion, CFX molecules remain adsorbed to the SW-CNT surface thanks to π-π interactions between CFX and SW-CNT aromatic rings.

4.3.7.2 Interaction energy in vacuum

The calculated interaction energy (E_{int}) and relaxed interaction energy ($E_{int\text{-}relax}$) for CFX with SW-CNT is reported in Table 11.

Table 11 E_{int} and $E_{int\text{-}relax}$ (kcal mol^{-1}) in vacuum between SW-CNT and 1, 2, 4 and 8 molecules of n and zCFX. xCFX out (x = n or z): CFXs adsorbed on the outer SW-CNT surface, xCFX ins (x = n or z): CFXs adsorbed on the inner surface.

	1 CFX		2 CFX		4 CFX		8 CFX	
Conf.	E_{int}	$E_{int\text{-}realx}$	E_{int}	$E_{int\text{-}realx}$	E_{int}	$E_{int\text{-}realx}$	E_{int}	$E_{int\text{-}realx}$
zCFX out	-26.8	-25.7	-17.9	-17.4	-22.3	-20.3	-21.7	-20.2
nCFX out	-24.9	-23.8	-26.2	-25.1	-26.0	-25.2	-25.1	-23.9
zCFX ins	-34.9	-33.3	-39.5	-38.3	-29.4	-27.8	-31.9	-30.7
nCFX ins	-43.2	-41.3	-42.3	-39.3	-40.1	-38.1	-34.3	-33.0

All the calculated E_{int} and $E_{int\text{-}relax}$ are negative and presents the same trend, with the exception of an increase in energy values (from 0.5 to 3.0 kcal mol^{-1}) observed passing from E_{int} to $E_{int\text{-}realx}$, indicating that the energy cost to bring CFX and SW-CNT from their minimum geometry configuration to those that take on the CFX-SW-CNT complex is minimal . In general, as shown by the data reported in Table 11, CFX molecules interact more strongly with the inner surface than with the outer surface. nCFX molecules interact more strongly with the SW-CNT surface compared to zCFX molecules, except when only one zCFX molecule is adsorbed to the outer surface. The increase in the number of CFXs molecules leads to a decrease in the E_{int}, a behavior that can be explained by observing in

Figure 2, 3, 4 and 5; when more CFXs molecules are adsorbed, they interact with each other (H-bond) leading to a decrease in the interaction between the quinolone rings of CFX and the aromatic rings of SW-CNT. However, this trend presents some anomalies. Indeed, a decrease in E_{in} value is observed for zCFX, going from two to four molecules adsorbed to the outer surface. Such behavior could be related to the conformation assumed by the two molecules of zCFX (Figure 19a). The same behavior is observed for the adsorption of 4 and 8 zCFX molecules to the internal surface of SW-CNT, when a decrease in interaction energy occurs. Another anomaly is reported for the absorption of zCFX on the inner surface, given that it passes from one to two molecules. An decrease in E_{int} values can be observed, and it could be explained by the fact that one zCFX molecule assumes a cyclic configuration (Figure 18c), while when two zCFX molecules are present they remain planar (Figure 19c). As reported in other works, the interaction between molecules and CNT surface depends on Lennard-Jones (LJ) potential, without considering the electrostatic potential and solvent effects[101,121]. The LJ potential was calculated on the minimum geometry configuration using Gromacs g_energy tool, and the values were very similar to those calculated for the E_{int} (see Table A6 in appendix B).

4.3.7.3 MD simulation in water

The calculations began by placing the CFXs molecules close to the surface of SW-CNT. The trajectory analysis showed that the CFX molecules remain adsorbed to the SW-CNT surface in direct contact with the SW-CNT walls, without any H_2O molecule mediating the adsorption process. zCFX and nCFX are parallel to the outer surface of SW-CNT. Contrary to vacuum simulations, zCFX, adsorbed to the inner surface, has now a linear conformation and is parallel to the SW-CNT surface. The change in its behaviour is due to the formation of H-bonds between zCFX and water, which prevents the formation of the inter and intramolecular H-bond. The minimum geometry configuration for one zCFX adsorbed to the inner surface along with other important configurations are reported in Figure 27.

In addition, an analysis of H-bonds was performed to understand how the solvent influences the interactions between CFX-CFX. The average number of H-bonds between CFX and CFX and between CFX and water is shown in the Table 12.

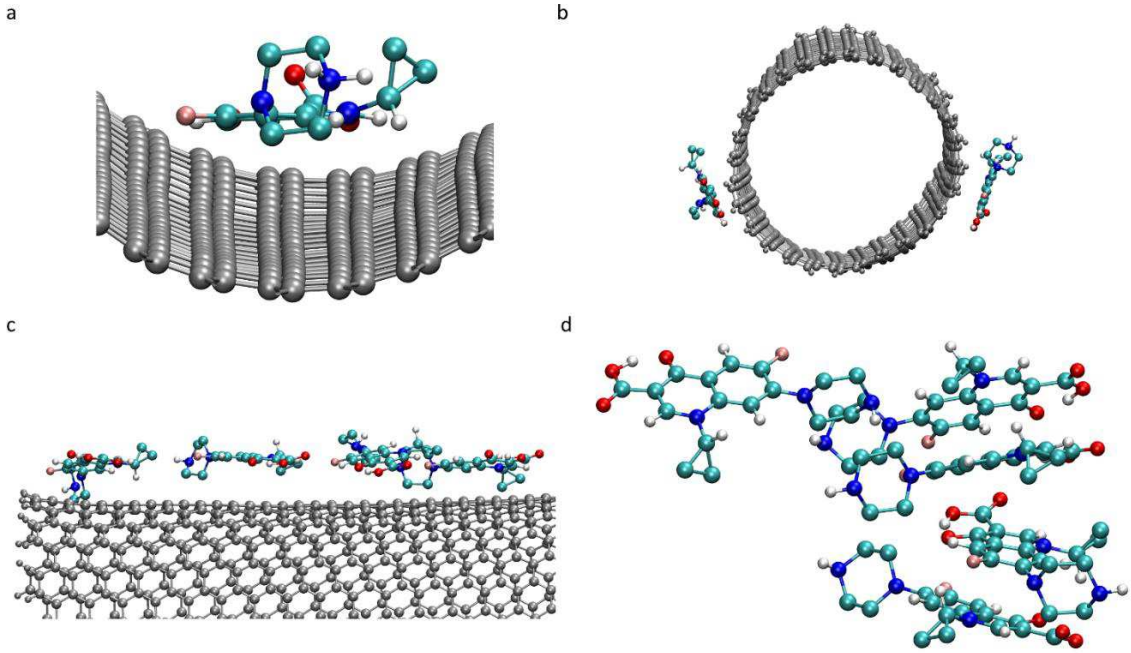

Figure 27 The most important minimum geometry configuration. a) zCFX, adsorbed on the inner surface; b) nCFX adsorbed on the outer surface c) four nCFX molecules adsorbed on the outer surface, d) five of eight nCFX molecules adsorbed on the inner surface in water.

Table 12 Average number of H-bonds between CFX molecules and between CFX and water for the adsorption of 1, 2, 4 and 8 CFX molecules. Where n° of ads CFX represents the absorption of 1, 2, 4, 8 CFX molecules, CFX-CFX is the average of H-bond between CFX molecules and w-CFX is the average of H-bond between water and CFX molecules.

	zCFX out		nCFX out		zCFX ins		nCFX ins	
n° ads CFX	CFX-CFX	w-CFX	CFX-CFX	w-CFX	CFX-CFX	w-CFX	CFX-CFX	w-CFX
1	-	9.3	-	5.2	-	8.5	-	4.8
2	0.2	18.1	0.0	10.4	0.2	16.4	0.1	8.8
4	0.0	37.1	3.0	20.4	0.1	33.4	0.2	17.9
8	0.5	72.5	0.3	40.0	4.2	54.2	0.1	30.4

The data in Table 12 show that the number of H-bonds between CFX and CFX is close to zero. For the adsorption of two CFXs, where all molecules are parallel to the SW-CNT surface, the molecules seems to interact less with each other compared to the behaviour observed in the vacuum, being the number of H-bonds between CFX-CFX close to zero. It is also interesting to note that 2 nCFX molecules interacted at the beginning of the simulation, but after 0.79 ns they tended to separate and not interact until the end of the simulation, when they were adsorbed to the outer surface (Figure 27b).

However, for the adsorption of four nCFX molecules on the outer surface, the number of H-bonds is 3.0 between CFX molecules, due to the linear conformation of the molecules (see Figure 27c). Even for 8 zCFX molecules absorbed to the inner surface the number of H-bonds is greater than zero (4.2), due to the "sandwich" structure observed for the 8 molecules (Figure 27d). The H-bond values calculated between CFX and water are completely different. In all cases, the number of H-bonds increases with the increase of the number of molecules, and the number of H-bonds in zCFX seems to be about double the number calculated for nCFX. The average number of H-bonds for adsorption of CFXs to the outer surface is slightly higher than the number calculated for adsorption to the inner surface. The data confirm that the molecules seem to interact less with each other and more with the solvent.

The r_m *vs.* time curves calculated between the surfaces of CFX and SW-CNT were used to clarify how the solvent affects CFX absorption. Also in this case, the analysis of r_m *vs.* time curves indicates that CFX stayed in contact with the surface along the entire trajectory in all cases. The $\overline{r_m}$, calculated from the graph of r_m vs time are between 2.76 ± 0.02 Å and 3.07 ± 0.02 Å, indicating that these are the minimum distances between CFX and SW-CNT. The values are very similar to those calculated for the absorption of CFX in vacuum (from 2.64 ± 0.01 Å to 3.22 ± 0.01 Å), indicating that the absorption distance is not affected by the presence of the solvent. The values of $\overline{r_m}$ for one zCFX and one nCFX are similar for the adsorption to both the outer (3.03 ± 0.02 Å and 3.05 ± 0.02 Å respectively) and the inner surface (2.80 ± 0.02 Å and 2.82 ± 0.02 Å respectively). As in the vacuum simulation, the molecules seem to be closer when adsorbed to the inner surface. The r_m *vs.* time curves present constant values. The same behaviours are observed in $\overline{r_m}$ trends and in graph r_m *vs.* time for the absorption of 2, 4 and 8 CFX molecules; however, in the case of adsorption to the inner surface of eight z and nCFX molecules, they do not present a constant value. For zCFX, a slight decrease in the curves are observed around 2 ns (see Figure 28a-c).

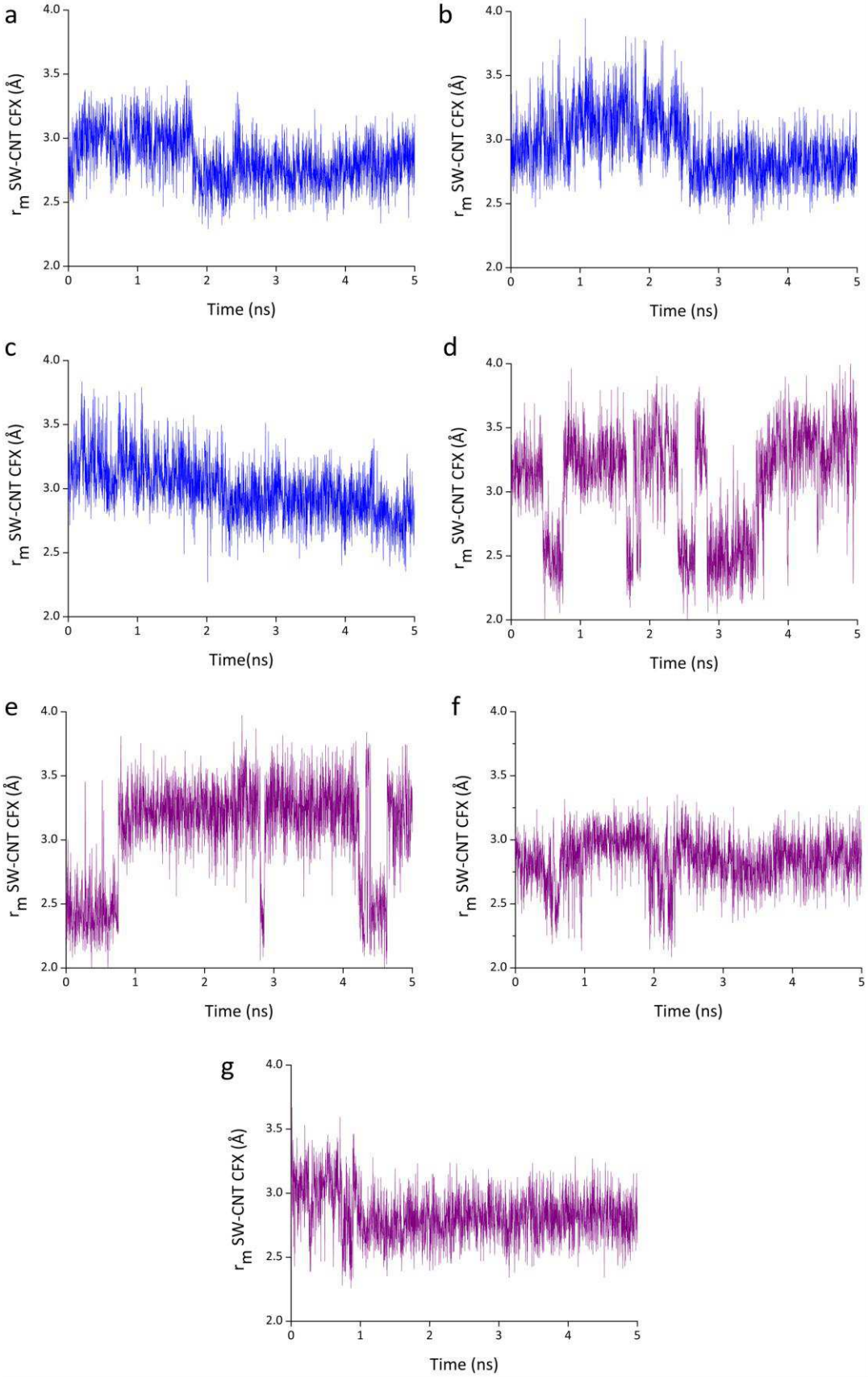

Figure 28 Curve of r_m vs time for: a) zCFX 2 b) zCFX 4 c) zCFX 7 for the adsorption of eight zCFX molecules on the inner surface in water; d) nCFX 2 e) nCFX 3 f) nCFX 4 g) nCFX5 for the adsorption of eight nCFX molecules on the inner surface in water.

Trajectory analysis shows that four out of eight adsorbed zCFX molecules (highlighted in red in Figure 29a) presented a "sandwich" configuration at the beginning of the simulation. After about 2ns, where a step-trend in the value of r_m is observed, the structure taken by the molecules changed: the molecules were divided in two groups (highlighted in red and blue in the Figure 29b) and did not interact with each other.

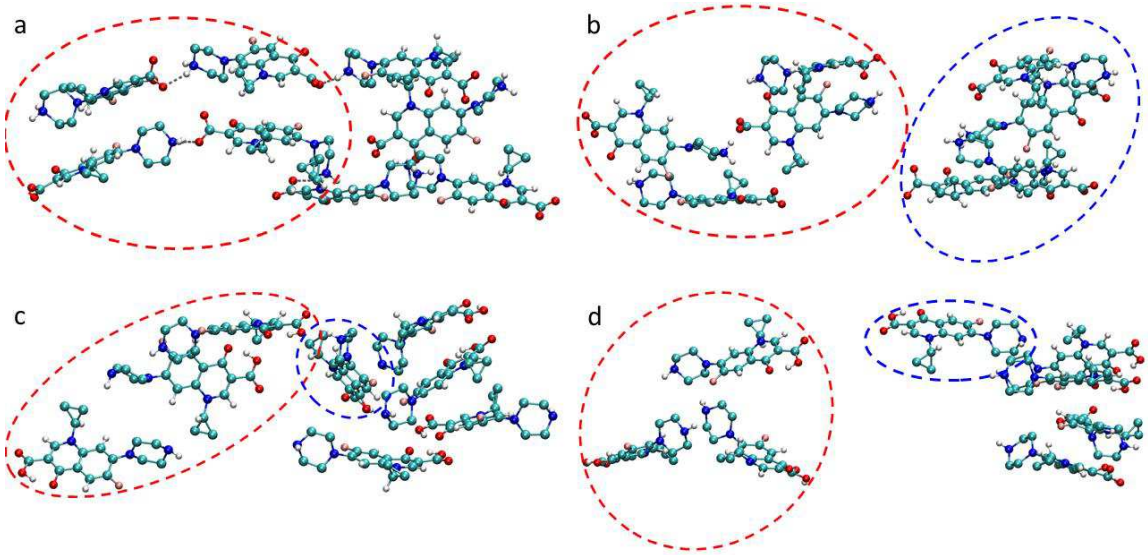

Figure 29 Snapshot from the eight zCFX molecules at the beginning of the simulation (a); and after 2ns of beginning of the simulation (b). 8 nCFX molecules at the beginning of the simulation (c); and at the end of the simulation (d). For clarity, the structure of the SW-CNT has not been reported.

A similar behaviour is observed for the adsorption of 8 nCFX molecules to the inner surface; the non-constant value observed in r_m *vs*. time graphs is due to the change in the structure taken by the eight molecules during the simulation (see Figure 29c and 29d). At the beginning of the simulation, all molecules seemed to interact with each other, but after 1 ns a progressive removal of three molecules took place (nCFX2 nCFX3 nCFX4), and at the end of the simulation the three molecules did not interact with the remaining molecules (see Figure 29d). Moreover, a change in the position of nCFX5 (highlighted in blue in figure 29c and 29d) from parallel to orthogonal with respect to the sandwich structure was observed.

Finally, the RDF curves calculated between every pair of atoms of SW-CNT and CFX are reported in Figure 30. The curves show shapes similar to those obtained in vacuum. The notable peak positions occur in the range from 4.5 Å to 5.1 Å; however, the range of these

values is smaller than the calculated value, because the CFX molecules interact less with each other and more with the solvent, having a more compact adsorption around SW-CNT. However, the RDF curves for eight nCFX molecules adsorbed to the inner surface are wider than those reported for the other cases, due to the fact that some CFX molecules present a “sandwich” configuration (Figure 28e), leading to a less compact adsorption around SW-CNT. In conclusion, the introduction of the solvent led to substantial changes in the morphology of the CFX-SW-CNT system, because the CFX molecules are dispersed on the surface of SW-CNT and interact less with each other.

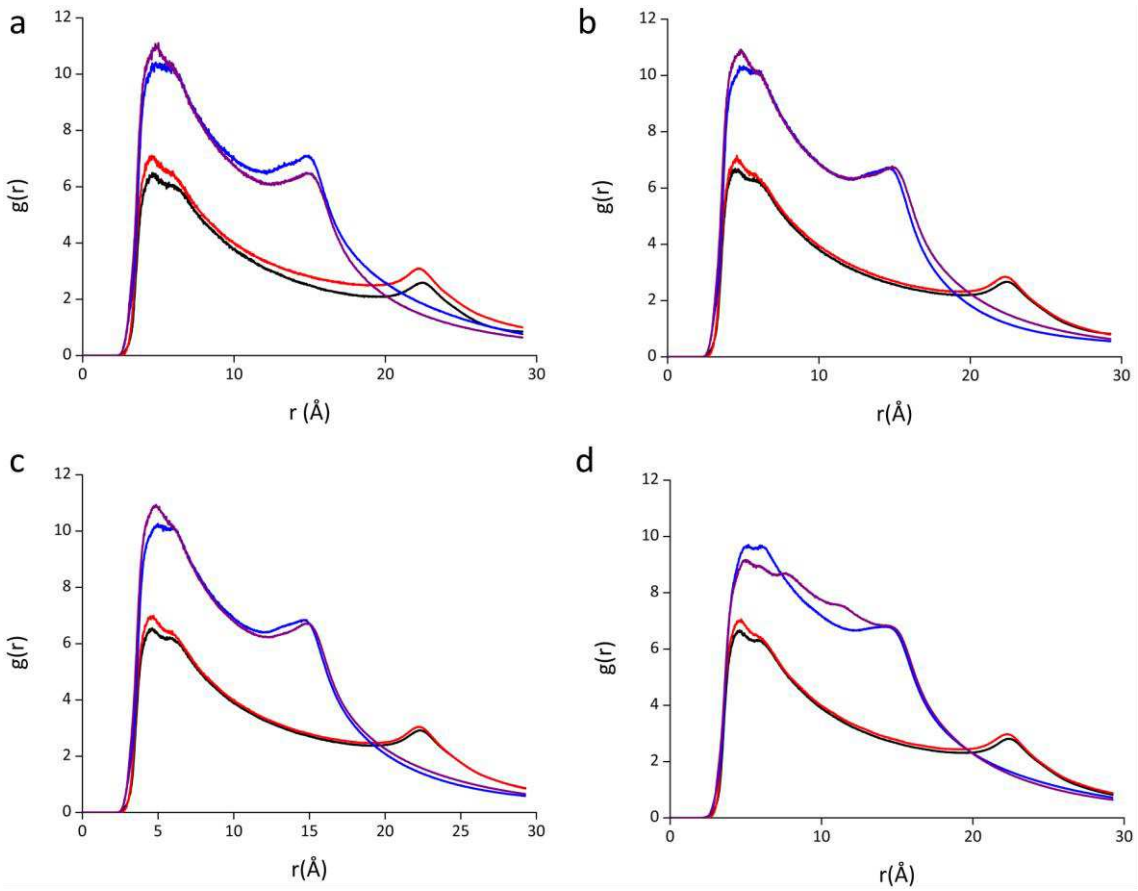

Figure 30 RDFs Calculated between SW-CNT surface and centre of mass (COM) of CFX in water for a) 1, b) 2, c) 4, d) 8 CFX molecules. Black: zCFX adsorbed on the outer surface of SW-CNT, blue: zCFX adsorbed on the inner surface of SW-CNT, red: nCFX adsorbed on the outer surface of SW-CNT, purple: nCFX adsorbed on the inner surface of SW-CNT.

4.3.7.4 Interaction energy in water

As observed for the simulations in vacuum, the interaction between CFX molecules and SW-CNT surface depended on LJ potential. In Table 13 the values calculated between CFX and SW-CNT on the minimum geometry configuration are reported.

Table 13 LJ_{int} (kcal mol^{-1}) in water between SW-CNT and 1, 2, 4 and 8 molecules of n and zCFX. xCFX out (x = n or z): CFXs adsorbed on the outer SW-CNT surface. xCFX ins (x = n or z): CFXs adsorbed on the inner surface.

LJ_{int}	1 CFX	2 CFX	4 CFX	8 CFX
zCFX out	-22.7	-21.8	-23.5	-22.9
nCFX out	-25.4	-24.4	-24.5	-24.4
zCFX ins	-37.9	-35.9	-35.2	-36.2
nCFX ins	-37.8	-37.1	-36.9	-32.3

nCFX present high LJ_{int} potential values in respect to zCFX in all cases except when one z and one nCFX molecule are adsorbed on the inner surface (in this case the LJ_{int} values are similar). For the adsorption of two molecules, a slight decrease in the LJ_{int} potential values can be observed; the strongest interaction is observed for nCFX adsorbed both to the outer and the inner surface. Such trend can be explained by observing that the 2 zCFX molecules interact with each other and could lead to a decrease in the interaction between the aromatic rings of zCFX and SW-CNT, while the 2 nCFX molecules are dispersed on the SW-CNT surface (Figure 27b). For what concerns the adsorption of four CFX molecules, there is a decrease of the LJ_{int} values for the adsorption on the outer surface and an increase for the adsorption to the inner surface. Finally, for the adsorption of eight CFX molecules, a little increase in LJ_{int} values has been observed in the case of adsorption to the outer surface, while for adsorption to the inner surface, there is an increase for nCFX while an decrease for zCFX.

4.3.7.5 Free energy calculation

Figure 31 describes the PMF profile along the reaction coordinate for the adsorption to the outer (Figure 31a) and inner (figure 31b) of SW-CNT surface (the PMF curves have been truncated at the minimum point). For the adsorption of zCFX to the outer surface the energy minimum is located at -9.5 kcal mol^{-1} at the distance of 13.02 Å from the SW-CNT center of mass (COM), while for nCFX the minimum is located at -3.6 kcal mol^{-1} at the

distance 12.61 Å. The values are in good agreement with the $\overline{r_m}$ values calculated above. In both cases, an immediate increase in the free energy was observed due to the decrease in the interaction between CFX and SW-CNT. Furthermore, a change in the slope of the free energy trend was observed at 14.21 Å for zCFX and at 14.69 Å for nCFX. When zCFX and SW-CNT reach the distance of 16.2 Å from SW-CNT COM, a plateau in the free energy is observed; for nCFX the plateau is observed at a distance of 18.5 Å; indeed, nCFX begins to interact with the SW-CNT wall at a greater distance compared to zCFX.

The PMF curves for the adsorption to the inner surface (figure 31b) show that the minimum energy is located at -12.5 kcal mol^{-1} for zCFX and at -20.9 kcal mol^{-1} for nCFX; moreover, both curves have sigmoid shapes. The first plateau, related to the interaction with the inner wall of CNT, starts at 25.92 Å for zCFX and 19.78 Å for nCFX, while the second plateau, due to the end of the interaction with the inner wall, starts at 37.88 Å for both zCFX and nCFX. The adsorption free energy (ΔG_{ads}) between CFX and SW-CNT calculated as difference between the highest (where the values of the PMF converge to a stable value at large COM distance) and lowest values of the PMF curves (Figure 31) are reported in table 14.

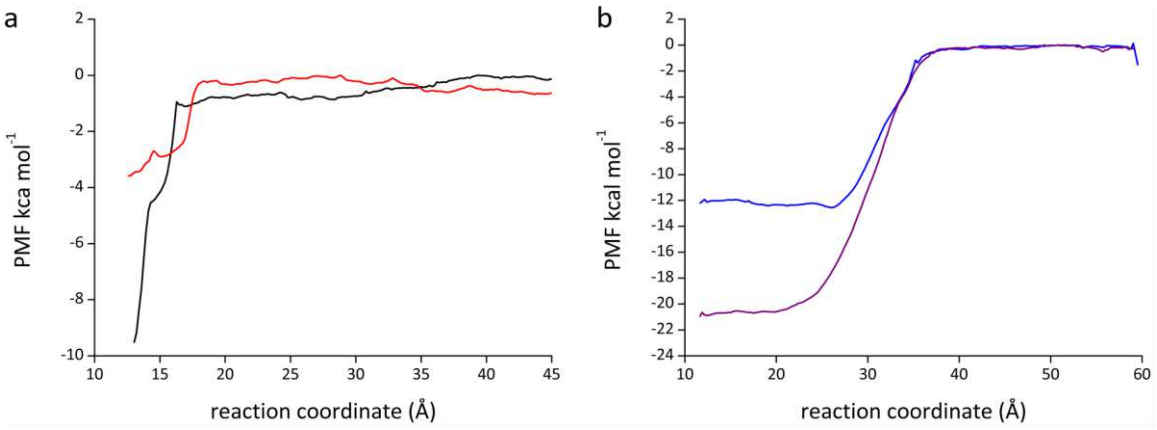

Figure 31 Potential of mean force curve (truncated at minimum point) for: a) adsorption to the outer surface for zCFX (black curve) and nCFX (red curve); b) adsorption to the inner surface for zCFX (blue curve) and nCFX (purple curve). The reaction coordinate as a function on the centre of mass (COM) distance of CFX and SW-CNT.

The results show that the ΔG_{ads} is negative in all cases, indicating that the adsorption process is thermodynamically favoured. For the adsorption to the outer surface, zCFX

shows a lower ΔG_{ads} value compared to nCFX, while an opposite behavior is observed for the adsorption to the inner surface.

Table 14 ΔG_{ads} (kcal mol^{-1}) for zCFX and nCFX for the adsorption to the outer and inner surface of SW-CNT.

	ΔG_{ads}
zCFX out	-9.5
nCFX out	-3.6
zCFX ins	-12.2
nCFX ins	-20.9

ΔG_{ads} for adsorption of CFX on CNT can be found in literature; Li et al.[91] studied the adsorption of CFX on SW-CNT and calculated ΔG = -8.7 Kcal mol^{-1}, while Ncibi et al.[93] optimized the removal of CFX from aqueous solutions using CNT. The adsorption experiments were conducted at pH from 3 to 11 and reported a ΔG of -9.2 Kcal mol^{-1}. Moreover, in both the experiments no chemical systems (such as surfactants) were used to prevent the agglomeration of nanotubes,[122] because they could affect the CFX adsorption process. The data reported in the literature are in good agreement with those calculated by us for the adsorption of zCFX which, by the way, is the most abundant form in water. Indeed, the mole fractions of the zCFX and nCFX species reach the maximum values at the isoelectric point (pH 7), and zCFX is the most stable species,[26,27] as it seems to interact more strongly with water. In order to better understand this phenomena, a calculation of the hydration energy (E_{hyd}) for the single antibiotic (both forms of CFX in water without the CNT) was carried out. E_{hyd} is -104.9 kcal mol^{-1} for zCFX and -36.2 kcal mol^{-1} for nCFX, indicating that zCFX interacts more strongly with water compared to nCFX. The results could also explain the change in the behavior for the adsorption on the inner and outer surfaces. The spatial distribution function (SDF, Figure 32) calculated between water and CFX showed that water distributions around zCFX and nCFX are similar when the molecules are absorbed to the outer surface, although there seems to be a slightly greater density around zCFX (Figure 32a and 32c). Instead, in the case of the absorption to the inner surface a drastic change in water density around the CFX molecules is observed (Figure 32b and 32d); an increase in water density was observed for zCFX, while for nCFX density decreases. This behavior may be related to the fact that the nanotubes in which water molecules are placed constitute a hydrophobic environment, so the

molecules will tend to interact more with zCFX, which has a more negative E_{hyd} in respect to nCFX, leading to a possible decrease in the interaction between zCFX and the SW-CNT wall. Moreover, in a realistic situation; the molecules could experience difficulties in adsorption to the inert surface of CNT, due to the aggregation that such systems have when used in water.[90]

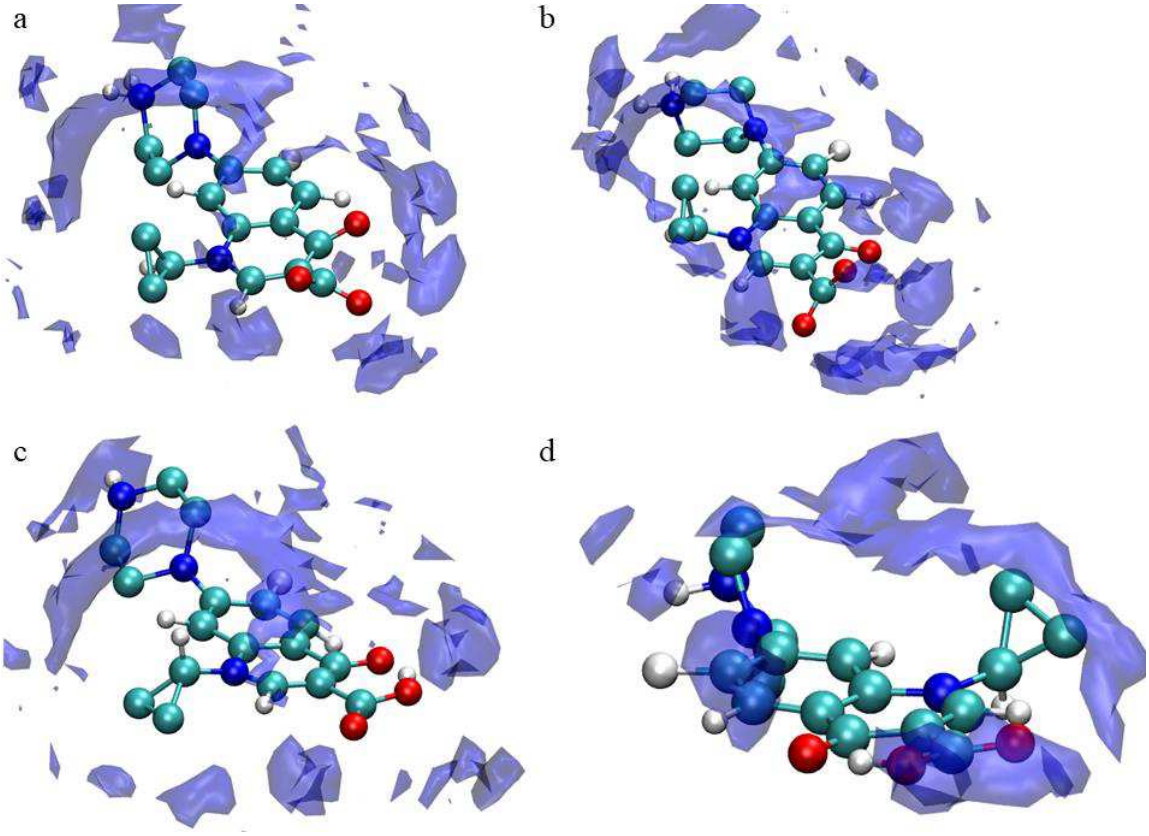

Figure 32 Spatial distribution function (SDF), calculated between water and a) zCFX adsorbed to the outer surface, b) zCFX adsorbed to the inner surface, c) nCFX adsorbed to the outer surface and d) nCFX adsorbed to the inner surface. Isovalue 14.

4.3.8 Conclusions

MD simulations were carried out to investigate the adsorption of both neutral and zwitterionic form of CFX on SW-CNT in vacuum and water. The trajectory analysis and the calculation of r_m *vs.* time curve show that CFX remains adsorbed to the surface of SW-CNT both in vacuum and in water thanks to π-π interactions. The calculated E_{int} and $E_{int\text{-}relax}$ in vacuum are negative, and in general CFX molecules interact more strongly with the inner surface than with the outer surface; the calculation of the LJ_{int} potential gave values similar to those obtained for E_{int}. However, a change in SW-CNT-CFX morphology was

observed after the solvent was added; CFX molecules tend to form less H-bonds between themselves than with water, leading to a dispersion of the molecules on the SW-CNT surface. Finally, using COM pulling and umbrella sampling technique, we calculated ΔG_{ads} for zCFX and nCFX for the adsorption to the outer and inner surface of SW-CNT, finding out that adsorption is thermodynamically favoured and CFX molecules seem to interact more strongly with the inner surface than with the outer surface of SW-CNT. zCFX has a lower ΔG_{ads} than nCFX on the outer surface. An opposite behaviour was observed for adsorption to the inner surface. The calculated ΔG_{ads} for the adsorption of zCFX on the outer surface appears to be in good agreement with the data reported in the literature. Indeed, in a real situation the CFX molecules could experience difficulties in adsorption to the inert surface of CNT, due to the aggregation that such systems have when they are used in water solution.

4.4 References

[1] P. C. Appelbaum, P. a. Hunter, *Int. J. Antimicrob. Agents* **2000**, *16*, 5–15.

[2] P. Ball, *J. Antimicrob. Chemother.* **2000**, *46*, 17–24.

[3] J. M. Blondeau, *Surv. Ophthalmol.* **2004**, *49*, S73–S78.

[4] M. Martinez, P. McDermott, R. Walker, *Vet. J.* **2006**, *172*, 10–28.

[5] J. M. Beale, J. H. Block, in *Wilson Gisvold's Textb. Org. Med. Pharm. Chem.*, **2011**, pp. 206–214.

[6] A. Rusu, G. Hancu, V. Uivaros, *Environ. Chem. Lett.* **2015**, *13*, 21–36.

[7] A. Fàbrega, S. Madurga, E. Giralt, J. Vila, *Microb. Biotechnol.* **2009**, *2*, 40–61.

[8] K. J. Aldred, R. J. Kerns, N. Osheroff, *Biochemistry* **2014**, *53*, 1565–1574.

[9] C. Levine, H. Hiasa, K. J. Marians, *Biochim. Biophys. Acta* **1998**, *1400*, 29–43.

[10] J. J. Champoux, *Annu. Rev. Biochem.* **2001**, *70*, 369–413.

[11] Y. Pommier, E. Leo, H. Zhang, C. Marchand, *Chem. Biol.* **2010**, *17*, 421–433.

[12] E. L. Zechiedrich, A. B. Khodursky, S. Bachellier, R. Schneider, D. Chen, D. M. J. Lilley, N. R. Cozzarelli, *J. Biol. Chem.* **2000**, *275*, 8103–8113.

[13] R. W. Deibler, S. Rahmati, L. E. Zechiedrich, *Genes Dev.* **2001**, *15*, 748–761.

[14] D. C. Hooper, *Clin. Infect. Dis.* **2001**, *32 Suppl 1*, S9–S15.

[15] V. Anderson, N. Osheroff, *Curr. Pharm. Des.* **2001**, *7*, 339–355.

[16] L. A. Mitscher, *Chem. Rev.* **2005**, *105*, 559–592.

[17] K. Drlica, H. Hiasa, R. Kerns, M. Malik, A. Mustaev, X. Zhao, *Curr. Top. Med. Chem.* **2009**, *9*, 981–998.

[18] D. M. Livermore, R. Hope, R. Reynolds, R. Blackburn, A. P. Johnson, N. Woodford, *J. Antimicrob. Chemother.* **2013**, *68*, 2667–2674.

[19] L. S. Redgrave, S. B. Sutton, M. A. Webber, L. J. V Piddock, *Trends Microbiol.* **2014**, *22*, 438–445.

[20] J. Sun, S. Sakai, Y. Tauchi, Y. Deguchi, J. Chen, R. Zhang, K. Morimoto, *Eur. J. Pharm. Biopharm.* **2002**, *54*, 51–58.

[21] S. Lemaire, P. M. Tulkens, F. Van Bambeke, *Antimicrob. Agents Chemother.* **2011**, *55*, 649–658.

[22] D. L. Ross, C. M. Riley, *Int. J. Pharm.* **1990**, *63*, 237–250.

[23] J. Barbosa, R. Bergés, V. Sanz-Nebot, *J. Chromatogr. A* **1998**, *823*, 411–422.

[24] H.-R. Park, C.-H. Oh, H.-C. Lee, J.-K. Lee, K. Yang, K.-M. Bark, *Photochem. Photobiol.* **2002**, *75*, 237–248.

[25] K. A. K. Musa, L. a. Eriksson, *J. Phys. Chem. A* **2009**, *113*, 10803–10810.

[26] A. Rusu, G. Tóth, L. Szocs, J. Kökösi, M. Kraszni, Á. Gyéresi, B. Noszál, *J. Pharm. Biomed. Anal.* **2012**, *66*, 50–57.

[27] G. Volgyi, G. Vizseralek, K. Takacs-Novak, A. Avdeef, K. Y. Tam, *Eur. J. Pharm. Sci.* **2012**, *47*, 21–27.

[28] J. Tomasi, B. Menucci, R. Cammi, *Chem. Rev.* **2005**, *8*, 2999–3093.

[29] G. P. Vitorino, G. D. Barrera, M. R. Mazzieri, R. C. Binning, D. E. Bacelo, *Chem. Phys. Lett.* **2006**, *432*,

538–544.

[30] S. Chalmet, W. Harb, M. F. Ruiz-Lopez, *J. Phys. Chem. A.* **2001**, *105*, 11574–11581.

[31] P. Nagy, K. Takács-Novák, *Phys. Chem. Chem. Phys.* **2004**, *6*, 2838–2848.

[32] A. Lambert, J. B. Regnouf-de-Vains, M. F. Ruiz-López, *Chem. Phys. Lett.* **2007**, *442*, 281–284.

[33] C. E. Lin, Y. J. Deng, W. S. Liao, S. W. Sun, W. Y. Lin, C. C. Chen, *J. Chromatogr. A* **2004**, *1051*, 283–290.

[34] A. V. Gerasimenko, E. T. Karaseva, A. V. Polishchuk, *Acta Crystallogr. Sect. E Struct. Reports Online* **2008**, *64*, m378.

[35] A. V. Polishchuk, A. V. Gerasimenko, K. A. Gayvoronskaya, E. T. Karaseva, *Acta Crystallogr. Sect. E Struct. Reports Online* **2008**, *64*, m931–m932.

[36] P. C. Sharma, A. Jain, S. Jain, R. Pahwa, M. S. Yar, *J. Enzyme Inhib. Med. Chem.* **2010**, *25*, 577–589.

[37] World Health Organization, *The Selection and Use of Essential Medicines 2017*, **2017**.

[38] C. Herold, M. Ocker, M. Ganslmayer, H. Gerauer, E. G. Hahn, D. Schuppan, *Br. J. Cancer* **2002**, *86*, 443–448.

[39] O. Aranha, R. Grignon, N. Fernandes, T. J. McDonnell, D. P. Wood Jr., F. H. Sarkar, *Int J Oncol* **2003**, *22*, 787–794.

[40] A. C. Pinto, J. N. Moreira, S. Simões, *Cancer Chemother. Pharmacol.* **2009**, *64*, 445–454.

[41] L. A. Bourikas, G. Kolios, V. Valatas, G. Notas, I. Drygiannakis, I. Pelagiadis, P. Manousou, S. Klironomos, I. A. Mouzas, E. Kouroumalis, *Br. J. Pharmacol.* **2009**, *157*, 362–370.

[42] M. James, T. Murtola, R. Schulz, J. C. Smith, B. Hess, E. Lindahl, *SoftwareX* **2015**, *1–2*, 19–25.

[43] N. Schmid, A. P. Eichenberger, A. Choutko, S. Riniker, M. Winger, A. E. Mark, W. F. Van Gunsteren, *Eur Biophys J* **2011**, *40*, 843–856.

[44] K. B. Koziara, M. Stroet, A. K. Malde, A. E. Mark, *J. Comput. Aided. Mol. Des.* **2014**, *28*, 221–233.

[45] P. G. Kusalik, M. Svishchev, *Science (80-.).* **1994**, *265*, 1219–1221.

[46] A. K. Malde, L. Zuo, M. Breeze, M. Stroet, D. Poger, P. C. Nair, C. Oostenbrink, A. E. Mark, *J. Chem. Theory Comput.* **2011**, *7*, 4026–4037.

[47] T. Darden, D. York, L. Pedersen, T. Darden, D. York, L. Pedersen, *J. Chem. Phys.* **1993**, *89*, 10089–10092.

[48] U. Essmann, L. Perera, M. L. Berkowitz, T. Darden, H. Lee, U. Essmann, L. Perera, M. L. Berkowitz, T. Darden, H. Lee, et al., *J. Chem. Phys.* **1995**, *103*, 8577–8593.

[49] B. Hess, H. Bekker, H. J. C. Berendsen, J. G. E. M. Fraaije, *J. Comput. Chem.* **1997**, *18*, 1463–1472.

[50] H. J. C. Berendsen, J. P. M. Postma, W. F. Van Gunsteren, A. Dinola, J. R. Haak, H. J. C. Berendsen, J. P. M. Postma, W. F. Van Gunsteren, A. Dinola, J. R. Haak, *J. Chem. Phys.* **1984**, *81*, 3684–3690.

[51] G. Bussi, D. Donadio, M. Parrinello, G. Bussi, D. Donadio, M. Parrinello, *J. Chem. Phys.* **2007**, *126*, 0141011–0141017.

[52] M. Parrinello, A. Rahman, *J. Appl. Phys.* **1981**, *52*, 7182–7190.

[53] M. J. Frisch, G. W. Trucks, H. B. Schlegel, G. E. Scuseria, M. A. Robb, J. R. Cheeseman, G. Scalmani, V. Barone, B. Mennucci, G. A. Petersson, et al., *Gaussian, Inc., Wallingford CT,* **2009**.

[54] A. D. Becke, *J. Chem. Phys.* **1993**, *98*, 1372–1377.

[55] J. Tirado-Rives, W. Jorgensen, *J. Chem. Theory …* **2008**, 297–306.

[56] a. K. Rappe, C. J. Casewit, K. S. Colwell, W. a. Goddard III, W. M. Skiff, *J. Am. Chem. Soc.* **1992**, *114*, 10024–10035.

[57] G. Scalmani, M. J. Frisch, B. Mennucci, J. Tomasi, R. Cammi, V. Barone, *J. Chem. Phys.* **2006**, *124*, DOI 10.1063/1.2173258.

[58] I. Turel, P. Bukovec, M. Quirós, *Int. J. Pharm.* **1997**, *152*, 59–65.

[59] J. Kreutzer, P. Blaha, U. Schubert, *Comput. Theor. Chem.* **2016**, *1084*, 162–168.

[60] I. Turel, A. Golobic, *Anal. Sci.* **2003**, *19*, 329–330.

[61] V. M. Nurchi, G. Crisponi, J. I. Lachowicz, M. Antonietta, M. Peana, S. Medici, D. Veclani, M. Tolazzi, A. Melchior, *Eur. J. Pharm. Sci.* **2016**, *93*, 380–391.

[62] A. Rusu, G. Hancu, V. Uivarosi, *Environ. Chem. Lett.* **2015**, *13*, 21–36.

[63] P. Collignon, J. H. Powers, T. M. Chiller, A. Aidara-Kane, F. M. Aarestrup, *Clin. Infect. Dis.* **2009**, *49*, 132–141.

[64] K. Kümmerer, *Chemosphere* **2009**, *75*, 417–434.

[65] E. Topp, R. Chapman, M. Devers-lamrani, A. Hartmann, R. Marti, F. Martin-, L. Sabourin, A. Scott, M. Sumarah, **2013**, *178*, 173–178.

[66] H. Thi, T. Thuy, L. P. Nga, **2011**, 835–841.

[67] K. Kümmerer, *Pharmaceuticals in the Environment*, Springer-Verlag Berlin Heidelberg, **2004**.

[68] I. Ebert, J. Bachmann, U. Huhnen, A. Kuster, C. Kussatz, D. Maletzki, C. Schluter, *Environ. Toxicol. Chem.* **2011**, *30*, 2786–2792.

[69] A. Albini, S. Monti, *Chem. Soc. Rev.* **2003**, *32*, 238–250.

[70] M. Sturini, A. Speltini, F. Maraschi, A. Profumo, L. Pretali, E. Fasani, A. Albini, *Environ. Sci. Technol.* **2010**, *44*, 4564–4569.

[71] M. Sturini, A. Speltini, F. Maraschi, L. Pretali, A. Profumo, E. Fasani, A. Albini, R. Migliavacca, E. Nucleo, *Water Res.* **2012**, *46*, 5575–5582.

[72] J. Rivera-utrilla, M. Sánchez-polo, M. Á. Ferro-garcía, G. Prados-joya, R. Ocampo-Perez, *Chemosphere* **2013**, *9*, 1268–1287.

[73] I. Gehrke, A. Geiser, A. Somborn-schulz, *Nanotechnol. Sci. Appl.* **2015**, *8*, 1–17.

[74] J. M. Pisciotta, J. J. Dolceamore Jr, *J. Biochem. Technolgy* **2016**, *8*, 327–343.

[75] J. Kammerer, R. Carle, D. R. Kammerer, *J. Agric. Food Chem.* **2011**, *59*, 22–42.

[76] E. Worch, *Adsorption Technology in Water Treatment: Fundamentals, Processes, and Modeling*, De Gruyter, Berlin/Boston, **2012**.

[77] S. Iijima, *Lett. to Nat.* **1991**, *353*, 56–58.

[78] R. Bacon, *J. Appl. Phys.* **1960**, *31*, 283–290.

[79] M. S. Dresselhaus, G. Dresselhaus, J. C. Charlier, E. Hernández, *Philos. Trans. Math. Phys. Eng. Sci.* **2016**, *362*, 2065–2098.

[80] W. Zhang, Z. Zhang, Y. Zhang, *Nanoscale Res. Lett.* **2011**, *6*, 555.

[81] A. Eatemadi, H. Daraee, H. Karimkhanloo, M. Kouhi, N. Zarghami, A. Abolfaz, M. Abasi, Y. Hanifehopour, S. Woo Joo, *Nanoscale Res. Lett.* **2014**, *9*, 393.

[82] P. X. Hou, S. Bai, Q. H. Yang, C. Liu, H. M. Cheng, *Carbon N. Y.* **2002**, *40*, 81–85.

[83] R. Hirlekar, M. Yamagar, H. Garse, M. Vij, V. Kadam, *Asian J. Pharm. Clin. Res.* **2009**, *2*, 17–27.

[84] L. Chico, V. Crespi, L. Benedict, S. Louie, M. Cohen, *Phys. Rev. Lett.* **1996**, *76*, 971–974.

[85] M. José-Yacamán, M. Miki-Yoshida, L. Rendón, J. G. Santiesteban, *Appl. Phys. Lett.* **1993**, *62*, 657–659.

[86] E. Abbasi, S. F. Aval, A. Akbarzadeh, M. Milani, H. T. Nasrabadi, S. Woo joo, Y. Hanifehpour, K. Nejati-Koshki, R. Pashaei-Asl, *Nanoscale Res. Lett.* **2014**, *9*, 247.

[87] M. F. L. De Volder, S. H. Tawfick, R. H. Baughman, A. J. Hart, *Science (80-.).* **2013**, *339*, 535–539.

[88] K. Yang, X. Wang, L. Zhu, B. Xing, *Environ. Sci. Technol.* **2006**, *40*, 5804–5810.

[89] K. Yang, L. Z. Zhu, B. S. Xing, *Environ. Sci. Technol.* **2006**, *40*, 1855–1861.

[90] O. G. Apul, T. Karanfil, *Water Res.* **2015**, *68*, 34–55.

[91] H. Li, D. Zhang, X. Han, B. Xing, *Chemosphere* **2014**, *95*, 150–155.

[92] H. Peng, B. Pan, M. Wu, Y. Liu, D. Zhang, B. Xing, *J. Hazard. Mater.* **2012**, *233–234*, 89–96.

[93] M. C. Ncibi, M. Sillanpää, *J. Hazard. Mater.* **2015**, *298*, 102–110.

[94] L. K. Boateng, J. Heo, J. R. V Flora, Y. Park, Y. Yoon, *Sep. Purif. Technol.* **2013**, *116*, 471–478.

[95] J. Chen, X. Wang, C. Dai, S. Chen, Y. Tu, *Phys. E Low-dimensional Syst. Nanostructures* **2014**, *62*, 59–63.

[96] F. J. A. L. Cruz, J. J. de Pablo, J. P. B. Mota, *RSC Adv.* **2014**, *4*, 1310–1321.

[97] T. Panczyk, P. Wolki, A. Jagusiak, M. Drach, *RSC Adv.* **2014**, *4*, 47304–47312.

[98] B. Yu, S. Fu, Z. Wu, H. Bai, N. Ning, Q. Fu, *Compos. Part A* **2015**, *73*, 155–165.

[99] D. Zhao, C. Peng, J. Zhou, *Phys. Chem. Chem. Phys.* **2015**, *17*, 840–850.

[100] J. Comer, R. Chen, H. Poblete, A. Vergara-jaque, J. E. Riviere, *ACS Nano* **2015**, *9*, 11761–11774.

[101] Z. Li, T. Tozer, L. Alisaraie, *J. Phys. Chem. C* **2016**, *120*, 4061–4070.

[102] L. Cai, W. Lv, H. Zhu, Q. Xu, *Phys. E Low-dimensional Syst. Nanostructures* **2016**, *81*, 226–234.

[103] D. Roccatano, E. Sarukhanyan, R. Zangi, *J. Chem. Phys.* **2017**, *146*, 74703.

[104] E. Mehrjouei, H. Akbarzadeh, A. N. Shamkhali, M. Abbaspour, S. Salemi, P. Abdi, *Mol. Pharm.* **2017**, *14*, 2273–2284.

[105] Z. Hasanzade, H. Raissi, *J. Mol. Model.* **2017**, *23*, 36.

[106] X. Peng, F. L. Y. Lam, Y. Wang, Z. Liu, *J. Colloid Interface Sci.* **2015**, *460*, 349–360.

[107] Y. Patiño, E. Díaz, S. Ordóñez, *Chemosphere* **2015**, *119*, S124–S130.

[108] X. Zhu, D. C. W. Tsang, F. Chen, S. Li, X. Yang, *Environ. Technol.* **2015**, *36*, 3094–3102.

[109] H. Peng, B. Pan, M. Wu, R. Liu, D. Zhang, D. Wu, B. Xing, *J. Hazard. Mater.* **2012**, *212*, 342–348.

[110] Y. Patiño, E. Díaz, S. Ordóñez, E. Gallegos-suarez, A. Guerrero-ruiz, *Chemosphere* **2015**, *136*, 174–180.

[111] F. Yu, S. Sun, S. Han, J. Zheng, J. Ma, *Chem. Eng. J.* **2016**, *285*, 588–595.

[112] V. V Chaban, T. I. Savchenko, S. M. Kovalenko, O. V Prezhdo, *J. Phys. Chem. B* **2010**, *114*, 13481–

13486.

[113] J. Kastner, *Adv. Rev.* **2011**, *1*, 932–942.

[114] W. Humphrey, A. Dalke, K. Schulten, *J. Mol. Graph.* **1996**, *14*, 33–38.

[115] U. C. Singh, P. A. Kollman, *J. Comput. Chem.* **1984**, *5*, 129–145.

[116] Q. Sun, H. Xie, J. Chen, X. Li, Z. Wang, L. Sheng, *Chemosphere* **2013**, *92*, 429–434.

[117] K. Johannes, *Adv. Rev.* **2011**, *1*, 932–942.

[118] G. Bussi, D. Donadio, M. Parrinello, *J. Chem. Phys.* **2007**, *126*, 0141011–0141017.

[119] J. S. Hub, B. L. De Groot, D. Van Der Spoel, *J. Chem. Theory Comput.* **2010**, *6*, 3713–3720.

[120] O. Cramariuc, T. Rog, M. Javanainen, L. Monticelli, A. V. Polishchuk, I. Vattulainen, *Biochim. Biophys. Acta - Biomembr.* **2012**, *1818*, 2563–2571.

[121] T. A. Hilder, J. M. Hill, *Micro Nano Lett.* **2008**, 41–49.

[122] R. Atif, F. Inam, *Beilstein J. Nanotechnol.* **2016**, *7*, 1174–1196.

Final Remarks

In this thesis, computational methods (the quantum mechanics method and molecular dynamics simulations in particular) were used to study the reactivity of two classes of compounds and their interaction with carbon-based materials; the two classes are platinum-based antitumor drugs (chapter 3) and fluoroquinolones antimicrobials compounds (chapter 4).

The first part of chapter 3 focuses on the hydrolysis reaction of *cis*-[$Pt(PMe_3)_2$(etga)], cis-[$Pt(PMe_3)_2$(3-Hfl)]$^+$ containing ethyl gallate (etga) and 3-Hydroxyflavone(3-HFl), designed to try to limit the side effects of cisplatin, studied by means of density functional theory (DFT) calculations. The calculations showed that:

- The rate determining step is the first step of the hydrolysis reaction and that the formation of the hydroxo species is observed in both complexes.

- The activation energies are significantly lower than those calculated for cisplatin.

- High hydrolysis reaction rate that might make such complexes subject to fast degradation, causing potentially poor pharmacological activity.

In the second part of chapter 3 the complete mechanism of action (hydrolysis reaction, reaction with DNA bases and reaction with cysteine) of phenanthriplatin, a monofunctional platinum complex, was studied by means of DFT calculations. Moreover, a comparison between phenanthriplatin and cisplatin was made with the aim of understanding why phenanthriplatin presents a higher cytotoxicity activity compared to cisplatin. The calculations showed that:

- The hydrolysis reaction showed that phenanthriplatin's activation energy barrier is close to the energy barriers obtained for the first hydrolysis of cisplatin.

- Phenanthriplatin reacts with both guanine and adenine bases; with the latter, the formation of two products, N7 and N1, occurs, and the reaction rate follows the order N7-guanine > N7-adenine > N1-adenine.

- The reaction with guanine is kinetically favoured in phenanthriplatin in respect to cisplatin.

- The reaction between phenanthriplatin and cysteine showed that such reaction is disadvantageous, both kinetically and thermodynamically, in phenanthriplatin in respect to cisplatin.

- This can explain why phenanthriplatin is more cytotoxic than cisplatin.

In the last part of chapter 3 the non-covalent interaction between graphene prototypes, new candidates as drugs delivery systems, and cisplatin were investigated through MP2 and DFT calculation:

- Different orientations of cisplatin in respect to the circumcoronene (one parallel and three perpendicular) were taken into account.

- Different DFT functional were tested and compared with the interaction energy obtained from MP2 calculations.

- The best DFT functional is M62X-D3, which was used to obtain the energy profiles.

- The parallel orientation presents the highest value of interaction energy in vacuum.

- The density of states (DOS) analysis showed that when cisplatin is adsorbed with perpendicular orientations a destabilization of the circumcoronene electronic structure is observed.

- Finally, the introduction of the solvent does not drastically change the interaction energy profiles between cisplatin and circumcoronene.

- Favourable adsorption of cisplatin on graphene can be predicted.

As regards the fluoroquinolones (FQs) antimicrobials compounds, in the first part of chapter 4 the relative stability and photochemical behaviour of the different protonation states of CFX in gas phase and in water was studied by means of molecular dynamics simulations and DFT calculations. The calculations showed that:

- The predominance of the zwitterionic form in water in respect to the neutral form, thanks to the introduction of a discrete-continuum approach.

- The result was further confirmed through the calculated absorption UV-Vis spectra.

- Finally, the protonation sequence was confirmed through the comparison with the crystalline structures found in the literature, through the calculation of the relative stability for such species and the calculated absorption UV-Vis spectra.

In the last part of chapter 4 the adsorption of both neutral and zwitterionic forms of CFX to the inner and outer surface of carbon nano-tubes (CNTs) in vacuum and in water was studied through molecular dynamics simulations. The simulation results showed that:

- CFX remains adsorbed to the surface of CNT both in vacuum and in water thanks to π-π interactions.

- Change in CNT-CFX morphology was observed after the solvent was added; CFX molecules tend to form fewer hydrogen bonds between themselves and more with water, leading to a dispersion of the molecules on the CNT surface.

- The adsorption Gibbs free energy (ΔG_{ads}) were carried out for the adsorbed zCFX and nCFX using the umbrella sampling technique, finding out that adsorption is thermodynamically favoured.

- CFX molecules seem to interact more strongly with the inner surface than with the outer surface of CNT.

- ΔG_{ads} values are in good agreement with the data reported in the literature.

In conclusion, the use of computational chemistry can help to rationalize the experimental data and to investigate various mechanicistic hypothesis.

Appendix A

3.2 Hydrolysis Reaction in Triphenylphosphane Pt(II) Complexes Containing Biologically Active Natural Polyphenols: DFT Study.

Table A1 Relevant bond distances (Å) and angles (°) in first step of the hydrolysis in *cis*-[Pt(PMe_3)$_2$(etga)]. O(L) is the leaving oxygen of the ligand . P(c) is phosphorus in *cis* to leaving group. P(t) is phosphorus in *trans* to leaving group. O(ent.) is entering water oxygen.

Bond Distances									
O1 path	**R1**	**RA1**	**TS1**	**PA1**	**O2 path**	**R1**	**RA1**	**TS1**	**PA1**
Pt-O	2.033	2.034	2.029	2.064	Pt-O(L)	2.033	2.041	2.458	3.122
Pt-O(L)	2.041	2.055	2.459	3.230	Pt-O	2.041	2.048	2.055	2.068
Pt-P(t)	2.256	2.251	2.213	2.261	Pt-P(t)	2.256	2.253	2.214	2.264
Pt-P(c)	2.256	2.268	2.272	2.259	Pt-P(c)	2.256	2.265	2.258	2.257
Pt-O(ent.)	-	3.714	2.332	2.056	Pt-O(ent.)	-	3.859	2.335	2.053
Angles									
O1 path	**R1**	**RA1**	**TS1**	**PA1**	**O2 path**	**R1**	**RA1**	**TS1**	**PA1**
O(ent.)-Pt-P	-	137	164	171	O(ent.)-Pt-P	-	140	162	173
O(L)-Pt-P(t)	167	170	129	119	O(L)-Pt-P(t)	173	172	130	113
O(L)-Pt-P(c)	90	90	97	111	O(L)-Pt-P(c)	83	89	98	108

Table A2 Relevant bond distances (Å) and angles (°) in second step of the hydrolysis in *cis*-Pt(PMe_3)$_2$(etga). O(L) is the oxygen of the leaving ligand. P(c) is phosphorus in *cis* to leaving group. P(t) is phosphorus in *trans* to leaving group. Ow is the coordinated water oxygen and O(ent.) is entering water oxygen.

Bond Distances											
O1 path	**R2**	**RA2**	**TS2**	**PA2**	**P2**	**O2 path**	**R2**	**RA2**	**TS2**	**PA2**	**P2**
Pt-O(L)	2.064	2.076	2.452	3.492	-	Pt-O(L)	2.068	2.079	2.468	3.635	-
Pt-Ow	2.056	2.058	2.034	2.043	2.042	Pt-Ow	2.053	2.057	2.032	2.048	2.042
Pt-P(t)	2.259	2.256	2.213	2.262	2.255	Pt-P(t)	2.257	2.256	2.213	2.264	2.257
Pt-P(c)	2.261	2.270	2.278	2.264	2.257	Pt-P(c)	2.264	2.267	2.282	2.264	2.255
Pt-O(ent.)	-	3.973	2.406	2.072	2.042	Pt-O(ent.)	-	3.829	2.412	2.071	2.042
Angles											
O1 path	**R2**	**RA2**	**TS2**	**PA2**	**P2**	**O2 path**	**R2**	**RA2**	**TS2**	**PA2**	**P2**
O(ent.)-Pt-P	-	140	149	173	171	O(ent.)-Pt-P	-	140	147	172	171
O(L)-Pt-P(t)	166	164	138	124	-	O(L)-Pt-P(t)	164	164	140	128	-
O(L)-Pt-P(c)	86	84	96	112	-	O(L)-Pt-P(c)	92	93	95	111	-

Table A3 Energy values (kcal mol^{-1}) associated to the hydrolysis reaction pathway for *cis*-[$Pt(PMe_3)_2$(etga)], *cis*-[$Pt(PMe_3)_2$(3-Hfl)], *cis*-[$Pt(Cl)_2(PMe_3)_2$] and cisplatin, in PCM water.

First step	**R1 → RA1**	**RA1 → TS1**	**TS1 → PA1**	**PA1 → P1**
cis-$Pt(PMe_3)_2$(etga) O1	–1.9	22.8	10.7	–
cis-$Pt(PMe_3)_2$(etga) O2	–3.0	18.7	7.1	–
cis-$[Pt(PMe_3)_2(3\text{-Hfl})]^+$ O1	1.6	14.4	7.4	–
cis-$[Pt(PMe_3)_2(3\text{-Hfl})]^+$ O2	–0.9	15.7	9.1	–
cis-$Pt(Cl)_2(PMe_3)_2$	0.2	11.3	1.8	7.2
Cisplatin	–1.8	21.4	2.4	12.1
Second step	**R2 → RA2**	**RA2→ TS2**	**TS2 → PA2**	**PA2 → P2**
cis-$Pt(PMe_3)_2$(etga) O1	–2.5	15.1	0.7	14.1
cis-$Pt(PMe_3)_2$(etga) O2	–3.1	14.7	0.4	14
cis-$[Pt(PMe_3)_2(3\text{-Hfl})]^+$ O1	0.7	11.9	–1.1	2.3
cis-$[Pt(PMe_3)_2(3\text{-Hfl})]^+$ O2	0.7	9.5	–2.9	0.6
cis-$Pt(Cl)_2(PMe_3)_2$	–4.5	12.9	3.0	16.2
cisplatin	–6.5	21.1	4.8	17.5

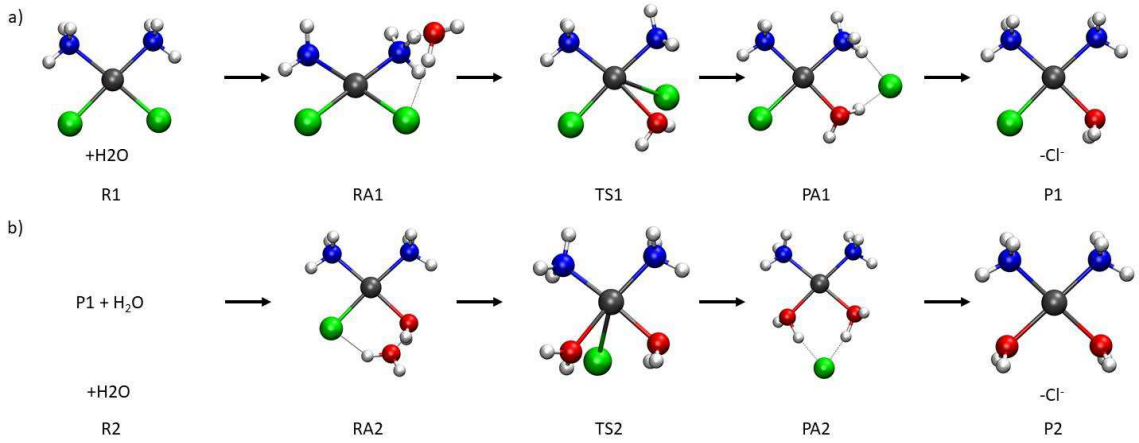

Figure A1 DFT calculated structures of: a) first hydrolysis of cisplatin; b) second hydrolysis. Relevant bond distances and angles are reported in Table A4.

Table A4 Relevant bond distances (Å) and angles (°) in cisplatin. N(c) is nitrogen in *cis* to leaving group. N(t) is nitrogen in trans to leaving group. Ow is the coordinated water oxygen and O(ent.) is the entering water oxygen.

Bond Distances											
First hydrolysis	**R1**	**RA1**	**TS1**	**PA1**	**P1**	Second hydrolysis	**R2**	**RA2**	**TS2**	**PA2**	**P2**
Pt-Cl	2.308	2.314	2.316	2.314	2.284	Pt-Ow	2.101	2.075	2.083	2.055	2.102
Pt-Cl(l)	2.308	2.322	2.747	3.901	-	Pt-Cl(l)	2.284	2.299	2.722	3.770	-
Pt-N(t)	2.089	2.078	2.063	2.047	2.030	Pt-N(t)	2.103	2.091	2.067	2.057	2.033
Pt-N(c)	2.089	2.087	2.073	2.077	2.103	Pt-N(c)	2.030	2.041	2.029	2.056	2.033
Pt-O(ent.)	-	3.695	2.389	2.049	2.101	Pt-O(ent.)	-	3.592	2.327	2.055	2.103
Angles											
	R1	**RA1**	**TS1**	**PA1**	**P1**		**R2**	**RA2**	**TS2**	**PA2**	**P2**
O(ent.)-Pt-N	-	122	151	176	176	O(ent.)-Pt-N	-	113	160	177	179
Cl(l)-Pt-N(t)	178	178	140	137	-	Cl(l)-Pt-N(t)	176	176	130	131	-
Cl(l)-Pt-N(c)	84	85	76	51	-	Cl(l)-Pt-N(c)	87	87	101	131	-

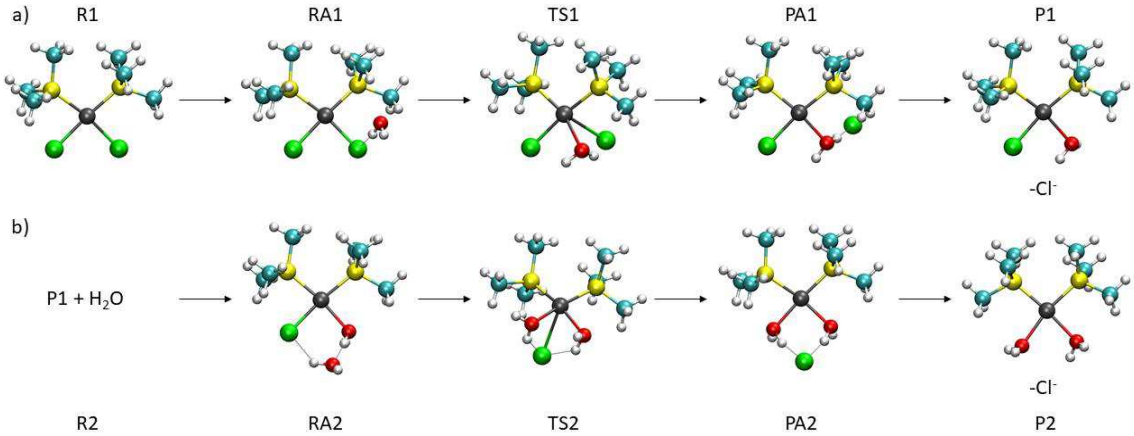

Figure A2 DFT calculated structures of: a) the first hydrolysis of *cis*-$Pt(PMe_3)_2(Cl)_2$; b) second hydrolysis of *cis*-$Pt(PMe_3)_2(Cl)_2$. Relevant bond distances and angles are reported in Table A5.

Table A5 Relevant bond distances (Å) and angles (°) in *cis*-$[Pt(Cl)_2(PMe_3)_2]$. P(c) is phosphorus in *cis* to leaving group. P(t) is phosphorus in trans to leaving group. Ow is the coordinated water and O(ent.) is the entering water oxygen.

Bond Distances											
First hydrolysis	**R1**	**RA1**	**TS1**	**PA1**	**P1**	Second hydrolysis	**R2**	**RA2**	**TS2**	**PA2**	**P2**
Pt-Cl	2.381	2.383	2.389	2.378	2.358	Pt-Ow	2.210	2.172	2.185	2.143	2.207
Pt-Cl(L)	2.359	2.375	2.766	3.852	-	Pt-Cl(L)	2.358	2.372	2.853	3.657	-
Pt-P(t)	2.278	2.272	2.226	2.250	2.251	Pt-P(t)	2.288	2.287	2.247	2.267	2.275
Pt-P(c)	2.268	2.277	2.266	2.282	2.288	Pt-P(c)	2.251	2.261	2.247	2.267	2.272
Pt-O(ent.)	-	3.817	2.383	2.114	2.210	Pt-O(ent.)	-	3.863	2.265	2.151	2.229
Angles											
	R1	**RA1**	**TS1**	**PA1**	**P1**		**R2**	**RA2**	**TS2**	**PA2**	**P2**
O(ent.)-Pt-P	-	124	155	170	168	O(ent.)-Pt-P	-	113	168	177	174
Cl(L)-Pt-P(t)	170	170	132	132	-	Cl(L)-Pt-P(t)	176	176	122	134	-
Cl(L)-Pt-P(c)	88	89	82	70	-	Cl(L)-Pt-P(c)	84	84	105	127	-

Table A6 Relevant bond distances (Å) and angles (°) in first step of the hydrolysis in *cis*-[Pt(PMe_3)$_2$(3-Hfl)]. O(L) is the oxygen of the leaving ligand. P(c) is phosphorus in *cis* to leaving group. P(t) is phosphorus in *trans* to leaving group. O(ent.) is the entering water oxygen.

Bond Distances									
O1 path	**R1**	**RA1**	**TS1**	**PA1**	**O2 path**	**R1**	**RA1**	**TS1**	**PA1**
Pt-O	2.059	2.069	2.064	2.070	Pt-O(L)	2.059	2.077	2.499	3.149
Pt-O(L)	2.079	2.090	2.468	3.166	Pt-O	2.079	2.087	2.090	2.112
Pt-P(t)	2.258	2.255	2.221	2.250	Pt-P(t)	2.265	2.261	2.227	2.278
Pt-P(c)	2.265	2.271	2.268	2.277	Pt-P(c)	2.258	2.266	2.260	2.252
Pt-O(ent.)	-	3.570	2.422	2.151	Pt-O(ent.)	-	3.743	2.342	2.059
Angles									
O1 path	**R1**	**RA1**	**TS1**	**PA1**	**O2 path**	**R1**	**RA1**	**TS1**	**PA1**
O(ent.)-Pt-P	-	121	1556	175	O(ent.)-Pt-P	-	136	161	176
O(L)-Pt-P(t)	171	168	136	125	O(L)-Pt-P(t)	171	170	135	122
O(L)-Pt-P(c)	91	92	100	113	O(L)-Pt-P(c)	90	93	102	113

Table A7 Relevant bond distances (Å) and angles (°) in second step of the hydrolysis in *cis*-[Pt(PMe3)2(3-Hfl)]. O(L) is the oxygen of the leaving ligand. P(c) is phosphorus in cis to leaving group. P(t) is phosphorus in trans to leaving group. Ow is the coordinated water oxygen and O(ent.) is the entering water oxygen.

Bond Distances											
O1 path	**R2**	**RA2**	**TS2**	**PA2**	**P2**	**O2 path**	**R2**	**RA2**	**TS2**	**PA2**	**P2**
Pt-O(L)	2.070	2.094	2.540	3.812	-	Pt-O(L)	2.112	2.135	2.254	3.863	-
Pt-Ow	2.151	2.159	2.115	2.134	2.182	Pt-Ow	2.059	2.066	2.052	2.050	2.029
Pt-P(t)	2.277	2.271	2.232	2.283	2.287	Pt-P(t)	2.252	2.249	2.223	2.251	2.240
Pt-P(c)	2.250	2.253	2.253	2.250	2.240	Pt-P(c)	2.278	2.283	2.278	2.281	2.287
Pt-O(ent.)	-	3.354	2.349	2.049	2.029	Pt-O(ent.)	-	3.565	2.522	2.149	2.182
Angles											
O1 path	**R2**	**RA2**	**TS2**	**PA2**	**P2**	**O2 path**	**R2**	**RA2**	**TS2**	**PA2**	**P2**
O(ent.)-Pt-P	-	123	152	172	168	O(ent.)-Pt-P	-	126	147	167	165
O(L)-Pt-P(t)	165	165	139	132	-	O(L)-Pt-P(t)	168	168	147	130	-
O(L)-Pt-P(c)	93	94	87	126	-	O(L)-Pt-P(c)	90	90	95	128	-

3.3 Phenanthriplatin, an Unconventional Platinum Drug: Disentangling the Hydrolysis and DNA-binding Mechanisms by Theoretical Calculations.

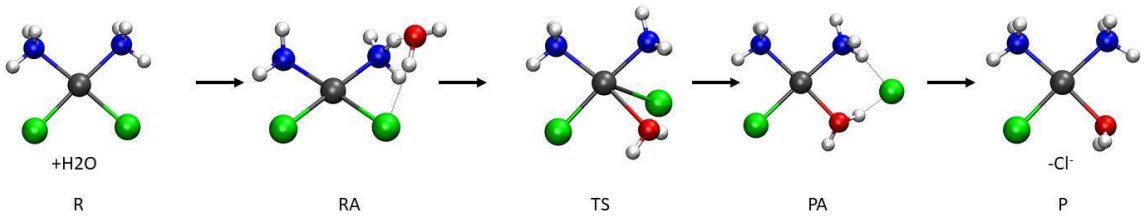

Figure A3 Optimized structures for first step of the hydrolysis reaction of cisplatin.

Table A8 Relevant bond distances (Å) and angles (°) for optimized isomer P of phenanthriplatin, O(ent.) is entering water oxygen.

Bond Distances					
Isomer P	**R**	**RA**	**TS**	**PA**	**P**
Pt-Cl	2.308	2.321	2.781	3.164	-
Pt-N1	2.105	2.095	2.093	2.102	2.122
Pt-N2	2.062	2.067	2.061	2.063	2.053
Pt-N3	2.145	2.134	2.114	2.081	2.062
Pt-O(ent.)	-	3.562	2.302	2.100	2.132
Angles					
Isomer P	**R**	**RA**	**TS**	**PA**	**P**
Cl-Pt-N1	85.44	86.45	78.50	72.06	-
Cl-Pt-N2	89.82	89.94	95.18	98.25	-
Cl-Pt-N3	178.72	179.05	128.54	116.78	-
O(ent.)-Pt-N1	-	52.14	83.12	82.21	86.26
O(ent.)-Pt-N2	-	126.24	92.89	92.52	90.83
O(ent.)-Pt-N3	-	118.46	162.23	177.02	178.38

Table A9 Relevant bond distances (Å) and angles (°) for optimized isomer M of phenanthriplatin, O(ent.) is entering water oxygen.

Bond Distances					
Isomer M	**R**	**RA**	**TS**	**PA**	**P**
Pt-Cl	2.308	2.323	2.796	3.438	-
Pt-N1	2.105	2.097	2.090	2.094	2.122
Pt-N2	2.062	2.068	2.060	2.069	2.054
Pt-N3	2.145	2.133	2.113	2.082	2.063
Pt-O(ent.)	-	3.604	2.318	2.081	2.134
Angles					
Isomer M	**R**	**RA**	**TS**	**PA**	**P**
Cl-Pt-N1	85.28	86.65	76.46	62.42	-
Cl-Pt-N2	90.05	89.55	101.11	113.73	-
Cl-Pt-N3	179.12	178.95	128.50	122.55	-
O(ent.)-Pt-N1	-	50.99	82.39	83.44	85.97
O(ent.)-Pt-N2	-	125.09	93.76	92.36	91.73
O(ent.)-Pt-N3	-	119.16	162.81	177.00	179.20

Table A10 Relevant bond distances (Å) and angles (°) for the first step of the hydrolysis of cisplatin, O(ent.) is entering water oxygen, Cl1(l) is the leaving Cl atom (see Figure A4).

Bond Distances					
first step	**R**	**RA**	**TS**	**PA**	**P**
Pt-Cl1(L)	2.326	2.340	2.791	3.885	-
Pt-N1	2.123	2.119	2.104	2.106	2.136
Pt-N2	2.123	2.111	2.099	2.071	2.054
Pt-Cl2	2.326	2.330	2.329	2.330	2.299
Pt-O(ent.)	-	3.604	2.395	2.075	-
Angles					
first step	**R**	**RA**	**TS**	**PA**	**P**
Cl1(L)-Pt-N1	83.36	85.11	75.21	51.69	-
Cl1(L)-Pt-N2	177.90	177.66	137.37	136.66	-
Cl1(L)-Pt-Cl2	94.54	94.06	102.30	126.22	-
O(ent.)-Pt-N1	-	51.83	86.88	87.67	87.43
O(ent.)-Pt-N2	-	120.79	154.36	176.80	176.03
O(ent.)-Pt-Cl2	-	127.50	89.23	90.40	89.11

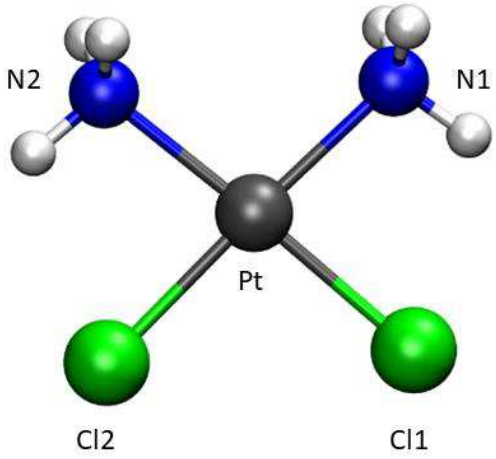

Figure A4 atom labels for the first step hydrolysis reaction of cisplatin.

Table A11 Relative Gibbs free energy values (kcal mol^{-1}), associated to the hydrolysis reaction pathway for isomer P and isomer M of phenanthriplatin and first (cisplatin-I) hydrolysis reaction of cisplatin, in PCM water.

G	R → RA	RA → TS	TS → PA	PA → P
Complex P	5.3	22.4	-5.8	1.0
Complex M	5.1	23.9	-9.8	3.0
Cisplatin	4.2	23.4	-14.4	4.9

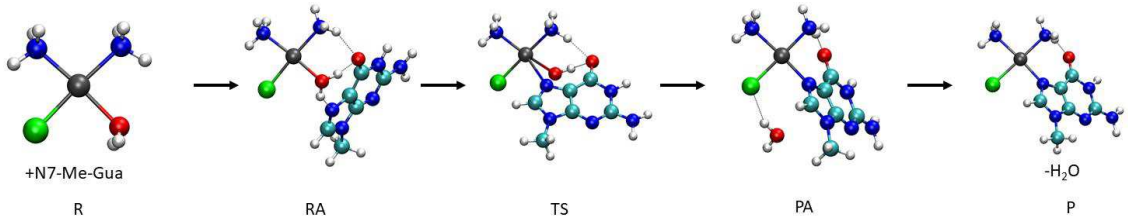

Figure A5 Optimized structures for first step for the reaction between N7-9-methylguanine and cisplatin.

Table A12 Relevant bond distances (Å) and angles (°) for optimized isomer P of phenanthriplatin, N7 is entering nitrogen atom in N7 position of N7-Me-Gua, O(w) is the oxygen atom of water coordinated to Pt.

Bond Distances					
Isomer P + N7-Me-Gua	**R**	**RA**	**TS**	**PA**	**P**
Pt-O(w)	2.133	2.076	2.363	3.98	-
Pt-N1	2.122	2.113	2.083	2.093	2.100
Pt-N2	2.053	2.061	2.069	2.074	2.070
Pt-N3	2.062	2.084	2.086	2.107	2.105
Pt-N7	-	4.241	2.610	2.051	2.061
Angles					
Isomer P + N7-Me-Gua	**R**	**RA**	**TS**	**PA**	**P**
O(w)-Pt-N1	86.26	89.52	82.11	45.54	-
O(w)-Pt-N2	90.83	88.05	95.99	133.41	-
O(w)-Pt-N3	178.38	175.92	156.88	126.49	-
N7-Pt-N1	-	78.00	90.96	88.26	89.33
N7-Pt-N2	-	99.34	88.95	90.06	89.60
N7-Pt-N3	-	152.83	135.64	178.21	178.11

Table A13 Relevant bond distances (Å) and angles (°) for optimized isomer M of phenanthriplatin, N7 is entering nitrogen atom in N7 position N7-Me-Gua, O(w) is the oxygen atom of water coordinated to Pt.

Bond Distances					
Isomer M + N7-Me-Gua	**R**	**RA**	**TS**	**PA**	**P**
Pt-O(w)	2.134	2.073	2.373	3.945	-
Pt-N1	2.122	2.115	2.085	2.091	2.100
Pt-N2	2.054	2.059	2.068	2.076	2.071
Pt-N3	2.063	2.087	2.088	2.109	2.107
Pt-N7	-	4.217	2.597	2.049	2.058
Angles					
Isomer M + N7-Me-Gua	**R**	**RA**	**TS**	**PA**	**P**
O(w)-Pt-N1	85.97	89.84	82.54	46.41	-
O(w)-Pt-N2	91.73	87.61	96.57	133.94	-
O(w)-Pt-N3	179.20	176.02	154.05	125.53	-
N7-Pt-N1	-	82.75	89.92	88.73	89.75
N7-Pt-N2	-	95.97	88.57	89.62	89.66
N7-Pt-N3	-	152.2	136.94	178.66	178.31

Table A14 Relevant bond distances (Å) and angles (°) for optimized isomer P of phenanthriplatin, N7 is entering nitrogen atom in N7 position of N7-Me-Ade, O(w) is the oxygen atom of water coordinated to Pt.

Bond Distances					
Isomer P + N7-Me-Ade	**R**	**RA**	**TS**	**PA**	**P**
Pt-O(w)	2.133	2.042	2.356	4.003	-
Pt-N1	2.122	2.111	2.095	2.103	2.113
Pt-N2	2.053	2.064	2.067	2.078	2.071
Pt-N3	2.062	2.111	2.090	2.111	2.110
Pt-N7	-	4.384	2.652	2.049	2.054
Angles					
Isomer P + N7-Me-Ade	**R**	**RA**	**TS**	**PA**	**P**
O(w)-Pt-N1	86.26	86.20	81.38	44.44	-
O(w)-Pt-N2	90.83	91.08	95.90	131.94	-
O(w)-Pt-N3	178.38	179.41	155.77	125.48	-
N7-Pt-N1	-	64.49	89.53	87.73	88.26
N7-Pt-N2	-	112.54	91.47	90.36	90.45
N7-Pt-N3	-	155.10	134.93	179.39	178.92

Table A15 Relevant bond distances (Å) and angles (°) for isomer M of phenanthriplatin, N7 is entering nitrogen atom in N7 position of N7-Me-Ade, O(w) is the oxygen atom of water coordinated to Pt.

Bond Distances					
Isomer M + N7-Me-Ade	**R**	**RA**	**TS**	**PA**	**P**
Pt-O(w)	2.134	2.042	2.360	4.110	-
Pt-N1	2.122	2.111	2.097	2.102	2.114
Pt-N2	2.054	2.064	2.064	2.072	2.066
Pt-N3	2.063	2.111	2.094	2.113	2.113
Pt-N7	-	4.367	2.632	2.044	2.050
Angles					
Isomer M + N7-Me-Ade	**R**	**RA**	**TS**	**PA**	**P**
O(w)-Pt-N1	85.97	86.04	82.20	42.25	-
O(w)-Pt-N2	91.73	91.21	95.87	136.83	-
O(w)-Pt-N3	179.2	179.56	153.28	126.60	-
N7-Pt-N1	-	64.41	89.74	87.715	88.68
N7-Pt-N2	-	113.43	89.35	90.32	89.84
N7-Pt-N3	-	154.17	136.12	178.70	178.31

Table A16 Relevant bond distances (Å) and angles (°) for isomer P of phenanthriplatin, N1 is entering nitrogen atom in N1 position of N1-Me-Ade, O(w) is the oxygen atom of water coordinated to Pt.

Bond Distances					
Isomer P + N1-Me-Ade	**R**	**RA**	**TS**	**PA**	**P**
Pt-O(w)	2.133	2.036	2.361	3.634	-
Pt-N1	2.122	2.116	2.102	2.107	2.121
Pt-N2	2.053	2.061	2.058	2.068	2.063
Pt-N3	2.062	2.115	2.097	2.117	2.117
Pt-N1'	-	4.416	2.097	2.064	2.067
Angles					
Isomer P + N1-Me-Ade	**R**	**RA**	**TS**	**PA**	**P**
O(w)-Pt-N1	86.26	85.73	82.77	51.93	-
O(w)-Pt-N2	90.83	91.02	94.46	125.19	-
O(w)-Pt-N3	178.38	179.22	152.04	104.65	-
N1'-Pt-N1	-	62.27	86.91	87.73	87.90
N1'-Pt-N2	-	114.89	91.34	89.95	89.95
N1'-Pt-N3	-	154.07	136.25	178.16	178.05

Table A17 Relevant bond distances (Å) and angles (°) for isomer M of phenanthriplatin, N1 is entering nitrogen atom in N1 position of N1-Me-Ade, O(w) is the oxygen atom of water coordinated to Pt.

Bond Distances					
Isomer M + N1-Me-Ade	**R**	**RA**	**TS**	**PA**	**P**
Pt-O(w)	2.134	2.035	2.351	4.001	-
Pt-N1	2.122	2.117	2.100	2.107	2.121
Pt-N2	2.054	2.061	2.063	2.072	2.064
Pt-N3	2.063	2.115	2.093	2.120	2.123
Pt-N1	-	4.394	2.662	2.065	2.064
Angles					
Isomer M + N1-Me-Ade	**R**	**RA**	**TS**	**PA**	**P**
O(w)-Pt-N1	85.97	86.1	81.56	44.18	-
O(w)-Pt-N2	91.73	90.90	95.38	135.54	-
O(w)-Pt-N3	179.2	179.61	155.88	110.03	-
N1-Pt-N1	-	61.99	86.52	87.71	87.98
N1-Pt-N2	-	114.73	93.55	90.28	90.25
N1-Pt-N3	-	153.46	133.75	176.94	176.68

Table A18 Relevant bond distances (Å) and angles (°) for the first step of the reaction between N7-Me-Gua and cisplatin, N7 is entering nitrogen atom in N7 position of N7-Me-Gua, O(w) is the oxygen atom of water coordinated to Pt.

Bond Distances					
Cisplatin + N7-Me-Gua	**R**	**RA**	**TS**	**PA**	**P**
Pt-O(w)	2.131	2.086	2.363	4.227	-
Pt-N1	2.136	2.132	2.121	2.107	2.115
Pt-N2	2.054	2.071	2.08	2.096	2.092
Pt-Cl2	2.299	2.313	2.317	2.337	2.326
Pt-N7	-	3.878	2.547	2.056	2.061
Angles					
Cisplatin + N7-Me-Gua	**P**	**RA**	**TS**	**PA**	**P**
O(w)-Pt-N1	87.43	85.94	88.2	129.56	-
O(w)-Pt-N2	176.03	175.93	154.25	129.33	-
O(w)-Pt-Cl2	89.11	90.80	90.45	50.90	-
N7-Pt-N1	-	104.48	87.74	89.91	91.03
N7-Pt-N2	-	138.3	135.4	176.12	175.30
N7-Pt-Cl2	-	71.79	90.86	90.73	89.96

Table A19 Relative Gibbs free energy values (kcal mol^{-1}), associated to the reaction between 9-methylguanine 9-methyladenine and isomer P and isomer M of phenanthriplatin and cisplatin, in PCM water.

G	**R → RA**	**RA → TS**	**TS → PA**	**PA →P**
Complex-P + N7-Me-Gua	-4.3	13.9	-26.8	-5.0
Complex-M+ N7-Me-Gua	-3.0	13.6	-27.2	-5.2
Complex-P + N7-Me-Ade	3.6	15.2	-30.4	-2.8
Complex-M + N7-Me-Ade	4.3	14.4	-30.8	-3.6
Complex-P + N1-Me-Ade	1.6	16.9	-30.3	-6.2
Complex-M + N1-Me-Ade	1.8	16.9	-31.2	-5.1
Cisplatin + N7-Me-Gua	-3.2	14.8	-26.7	-6.8
CisplatinN7-Me-Gua + N7'-Me-Gua	-4.3	16.6	-30.6	-3.3

Table A20 Relevant bond distances (Å) and angles (°) for RA in π-π interaction for isomer M, where Nb is the nitrogen atom of the bases, O(w) is the oxygen atom of water coordinated. At M06 level of theory.

Bond Distances			
Isomer M	**N7-Me-Gua**	**N7-Me-Ade**	**N1-Me-Ade**
Pt-O(w)	2.068	2.039	2.038
Pt-N1	2.108	2.109	2.109
Pt-N2	2.064	2.064	2.065
Pt-N3	2.089	2.115	2.118
Pt-Nb	4.037	4.037	4.072
Angles			
Isomer M	**N7-Me-Gua**	**N7-Me-Ade**	**N1-Me-Ade**
O(w)-Pt-N1	83.83	88.14	87.85
O(w)-Pt-N2	90.75	87.54	88.20
O(w)-Pt-N3	179.57	176.90	176.89
Nb-Pt-N1	121.09	123.39	122.38
Nb-Pt-N2	53.43	52.71	54.31
Nb-Pt-N3	143.10	139.43	138.61

Table A21 Relevant bond distances (Å) and angles (°) for TS in π-π interaction for isomer M, where Nb is the nitrogen atom of the bases, O(w) is the oxygen atom of water coordinated. At M06 level of theory

Bond Distances			
Complex M	**N7-Me-Gua**	**N7-Me-Ade**	**N1-Me-Ade**
Pt-O(w)	2.373	2.360	2.348
Pt-N1	2.085	2.097	2.101
Pt-N2	2.068	2.064	2.061
Pt-N3	2.088	2.094	2.091
Pt-Nb	2.597	2.634	2.672
Angles			
Complex M	**N7-Me-Gua**	**N7-Me-Ade**	**N1-Me-Ade**
O(w)-Pt-N1	82.55	82.45	81.01
O(w)-Pt-N2	96.56	95.88	96.05
O(w)-Pt-N3	154.05	153.14	156.07
Nb-Pt-N1	89.90	88.90	88.07
Nb-Pt-N2	88.59	90.34	91.72
Nb-Pt-N3	136.93	136.18	133.97

Table A22 Relevant bond distances (Å) and angles (°) of TS obtained by the rotation of the phenanthridine ligand in $[Pt(NH_3)_2(Ade)(phenanthridine)]^{2+}$, where Nb is the nitrogen atom of the bases.

Bond Distances	**N7-Me-Ade**	**N1-Me-Ade**
Pt-N1	2.115	2.115
Pt-N2	2.138	2.127
Pt-N3	2.133	2.121
Pt-Nb	2.045	2.069
Angles	**N7-Me-Ade**	**N1-Me-Ade**
Nb-Pt-N1	83.95	84.72
Nb-Pt-N2	96.50	90.67
Nb-Pt-N3	170.46	170.75

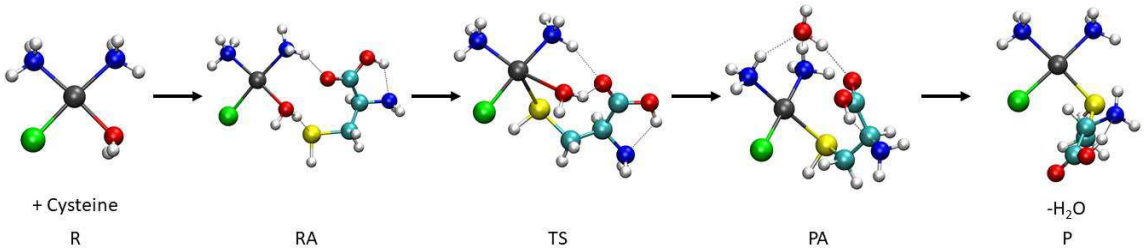

Figure A6 Optimized structures for the reaction between cisplatin and cysteine.

Table A23 Relevant bond distances (Å) and angles (°) for optimized isomer P of phenanthriplatin, O(w) is the oxygen atom of water coordinated to Pt.

Bond Distances					
Isomer P	**R**	**RA**	**TS**	**PA**	**P**
Pt-O(w)	2.133	2.090	2.525	4.042	-
Pt-N1	2.122	2.115	2.100	2.106	2.136
Pt-N2	2.053	2.056	2.063	2.073	2.056
Pt-N3	2.062	2.079	2.105	2.123	2.128
Pt-S	-	4.833	2.775	2.371	2.380
Angles					
Isomer P	**R**	**RA**	**TS**	**PA**	**P**
O(w)-Pt-N1	86.26	85.18	91.16	46.06	-
O(w)-Pt-N2	90.83	90.25	89.88	136.91	-
O(w)-Pt-N3	178.38	179.24	154.42	126.93	-
S-Pt-N1	-	112.26	87.36	92.51	87.89
S-Pt-N2	-	63.34	93.30	88.33	94.45
S-Pt-N3	-	147.01	132.89	176.09	179.09

Table A24 Relevant bond distances (Å) and angles (°) for optimized isomer M of phenanthriplatin, O(w) is the oxygen atom of water coordinated to Pt.

Bond Distances					
Isomer M	**R**	**RA**	**TS**	**PA**	**P**
Pt-O(w)	2.134	2.081	2.480	4.063	-
Pt-N1	2.122	2.112	2.099	2.105	2.135
Pt-N2	2.054	2.059	2.063	2.073	2.056
Pt-N3	2.063	2.082	2.098	2.125	2.128
Pt-S	-	4.768	2.858	2.368	2.380
Angles					
Isomer M	**R**	**RA**	**TS**	**PA**	**P**
O(w)-Pt-N1	85.97	85.06	86.74	45.52	-
O(w)-Pt-N2	91.73	90.71	93.61	135.83	-
O(w)-Pt-N3	179.20	179.48	154.11	127.83	-
S-Pt-N1	-	102.51	87.82	92.53	87.84
S-Pt-N2	-	74.77	92.03	88.18	94.25
S-Pt-N3	-	150.38	132.29	176.32	177.92

Table A25 Relevant bond distances (Å) and angles (°) for optimized cisplatin, O(w) is the oxygen atom of water coordinated to Pt.

Bond Distances					
Cisplatin	**R**	**RA**	**TS**	**PA**	**P**
Pt-O(w)	2.131	2.110	2.402	3.444	-
Pt-N1	2.136	2.116	2.121	2.123	2.149
Pt-N2	2.054	2.059	2.097	2.094	2.119
Pt-Cl2	2.299	2.314	2.318	2.324	2.308
Pt-S	-	4.178	2.776	2.359	2.359
Angles					
Cisplatin	**P**	**RA**	**TS**	**PA**	**P**
O(w)-Pt-N1	87.435	86.08	82.11	56.16	-
O(w)-Pt-N2	176.03	176.71	144.44	57.09	-
O(w)-Pt-Cl2	89.11	89.52	93.58	121.52	-
S-Pt-N1	-	98.22	90.57	91.13	89.92
S-Pt-N2	-	131.22	132.10	175.03	176.41
S-Pt-Cl2	-	78.32	88.66	90.73	91.67

Table A26 Relative Gibbs free energy values (kcal mol^{-1}), associated to the reaction between cysteine and Isomer P and isomer M of phenanthriplatin and cisplatin, in PCM water.

G	R → RA	RA → TS	TS → PA	PA → P
Complex P	2.3	15.1	-24	-2.9
Complex M	0.6	20.4	-27.2	-5.3
cisplatin	2.4	13.5	-24.5	-5.6

Appendix B

4.2 Chemical Properties: Inside the Acidity of Fluoroquinolone Antibacterials

Table A1 Relevant bond distances (Å) and angles (°) for CFX^-, nCFX and zCFX in optimized structures.

Distance	CFX^-	nCFX	zCFX-N4'
C11-O12	1.261	1.216	1.261
C11-O11	1.251	1.336	1.250
C11-C3	1.546	1.488	1.547
C2-N1	1.362	1.345	1.362
C9-N1	1.395	1.404	1.393
N1-C12	1.452	1.458	1.452
C4-O4	1.239	1.257	1.238
N1'-C2'	1.465	1.467	1.460
C2'-C3'	1.534	1.535	1.523
C3'-N4'	1.466	1.465	1.509
N4'-C5'	1.467	1.466	1.510
C5'-C6'	1.530	1.531	1.520
C6'-N1'	1.477	1.479	1.470
Angles	**CFX^-**	**nCFX**	**zCFX-N4'**
O12-C11-C3	115.3	123.5	115.2
O11-C11-C3	118.0	115.2	118.0
O4-C4-C3	126.3	122.7	126.5
O4-C4-C10	119.3	121.9	119.2
C2-N1-C9	119.2	119.8	119.1
C2-N1-C12	119.9	119.7	119.9
C9-N1-C12	120.6	120.3	120.7
C7-N1'-C2'	117.9	118.5	117.9
C7-N1'-C6'	117.4	118.7	117.1
C2'-N1'-C6'	111.8	112.1	111.6
C3'-N4'-C5'	110.7	110.7	112.1

Table A2 Relevant bond distances (Å) and angles (°) for the zCFX-N4', zCFX-N1 and zCFX-N1' optimized structures.

Distance	zCFX-N4'	zCFX-N1	zCFX-N1'
C11-O12	1.261	1.244	1.259
C11-O11	1.250	1.246	1.249
C11-C3	1.547	1.548	1.547
C2-N1	1.362	1.486	1.364
C9-N1	1.393	1.486	1.388
N1-C12	1.452	1.516	1.454
C4-O4	1.238	1.222	1.234
N1'-C2'	1.460	1.469	1.525
C2'-C3'	1.523	1.536	1.531
C3'-N4'	1.509	1.464	1.460
N4'-C5'	1.510	1.466	1.460
C5'-C6'	1.520	1.531	1.532
C6'-N1'	1.470	1.479	1.570
Angles	**zCFX-N4'**	**zCFX-N1**	**zCFX-N1'**
O12-C11-C3	115.2	115.9	115.2
O11-C11-C3	118.0	113.3	117.5
O4-C4-C3	126.5	122.0	126.9
O4-C4-C10	119.2	121.9	118.9
C2-N1-C9	119.1	115.2	119.0
C2-N1-C12	119.9	108.7	120.0
C9-N1-C12	120.7	111.5	120.7
C7-N1'-C2'	117.9	119.1	113.8
C7-N1'-C6'	117.1	120.1	112.9
C2'-N1'-C6'	111.6	112.4	112.0
C3'-N4'-C5'	112.1	110.7	111.9

Table A3 Relevant bond distances (Å) and angles (°) for the calculated structures of zCFX-N4', H_2CFX-O11 and H_2CFX-N1', H_2CFX-N1'.

Distance	**zCFX-N4'**	**H_2CFX^+-O11**	**H_2CFX^+-N1**	**H_2CFX^+-N1'**
C11-O12	1.261	1.216	1.244	1.259
C11-O11	1.25	1.336	1.245	1.248
C11-C3	1.547	1.489	1.549	1.549
C2-N1	1.362	1.346	1.486	1.364
C9-N1	1.393	1.402	1.484	1.387
N1-C12	1.452	1.459	1.517	1.454
C4-O4	1.238	1.255	1.220	1.233
N1'-C2'	1.460	1.461	1.463	1.519
C2'-C3'	1.523	1.523	1.522	1.518
C3'-N4'	1.509	1.509	1.508	1.507
N4'-C5'	1.510	1.509	1.509	1.507
C5'-C6'	1.520	1.520	1.520	1.518
C6'-N1'	1.470	1.471	1.473	1.521
Angles	**zCFX-N4'**	**H_2CFX^+-O11**	**H_2CFX^+-N1**	**H_2CFX^+-N1'**
O12-C11-C3	115.2	123.4	116.0	115.1
O11-C11-C3	118.0	115.2	113.1	117.5
O4-C4-C3	126.5	122.9	122.4	127.1
O4-C4-C10	119.2	121.8	121.6	118.8
C2-N1-C9	119.1	119.7	115.2	119.0
C2-N1-C12	119.9	119.7	108.8	120.0
C9-N1-C12	120.7	120.4	111.6	120.7
C7-N1'-C2'	117.9	118.4	118.6	113.3
C7-N1'-C6'	117.1	118.1	119.0	112.4
C2'-N1'-C6'	111.6	111.9	112.1	111.0
C3'-N4'-C5'	112.1	112.0	111.8	111.9

Table A4 Relevant bond distances (Å) and angles (°) for the calculated structures of H_2CFX^+-O11, H_3CFX^{2+}-N1, H_3CFX^2+-N1', H_3CFX^{2+}-O4.

Distance	H_2CFX^+-O11	H_3CFX^{2+}-N1	H_3CFX^{2+}-N1'	H_3CFX^{2+}-O4
C11-O12	1.216	1.206	1.214	1.208
C11-O11	1.336	1.326	1.335	1.336
C11-C3	1.489	1.521	1.492	1.505
C2-N1	1.346	1.462	1.346	1.333
C9-N1	1.402	1.486	1.397	1.395
N1-C12	1.459	1.543	1.461	1.468
C4-O4	1.255	1.230	1.247	1.334
N1'-C2'	1.461	1.464	1.521	1.464
C2'-C3'	1.523	1.525	1.519	1.524
C3'-N4'	1.509	1.509	1.507	1.508
N4'-C5'	1.509	1.509	1.506	1.509
C5'-C6'	1.520	1.520	1.518	1.520
C6'-N1'	1.471	1.472	1.523	1.474
Angles	**H_2CFX^+-O11**	**H_3CFX^{2+}-N1**	**H_3CFX^{2+}-N1'**	**H_3CFX^{2+}-O4**
O12-C11-C3	123.4	121.4	123.1	121.1
O11-C11-C3	115.2	115.9	115.4	118.4
O4-C4-C3	122.9	121.0	123.7	117.3
O4-C4-C10	121.8	123.0	121.1	122.8
C2-N1-C9	119.7	115.4	119.7	120.5
C2-N1-C12	119.7	112.3	119.9	119.3
C9-N1-C12	120.4	109.6	120.4	120.1
C7-N1'-C2'	118.4	120.4	113.7	119.5
C7-N1'-C6'	118.1	121.3	112.1	120.4
C2'-N1'-C6'	111.9	112.4	111.0	112.4
C3'-N4'-C5'	112.0	112.1	112.0	112.0

4.3 Antibacterial Fluoroquinolones as Pollutants: Adsorption on Carbon Nano-tube, a Molecular Dynamics Simulation Study

Table A5 MK charges and atomic mass used in nCFX and zCFX, the atoms numbering is reported in Scheme 11.

	zCFX		nCFX	
Atom	Charge	Mass	Charge	Mass
N_1	0.031	14.0067	-0.059	14.0067
C_{12}	0.151	12.0110	0.157	12.0110
H_{12}	0.079	1.0080	0.090	1.0080
C_{13}	0.000	14.0270	0.012	14.0270
C_{14}	0.000	14.0270	0.012	14.0270
C_2	-0.110	12.0110	0.109	12.0110
H_2	0.138	1.0080	0.105	1.0080
C_3	-0.261	12.0110	-0.471	12.0110
C_{11}	0.706	12.0110	-0.471	12.0110
O_1	-0.759	15.9994	-0.584	15.9994
O_2	-0.759	15.9994	-0.652	15.9994
C_4	0.539	12.0110	0.576	12.0110
O_3	-0.607	15.9994	-0.620	15.9994
C_{10}	-0.179	12.0110	-0.143	12.0110
C_5	-0.145	12.0110	-0.201	12.0110
H_5	0.147	1.0080	0.173	1.0080
C_6	0.105	12.0110	0.178	12.0110
F_1	-0.149	18.9984	-0.150	18.9984
C_7	0.180	12.0110	0.104	12.0110
C_8	-0.203	12.0110	-0.174	12.0110
H_8	0.071	1.0080	0.079	1.0080
C_9	0.068	12.0110	0.134	12.0110
$N_{1'}$	-0.287	14.0067	-0.205	14.0067
$C_{2'}$	0.202	14.0270	0.110	14.0270
$C_{3'}$	0.172	14.0270	0.223	14.0270
$N_{4'}$	-0.186	14.0067	-0.758	14.0067
$H_{4'}$	0.341	1.0080	0.386	1.0080
H_{-z-n}	0.341	1.0080	0.458	1.0080
C_5'	0.172	14.0270	0.223	14.0270
$C_{6'}$	0.202	14.0270	0.110	14.0270

Table A6 LJ_{int} in vacuum between SW-CNT and 1, 2, 4 and 8 molecules of n and zCFX. xCFX out (x = n or z): CFXs adsorbed on the outer SW-CNT surface, xCFX ins (x = n or z): CFXs adsorbed on the inner surface.

LJ_{int} kcal mol^{-1}	**1 CFX**	**2 CFX**	**4 CFX**	**8 CFX**
zCFX out	-26.8	-17.9	-22.3	21.8
nCFX out	-24.9	-26.2	-26.5	-25.1
zCFX ins	-34.9	-39.5	-29.4	-31.9
nCFX ins	-43.2	-43.2	-40.1	-34.3

List of publications

1. M. M. Dell'Anna, V. Censi, B. Carrozzini, R. Caliandro, N. Denora, M. Franco, D. Veclani, A. Melchior, M. Tolazzi, P. Mastrorilli, «*Triphenylphosphane Pt(II) complexes containing biologically active natural polyphenols: Synthesis, crystal structure, molecular modeling and cytotoxic studies*» *J. Inorg. Biochem.* 2016, *163*, 346–361.

2. V. M. Nurchi, G. Crisponi, J. I. Lachowicz, M. Antonietta, M. Peana, S. Medici, D. Veclani, M. Tolazzi, A. Melchior, «*Fluoroquinolones: A micro-species equilibrium in the protonation of amphoteric compounds*» Eur. J. Pharm. Sci. 2016, 93, 380–391.

3. Manuscript in preparation for PCCP Journal: D. Veclani, A. Melchior, M. Tolazzi, J. P. Ceron Carrasco «Monofunctional platinum anticancer drugs: disentangling their hydrolysis and DNA-binding mechanisms by theoretical calculations». Will be submit to Phys Chem Chem Phys

4. Manuscript in preparation: D. Veclani, A. Melchior, M. Tolazzi «Adsorption of Ciprofloxacin on Carbon Nanotubes: a Molecular Dynamics Study».

Journal of Inorganic Biochemistry 163 (2016) 346–361

Contents lists available at ScienceDirect

Journal of Inorganic Biochemistry

journal homepage: www.elsevier.com/locate/jinorgbio

Triphenylphosphane Pt(II) complexes containing biologically active natural polyphenols: Synthesis, crystal structure, molecular modeling and cytotoxic studies

Maria Michela Dell'Anna [a,*], Valentina Censi [a], Benedetta Carrozzini [b], Rocco Caliandro [b], Nunzio Denora [c], Massimo Franco [c], Daniele Veclani [d], Andrea Melchior [d], Marilena Tolazzi [d], Piero Mastrorilli [a]

[a] DICATECh, Politecnico di Bari, via Orabona, 4, I-70125 Bari, Italy
[b] Institute of Crystallography CNR, via Amendola, 122/o, I-70126 Bari, Italy
[c] Department of Pharmacy, University of Bari, via Orabona, 4, I-70125 Bari, Italy
[d] Dipartimento Politecnico di Ingegneria e Architettura, Laboratori di Tecnologie Chimiche, University of Udine, via del Cotonificio 108, I-33100 Udine, Italy

ARTICLE INFO

Article history:
Received 17 March 2016
Received in revised form 25 July 2016
Accepted 9 August 2016
Available online 9 August 2016

Keywords:
Platinum(II) complexes
Cytotoxic activity
Natural polyphenols
Flavonoids
DFT

ABSTRACT

Platinum complexes bearing phosphane ligands in *cis* configuration with deprotonated flavonoids (3-hydroxyflavone, quercetin) and deprotonated ethyl gallate were synthesized starting from *cis*-[$PtCl_2(PPh_3)_2$]. In all cases, *O,O′* chelate structures were obtained. While quercetin and ethyl gallate complexes are quite stable in solution, the 3-hydroxyflavonate complex undergoes a slow aerobic photodegradation in solution with formation of salicylic and benzoic acids. The X-ray diffraction structures of quercetin and ethyl gallate complexes are reported. Cell cycle studies (in the dark) of the complexes in two human cell lines revealed that the cytotoxic activity of the complex bearing 3-hydroxyflavonate is higher than those exhibited by 3-hydroxyflavone or by *cis*-[$PtCl_2(PPh_3)_2$] alone. Density functional theory studies on the hydrolysis pathway for the 3-hydroxyflavone and ethyl gallate complexes explained the different cytotoxic activity observed for the two compounds on the basis of the different intermediates formed during hydrolysis (relatively inert hydroxy Pt complexes for ethyl gallate and monoaqua complexes for 3-hydroxyflavone).

1. Introduction

The discovery of antiproliferative activity of cisplatin by Rosenberg et al. [1] in 1965 contributed to the development of cancer chemotherapy. Today cisplatin is a widely used drug in chemotherapy, but its applicability has many disadvantages, as it causes many severe side effects including: nephrotoxicity, neurotoxicity, myelotoxicity, hematological toxicity and gastrointestinal reactions [2–4]. In addition, some tumors have acquired resistance to cisplatin, while others develop resistance after the initial treatment. In view of these limitations, research has been extended to other platinum complexes. A large number of platinum analogs have been tested during the last 30 years [5]. Unfortunately, the vast majority of these compounds were rejected in preclinical or early clinical stages of testing (only carboplatin and oxaliplatin, Scheme 1, are in world-wide clinical use) and the discovery of a new platinum drug more selective and less toxic than cisplatin is still highly desirable.

Recently, the antitumor activity of dietary flavonoids (flavus = yellow), which are primarily benzo-γ-pyrone (phenylchromone) derivatives (Scheme 2), comprising a massive group of polyphenolic compounds [6–7] universally distributed in the plant kingdom, has been reviewed [8]. The pharmacological effects of flavonoids include induction of apoptosis, suppression of protein tyrosine kinase activity, antiproliferation, antimetastatic and antiinvasive effects, and antiangiogenesis [8].

Because of structural differences, flavonoids are divided into eight different groups, flavonols being one of them. 3-Hydroxyflavone (Scheme 3a) is the backbone of all flavonols [9], while quercetin (Scheme 3b) is another very important flavonol with well-known anticancer activity [10]. Due to their polyphenolic structure, flavonols are effective metal ion chelators, playing a key role in the initiation of free radical and antioxidant processes [11]. Moreover flavonols can intercalate into deoxyribonucleic acid (DNA) as well as covalently bind to DNA and proteins [12–13]. As a result of these characteristics, flavonols have complex biological interactions and in some therapies they are combined with cisplatin increasing efficacy over individual treatments [14] and reducing side effects associated with cisplatin [15]. However, combinations of flavonols with platinum are poorly understood, although multiple theories currently exist trying to explain the interactions between cisplatin and flavonols [16].

Like flavonols, also plant phenols, such as ethyl gallate (Scheme 3c), have antitumor activity [17–20] and can effectively bind metal ions.

* Corresponding author.
E-mail address: mariamichela.dellanna@poliba.it (M.M. Dell'Anna).

http://dx.doi.org/10.1016/j.jinorgbio.2016.08.006
0162-0134/

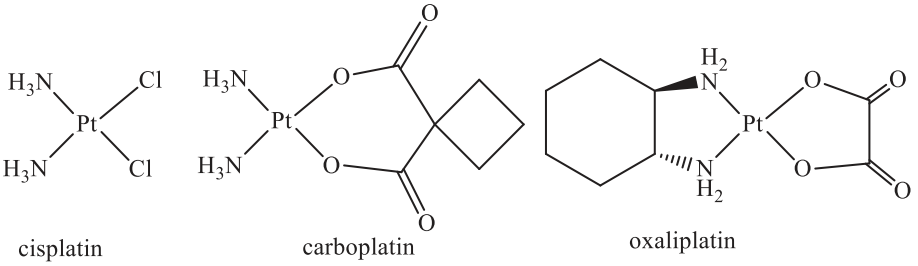

Scheme 1. Platinum based anticancer drugs used in clinical therapies.

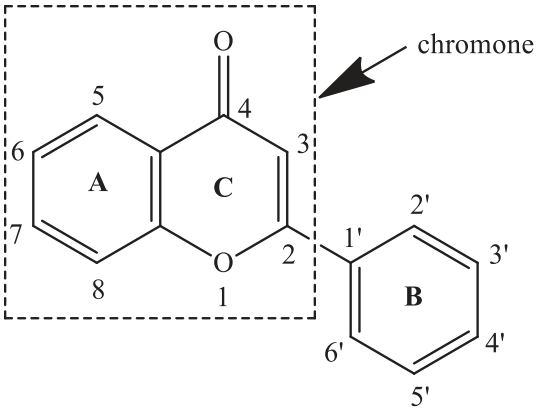

Scheme 2. Flavone backbone.

All these considerations prompted us to check whether platinum complexes of natural polyphenols would exhibit synergic cytotoxic activity. Although since the early 1980s scientists have investigated more than 40 metal–flavonoid complexes [21–22], to the best of our knowledge Pt(II) complexes with 3-hydroxyflavone and ethyl gallate as ligands have never been synthesized. On the contrary, the synthesis of a platinum(II) complex with quercetin has already been reported [23]. Its formula is *cis*-[$Pt(NH_3)_2$(que)] (que = dianion of quercetin) and a complexation of platinum(II) to the ligand through oxygen atoms at $C^{3'}$ and $C^{4'}$ was hypothesized, although neither XRD (X-ray diffraction) nor citotoxicity studies were carried out.

Phosphane ligands with hydrophobic character have been shown to increase in some cases the cytotoxicity of their platinum complexes, possibly by enhancing the cellular membrane transfer process [24]. In previous works [25–26], interesting results were obtained by synthetizing platinum compounds bearing two mutually *cis* triphenylphosphanes with bioactive ligands. In these studies, it has been reported that Pt(II) complexes containing PPh_3 and the N7-coordinated anionic ligand 8-MTT (8-(methylthio)theophyllinate) have a remarkable cytotoxic activity on some cancer cell lines. This antiproliferative activity on both cisplatin-sensitive T2 and cisplatin-resistant SKOV3 cell lines decreased when PPh_3 was substituted by the more hydrophilic 1,3,5-triaza-7-phosphaadamantane (PTA) ligand. Although the total replacement of the usually employed amine carrier ligands (Scheme 1) for air and water stable triarylphosphanes may exhibit some disadvantages (the major of them being that a tertiary phosphane cannot establish any hydrogen bond with the DNA backbone), however it has been found that triarylphosphane ligands may stabilize DNA-Pt adducts through π-π interactions occurring between the phosphane phenyl groups and the nucleobases [27]. For this reason, recently a series of platinum compounds where the two ammonia ligands of cisplatin and cisplatin analogs were replaced by phosphanes have been prepared and biologically characterized [28–29]. In some cases promising interactions between DNA (or cell proteins) and platinum complexes bearing two phosphane groups in mutually *cis* position have been found and studied [30–34], in spite of the poor antiproliferative activity of *cis*-[$PtCl_2(PPh_3)_2$] [35]. Moreover, PR_3 ligand has a kinetic *trans* effect stronger than NH_3, which can facilitate the leaving group displacement by H_2O in the human cell. The ligand release by hydrolysis is a key-step for the DNA-adduct formation and attracted numerous

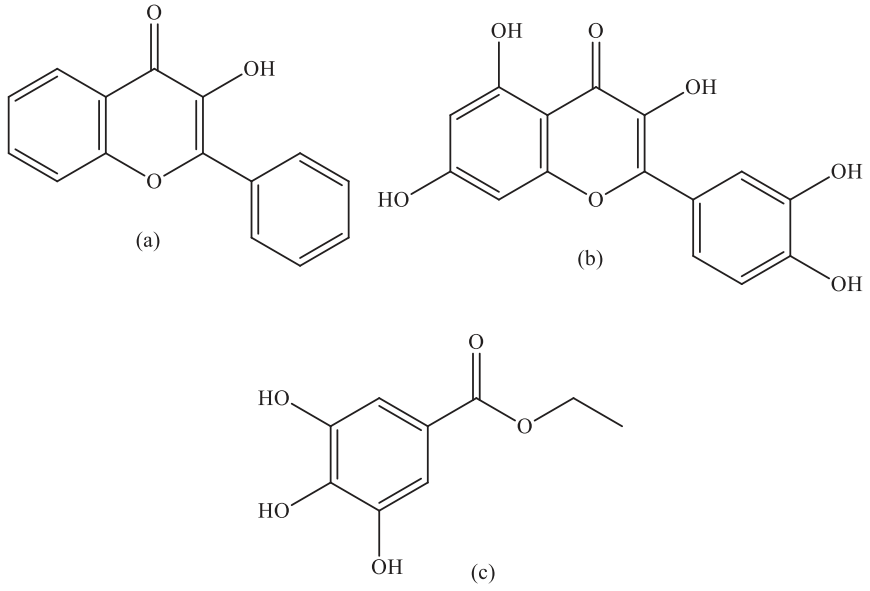

Scheme 3. (a) 3-Hydroxyflavone; (b) quercetin; (c) ethyl gallate.

experimental studies [36]. Furthermore, in the last decade a variety of theoretical approaches have been applied to obtain an accurate picture of the hydrolysis mechanism of Pt(II)-based anticancer drugs and ultimately of the structure-activity relationship [37–41]. In this framework, we started a project aiming at preparing new platinum complexes containing triphenylphosphane as carrier ligand and flavonolates or natural polyphenolates as leaving groups. Herein, we report on the synthesis, characterization, cytotoxicity and DFT studies of *cis*-[Pt(PPh_3)$_2$(que)] (**1**, que = dianion of quercetin), *cis*-[Pt(PPh_3)$_2$(3-Hfl)]Cl (**2**, 3-Hfl = monoanion of 3-hydroxyflavone), and *cis*-[Pt(PPh_3)$_2$(etga)] (**3**, etga = dianion of ethyl gallate).

2. Experimental section

2.1. Material and methods

Tap water was de-ionized by ionic exchange resins (Millipore) before use. All chemicals and solvents were purchased from commercial suppliers and used without further purification. *cis*-Pt(PPh_3)$_2$$Cl_2$ was synthetized according to literature procedures [42].

Melting points were determined with a Büchi Melting Point B-540 apparatus and are uncorrected. Elemental analyses were carried out with a Perkin Elmer 2400 CHN Elemental Analyzer at the Microanalytical Laboratory of the University of Bari, Department of Pharmacy. IR spectra were recorded on a Bruker-Vector 22 spectrometer. NMR spectra were recorded on a BRUKER Avance 400 spectrometer; frequencies are referenced to Me_4Si (^{1}H and ^{13}C), 85% H_3PO_4 (^{31}P) and H_2PtCl_6 (^{195}Pt). The signal attributions and coupling constant assessment were made on the basis of a multinuclear NMR analysis of each compound including, besides 1D spectra, ^{1}H—^{31}P HMQC, ^{1}H—^{195}Pt HMQC, ^{1}H—^{13}C HSQC, ^{1}H—^{13}C HMBC and ^{1}H COSY. High resolution mass spectrometry (HR-MS) analyses were performed using a time-of-flight mass spectrometer equipped with an electrospray ion source (Bruker micrOTOF). The sample solutions were introduced by continuous infusion with the aid of a syringe pump at a flow rate of 180 μL/min. The instrument was operated at end plate offset −500 V and capillary −4500 V. Nebulizer pressure was 1.5 bar (N_2), and the drying gas (N_2) flow was 10 L/min. Capillary exit and skimmer 1 were 120 and 40 V, respectively. The drying gas temperature was set at 220 °C. The calculated (exact mass) and the experimental (accurate) *m/z* values were compared considering the principal ion (which gives the most intense peak) of the isotope pattern. The software used for the calculated HRMS-spectra is Bruker Daltonics Data Analysis (version 3.3).

2.2. Synthesis of cis-[Pt(PPh_3)$_2$(que)] (que = dianion of quercetin) (**1**)

A solution of KOH (2.90 mmol, 162.7 mg) in ethanol (7.0 mL) kept at 40 °C was added dropwise to a clear yellow solution of *cis*-[$PtCl_2$(PPh_3)$_2$] (1.45 mmol, 1.149 g) and quercetin (1.45 mmol, 0.439 g) in CH_2C1_2 (80 mL) at room temperature under stirring. After overnight stirring at room temperature, the resulting dark orange reaction mixture was filtered (in order to remove KCl) and dried under reduced pressure. The red orange residue was dissolved in CH_2Cl_2 (10 mL) and added of *n*-hexane (30 mL), which caused the formation of a red-orange precipitate. This solid was filtered after overnight cooling at 4 °C, washed with *n*-hexane (3 × 10 mL) and dried under vacuum.

Yield: 1.073 g, 72%. Mp = 212.5 °C (dec).

Relevant ^{1}H and ^{13}C{^{1}H} NMR features are reported in Tables 3 and 2, respectively, except those belonging to PPh_3 groups. PPh_3 region: ^{1}H NMR (400 MHz, dmso-d_6, 25 °C) δ = 7.45 ppm (m, 12H, H_{ortho}), 7.42 ppm (m, 6H, H_{para}), 7.29 ppm (m, 12H, H_{meta}); ^{13}C{^{1}H} NMR (100 MHz dmso-d_6, 25 °C) δ = 134.7 ppm (s, C_{ortho}), 131.6 (s, C_{para}), 128.8 (s, C_{ipso}), 128.6 (s, C_{meta}).

^{31}P{^{1}H} NMR (121.5 MHz, dmso-d_6, 25 °C): δ = 9.6 ppm (d, $^2J_{PP}$ = 23 Hz, $^1J_{PtP}$ = 3565 Hz); 8.3 ppm (d, $^2J_{PP}$ = 23 Hz, $^1J_{PtP}$ = 3600 Hz).

^{195}Pt{^{1}H} NMR (85.99 MHz, dmso-d_6, 25 °C): δ = −4062 ppm (dd, $^1J_{PtP}$ = 3565 Hz, $^1J_{PtP}$ = 3600 Hz).

IR (KBr, cm^{-1}): 3372–3633 (b, m, O—H), 3058 (m, C—H), 1650 (s, C═O), 1617 (s, C═C), 1515 (s, C═C), 1491 (s, C═C), 1426 (s, C═C), 1354 (m, O—H), 1270 (s, C-O-C), 1162 (m, O—H), 1099 (m, C—H), 997 (m, C-O-C), 741 (m, C—H), 530 (m, Pt—O).

HRMS (ESI, acetonitrile, positive ion mode) *m/z*: calcd. for $C_{51}H_{38}O_7P_2Pt$ $[M]^+$ 1019.1740; found 1019.1681. HRMS (ESI, acetonitrile, negative ion mode) *m/z*: calcd. for $C_{51}H_{37}O_7P_2Pt$ $[M-H]^-$ 1018.1672; found 1018.1678.

2.3. Synthesis of cis-[Pt(PPh_3)$_2$(3-Hfl)]Cl (3-Hfl = monoanion of 3-hydroxyflavone) (**2**)

A solution of KOH (0.64 mmol, 35.9 mg) in ethanol (4.5 mL) kept at 40 °C was added dropwise to a clear yellow solution of *cis*-[$PtCl_2$(PPh_3)$_2$] (0.64 mmol, 506.0 mg) and 3-hydroxyflavone (0.64 mmol, 152.5 mg) in CH_2Cl_2 (40 mL) at room temperature under stirring. After overnight stirring at room temperature, the reaction mixture was filtered to remove KCl and the resulting orange solution was concentrated to 2 mL under reduced pressure and added of ethanol (10 mL). Addition of pentane (30 mL) caused the precipitation of an orange solid from the solution. The solid was washed with *n*-pentane (3 × 10 mL) and dried under vacuum.

Yield: 0.403 g, 63.5%. Anal. Calcd. for **2**, $C_{51}H_{39}O_3P_2PtCl$: C, 61.68; H, 3.93. Found: C, 61.09; H, 4.18. Mp = 219.1 °C (dec).

^{1}H and ^{13}C{^{1}H} NMR features are reported in Tables 3 and 2, respectively, except those belonging to PPh_3 groups. PPh_3 region: ^{1}H NMR (400 MHz, dmso-d_6, 25 °C) δ = 7.78–7.16 ppm; ^{13}C{^{1}H} NMR (100 MHz, dmso-d_6, 25 °C) δ = 135–128 ppm.

^{31}P{^{1}H} NMR (121.5 MHz, dmso-d_6, 25 °C): δ = 8.60 ppm (d, $^2J_{PP}$ = 24 Hz, $^1J_{PtP}$ = 3667 Hz); 4.26 ppm (d, $^2J_{PP}$ = 24 Hz, $^1J_{PtP}$ = 3991 Hz).

^{195}Pt{^{1}H} NMR (85.99 MHz, dmso-d_6, 25 °C): δ = −4077 ppm (dd, $^1J_{PtP}$ = 3667 Hz, $^1J_{PtP}$ = 3991 Hz).

IR (nujol mull, cm^1): 3059 (m, C—H), 1613 (s, C═O), 1568 (s, C═C), 1257 (m, C-O-C), 1093 (m, C—H), 996 (m, C-O-C), 755 (s, C—H), 515 (m, Pt—O).

HRMS (ESI, acetonitrile, positive ion mode) *m/z*: calcd. for $C_{51}H_{39}O_3P_2Pt$ $[M-Cl]^+$ 956.2021; found 956.2021.

2.4. Synthesis of cis-[Pt(PPh_3)$_2$(etga)] (etga = dianion of ethyl gallate) (**3**)

A solution of KOH (1.29 mmol, 72.4 mg) in ethanol (4.5 mL) kept at 40 °C was added dropwise to a clear yellow solution of *cis*-[$PtCl_2$(PPh_3)$_2$] (0.64 mmol, 0.505 g) and ethyl gallate (0.64 mmol, 126.8 mg) in CH_2Cl_2 (40 mL) at room temperature under stirring. After overnight stirring at room temperature, the reaction mixture was filtered to remove KCl and the resulting solution was evaporated under reduced pressure and added of CH_2Cl_2 (10 mL). Addition of *n*-pentane (30 mL) caused the precipitation of a yellow solid from the dark yellow solution. The solid was washed with *n*-pentane (3 × 10 mL) and dried under vacuum.

Yield: 0.376 g, 69.1%. Anal. Calcd. for **3**, $C_{39}H_{44}O_5P_2Pt$: C 58.97, H 4.15; found C 58.41, H 4.22.

IR (nujol mull, cm^{-1}): 3496 (s, O—H), 3049 (m, C—H), 2000–1813 (w, aromatic overtone), 1688 (s, C═O), 1591 (s, C═C), 596 (s, Pt—O).

^{1}H NMR (400 MHz dmso-d_6, 25 °C) δ = 7.44 ppm (m, 12H, $H_{ortho,}$ PPh_3), 7.43 ppm (m, 6H, $H_{para,}$ PPh_3), 7.28 ppm (m, 12H, $H_{meta,}$ PPh_3), 6.56 ppm (s, 1H, 6-H), 6.41 ppm (s, 1H, 2-H), 5.60 ppm (s, 1H, 5-H), 4.10 ppm (q, 2H, CH_2, $^3J_{HH}$ = 7.1 Hz), 1.20 ppm (t, 3H, CH_3, $^3J_{HH}$ = 7.1 Hz). ^{13}C{^{1}H} NMR (100 MHz dmso-d_6, 25 °C) δ = 167.2 ppm (s, CO), 163.1 ppm (s, C^3), 154.6 ppm (s, C^4), 144.6 (s, C^5), 134.8 ppm (s, $C_{ortho,}$ PPh_3), 131.8 ppm (s, $C_{para,}$ PPh_3), 128.8 ppm (s, $C_{meta,}$ PPh_3), 128.5 ppm (s, $C_{ipso,}$ PPh_3), 116.8 ppm (s, C^1), 109.6 ppm (s, C^2), 104.3 ppm (s, C^6), 59.9 8 s, CH_2), 14.8 (s, CH_3).

$^{31}P\{^1H\}$ NMR (121.5 MHz, dmso-d_6, 25 °C): δ = 11.2 ppm (d, $^1J_{PtP}$ = 3552 Hz, $^2J_{PP}$ = 24 Hz); 6.4 ppm (d, $^1J_{PtP}$ = 3660 Hz, $^2J_{PP}$ = 24 Hz).

^{195}Pt NMR (85.99 MHz, dmso-d_6, 25 °C): δ = −4062 ppm (*pseudo* t).

HRMS (ESI, acetonitrile, positive ion mode) *m/z*: calcd. for $C_{45}H_{38}O_5P_2Pt$ $[M]^+$ 916.1841; found 916.1845; calcd. for $C_{45}H_{38}O_5P_2PtNa$ $[M + Na]^+$ 938.1739; found 938.1755; calcd. for $C_{45}H_{38}O_5P_2PtK$ $[M + K]^+$ 954.1478; found 954.1496.

2.5. Photodegradation of **2**

Four NMR tubes were filled with a dmso-d_6 solution (0.6 mL) of **2** (10^{-6} mol), two of them under aerobic conditions and the others under nitrogen atmosphere, using de-aerated solvent. Each tube was then capped and a ^1H NMR spectrum was immediately recorded. Afterwards, one of the NMR tubes under air and one under nitrogen were placed in the dark, leaving the others in the daylight. The solutions were checked by ^1H NMR after five days.

2.6. Crystallographic analysis

Compounds **1** and **3** underwent batch crystallization, by slow diffusion of *n*-pentane in a solution of tetrahydrofuran (thf) containing the respective complex. Crystals suitable for diffraction analysis were obtained after 2 weeks.

The single-crystal X-ray diffraction data for crystals **1** and **3** were collected on a Kappa CCD Nonius area detector diffractometer, in φ and ω scans mode. Reflection data were measured at 293 K, using graphite monochromated Mo Kα radiation (λ = 0.71073 Å). Data were corrected for Lorentz and polarization effects [43] and for absorption [44].

The structures were solved by the Patterson deconvolution procedure of SIR2014 [45] and refined by the full-matrix least-squares technique based on F^2 with SHELXL2014/7 [46], using collected reflections with $I \geq 2\sigma(I)$; up to 0.85 Å (crystal **1**) and 0.83 Å (crystal **3**) resolution; measured reflections with $|(I_{obs} - I_{cal})/\mathrm{SigW}(I)| > 10$ were excluded during the refinement process. The non-hydrogen atoms were refined with anisotropic thermal parameters. The aromatic, methyl and hydroxyl hydrogen atoms were placed in calculated positions, refined with isotropic thermal parameters [$U(H) = 1.2U\mathrm{eq(C)}$, $U(H) = 1.5U\mathrm{eq(Me,O)}$], and allowed to ride on their carrier atoms. The SQUEEZE routine in PLATON [47],designed to treat electron density of disordered and diffused solvents, was applied to improve the structure refinement for **1**. Crystallographic data collection and refinement parameters are given in Table 1.

Table 1
Crystal data, experimental details and refinement parameters for **1** and **3**.

	1	**3**
Chemical formula	$C_{51}H_{38}O_7P_2Pt$	$C_{45}H_{38}O_5P_2Pt$
M_r	1019.84	915.78
Crystal system	Orthorhombic	Triclinic
Space group	*Pbnb*	$P\bar{1}$
a, *b*, *c* (Å)	15.372, 22.066, 32.445	11.038, 12.269, 15.242
α, β, γ (°)	90.00, 90.00, 90.00	72.53, 85.17, 89.25
V (Å^3)	11,005.3	1961.9
Z	8	2
F(000)	4064	912
D_x (Mg m^{-3})	1.231	1.550
μ (mm^{-1})	2.65	3.70
Crystal shape	Prismatic	Rod-shaped
Color	Red	Pale yellow
Crystal size (mm)	0.25 × 0.25 × 0.10	0.25 × 0.13 × 0.03
No. of measured reflections	87,739	20,140
No. of independent reflections	9323	7162
R_{int}	0.175	0.127
θ values (°)	θ_{max} = 24.7, θ_{min} = 2.0	θ_{max} = 25.4, θ_{min} = 2.6
$R[F^2 > 2\sigma(F^2)]$, $wR(F^2)$, *S*	0.064, 0.178, 0.98	0.060, 0.167, 0.89
No. of observed reflections [$I > 2\sigma(I)$]	5316	4984
No. of parameters	553	479
$\Delta\rho_{max}$, $\Delta\rho_{min}$ (e Å^{-3})	2.01, −0.73	0.90, −1.54

Molecular graphics were generated by using MERCURY CSD 2.0 [48] and JAV [49]. Two atoms separated by less than the sum of their Van der Waals radii have been considered in contact: for intermolecular contacts the two atoms must belong to different symmetry-equivalent molecules, for intramolecular contacts the additional requirement is that the two atoms must be separated by more than 4 bonds. The cif files CCDC-1430059 for **1** and -1430058 for **3** contain the supplementary crystallographic data for this paper. These data can be obtained free of charge from the Cambridge Crystallographic Data Centre.

2.7. Computational details

In this work we studied the hydrolysis reaction for *cis*-$[Pt(PMe_3)_2(etga)]$, *cis*-$[Pt(PMe_3)_2(3\text{-Hfl})]^+$, and *cis*-$[PtCl_2(PMe_3)_2]$ by means of Density Functional Theory (DFT) calculations using mPW1PW91 functional, which has been previously demonstrated to provide reliable structures and energies for cisplatin and its derivatives [37]. Phenyls in PPh_3 groups have been replaced by methyl (Me) groups for computational convenience. Geometry optimizations were carried out in vacuum and with a 6-31 + G(d) basis set for all atoms except the platinum atom, which was described by the quasi-relativistic Stuttgart–Dresden pseudopotential (SDD) [50]. In order to confirm that stationary points were actually minima or transition state geometries, the analytical calculation of second derivatives of the energy and vibrational frequency analysis were carried out. Due to the key role of solvation in influencing thermodynamic and kinetic parameters in metal complex reactivity [51–55], environmental effects have been introduced by representing water surrounding the reagents, transition states and the products, as a polarizable continuum (PCM) [56]. Potential energy profiles were estimated from total electronic energies and adding zero point energy (ZPE) and thermal corrections at 298.15 K. Total electronic energies plus thermal corrections (instead of free energies) are reported in order to uniform our data to those obtained in previous works [37, 57]. DFT calculations were performed with the Gaussian 09 program [58].

2.8. Cytotoxicity assays and combination index (CI) calculations

Cell Lines: U87 cells from human glioblastoma and MCF-7 cells from breast carcinoma were grown in Dulbecco's modified Eagle's medium (DMEM, Euroclone). The complete culture medium was supplemented with 10% heat-inactivated fetal bovine serum (Euroclone), streptomycin (0.2 mg mL^{-1}), and penicillin (200 IU mL^{-1}). For U87 cells the complete medium was added with 1% of non-essential amino acids. Cells were incubated at 37 °C and 5% CO_2 in a humidified incubator. The cytotoxicity assays were performed as previously described [59]. Briefly, U87 cells from human glioblastoma and MCF-7 cells from breast carcinoma were exposed to tested compounds for a period of 72 h. All tested compounds were dissolved in dmso prior to their dilution with complete cell culture medium to the predetermined experimental concentrations (seven concentrations ranging from 0.10 to 200 μM). In all experiments the percentage of dmso never exceeded 1%. Cytotoxicity (IC_{50}) values for the tested compounds were determined using the metabolic reduction of the soluble 3-(4,5-dimethylthiazol-2-yl)-2,5-diphenyltetrazolium bromide (MTT) by a mitochondrial enzyme of cultured cells into an insoluble colored formazan product. In particular, cells were seeded at a density of about 5000 cells/well in a 96 well plate and incubated at 37 °C for 72 h in the presence and absence of the tested compounds. Untreated cells were used as positive control. Then, 10 μL of 5 mg mL^{-1} MTT solution was added to each well and the plates were incubated for additional 3 h at 37 °C. Next, cells were lysed by the addition of 150 μL of 50% (v/v) dmso and 50% (v/v) ethanol solution, and the absorbance of each individual well was measured using a microplate reader at 570 nm (Wallac Victor3, 1420 Multilabel Counter, Perkin-Elmer). The reported values are the average of triplicate measurements performed in three separate experiments.

The cytotoxic effects measured for tested compounds were further analyzed according to the Chou and Talalay method on CompuSyn software (ComboSyn, Inc., Paramus, NJ, USA) [60]. The combination index (CI) was calculated according to the equation of Chou-Talalay for two drugs: CI = (D)1/(Dx)1 + (D)2/(Dx)2, where (Dx)1 and (Dx)2 are the doses (concentrations) of Drug1 alone and Drug2 alone, respectively, that inhibit x% of cell viability. (D)1 and (D)2 are the doses of Drug1 and Drug2, respectively, used in combination (D)1 + (D)2, able to inhibit x% of cell viability. Complexes **2** and **3** were considered at a fixed-dose-ratio combination (1:1) of their building blocks [(D)1 = (D)2]. CI = 1 indicates an additive effect in the absence of synergism or antagonism; CI < 1 indicates synergism; CI > 1 indicates antagonism.

3. Results and discussion

3.1. Synthesis and characterization of platinum polyphenolate complexes

The synthesis of the platinum polyphenolate complexes was achieved by reaction of *cis*-$[PtCl_2(PPh_3)_2]$ with deprotonated forms of the selected biologically active natural polyphenols in dichloromethane/ethanol [61].

The reaction between *cis*-$[PtCl_2(PPh_3)_2]$ and quercetin leading to *cis*-$[Pt(PPh_3)_2(que)]$ (**1**, que = dianion of quercetin) is depicted in Scheme 4. The target complex was obtained in high yield and ca. 95% purity by slowly adding ethanolic KOH to a dichloromethane solution of *cis*-$PtCl_2(PPh_3)_2$. The presence of ca. 5% impurities, which we were not able to separate from the major product, prevented the use of complex **1** in cytotoxic essays. The formation of side-products in the synthesis of **1** is probably due to the presence of several coordination sites in quercetin [62,63]. Indeed, beside metal complexes whereby quercetin is bonded via $C^{3'}$-O and $C^{4'}$-O [64] as in **1**, metal(II) complexes of quercetin bonded through the keto group (C^4 = O) and the C^3—O oxygen atom are known [21,65,66] and, in principle, also C^7—O bonded metal complexes may form.

When we tried to obtain **1** by adding an ethanolic solution of the pre-formed salt of quercetin to a solution of *cis*-$[PtCl_2(PPh_3)_2]$, the reaction was even less selective and several platinum compounds formed, as shown by ^{31}P NMR analysis.

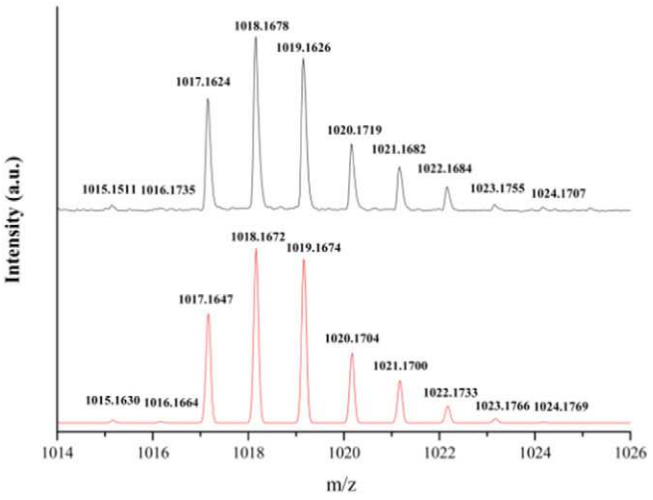

Fig. 1. Experimental (top) and calculated (bottom) HRMS-spectra of **1** showing the ion $[\mathbf{1} - H]^-$. The error between the calculated and observed isotopic patterns is 3.4 ppm.

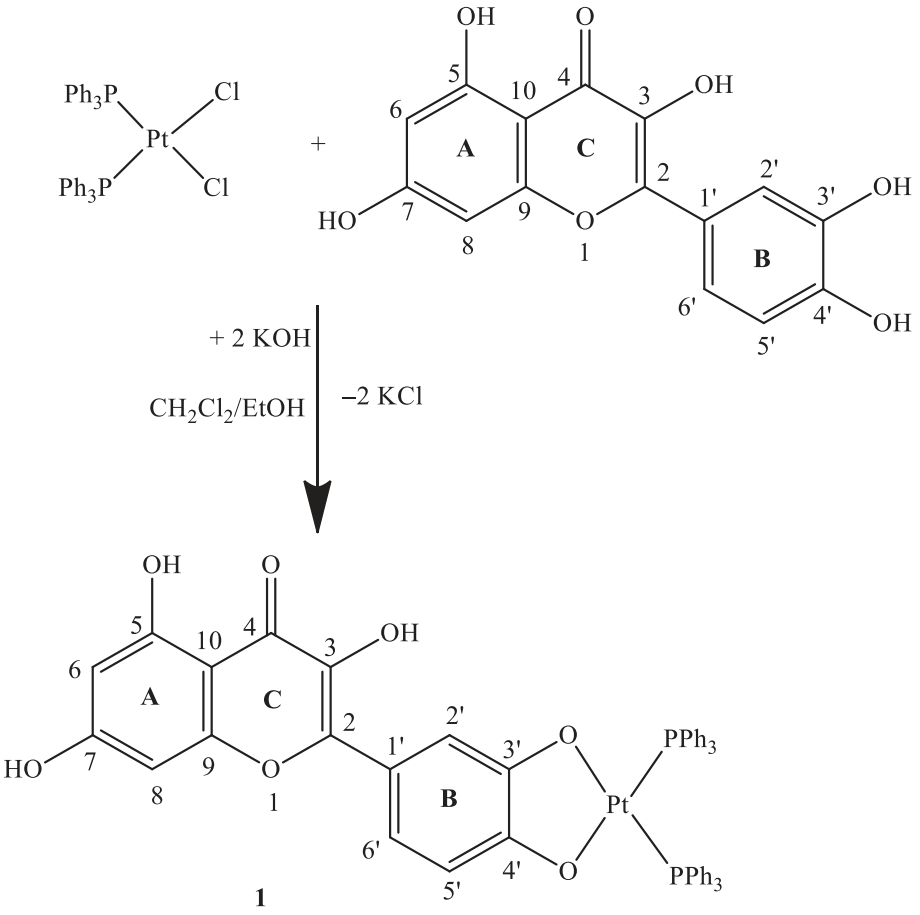

Scheme 4. Synthesis of *cis*-$[Pt(PPh_3)_2(que)]$ (que = dianion of quercetin) (**1**).

Table 2
^{13}C NMR spectral data of **1**, **2** , quercetin and 3-hydroxyflavone (dmso-d_6, 298 K). Bold typeface refers to largest changes in chemical shifts observed comparing free with metal coordinated ligand.

	Complex **1**	Quercetin	Complex **2**	3-Hydroxyflavone
C^2	128.9	135.6	**173.6**	**139.1**
C^3	149.4	146.8	**182.6**	**145.2**
C^4	175.5	175.7	**207.0**	**173.1**
C^5	161	160.6	125.5	124.8
C^6	98.5	98.1	128.9	124.5
C^7	163.8	163.8	134.3	133.7
C^8	93.6	93.3	118.3	118.4
C^9	156.3	156.1	155.2	154.6
C^{10}	103.2	103	121.8	121.2
C$^{1'}$	118.4	121.9	131.8	131.3
C$^{2'}$	114.1	115.1	128.2	127.6
C$^{3'}$	**166.6**	**147.6**	128.4	128.6
C$^{4'}$	**163.4**	**145.0**	129.1	129.6
C$^{5'}$	115.1	115.5	128.4	128.6
C$^{6'}$	118.1	119.9	128.2	127.6

The formula proposed for **1** was confirmed by HR ESI-MS analysis. The ESI-MS spectrogram in negative mode of a diluted acetonitrile solution of **1** showed an intense peak at *m/z* 1018.1678, whose isotope pattern is perfectly superimposable to that calculated for the anion $[C_{51}H_{37}O_7P_2Pt]^-$ (corresponding to [**1**-H]$^-$), obtained by deprotonation of an hydroxyl group under analysis conditions (Fig. 1).

The ^{31}P{^{1}H} NMR spectrum of **1** in dmso-d_6 showed two mutually coupled doublets ($^2J_{P,P}$ = 23 Hz) flanked by ^{195}Pt satellites at δ 9.6 ($^1J_{Pt,P}$ = 3565 Hz) and δ 8.3 ($^1J_{Pt,P}$ = 3600 Hz). The ^{31}P—^{31}P coupling constant indicates a structure in which the PPh_3 groups are mutually *cis*, while the direct ^{31}P—^{195}Pt coupling constant values are compatible with phosphane groups in *trans* position to an oxygen atom [64]. The ^{13}C{^{1}H} NMR spectrum of complex **1** showed a ca. 20 ppm downfield shift with respect to the free ligand of the carbon signals which are close to the coordination sites. The resonance of C$^{3'}$ and C$^{4'}$ signals were found (by means of ^{1}H—^{13}C HMBC and ^{1}H—^{13}C HSQC experiments, Figs. S1 and S2) at δ 166.6 and δ 163.4, respectively, with those of free quercetin falling at δ 143.6 and δ 145.0, respectively (Table 2). All ^{1}H NMR signals were unambiguously assigned by means of 1D and 2D NMR experiments (see Figs. S1–3) and are reported in Table 3. The signal of C^{5}OH ($\Delta\nu_{1/2}$ = 2 Hz) is much sharper than those of C^{3}OH ($\Delta\nu_{1/2}$ = 12 Hz) and C^{7}OH ($\Delta\nu_{1/2}$ = 94 Hz), probably due to the formation of intramolecular C^{5}OH···OC^4 hydrogen bond in solution. This is confirmed by the high value of the chemical shift found for the C^{5}OH proton (δ 12.64). The large broadness of the C^{7}OH proton signal is ascribable to the fast exchange with water. The ^{195}Pt{^{1}H} NMR spectrum of **1** consists of a doublet of doublets at δ −4062, in the region of Pt(II) phosphane complexes [64].

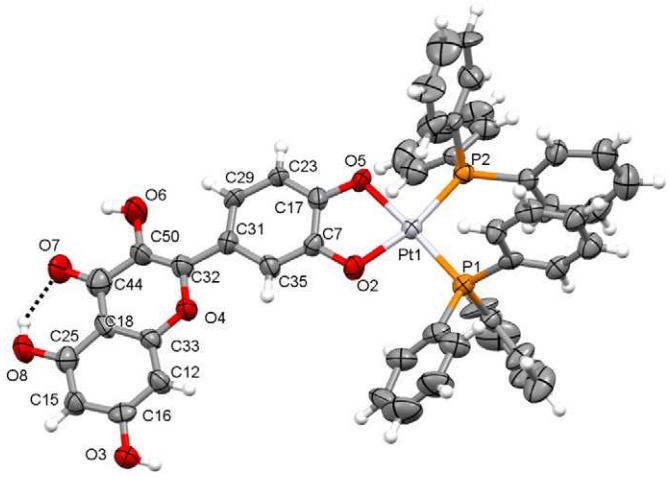

Fig. 2. ORTEP [68] drawing of **1**, by using ellipsoids at 50% probability level.

The IR spectrum of **1** showed broad bands at 3372–3633 cm^{-1} that can be assigned to the hydroxyl groups C^{7}O-H, C^{5}O-H and C^{3}O-H, along with the typical bands ascribed to the skeletal C═C (1650 and 1426 cm^{-1}) and C-O-C (1270 cm^{-1}) stretchings. All IR bands of coordinated deprotonated quercetin are only slightly shifted in comparison to those assigned to free quercetin [67]. In particular, the 1650 cm^{-1} band assigned to the C^4═O stretching (1661 cm^{-1} in free quercetin) confirms that the coordination of quercetin does not involve the oxygen atom of the carbonyl group (the 11 cm^{-1} red-shift can be due to ring deformation caused by platinum bonding to quercetin). Complex **1** was crystallized from thf/*n*-pentane to give crystals suitable for X-ray diffraction. An ORTEP [68] drawing of the molecule is shown in Fig. 2. Table 4 reports selected bond lengths and angles for **1**. The Pt atom has a distorted square-planar coordination geometry imposed by the *O,O′* chelation of quercetin. In the molecular unit of **1** the Pt atom is displaced from the mean plane passing through the basal atoms P1, P2, O5 and O2 by 3.0 Å. The Pt—P (2.25 Å) and Pt—O (2.06 Å) distances are similar to those reported for other triarylphosphane platinum(II) complexes containing chelating phenoxides [69]. Complex **1** has orthorhombic symmetry, and a large crystal cell (cell volume 11,005.3 Å^3, volume per atom 22.6 Å^3). The packing in the crystal cell is dominated by the interactions among the PPh_3 rings, which arrange them in planes perpendicular to the longer *c* axis (Fig. S4). The dianion of quercetin are instead arranged parallel to the *c* axis, spacing out the stacked PPh_3 ligands. The O8–H8 hydroxyl group and O7 give rise, also in the solid state, to an intramolecular hydrogen bond.

Table 3
^{1}H NMR spectral data of **1**, **2**, quercetin and 3-hydroxyflavone (dmso-d_6, 298 K).

	Complex **1**	Quercetin	Complex **2**	3-Hydroxyflavone
H^3	8.81	9.6	–	9.68
H^5	12.64	12.42	8.10 (d, $^3J_{H5,H6}$ = 8.4 Hz)	8.16 (d, $^3J_{H5,H6}$ = 8.1 Hz)
H^6	6.12 (d, $^4J_{H6,H8}$ = 2.1 Hz)	6.18 (d, $^4J_{H6,H8}$ = 2.0 Hz)	7.51 (m)	7.50 (m)
H^7	10.63	10.76	7.87 (m)	7.82 (m)
H^8	6.32 (d, $^4J_{H6,H8}$ = 2.1 Hz)	6.40 (d, $^4J_{H6,H8}$ = 2.0 Hz)	7.98 (d, $^3J_{H7,H8}$ = 7.7 Hz)	7.78 (d, $^3J_{H7,H8}$ = 8.0 Hz)
H$^{2'}$	7.00 (d, $^4J_{H2',H6'}$ = 2.0 Hz)	7.67 (d, $^4J_{H2',H6'}$ = 2.2 Hz)	8.24 (d, $^3J_{H2',H3'}$ = 7.7 Hz)	8.26 (d, $^3J_{H2',H3'}$ = 7.9 Hz)
H$^{3'}$	–	9.31	7.74 (m)	7.63 (m)
H$^{4'}$	–	9.39	7.55 (m)	7.54 (m)
H$^{5'}$	6.19 (d, $^3J_{H5',H6'}$ = 8.4 Hz)	6.89 (d, $^3J_{H5',H6'}$ = 8.3 Hz)	7.74 (m)	7.63 (m)
H$^{6'}$	7.25 (m)	7.53 (dd, 8.3 Hz, 2.2 Hz)	8.24 (d, $^3J_{H5',H6'}$ = 7.7 Hz)	8.26 (d, $^3J_{H5',H6'}$ = 7.9 Hz)

Table 4
Selected bond lengths [Å] and angles [°] for complex **1**.

Bond lengths			
Pt1-P2	2.253(2)	Pt1-O2	2.059(6)
Pt1-P1	2.249(3)	C17-O5	1.338(10)
Pt1-O5	2.055(6)	C7-O2	1.386(10)
Angles			
P1-Pt1-P2	98.67(9)	P2-Pt1-O2	167.27(19)
P2-Pt1-O5	84.78(18)	P1-Pt1-O2	93.48(18)
P1-Pt1-O5	176.51(18)	Pt1-O2-C7	108.0(57)
Pt2-O3'-C17	110.6(6)	O5-Pt1-O2	83.0(2)

DFT calculations on the relative stability of all the possible Pt-quercetin coordination isomers confirmed that the structure reported in Fig. 2 is the most stable one (see Scheme S1 and Table S1).

When 3-hydroxyflavone reacted with *cis*-$[PtCl_2(PPh_3)_2]$ under alkaline conditions, complex salt *cis*-$[Pt(PPh_3)_2(3\text{-Hfl})]Cl$ (**2**, 3-Hfl = monoanion of 3-hydroxyflavone) formed (Scheme 5), in which deprotonated 3-hydroxyflavone coordinates Pt through its O^3 and O^4 atoms. The formula proposed for **2** was indicated by HR ESI(+)-MS analysis which showed an intense peak at *m/z* 956.2021, whose isotope pattern is perfectly superimposable to that calculated for $[C_{51}H_{39}O_3P_2Pt]$ corresponding to the cation *cis*-$[Pt(PPh_3)_2(3\text{-Hfl})]^+$ (experimental and calculated HRMS-spectra are reported in Fig. S5).

The ionic structure for **2** was confirmed by comparing the dmso-d_6 solution $^{31}P\{^1H\}$ NMR signals of **2** before and after addition of solid $AgBF_4$. The addition of $AgBF_4$ to the yellow solution of **2** caused the immediate precipitation of AgCl, and the chemical shifts of the ^{31}P NMR signals of **2** did not change after replacement of the chloride with a poorly coordinating anion (BF_4^-), ruling out, for instance, the possibility of a neutral penta-coordinated structure [30] for **2**.

^1H, ^{31}P and ^{195}Pt NMR features of **2** (Table 3 and Experimental Section) are consistent with the structure proposed in Scheme 5. As for complex **1**, the $^{13}C\{^1H\}$ NMR spectrum of **2** showed a significant downfield shift of the carbon signals close to the coordination site (Table 2). On the contrary, the ^{13}C NMR chemical shift values belonging to nuclei of A- and B-rings were very similar to the ones reported for free 3-hydroxyflavone [70]. The IR spectrum of **2** exhibited a strong sharp peak at 1613 cm^{-1} which can be assigned to the coordinated carbonyl group, while no absorptions were observed in the O—H stretching region. The ca. 50 cm^{-1} red shift of the carbonyl band observed with respect to free 3-hydroxyflavone [62] indicates that the metal coordination involves the oxygen atom of the carbonyl group. Theoretical vibrational analysis qualitatively confirms the frequency (Table S2) of the coordinated carbonyl stretching mode (1593 cm^{-1}), red-shifted with respect to that calculated for the free ligand (1700 cm^{-1}).

Single crystals of **2** obtained by slow diffusion of *n*-pentane into the thf reaction solution were submitted to XRD analysis, but were not of sufficient quality to warrant a complete X-ray structure determination. Nonetheless, the collected data confirmed unambiguously for **2** the atom connectivity shown in Scheme 5, with the chlorine atom, whose refined occupancy was 0.45, placed in the same plane of the monoanion

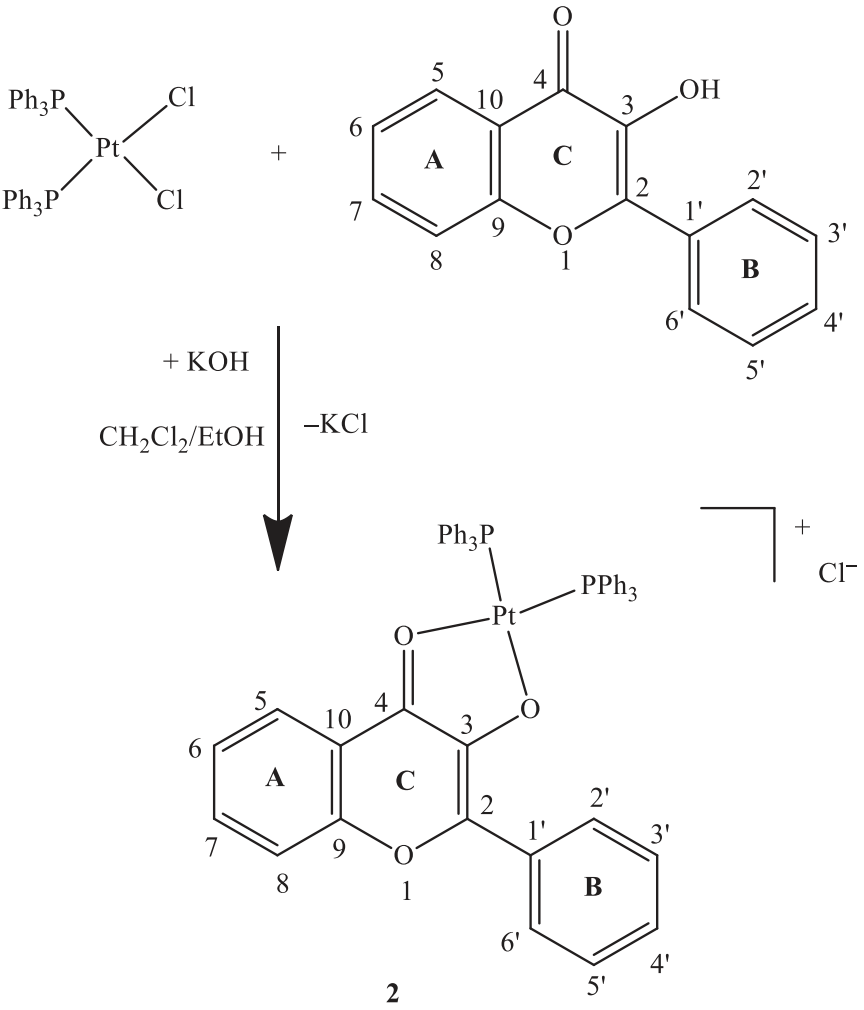

Scheme 5. Synthesis of *cis*-$[Pt(PPh_3)_2(3\text{-Hfl})]Cl$ (3-Hfl = monoanion of 3-hydroxyflavone) (**2**).

of 3-hydroxyflavone unit and far away from the coordination sphere of the platinum center. Three additional molecules were found in the elementary cell (vide infra), due to photodegradation processes.

Complex **3** was synthesized by reacting ethyl gallate with *cis*-$[PtCl_2(PPh_3)_2]$ under alkaline conditions (Scheme 6). The formula proposed for **3** was confirmed by HR ESI-MS analysis. The ESI-MS spectrogram in positive mode of **3** showed an intense peak at *m/z* 916.1845, whose isotope pattern is perfectly superimposable to that calculated for the radical cation $[C_{45}H_{38}O_5P_2Pt]^+$ (corresponding to $[\mathbf{3}]^+$, (experimental and calculated HRMS-spectra are reported in Fig. S6).

The $^{31}P\{^1H\}$ NMR spectrum of **3** in dmso-d_6 showed the expected doublets at δ 11.2 ($^1J_{Pt,P}$ = 3552 Hz) and δ 6.4 ($^1J_{Pt,P}$ 3660 Hz), while the $^{195}Pt\{^1H\}$ NMR spectrum showed a pseudo-triplet at δ −4400. The C^5—OH proton of **3** (δ 5.60) was significantly shielded respect to the free ligand (δ 9.30), presumably due to the weakening of the hydrogen bond system caused by Pt coordination. The $^{13}C\{^1H\}$ NMR spectrum confirmed the coordination of the C^3—O and C^4—O phenoxides onto Pt: C^3 and C^4 signals of the coordinated ethyl gallate were found at δ 163.1 and δ 154.6, ca. 18 ppm down-field shifted respect to the free ligand (δ 145.6 for C^3 and δ 138.3 for C^4).

Slow diffusion of *n*-pentane into a thf solution of **3** afforded crystals suitable for XRD analysis. An ORTEP [68] drawing of **3** is shown in Fig. 3, while relevant bond lengths and angles are collected in Table 5. The Pt atom adopts an almost square-planar coordination geometry imposed by the *O,O′* chelation of the dianion of ethyl gallate, as well as by the crystal packing on the PPh_3 ligands (Fig. S7). In the elementary cell, ethyl gallate moieties are all aligned in the (113) plane. Deviation from planarity of the PtP2O2 plane was observed, as measured by the improper dihedral angle value (3.2°), being the plane of the two P atoms rotated with respect to the plane of the ethyl gallate molecule.

3.2. Photo degradation of **2** under aerobic conditions

The photo degradation of 3-hydroxyflavone to 3-hydroxy-3-phenyl-1,2-indandione (**4**, Scheme 7) [71] is a well-known phenomenon, which has attracted the interest of the academic community [71–74], because it affects both biological and antioxidant activities [75] of 3-hydroxyflavone as well as its peculiar photochemical properties [76–81].

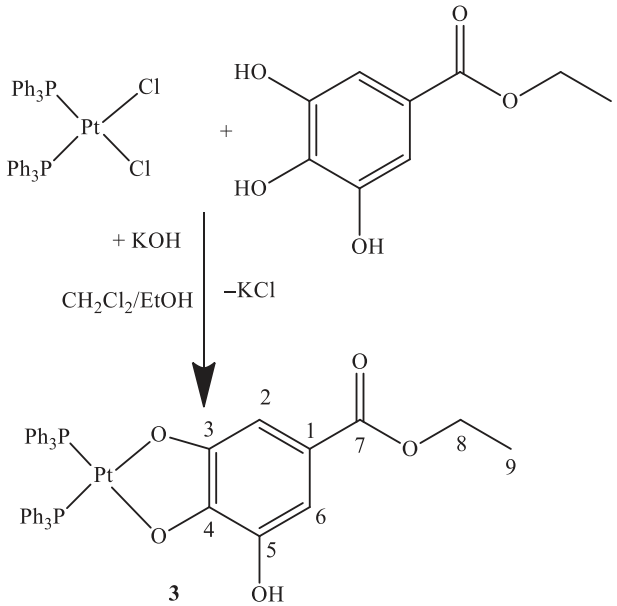

Scheme 6. Synthesis of *cis*-$[Pt(PPh_3)_2(etga)]$ (etga = dianion of ethyl gallate) (**3**).

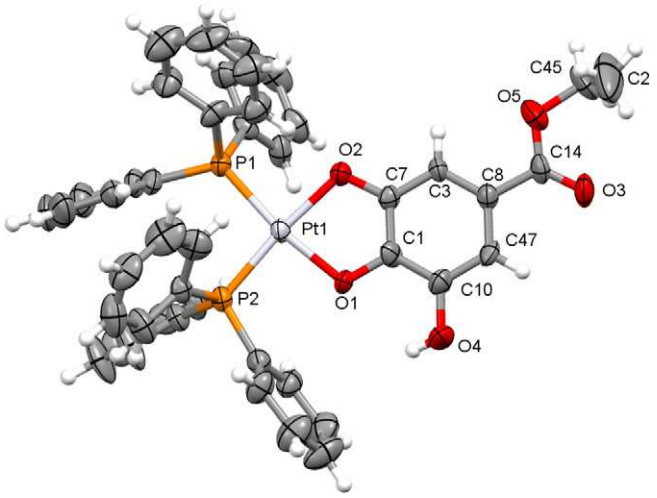

Fig. 3. ORTEP [68] drawing of **3** by using ellipsoids at 50% probability level.

Conrard and coworkers reported that Zn(II) and Pb(II) 3-hydroxyflavonate complexes decompose when exposed to daylight affording **4** under both aerobic and anaerobic conditions, thus indicating that the coordination to the metal center does not influence the decomposition pathway [82].

On the contrary, Berreau and coworkers reported that Pb(II), Zn(II), Ru(II) and other divalent metal flavonolate complexes undergo oxidative photochemical degradation with loss of CO [83] and formation of *O*-benzoyl salicylate complexes under aerobic conditions, and can act as catalysts for the photoinduced oxidative ring opening of 3-hydroxyflavone to give O-benzoyl salicylic acid (**5**) [84–85]. A similar behavior was observed by Speier and coworkers for Cu(II) flavonolate complexes under aerobic and thermal conditions [86].

In our case, we observed an oxidative photo degradation of **2** under aerobic conditions. In fact, when a dmso-d_6 solution of **2** was left standing under air in the daylight for five days, a new compound formed in ca. 10% yield, which was characterized by NMR (Fig. S8) and GC–MS as *O*-benzoyl salicylic acid (**5**). This compound was not observed when a similar solution of **2** was left standing for ten days either in the dark and/or in the absence of dioxygen.

In addition, as previously mentioned, XRD analyses of crystals obtained by a slow diffusion of *n*-pentane/thf solution of **2** kept one month under air in daylight showed in the elementary cell additional atoms beside those belonging to complex **2**. They have been placed to interpret clear peaks emerging in the difference Fourier electron density, and allowed to improve significantly the refinement of the whole structure. Such atoms are grouped to form three additional molecules: a salicylic acid, a thf (crystallization solvent) molecule and a fragment, which was tentatively identified as benzoic acid, but whose low resolution prevented a conclusive assignment.

On the basis of these observations, the photo degradation pathway followed by **2** should resemble the one already reported by Berreau

Table 5
Selected bond lengths [Å] and angles [°] for complex **3**.

Bond lengths			
Pt1-P1	2.261(3)	Pt1-O1	2.028(7)
Pt1-P2	2.260(3)	C7-O2	1.346(13)
Pt1-O2	2.053(7)	C1-O1	1.357(13)
Angles			
P1-Pt1-P2	99.17(10)	P1-Pt1-O1	169.9(2)
P1-Pt1-O2	87.6(2)	P2-Pt1-O1	90.4(2)
P2-Pt1-O2	172.3(2)	Pt1-O2-C7	109.6(6)
Pt1-O1-C1	110.3(6)	O1-Pt1-O2	83.1(3)

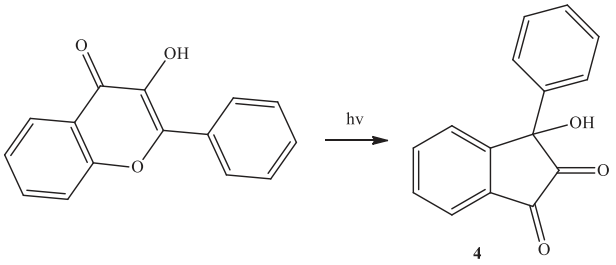

Scheme 7. Photo degradation of 3-hydroxyflavone in the absence of metal ions.

and coworkers for Ru(II) flavonolate complexes [83] (Scheme 8). Aerobic oxidation of **2** would result in a carbonyl Pt complex bonded to the anion of *O*-benzoyl salicylic acid. This intermediate can decompose, in the presence of adventitious water, to give **5** plus unidentified Pt species. The formation of salicylic acid and benzoic acid during slow crystallization of **2** in *n*-pentane/thf might then derive from hydrolysis of **5**.

3.3. DFT calculations

On the basis of a large number of experimental data, it is widely accepted that the hydrolysis of platinum(II) anticancer complexes is a bimolecular nucleophilic substitution (S_N2) which is the rate-determining step of the process leading to the formation of the adduct with DNA nucleobases [36]. In particular, for cisplatin the mono-aquo species is believed to be the key player, since it coordinates to the N7 atom of a guanine base in DNA producing a monofunctional adduct [36,87]. Once coordinated, the second chloride is released and platinum binds a second base producing the crosslink, which distorts DNA [36]. Due to their importance, the hydrolysis reactions of platinum complexes have been studied by means of a variety of theoretical methods in the last decade [37–41]. In our case, the activation energies for the hydrolysis reactions of complexes **2** and **3** have been calculated because they could be correlated to their potential synergic cytotoxicity, since polyphenols are released in solution.

The first hydrolysis leads to the ring-opening process, with the 3-Hfl and etga derivatives remaining mono-coordinated to the metal ion center. The second hydrolysis (second step) leads to the complete release of 3-Hfl and etga (Scheme 9). For comparison purposes, we considered also the hydrolysis of *cis*-[Pt(PMe_3)$_2$(Cl_2)] (see Supplementary Information), and that of cisplatin [37].

3.3.1. Hydrolysis reaction for *cis*-[Pt(PMe_3)$_2$(etga)]

The theoretical geometry of the model complex *cis*-[Pt(PMe_3)$_2$(etga)] (Table S3) is in excellent agreement with the experimental ones found for complex **3** (Table 5), thus confirming the reliability of the computational protocol used. In Fig. 4 the structures of reactants (R), products (P) and transition states (TS) are shown for both reaction paths of *cis*-[Pt(PMe_3)$_2$(etga)] (Scheme 9a). Relevant bond distances of all optimized complexes are reported in Table S3 and S4.

The reaction energy (E) profiles are shown in Fig. 5 (Table S5). The energy values are referred to the separated reactants (R) rather than reactant adducts (RA) (Fig. 4), since it is widely accepted that at the beginning of the reaction, the water molecule in the second coordination shell of the metal is possible only in vacuum, but it seems an artifact in solution [88,89]. The detachment of the etga ligand in the first hydrolysis can occur in two different ways (Scheme 9a): by breaking of the bond that involves the oxygen in α position to the OH group (O1 path) or the other Pt—O bond (O2 path). Both O1 and O2 paths (Fig. 4a) showed

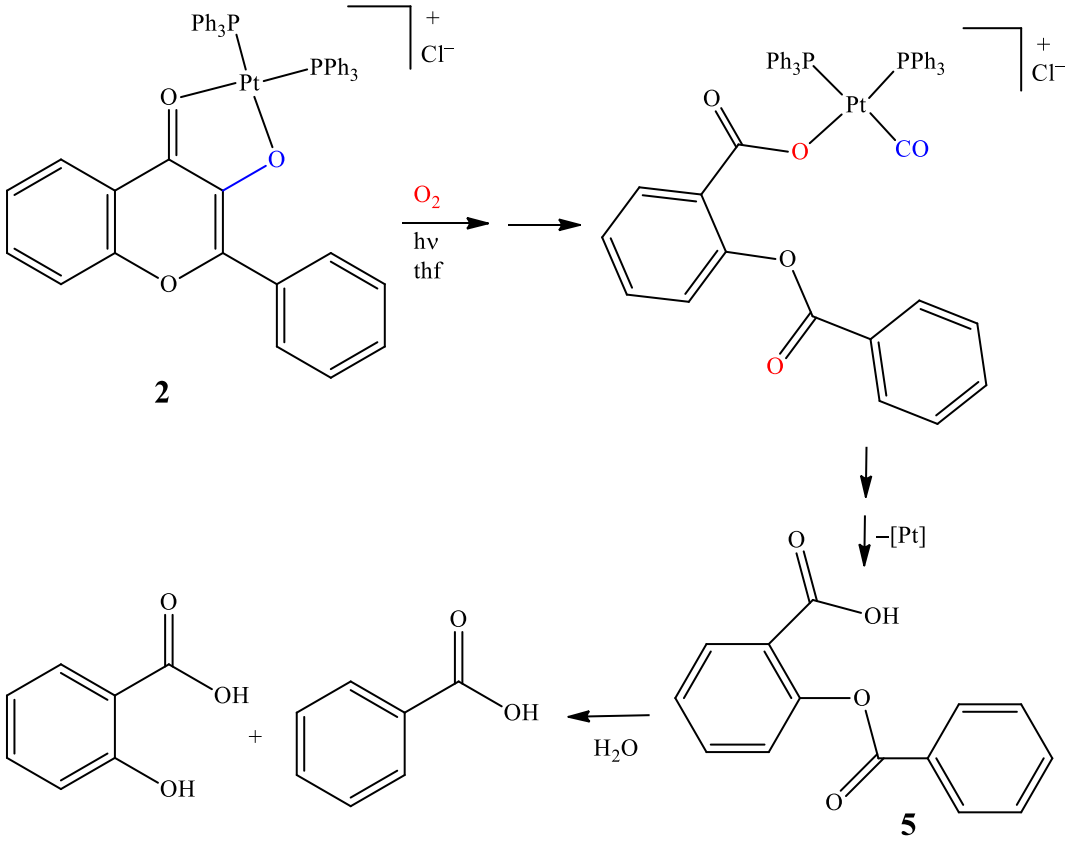

Scheme 8. Plausible pathway for the aerobic photo degradation of **2**. [Pt] represents undefined Pt species.

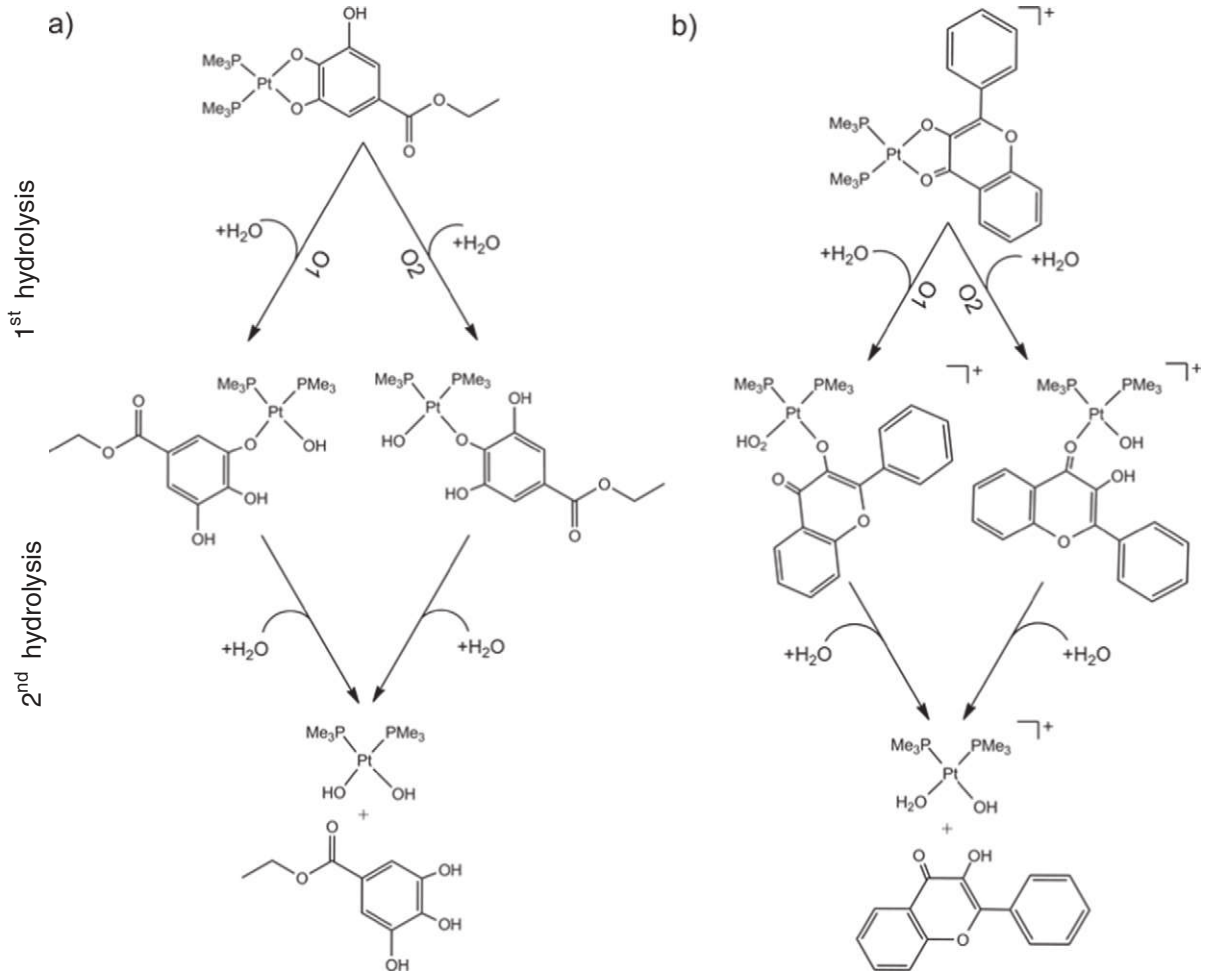

Scheme 9. Hydrolysis reactions for: a) *cis*-[Pt(PMe_3)$_2$(etga)] and b) *cis*-Pt[(PMe_3)$_2$(3-Hfl)]$^+$.

a proton transfer from the incoming water molecule to the closer oxygen of the ligand (OL). This result has been previously reported also for the hydrolysis of other platinum drugs under neutral conditions [39,40]. Mono- and di-hydroxo complexes should form under physiological conditions, although it has been reported that the local pH in the vicinity of macromolecules could be different from the physiological one [90,91].

The energy profiles for the first step of the hydrolysis indicate that the formation of the reactant adducts (RA1-O1 and RA1-O2) is energetically favored (Fig. 5a and Table S5).

Both transition states TS1-O1 and TS1-O2 have a penta-coordinated structure, with imaginary frequencies of 99.7 cm^{-1} for TS1-O1 and 157.8 cm^{-1} for TS1-O2 corresponding to the rupture of the platinum-ligand bond (Pt-OL) and the simultaneous formation of a new bond between the metal and a water molecule. The activation energies ($E_a = E_{transition\ state} - E_{reactants}$) for the two paths are rather different: for the O1 path E_a = 22.8 kcal mol^{-1}, while the O2 path shows a E_a = 18.7 kcal mol^{-1} (Table S5). According to these results, the release of ethyl gallate by the opening of the Pt—O2 bond is kinetically preferred. Furthermore, O2 pathway leads to the most stable product [ΔE = E(PA1-O1) – E(PA1-O2) = 3.6 kcal mol^{-1}]. This difference could be due to the formation of *two* hydrogen bonds in the case of PA1-O2 with respect to PA1-O1 where only *one* hydrogen bond is possible (Fig. 4a).

The transition states in the second hydrolysis have a penta-coordinated structure with imaginary frequencies of 103.9 cm^{-1} for TS2-O1 and 101.7 cm^{-1} for TS2-O2 (Fig. 4b) corresponding to the simultaneous rupture of the bond between platinum and the ligand (Pt-OL) and the formation of the metal-water bond. The calculated profiles (Fig. 5b) show that the two reaction paths have comparable activation energy [$\Delta E_a = E_a$(TS2-O1) – E_a(TS2-O2) = 0.4 kcal mol^{-1}, Table S5]. Also the final products (P2) have almost the same energy of TS2-O1 and TS2-O2 (Table S5).

As shown in Fig. 5 and Table S5, the first hydrolysis step has a higher activation energy with respect to the second step, irrespective of the ring opening order, thus the first hydrolysis process is the rate determining step (RDS) of the whole reaction leading to the release of ethyl gallate in solution.

Regarding the first hydrolysis (Fig. 5a), by comparing the energy profiles of *cis*-[Pt(PMe_3)$_2$(etga)] with those of the highly cytotoxic cisplatin, it appears that the E_a in O2 path is lower than the cisplatin one ($\Delta E_a = E_a$(TS1-O2) – E_a(cisplatin) = −2.7 kcal mol^{-1}); on the contrary the E_a in O1 path is higher than the one calculated for cisplatin (ΔE_a = +1.4 kcal mol^{-1}) (Fig. 5a and Table S5). For the second hydrolysis step, E_a values for both O1 and O2 paths are much lower than cisplatin one (ΔE_a = −6 kcal mol^{-1} for O1 path and ΔE_a = −6.4 kcal mol^{-1} for O2 path) (Fig. 5b and Table S5). The obtained results suggest that *cis*-[Pt(PMe_3)$_2$(etga)] leads to a mono-hydroxo complex with etga mono-coordinated to the metal, which promptly reacts with another water molecule giving the di-hydroxo species. The mono-hydroxo and di-hydroxo species are considered poorly reactive for DNA coordination, thus their formation can limit the efficacy of a platinum metallodrug

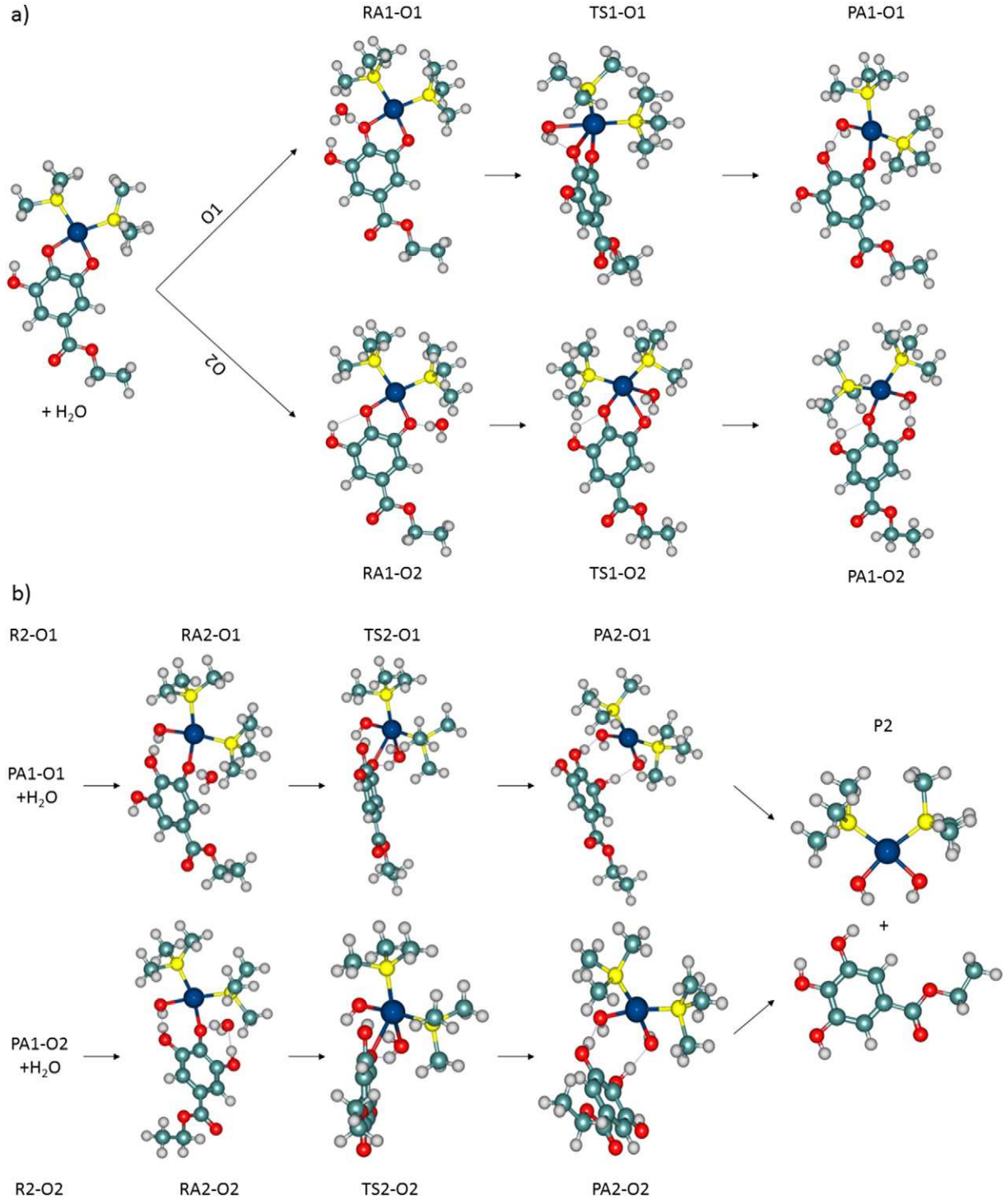

Fig. 4. Optimized structures for the hydrolysis reaction of *cis*-[Pt(PMe_3)$_2$(etga)]. a) First step; b) second step.

[92]. Furthermore, the low activation energy barriers of the second step and the consequent high hydrolysis reaction rate might make this complex subject to fast degradation, causing potentially poor pharmacological activity [93]. The obtained E_a value (11.3 kcal mol^{-1}) calculated for the first hydrolysis of *cis*-[$PtCl_2(PMe_3)_2$] (taken as a model for the biologically inactive (vide infra) *cis*-[$PtCl_2(PPh_3)_2$]) is much lower than the E_a calculated for *cis*-[Pt(PMe_3)$_2$(etga)] and cisplatin (Fig. 5 and Table S5). Then, the E_a calculated for the second hydrolysis of [Pt(PMe_3)$_2$(etga)] is close to that of *cis*-[$PtCl_2(PMe_3)_2$] (Fig. 5) and much lower than cisplatin. On this basis of DFT calculations, complex **3** should not be expected highly cytotoxic.

3.3.2. Hydrolysis reaction for *cis*-[Pt(PMe_3)$_2$(3-Hfl)]$^+$

In Fig. 6 the optimized structures of the complexes involved in the hydrolysis of *cis*-[Pt(PMe_3)$_2$(3-Hfl)]$^+$ are displayed, with relevant bond distances reported in Tables S6 and S7.

The energy profiles for the reactions in Scheme 9b are shown in Fig. 7 (values in Table S5).

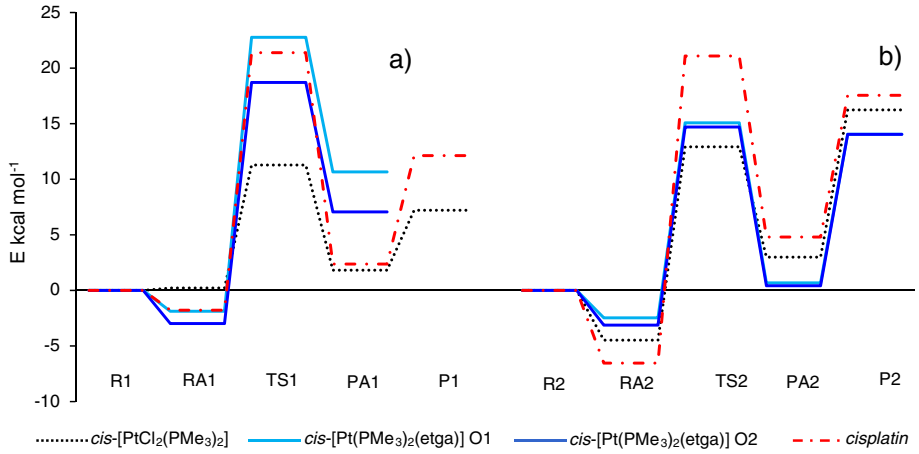

Fig. 5. Activation energy profiles of: a) the first and b) the second step of the hydrolysis reaction of *cis*-[Pt(PMe_3)$_2$(etga)] (both O1 and O2 paths), *cis*-[$PtCl_2(PMe_3)_2$] and cisplatin in PCM water. The energy values for cisplatin are taken from ref. [37].

The formation of the intermediate RA1-O2 is slightly energetically favored, while RA1-O1 formation energy is slightly positive. Also in this case, the transition states of both O1 and O2 paths have a penta-coordinated structure with imaginary frequencies of 87 cm^{-1} for TS-O1 and 78 cm^{-1} for TS-O2. The calculated E_a values are 14.4 kcal mol^{-1} and 15.7 kcal mol^{-1} for O1 and O2 path, respectively. The O1 opening produces the mono-aqua derivative, while in the O2 path a proton transfer leading to the mono-hydroxo complex occurs. Also the PA1-O1 is more stable than PA1-O2 [ΔE = E(PA1-O1) − E(PA1-O2) = −1.7 kcal mol^{-1}, Table S5]. In conclusion, in the first hydrolysis step the O1 path, leading to a monoaqua Pt complex, should be more favored than the O2 one (which leads to a monohydroxo Pt complex).

In the second hydrolysis (Fig. 7b), transition states with a penta-coordinated Pt geometry are obtained characterized by a single imaginary frequency (89 cm^{-1} for TS2-O1 and 83 cm^{-1} for TS2-O2). The calculated E_a values are 11.9 kcal mol^{-1} and 9.5 kcal mol^{-1} for O1 and O2 path, respectively (Table S5). Therefore, also for *cis*-[Pt(PMe_3)$_2$(3-Hfl)]$^+$ the first hydrolysis is the rate determining step of the whole process leading to the complete release of the 3-Hfl. Furthermore, by analyzing the obtained E_a values (Fig. 7b, Table S5), it emerges that the second hydrolysis step proceeds faster for *cis*-[Pt(PMe_3)$_2$(3-Hfl)]$^+$ (both O1 and O2 paths) than for cisplatin and *cis*-Pt(PMe_3)$_2$(egta). On the contrary, the first hydrolysis is slower for *cis*-[Pt(PMe_3)$_2$(3-Hfl)]$^+$ with respect to *cis*-[$PtCl_2(PMe_3)_2$] (Fig. 7a, Table S5).

In the O1 path the final product shows a proton transfer from the water molecule bonded to platinum to the closer oxygen of the ligand, while in the O2 path this does not occur. The final product of *cis*-[Pt(PMe_3)$_2$(3-Hfl)]$^+$ hydrolysis is the monoaqua-monohydroxo complex (*cis*-[Pt(PMe_3)$_2$(H_2O)(OH)]$^+$, Fig. 6b).

On the basis of DFT calculations, some synergic cytotoxic effect between platinum center and 3-hydroxyflavon leaving group effect might be expected for *cis*-Pt[(PMe_3)$_2$(3-Hfl)]$^+$, because the monoaqua platinum species formed in both first and second hydrolysis steps, could coordinate DNA [36]. On the other hand, the theoretical hydrolysis activation energy (mainly affected by the *trans* influence of the carrier ligand), is significantly lower with respect to cisplatin (Fig. 7) and could lead to fast deactivation of platinum compound and thus poorer biological activity [93].

3.4. Cytotoxicity

The antiproliferative potential of the new complexes **2** and **3** was assessed in human glioblastoma (U87) and human breast cancer (MFC-7) cells, being the first cellular line sensitive to cisplatin and the latter cisplatin resistant. Since complex **2** was found to be photosensitive (see paragraph *3.2*), cytotoxicity studies were carried out in the dark for all examined compounds, in order to avoid photodegradation processes. Complex **1** was not taken into consideration, due to the difficulty in separating it from the side-products formed in minor amounts during its synthesis.

For comparison purposes, the cytotoxicity of 3-hydroxyflavone, ethyl gallate and *cis*-[$PtCl_2(PPh_3)_2$] was evaluated under the same experimental conditions employed for the other metal complexes. Cellular viability was determined by colorimetric MTT assay [MTT = 3-(4,5-dimethylthiazol-2-yl)-2,5-diphenyltetrazolium bromide]. The viability of cells in the presence of the tested compounds was compared to that observed for control cultures and the inhibition of growth (%) was calculated. The half maximal inhibitory concentration (IC_{50}) values obtained following exposure to increasing concentrations (from 0.10 to 200 μM) of the different compounds for 72 h are shown in Table 6, which reports also the relevant IC_{50} values for cisplatin taken from the literature [94,95].

At the tested concentrations, the Pt complexes **2** and **3** showed a different biological effect on both U87 and MCF-7 cell lines (Table 6), being **2** more cytotoxic than **3**, following the same trend observed for the relevant ligands. In fact, 3-hydroxyflavone was found more cytotoxic than ethyl gallate on the examined cell lines. This behavior confirms what predicted by DFT calculations (see previous paragraph), that is complexes **2** and **3** easily lose their natural ligands with the consequence that their cytotoxicity is mainly affected by the biological activity of their leaving groups. Theoretical studies also predicted that the platinum species (intermediates and final product) obtained from the hydrolysis of complex **3** should poorly interact with DNA: thus the cytotoxicity of complex **3** is expected to be determined by ethyl gallate only (no synergic effect). Interestingly, considering the cytotoxicity on MFC-7 cells, complex **2** is more active than the basic compounds, i.e. 3-hydroxyflavone and *cis*-[$PtCl_2(PPh_3)_2$], the latter having a very negligible in vitro cytotoxicity (IC_{50} > 200 μM) for both studied cell lines. The synergism shown by **2** could be related to the formation of mono-aqua platinum species which are known to interact with DNA [36].

It is widely recognized that the anticancer mechanism of cisplatin and, by extension, of the related platinum drugs is formed by four steps: (i) cellular uptake, (ii) aquation/activation, (iii) DNA binding and (iv) cellular processing of DNA lesions leading to apoptosis [96]. Two pathways have been proposed for the first step: passive diffusion through the plasma membrane and active transport mediated by membrane proteins [97]. The majority of the academic world thinks that rapid diffusion is the predominant cisplatin uptake mechanism [98].

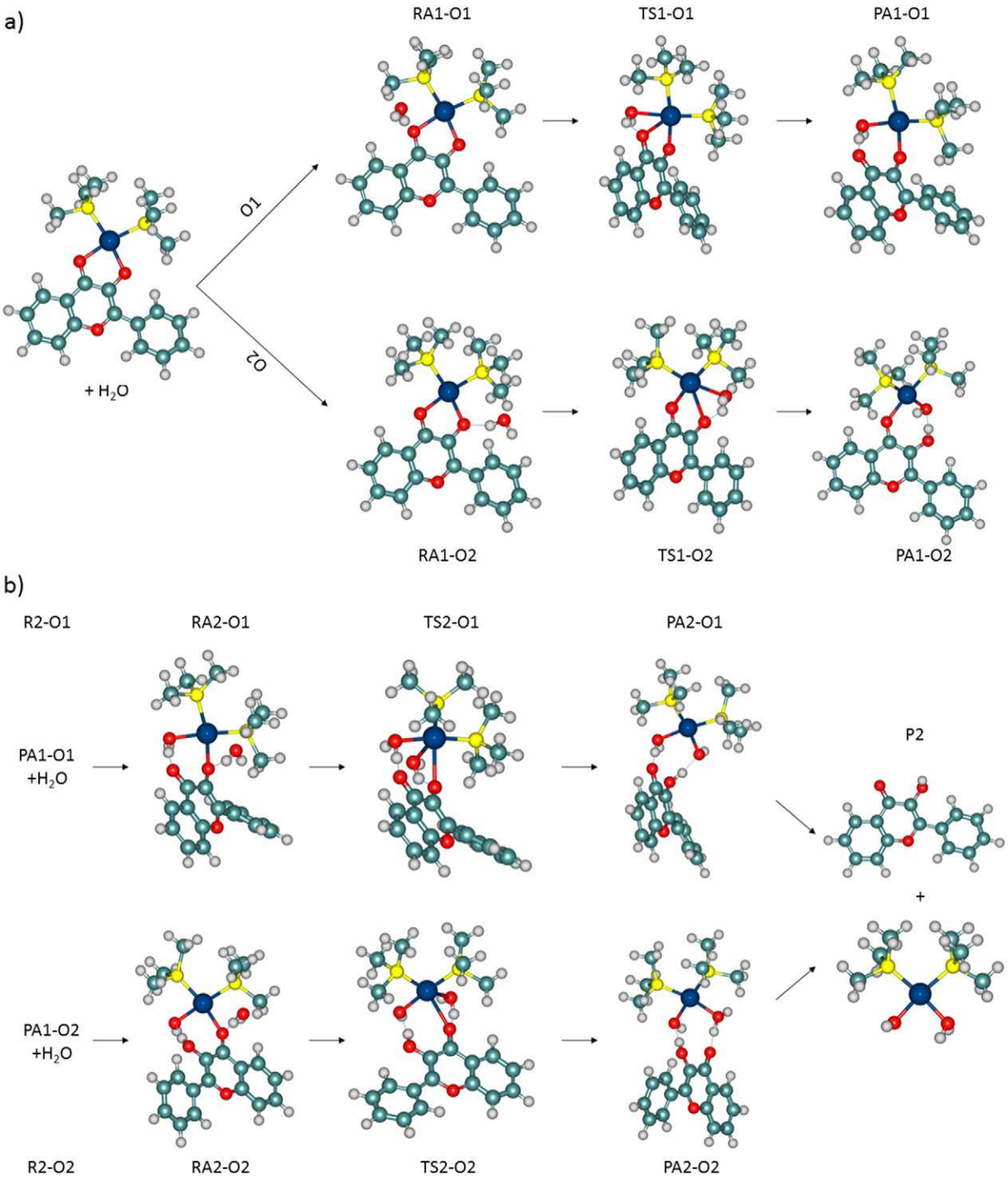

Fig. 6. Optimized structures for the hydrolysis reaction of *cis*-$[Pt(PMe_3)_2(3\text{-Hfl})]^+$. a) First step; b) second step.

For example, drug accumulation experiments [99] carried out on two different cancer lines (colon carcinoma and colon mesothelioma) have shown that the intracellular (nucleus + cytoplasm) Pt concentration was 3–6 μM after one hour of 5 μM cisplatin incubation. In other words, the measured intracellular Pt concentration was quite similar to the Pt concentration in the medium after only one hour of exposure.

In another study [100], cellular platinum accumulation measurements were carried out on MDA-MB-435 breast cancer cells and PC-3 cells after 2 h, 4 h and 6 h of treatment at 20 μM of cisplatin and of some new neutral and cationic Pt complexes. These experiments have shown that in most cases (including cisplatin) the cellular Pt concentration found after 2 h was approximately equal to that measured after 6 h. Notably, a higher platinum cellular uptake was found for cationic mononuclear platinum compounds with respect to cisplatin. Also Quirante and coworkers [101] noticed the same behavior for their cationic mononuclear Pt compounds.

To gain insights into the stability of complex **2** under physiological conditions, a 200 μM solution of **2** in cell culture media kept in the dark at 37 °C was time monitored by means of $^{31}P\{^1H\}$ and ^1H NMR. We found out that compound **2** completely lost its polyphenol ligand after 3 h under physiological conditions. On the basis of the all over reported findings, we could assume that 3 h might be a reasonable period of time for complex **2** to pass the cell's lipid bilayer (compound **2** bears lipophilic thiphenylphosphane ligands).

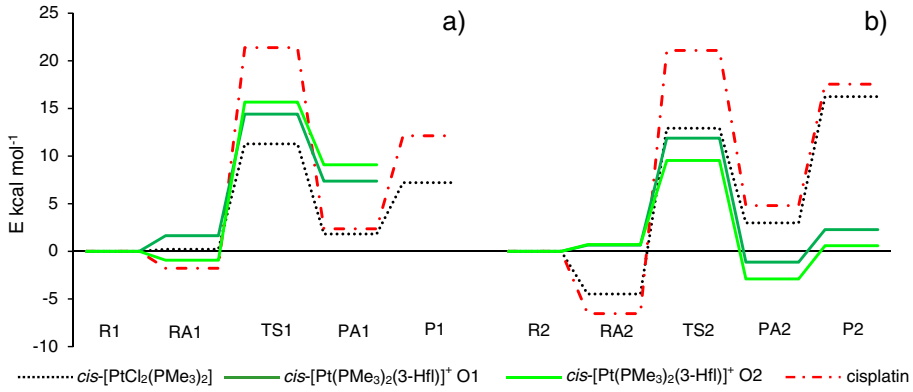

Fig. 7. Activation energy profiles of: a) the first and b) the second step of the hydrolysis reaction of *cis*-$[Pt(PMe_3)_2(3\text{-Hfl})]^+$ (both O1 and O2 paths), *cis*-$[PtCl_2(PMe_3)_2]$ and cisplatin in PCM water. The energy values for cisplatin are taken from ref. [37].

Table 6
Cytotoxicity of hydroxyflavone, ethyl gallate, Pt complex **2**, Pt complex **3**, *cis*-$[PtCl_2(PPh_3)_2]$ and cisplatin toward U87 and MCF-7 cancer cell lines.

	IC_{50} (μM)	
Compound	**U87**[a]	**MCF-7**[a]
Complex **2**	26.3 ± 2.1	55.2 ± 1.7
3-Hydroxyflavone	27.5 ± 2.3	108.1 ± 3.5
Complex **3**	123.7 ± 3.8	>200
Ethyl gallate	97.7 ± 2.6	>200
cis-$[PtCl_2(PPh_3)_2]$	>200	>200
Cisplatin	1.76 ± 0.22[b]	14 ± 3[c]

[a] Cells were seeded at a density of ~5000 cells per well into 96-well microliter plates. Following overnight incubation, cells were treated with a range of drug concentrations (from 0.10 to 200 μM) and incubated at 37 °C under a humidified atmosphere with 5% CO_2 for a period of 72 h. Data are the mean values ± SD of three independent experiments performed in triplicate.
[b] Data taken from ref. [94].
[c] Data taken from ref. [95].

On the other hand, some studies have reported that cell uptake per se may not necessarily give an indication of the level of the antitumor activity [102],

We also evaluated the combination index (CI), which allows to compare the single-drug dose-response to that of their combination. In complexes **2** and **3** the ratio between *cis*-$[PtCl_2(PPh_3)_2]$ and 3-hydroxyflavone or ethyl gallate was set to 1:1, respectively. The isobologram study evidenced that CI values were always >1 for complex **3**, indicating no synergic effect between the polyphenol ligand and the Pt moiety. For complex **2**, the observed CI value was <1 when the fractional effect (Fa) ranged from 0 to 0.7, and higher than 1 when Fa value was above 0.7 (Fig. 8).

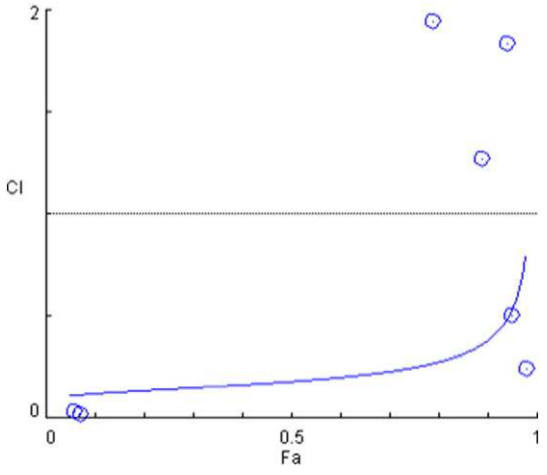

Fig. 8. CI/fractional effects (Fa) curve of complex **2** for MCF-7 cells. According to the equation of Chou-Talalay for two drugs [60], CI = (D)1/(Dx)1 + (D)2/(Dx)2, where (Dx)1 and (Dx)2 are the doses (concentrations) of 3-hydroxyflavone alone and *cis*-$[PtCl_2(PPh_3)_2]$ alone, respectively, that inhibit x% of cell viability. (D)1 and (D)2 are the doses of 3-hydroxyflavone and *cis*-$[PtCl_2(PPh_3)_2]$, respectively, used in combination [(D)1 + (D)2] {[(D)1 + (D)2] = dose of complex **2**, (D)1 = (D)2}, able to inhibit x% of cell viability. CI = 1 indicates an additive effect in the absence of synergism or antagonism; CI < 1 indicates synergism; CI > 1 indicates antagonism.

4. Conclusions

This article describes the synthesis and in vitro anticancer features of new *cis*-diphenylphosphane platinum(II) complexes bearing biologically active polyphenolate leaving group ligands. The coordination modes of deprotonated quercetin, 3-hydroxyflavone and ethylgallate to platinum(II) were determined in solution by NMR spectroscopy and in the solid state by X-ray diffraction. Biological assays carried out on complexes **2** and **3** indicate that these compounds did not show higher cytotoxicity compared to cisplatin for the considered cell lines (U87 and MCF-7). Theoretical calculations confirm that the studied complexes easily release their biologically active ligand in solution, thus suggesting a possible origin of the fact that their cytotoxicity is at least similar to that of their natural leaving groups.

Although complexes **2** and **3** have similar *O,O′* chelate structure, there is a small difference in their natural ligand coordination mode, being the leaving group a deprotonated α-hydroxy ketone in the first complex and a double deprotonated 1,2-diol in the second one. This small difference may affect the biological activity of the new compounds.

In fact, a biological synergic effect between the ligand and the starting platinum compound was interestingly observed for complex **2** bearing 3-hydroxyflavonate, for which mono-aqua platinum species (able to coordinate DNA) smoothly form in both first and second hydrolysis steps, according to theoretical studies. However, the cytotoxicity of cisplatin is still higher than that of complex **2** one because of a too fast hydrolysis rate of the latter, due to the higher *trans* effect of the carrier ligand.

When compound **3** is considered, theoretical calculations suggest that the lack of synergic cytotoxicity effect may be due either to production of relatively inert mono- and di-hydroxo complexes under physiological conditions (determined by ethyl gallate leaving group) and to a too fast hydrolysis rate (determined by carrier ligand features).

In conclusion, this study suggests that fine tuning of chemical parameters of both leaving groups and carrier ligands is a key step in designing biologically active Pt complexes. Therefore, further studies are warranted to synthesize new platinum(II) 3-hydroxoflavonate complexes bearing carrier ligands different than triarylphosphanes.

Acknowledgments

The authors thank Dr. Vito Filippo Capodiferro, Department of Pharmacy, University of Bari, Italy, for the elemental analyses, Mr. Giuseppe Chita for the diffraction data collection, Prof. Vito Gallo for the useful discussions and the Italian MIUR (PRIN project 2010–2011 n. 2010FPTBSH, NANOMED) for the financial support.

Appendix A. Supplementary data

Supplementary data to this article can be found online at http://dx.doi.org/10.1016/j.jinorgbio.2016.08.006.

References

[1] B. Rosenberg, L. Van Camp, T. Crigas, Nature 205 (1965) 698–699.
[2] S. Garattini, C. La Vecchia, Eur. J. Cancer 37 (2001) 128–147.
[3] L.R. Ferguson, A.E. Pearson, Mutat. Res. 355 (1996) 1–12.
[4] D. Lebwohl, R. Canetta, Eur. J. Cancer 34 (1998) 1522–1534.
[5] N.J. Wheate, S. Walker, G.E. Craig, R. Oun, Dalton Trans. 39 (2010) 8113–8127.
[6] J.B. Harborne, Nature, Distribution, and Function of Plant Flavonoids, in: V. Cody, E. Middleton Jr., J.B. Harborne (Eds.), Plant Flavonoids in Biology and Medicine: Biochemical, Pharmacological, and Structure-Activity Relationships, Alan R. Liss, Inc., New York 1986, pp. 15–24.
[7] J.B. Harborne, C.A. Williams, Phytochemistry 55 (2000) 481–504.
[8] R.F.V. de Souza, W.F. De Giovani, Redox Rep. 9 (2004) 97–104.
[9] H. Sakagami, Y. Jiang, K. Kusama, T. Atsumi, T. Ueha, M. Toguchi, I. Iwakura, K. Satoh, T. Fukai, T. Nomura, Anticancer Res. 20 (2000) 271–277.
[10] W. Ren, Z. Qiao, H. Wang, L. Zhu, L. Zhang, Med. Res. Rev. 23 (2003) 519–534.
[11] C. Kanadaswami, L.T. Lee, P.P.H. Lee, J.J. Hwang, F.C. Ke, Y.T. Huang, M.T. Lee, *in vivo*, 19 (2005) 895–910.
[12] K. C.D., P.A. Tarantilis, M.G. Polissiou, S. Diamantoglou, H.A. Tajmir-Riahi, Cell Biochem. Biophys. 49 (2007) 29–36.
[13] K. Janjua, A. Siddiqa, A. Yaqub, S. Sabahat, R. Qureshi, S. Haque, Spectrochim. Acta, Part A 74 (2009) 1135–1137.
[14] J. Lia, Y. Wanga, J.-C. Lei, Y. Hao, Y. Yanga, C.-X. Yangc, J.-Q. Yu, Nat. Prod. Res. 28 (2014) 683–689.
[15] Y. Wang, A. Han, E. Chen, R.K. Singh, C.O. Chichester, R.G. Moore, A.P. Singh, N. Vorsa, Int. J. Oncol. 46 (2015) 1924–1934.
[16] T.J. Zwang, K. Singh, M.S. Johal, C.R. Selassie, J. Med. Chem. 56 (2013) 1491–1498.
[17] M. Kviecinski, K. Felipe, T. Schoenfelder, L. de Lemos Wiese, M. Rossi, E. Goncalez, J. Felicio, D. Filho, R. Pedrosa, J. Ethnopharmacol. 117 (2008) 69–75.
[18] H. Cui, J. Yuan, X. Du, M. Wang, L. Yue, J. Liu, Oncol. Rep. 33 (2015) 1284–1290.
[19] T. Kalaivani, C. Rajasekaran, L. Mathew, J. Food Sci. 76 (2011) T144–T149.
[20] S. Mohan, K. Thiagarajan, R. Chandrasekaran, Nat. Prod. Res. 29 (2015) 366–369.
[21] M. Grazul, E. Budzisz, Coord. Chem. Rev. 253 (2009) 2588–2598.
[22] A. Kurzwernhart, W. Kandioller, É.A. Enyedy, M. Novak, M.A. Jakupec, B.K. Keppler, C.G. Hartinger, Dalton Trans. 42 (2013) 6193–6202.
[23] J. Stawinaska, M. Ciesalak-Golonka, Transit. Met. Chem. 26 (2001) 153–159.
[24] A. Medrano, S.M. Dennis, A. Alvarez-Valdés, J. Perles, T. McGregor Mason, A.G. Quiroga, Dalton Trans. 44 (2015) 3557–3562.
[25] A. Romerosa, P. Bergamini, V. Bertolasi, A. Canella, M. Cattabriga, R. Gavioli, S. Manas, N. Mantovani, L. Pellacani, Inorg. Chem. 43 (2004) 905–913.
[26] P. Bergamini, V. Bertolasi, L. Marvelli, A. Canella, R. Gavioli, N. Mantovani, S. Manas, A. Romerosa, Inorg. Chem. 46 (2007) 4267–4276.
[27] D. Montagner, E. Zangrando, B. Longato, Inorg. Chem. 47 (2008) 2688–2695.
[28] M. Ravera, E. Gabano, M. Sardi, E. Monti, M.B. Gariboldi, D. Osella, Eur. J. Inorg. Chem. (2012) 3441–3448.
[29] P. Bergamini, V. Ferretti, P. Formaglio, A. Marchi, L. Marvelli, F. Sforza, Polyhedron 78 (2014) 54–61.
[30] M. Frezza, Q.P. Dou, Y. Xiao, H. Samouei, M. Rashidi, F. Samari, B. Hemmateenejad, J. Med. Chem. 54 (2011) 6166–6176.
[31] S. Bombard, M.B. Gariboldi, E. Monti, E. Gabano, L. Gaviglio, M. Ravera, D. Osella, J. Biol. Inorg. Chem. 15 (2010) 841–850.
[32] C. Mugge, C. Rothenburger, A. Beyer, H. Gorls, C. Gabbiani, A. Casini, E. Michelucci, I. Landini, S. Nobili, E. Mini, L. Messori, W. Weigand, Dalton Trans. 40 (2011) 2006–2016.
[33] T. Řezníček, L. Dostál, A. Růžička, J. Vinklárek, M. Řezáčová, R. Jambor, Appl. Organomet. Chem. 26 (2012) 237–245.
[34] C. Mugge, E. Micheucci, F. Boscaro, C. Gabbiani, L. Messori, W. Weigand, Metallomics 3 (2011) 987–990.
[35] S.J. Berners-Price, P.J. Sadler, Structure and Bonding, Bioinorganic Chemistry, vol. 70, Springer, Berlin/Heidelberg, Germany 1988, pp. 27–102.
[36] E.R. Jamieson, S.J. Lippard, Chem. Rev. 99 (1999) 2467–2498.
[37] A. Melchior, E. Sánchez Marcos, R.R. Pappalardo, J.M. Martínez, Theor. Chem. Accounts 128 (2011) 627–638.
[38] A. Melchior, J.M. Martínez, R.R. Pappalardo, E. Sánchez Marcos, J. Chem. Theory Comput. 9 (2013) 4562–4573.
[39] M. Pavelka, M.F.A. Lucas, N. Russo, Chem. Eur. J. 13 (2007) 10108–10116.
[40] M.F.A. Lucas, M. Pavelka, M.E. Alberto, N. Russo, J. Phys. Chem. B 113 (2009) 831–838.
[41] A. Melchior, M. Tolazzi, J.M. Martínez, R.R. Pappalardo, E. Sánchez Marcos, J. Chem. Theory Comput. 11 (2015) 1735–1744.
[42] F.R. Hertley, in: P.L. Robinson (Ed.) The Chemistry of Palladium and Platinum, vol. 14, Applied Science, London 1973, p. 458.
[43] A.J.M. Duisenberg, L.M.J. Kroon-Batenburg, A.M.M. Schreurs, J. Appl. Crystallogr. 36 (2003) 220–229.
[44] G.M. Sheldrick, SADABS, Absorption Correction Program, University of Göttingen, Germany, 2008.
[45] M.C. Burla, R. Caliandro, B. Carrozzini, G.L. Cascarano, C. Cuocci, C. Giacovazzo, M. Mallamo, A. Mazzone, G. Polidori, J. Appl. Crystallogr. 48 (2015) 306–309.
[46] G.M. Sheldrick, Acta Crystallogr. C71 (2015) 3–8.
[47] A.L.J. Spek, J. Appl. Crystallogr. 36 (2003) 7–13.
[48] C.F. Macrae, I.J. Bruno, J.A. Chisholm, P.R. Edgington, P. McCabe, E. Pidcock, L. Rodriguez-Monge, R. Taylor, J. van de Streek, P.A. Wood, J. Appl. Crystallogr. 41 (2008) 466–470.
[49] M.C. Burla, R. Caliandro, M. Camalli, B. Carrozzini, G.L. Cascarano, C. Giacovazzo, M. Mallamo, A. Mazzone, G. Polidori, R. Spagna, J. Appl. Crystallogr. 45 (2012) 357–361.
[50] D. Andrae, U. Häußermann, M. Dolg, H. Stoll, H. Preuß, Theor. Chim. Acta 77 (1990) 123–141.
[51] F. Endrizzi, A. Melchior, M. Tolazzi, L.F. Rao, Dalton Trans. 44 (2015) 13835–13844.
[52] P. Di Bernardo, P.L. Zanonato, F. Benetollo, A. Melchior, M. Tolazzi, L. Rao, Inorg. Chem. 51 (2012) 9045–9055.
[53] A. Melchior, E. Peralta, M. Valiente, C. Tavagnacco, F. Endrizzi, M. Tolazzi, Dalton Trans. 42 (2013) 6074–6082.
[54] S. Del Piero, R. Fedele, A. Melchior, R. Portanova, M. Tolazzi, E. Zangrando, A. Melchior, Inorg. Chem. 46 (2007) 1406.
[55] C. Comuzzi, A. Melchior, P. Polese, R. Portanova, M. Tolazzi, Inorg. Chem. 42 (2003) 8214–8222.
[56] J. Tomasi, B. Mennucci, R. Cammi, Chem. Rev. 105 (2005) 2999–3093.
[57] M.E. Alberto, M.F.A. Lucas, M. Pavelka, N. Russo, J. Phys. Chem. B 113 (2009) 14473–14479.
[58] M.J. Frisch, G.W. Trucks, H.B. Schlegel, G.E. Scuseria, M.A. Robb, J.R. Cheeseman, G. Scalmani, V. Barone, B. Mennucci, G.A. Petersson, et al., Gaussian, Inc., Wallingford CT (2009).
[59] N. Margiotta, N. Denora, S. Piccinonna, V. Laquintana, F.M. Lasorsa, M. Franco, G. Natile, Dalton Trans. 43 (2014) 16252–16264.
[60] T.C. Chou, P. Talalay, Adv. Enzym. Regul. 22 (1984) 27–55.
[61] R.T. Boeré, C.J. Willis, Inorg. Chem. 24 (1985) 1059–1065.
[62] R.F.V. de Souza, E.M. Sussuchi, W.F. De Giovani, Synth. React. Inorg. Met.-Org. Chem. vol 33 (7) (2003) 1125–1144.
[63] K. Lemanska, H. Szymudiak, B. Tyrakowska, R. Zielinski, A.E.M.F. Soffers, I.M.C.M. Rietjens, Biol. Med. 31 (2001) 869–881.
[64] G.K. Anderson, M.J. Arendse, N.P. Rath, Inorg. Chem. 38 (1999) 5864–5869.
[65] J. Zhou, L. Wang, J. Wang, N. Tang, Transition Met. Chem. (Dordrecht, Neth.) 26 (2001) 57–63.
[66] D. Malesev, V. Kunti, J. Serb. Chem. Soc. 72 (2007) 921–939.
[67] K. Nakamoto, Infrared and Raman Spectra of Inorganic and Coordination Compounds, 5th edit Wiley, New York, 1997 Pt B, pp. 7, 169 and 172.
[68] L.J. Farrugia, J. Appl. Crystallogr. 45 (2012) 849–854.
[69] P. Bergamini, E. Marchesi, V. Bertolasi, M. Fogagnolo, L. Scarpantonio, S. Manfredini, S. Vertuani, A. Canella, Eur. J. Inorg. Chem. 9 (2008) 529–537.
[70] D.C. Burns, D.A. Ellis, R.E. March, Magn. Reson. Chem. 45 (2007) 835–845.
[71] P. Donato, D. Raneri, G. Guglielmo, P. Ficarra, R. Ficarra, J. Pharm. Biomed. Anal. 35 (2004) 389–397.
[72] T. Matsuura, T. Takemoto, R. Nakashima, Tetrahedron 29 (1973) 3337–3340.
[73] I. Yokoe, K. Higugi, Y. Shirataki, M. Komatsu, Chem. Pharm. Bull. 29 (1981) 894–898.
[74] M. Sisa, S.L. Bonnet, D. Ferreira, J.H. Van der Westhuizen, Molecules 15 (2010) 5196–5245.
[75] C. Rice-Evans, Curr. Med. Chem. 8 (2001) 797–807.
[76] P. Chou, D. McMorrow, T.J. Aartsma, M. Kasha, J. Phys. Chem. 88 (1984) 4596–4599.
[77] E. Biagtan, E. Goldberg, R. Stephens, E. Valeroso, J. Harmon, Nucl. Instrum. Methods Phys. Res., Sect. B 114 (1996) 88–90.
[78] S. Carturan, A. Quaranta, G. Maggioni, M. Bonafini, G. Della Mea, Sens. Actuators, A 113 (2004) 288–292.
[79] V.V. Shynkar, A.S. Klymchenko, C. Kunzelmann, G. Duportail, C.D. Muller, A.P. Demchenko, J.-M. Freyssinet, Y. Mely, J. Am. Chem. Soc. 129 (2007) 2187–2193 and references therein.
[80] B. Gerard, G. Jones II, J.A. Porco Jr., J. Am. Chem. Soc. 126 (2004) 13620–13621.
[81] B.J. Schwartz, L.A. Peteanu, C.B. Harris, J. Phys. Chem. 96 (1992) 3591–3598 and references therein.
[82] S. Protti, A. Mezzetti, C. Lapouge, J.-P. Cornard, Photochem. Photobiol. Sci. 7 (2008) 109–119.
[83] S.L. Saraf, T.J. Fish, A.D. Benninghoff, A.A. Buelt, R.C. Smith, L.M. Berreau, Organometallics 33 (2014) 6341–6351.
[84] K. Grubel, S.L. Saraf, S.N. Anderson, B.J. Laughlin, R.C. Smith, A.M. Arif, L.M. Berreau, Inorg. Chim. Acta 407 (2013) 91–97.
[85] K. Grubel, A.R. Marts, S.M. Greer, D.L. Tierney, C.J. Allpress, S.N. Anderson, B.J. Laughlin, R.C. Smith, A.M. Arif, L.M. Berreau, Eur. J. Inorg. Chem. (2012) 4750–4757.
[86] J.S. Pap, J. Kaizer, G. Speier, Coord. Chem. Rev. 254 (2010) 781–793.
[87] M.S. Davies, S.J. Berners-Price, T.W. Hambley, Inorg. Chem. 39 (2000) 5603–5613.
[88] J.K.C. Lau, D.V. Deubel, J. Chem. Theory Comput. 2 (2006) 103–106.

[89] D.V. Deubel, J. Am. Chem. Soc. 126 (2004) 5999–6004.
[90] J. Vinje, E. Sletten, J. Kozelka, Chem. Eur. J. 11 (2005) 3863–3871.
[91] G. Lamm, G.R. Pack, Proc. Natl. Acad. Sci. U. S. A. 87 (1990) 9033–9036.
[92] S.J. Berners-Price, T.G. Appleton, in: L.R. Kelland, N.P. Farrell (Eds.), Humana Press, Totowa, NJ 2000, pp. 3–35.
[93] M.E. Alberto, V. Butera, N. Russo, Inorg. Chem. 50 (2011) 6965–6971.
[94] A.A. Recio Despaigne, J.G. Da Silva, P.R. da Costa, R.G. dos Santos, H. Beraldo, Molecules 19 (2014) 17202–17220.
[95] J.J. Wilson, S.J. Lippard, J. Med. Chem. 55 (2012) 5326–5336.
[96] T.C. Johnstone, K. Suntharalingam, S.J. Lippard, Chem. Rev. 116 (2016) 3436–3486.
[97] N.D. Eljack, H.-Y.M. Ma, J. Drucker, C. Shen, T.W. Hambley, E.J. New, T. Friedrich, R.J. Clarke, Metallomics 6 (2014) 2126–2133.
[98] F. Arnesano, G. Natile, Coord. Chem. Rev. 253 (2009) 2070–2081.
[99] G. Hermann, P. Heffeter, T. Falta, W. Berger, S. Hanna, G. Koellensperger, Metallomics 5 (2013) 636–647.
[100] A.P. Neves, M.X.G. Pereira, E.J. Peterson, R. Kipping, M.D. Vargas, F.P. Silva-Jr, J.W.N. Carneiro, N.P. Farrell, J. Inorg. Biochem. 119 (2013) 54–64.
[101] J. Albert, R. Bosque, M. Crespo, J. Granell, C. López, R. Martín, A. González, A. Jayaraman, J. Quirante, C. Calvis, J. Badía, L. Baldomà, M. Font-Bardia, M. Cascante, R. Messeguere, Dalton Trans. 44 (2015) 13602–13614.
[102] A.C. Komor, J.K. Barton, Chem. Commun. 49 (2013) 3617–3630.

European Journal of Pharmaceutical Sciences 93 (2016) 380–391

Contents lists available at ScienceDirect

European Journal of Pharmaceutical Sciences

journal homepage: www.elsevier.com/locate/ejps

Fluoroquinolones: A micro-species equilibrium in the protonation of amphoteric compounds

Valeria M. Nurchi [a,*], Guido Crisponi [a], Joanna I. Lachowicz [a], Maria Antonietta Zoroddu [b], Massimiliano Peana [b], Serenella Medici [b], Daniele Veclani [c], Marilena Tolazzi [c], Andrea Melchior [c,*]

[a] Dipartimento di Scienze Chimiche e Geologiche, Università di Cagliari, Cittadella Universitaria, 09042, Monserrato-Cagliari, Italy
[b] Dipartimento di Chimica e Farmacia, Via Vienna 2, 07100 Sassari, Italy
[c] Dipartimento Politecnico, Laboratori di Tecnologie Chimiche, Università di Udine, Via del Cotonificio 108, 33100 Udine, Italy

ARTICLE INFO

Article history:
Received 27 July 2016
Received in revised form 27 August 2016
Accepted 28 August 2016
Available online 30 August 2016

Keywords:
Fluoroquinolones
Potentiometry
Spectrophotometry
NMR
Protonation micro-constants
DFT computational study

ABSTRACT

The knowledge of the speciation of fluoroquinolones is of great actuality for the implications on the activity, bioavailability and pharmacokinetics. Literature reports a number of contrasting evaluations on the existence of tautomeric forms of mono-protonated species, described by a set of protonation micro-constants. Here the protonation sequence and the related protonation constants of four representative molecules are evaluated by a combined potentiometric-spectrophotometric method. The experimental observations necessary to differentiate between a protonation scheme represented by macro-constants alone, and the one that requires the introduction of a micro-protonation scheme, are clearly delineated based on a careful analysis of experimental data and of simulated models. The role of the medium was investigated and UV–vis spectra in water- methanol solution were analyzed. The existence of the zwitterionic species alone at physiological pH in water, and an increase of the relative amount of the neutral species with the lipophilicity of the medium were remarked. This surely affects the bioavailability of FQs, with the increase of the neutral species when the molecules approach the local lipophilic environment close to the cellular membranes. NMR studies allowed the attribution of the protonation sites of the different forms. Quantum chemical evaluation of all the possible existent forms with different protonation degrees and in different sites strongly substantiates the experimental results. The study of the relevant frontier molecular orbitals completed the detailed theoretical characterization of the species.

1. Introduction

Quinolones are a family of synthetic antibacterial agents, structurally related to nalidixic acid, introduced in clinical practice in the sixties for the treatment of urinary infections (Emmerson and Jones, 2003). Quinolones are based on the skeleton of 4-oxo-1,4-dihydro-3-quinolinecarboxylic acid (Scheme 1a), whose pharmacological and pharmacokinetic properties were improved by the insertion of a fluorine atom in position 6 and successively of a piperazine unit in position 7 (Scheme 1b).

The mechanism by which fluoroquinolones (FQ) exert their antibacterial activity consists in the inhibition of the activity of bacterial topoisomerase by interaction with the single stranded DNA gyrase (Fan et al., 1995). The significance of the pH both in the activity and in the pharmacokinetics of a drug is well known and principally related to its acid-base properties. The knowledge of the speciation pattern of a drug is therefore of paramount importance from the pharmacological point of view (Park et al., 2002). The protonation equilibria of FQs have received wide attention and several techniques have been used to evaluate both the equilibrium constants and the proton coordination sites (Ross and Riley, 1990; Takács-Novák et al., 1990; Rusu et al., 2012; Ross and Riley, 1992; Wallis et al., 1994; Hernàndez-Borrell and Montero, 1997; Park et al., 2000). FQs are ampholyte compounds, which present multiple sites that can be protonated depending on the pH. However, the reported acid–base properties of FQs are controversial with regard to the values of protonation constants and the number of basic sites (Rusu et al., 2012). The FQs might exist in five different pH-dependent protonation species, namely di-cation H_3FQ^{2+}, cation H_2FQ^{+}, zwitterion zHFQ, neutral species nHFQ and anion FQ^{-}. A scheme of the possible equilibria involving these species is reported in the Supporting Information (ESI), together with the relationships between the micro- and macro-constants of protonation. At the isoelectric point of FQs in water (about pH 7), the mole fractions of the zHFQ and nHFQ species reach their maximum values. It seems that zHFQ is the most stable species (Ross and Riley, 1990; Barbosa et al., 1998), even if some theoretical works predict that the most stable species should be nHFQ (Musa and Eriksson, 2009; Vitorino et al., 2006). In these theoretical works the polarizable continuum model (PCM) was employed to simulate the

* Corresponding authors.
E-mail addresses: nurchi@unica.it (V.M. Nurchi), andrea.melchior@uniud.it (A. Melchior).

http://dx.doi.org/10.1016/j.ejps.2016.08.053
0928-0987/

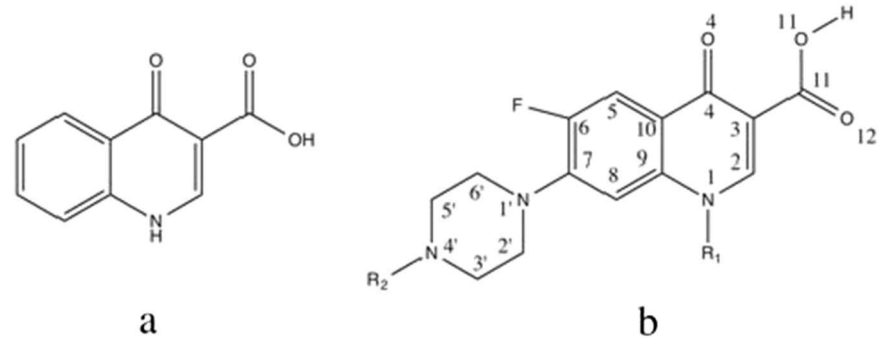

Scheme 1. a) Structure of 4-oxo-1,4-dihydro-3-quinolinecarboxylic acid and b) numbering scheme of fluoroquinolones.

solvent, but when a discrete-continuum approach was employed (i.e. some solvent molecules placed near the ionizable groups of solute) the reverse order of stability was obtained (Lambert et al., 2007).

The H_3FQ^{2+} species (existing only in extremely acidic conditions) can be protonated either at the piperazine ring (Rusu et al., 2012; Lin et al., 2004) or at carbonyl oxygen (Gerasimenko et al., 2008; Polishchuk et al., 2008).

The existence of micro-protonation equilibria implies tautomeric forms with the same degree of protonation, with the protons located on different basic sites of the molecule. In particular, in the zwitterion zHFQ the carboxylic group is in the negatively charged form (carboxylate) and the 4′ nitrogen atom in piperazine ring is protonated and positively charged. In the neutral form nHFQ, the carboxylic group is protonated, and the nitrogen atom not. The micro-protonation constants determine the relative amount of these two forms. The two tautomers have chemical properties markedly different, which depend on the different interactions with the medium and with the components of physiological barriers, thus determining both the solubility and the bioavailability of the molecule. The pharmacodynamics and the pharmacological properties strictly rely on the prevalence of the zwitterion or of the neutral species. The disagreement on the numerical values for the micro-constants reported in literature depends on the different used approaches, and on different assumptions, but mainly on the little attention paid to the information contained in the experimental results, which allows to discriminate whether micro-protonation equilibria exist or not, disregarding limiting assumptions that can invalidate the final conclusions. Moreover, once the existence of tautomers has been ascertained, this information allows quantifying their relative amounts through a correct and reliable evaluation of the micro-constants.

Table 1
Trade name, IUPAC formula, structure and acronym of studied compounds.

Name	IUPAC formula	Molecular structure and acronym
Ciprofloxacin	1-cyclopropyl-6-fluoro-4-oxo-7-(piperazin-1-yl)-1,4-dihydroquinoline-3-carboxylic acid	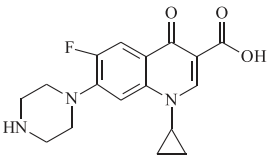
Lomefloxacin	1-ethyl-6,8-difluoro-7-(3-methylpiperazin-1-yl)-4-oxo-1,4-dihydroquinoline-3-carboxylic acid	**CFX** 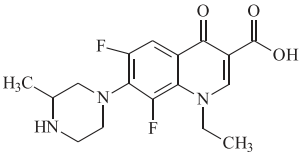
Norfloxacin	1-ethyl-6-fluoro-4-oxo-7-(piperazin-1-yl)-1,4-dihydroquinoline-3-carboxylic acid	**LFX** 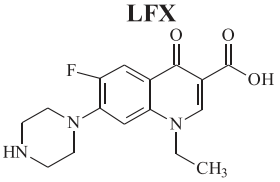
Ofloxacin	9-fluoro-3-methyl-10-(4-methylpiperazin-1-yl)-7-oxo-2,3-dihydro-7*H*-[1,4]oxazino[2,3,4-*ij*]quinoline-6-carboxylic acid	**NOR** 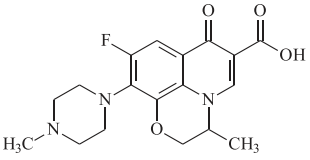 **OFL**

In this paper, we present a thorough study on the protonation equilibria of four representative FQs (Table 1) by using a robust combined potentiometric-spectrophotometric procedure of high precision and accuracy (Crisponi et al., 2004; Nurchi et al., 2013).

The experimental evidence necessary to introduce a micro-protonation scheme is discussed, following a careful analysis of UV–vis spectra and NMR data as a function of pH. The experimental indications are corroborated with the aid of simulated speciation models. The role of the medium on the molecular structure and relative stability of the differently protonated forms was investigated in water and in water-methanol solutions on the representative compound CFX.

Density Functional Theory (DFT) calculations were run to provide geometries, relative stability, absorption spectra of the different protonation states of CFX in gas phase and PCM solvent. A discrete-continuum approach was also introduced, to include explicit hydrogen bonds.

2. Experimental

2.1. Reagents

Lomefloxacin hydrochloride and Ofloxacin were Sigma products. Norfloxacin, and Ciprofloxacin were Fluka products. KOH and KCl, HCl and methanol were purchased from Aldrich. The compounds were used without further purification. Potassium hydroxide carbonate free solutions were prepared as reported in a previous paper (Nurchi et al., 2011).

2.2. Potentiometric-spectrophotometric measurements

2.2.1. Water solutions

Protonation equilibria were studied in a thermostatted glass cell equipped with a magnetic stirrer, a Metrohm LL UNITRODE glass electrode connected to a Metrohm 691 pH-meter, a microburet delivery tube connected to a Dosimat 665 Metrohm titrator, an inlet–outlet tube for Argon and a 0.2 cm path length fibre optic dip probe, connected to a Varian Cary 50 UV–vis spectrophotometer. This device allows potentiometric and spectrophotometric measurements on the same system at the same time. Ligand solutions (2.5×10^{-4} M; 0.1 M KCl ionic strength) were titrated at 25.0 °C with carbonate-free KOH 0.1 M (Albert and Serjeant, 1984). The electrode was calibrated daily by titrating HCl with KOH in the same experimental conditions as above and the resulting data were processed according to the Gran procedure (Gran, 1952). The ionization constants were calculated using Hyperquad2013 and HypSpec2014 programs (http://www.hyperquad.co.uk/HQ2013.htm, 2016). The first two protonation equilibria were followed with a base titration of the FQ solutions containing hydrochloric acid at a concentration twice than that of the ligand. The study of the third protonation step required the use of highly concentrated acid solutions and was studied only by UV–vis spectroscopy. Hydrochloric acid was used as the most suitable acid thanks to the non-oxidizing nature. Proper amounts of ligands were dissolved in HCl solutions ranging from 0.1 M to 6.0 M. The spectra of these solutions were collected in the range 200–450 nm using a 1 cm quartz cell. Instead of pH, H^o functions were used in the calculations (Hammett and Deyrup, 1932; Paul and Long, 1957; Aragoni et al., 1995).

Table 2
Protonation constants (log βi and log K_i) of the FQs.

Ligand	Log β1	Log K1	Log β2	Log K2	Log K2 spec data	Log β3	Log K3
NOR	8.78(2)	8.78	14.92(2)	6.14	6.12(2)	14.36	−0.56(2)
CFX	8.56(1)	8.56	14.61(2)	6.05	6.06(2)	13.89	−0.72(2)
LFX	9.01(1)	9.01	14.88(1)	5.87	5.85(3)	13.96	−0.92(3)
OFL	8.28(1)	8.28	14.28(1)	6.00	6.02(2)	13.48	−0.80(2)

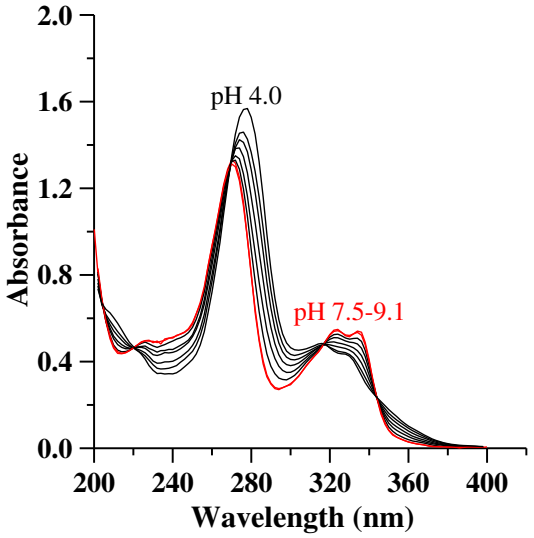

Fig. 1. UV–vis spectra acquired during the basic titration of CFX, as a "typical" case, in the spectral range 200–400 nm.

2.2.2. Water-methanol solutions

The titrations of CFX $2.5 \cdot 10^{-4}$ M were performed in a 50/50 water/methanol solution with KOH 0.1 M, at 25 °C and 0.1 M KCl ionic strength. The potentiometric and UV–vis data were collected in the same experimental conditions as in water alone.

2.3. NMR spectroscopy

Nuclear Magnetic Resonance (NMR) measurements were performed on a Bruker Ascend™ 400 MHz spectrometer equipped with a 5 mm automated tuning and matching broadband probe (BBFO) with z-gradients, as previously described (Zoroddu et al., 2007; Zoroddu et al., 2010; Peana et al., 2013; Zoroddu et al., 2008; Zoroddu et al., 2014; Zoroddu et al., 2009).

NMR experiments were carried out using 5–8 mM concentration of CFX or OFL in 90/10 (v/v) H_2O/D_2O or D_2O at 298 K in 5 mm NMR tubes. The pD values measured for the D_2O solutions were converted into the pH values using the deuterium isotopic correction pH = pD − 0.4 (Alner et al., 1967). 2D 1H-13C heteronuclear correlation

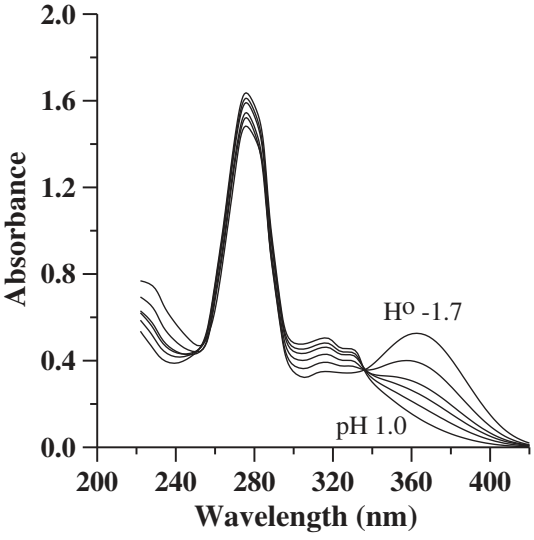

Fig. 2. UV–vis spectra acquired in the acidity range H° −1.7–pH 1.0, in the spectral range 200–420 nm for CFX, as a "typical" case.

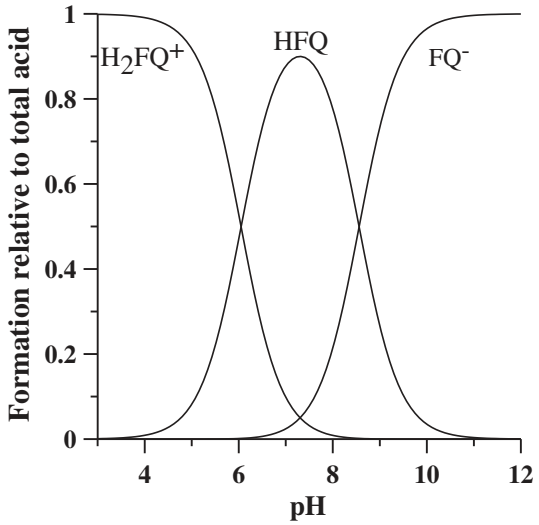

Fig. 3. Speciation plots of CFX, as a "typical" case.

spectra (HSQC) were acquired using a phase-sensitive sequence employing Echo-Antiecho-TPPI gradient selection with a heteronuclear coupling constant JXH = 145 Hz, and shaped pulses for all 180° pulses on f2 channel with decoupling during acquisition. Sensitivity improvement and gradients in back-inept were also used. Relaxation delays of 2 s and 90° pulses of about 10 μs were employed in all the experiments. Solvent suppression was carried out using excitation sculpting with gradients. The spin-lock mixing time of TOCSY experiments was obtained with MLEV17. 1H-1H TOCSY spectra were performed using mixing times of 60 ms. A combination of 1D, 2D TOCSY experiments were used to assign all the proton signals of the molecules at different pH values. All NMR data were processed with TopSpin (Bruker Instruments) software and analyzed by Sparky 3.11 and MestRe Nova 6.0.2 (Mestrelab Research S.L.) programs.

2.4. Computational details

DFT calculations have been carried out for the CFX fluoroquinolone. All geometries of CFX in different protonation states have been carried out in vacuum using the B3LYP functional (Becke, 1993; Lee et al., 1988) and a gaussian-type 6-311G(d,p) basis set for all atoms. This level of theory has been previously demonstrated to provide accurate geometries and thermochemical properties for many molecular systems (Endrizzi et al., 2015; Mendonça et al., 2013; Del Piero et al., 2006; Melchior et al., 2004; Melchior et al., 2013; Comuzzi et al., 2003; Fries et al., 2010).

Solvent effects were taken into account by two alternative ways: a) implicit solvent introduced by the PCM method (Tomasi et al., 2005); b) a discrete-continuum approach obtained by combining the PCM solvation with the effect of a small number water molecules placed close to the protonated groups of the solute. In the latter case, water molecules were selected by examining based the average number of waters that form hydrogen bonds with the ionizable groups of CFX in a molecular dynamics simulation (performed using Gromacs 5.0.4) (搖Hess, 2008) using the GROMOS force field (Schmid et al., 2011). A cluster composed by 10 water molecules and CFX was constructed by taking a representative snapshot from the MD simulation and then optimized at DFT level. In all cases, to confirm that stationary points were true minima,

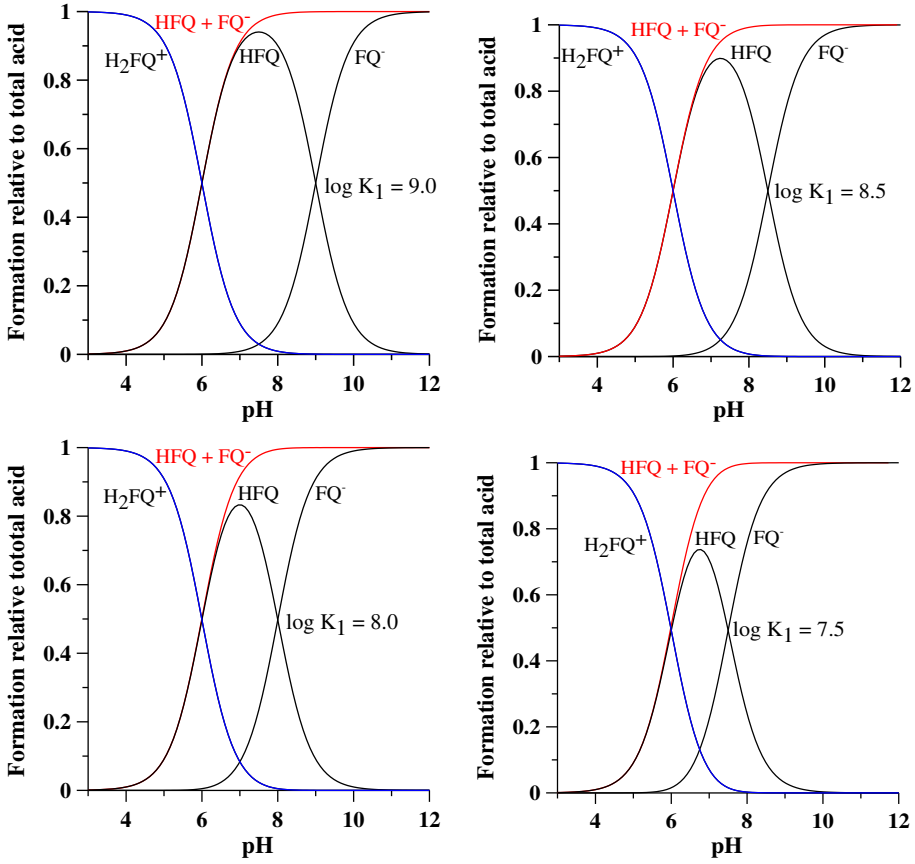

Fig. 4. Speciation plots of simple bi-protic acids with log K 2 = 8 and variable log K 1. The trend of the sum of the relative concentration of the species HFQ and FQ^- is remarked as red line. (For interpretation of the references to color in this figure legend, the reader is referred to the web version of this article.)

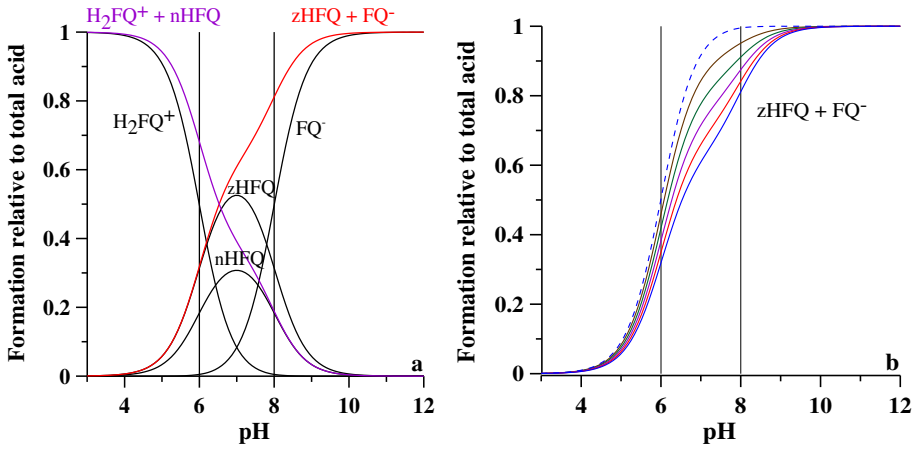

Fig. 5. Speciation plots of a diprotic acids that present micro-protonation equilibria with macro-constants log $K_1 = 8$ and log $K_2 = 6$ and micro-constants log $K_{zHFQ} = 7.8$ and log $K_{nHFQ} = 7.5671$.

vibrational analysis has been carried out to confirm the absence of imaginary frequencies. Free energies were calculated by the total electronic energies and adding zero point energy (ZPE) and thermal corrections at 298.15 K.

Excitation spectra of the H_3FQ^{2+}, H_2FQ^+, zHFQ, nHFQ and FQ^- were calculated using the time-dependent formalism (TD-DFT) (Scalmani et al., 2006). DFT calculations were performed with the Gaussian 09 program (Frisch et al., 2009).

3. Results and discussion

Three protonation steps characterize the studied FQs, the first takes place around pH 8.5, the second around pH 6 and the last at highly acidic conditions, according to the general scheme:

$$FQ^- + H^+ \rightleftarrows HFQ \quad (1)$$

$$HFQ + H^+ \rightleftarrows H_2FQ^+ \quad (2)$$

$$H_2FQ^+ + H^+ \rightleftarrows H_3FQ^{2+} \quad (3)$$

The first two protonation equilibria were studied by potentiometric titrations alone at 0.1 M KCl ionic strength. The resulting data were processed by Hyperquad program (http://www.hyperquad.co.uk/HQ2013.htm, 2016) and allowed the calculation of the protonation constants, log K_1 and log K_2 (Table 2).

The three protonation constants K_1, K_2 and K_3 are defined on the base of the equilibria 1–3 as

$K_1 = \frac{[HFQ]}{[FQ^-][H^+]}$, $K_2 = \frac{[H_2FQ^+]}{[HFQ][H^+]}$ and $K_3 = \frac{[H_3FQ^{2+}]}{[H_2FQ^+][H^+]}$, and the cumulative protonation constants, according to IUPAC (http://www.iupac.org/goldbook/P04909.pdf), as $\beta_1 = K_1$, $\beta_2 = K_1K_2$ and $\beta_3 = K_1K_2K_3$.

The UV–vis spectra, collected during the basic titration of CFX, as a "typical" case, relative to the first two protonation steps in the pH range 4–9.1, are presented in Fig. 1. The analogous spectra for all the four fluoroquinolones are reported in Supplementary Information (Fig. S1s). No spectral change occurs during the first protonation step. Evidence of that is given by the overlapping of the spectrum collected at pH 9.1, where the deprotonated species FQ^- exists at 50–90%, and that at pH 7.5, where the concentration of the neutral form HFQ reaches its maximum (both spectra are reported in red in Fig. 1).

At lower pH values, where the second protonation step occurs, major variations are the decrease of the intensity of the principal band at about 280 nm accompanied by its shift to lower wavelengths, and the increase of the bands between 320 and 360 nm. Sharp isosbestic points are observed. These remarkable spectral variations connected with the second protonation equilibrium permitted a further evaluation of log K_2 (Table 2, log K_2 spec data).

The study of the third protonation step, conducted by UV–vis spectroscopy, required the use of highly concentrated acid solutions. Proper amounts of ligands were dissolved in HCl solutions ranging from 0.1 M to 6.0 M. Instead of pH, H^o functions were used in the calculations (Hammett and Deyrup, 1932; Paul and Long, 1957; Aragoni et al., 1995). The resulting spectra for some representative solutions of CFX, as a "typical" case, are reported in Fig. 2.

By increasing acid concentration a new band appears at 360–400 nm for all four ligands (Fig. 2 and Fig. S2s), accompanied by a decrease of the other bands. In the case of OFL, also a red shift of the intense band at 292 nm is observed. Sharp isosbestic points accompany spectral variations. It has to be underlined that the ionic strength at which that data were collected was not constants due to the extremely acid working solutions. The log K_3 values obtained from these data are reported in Table 2.

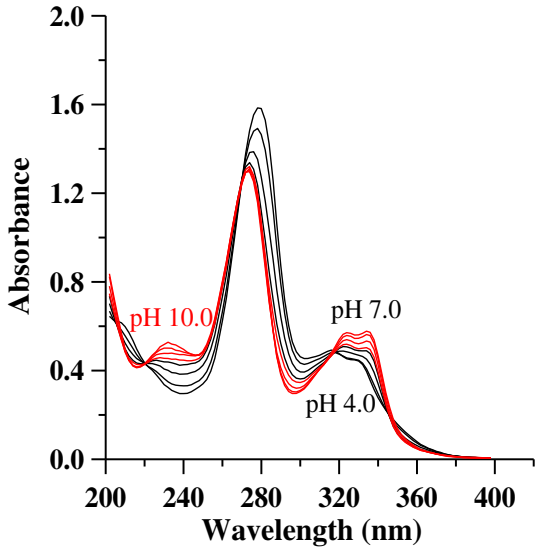

Fig. 6. UV–vis spectra acquired during the basic titration of CFX in 50:50 water-methanol, in the spectral range 200–420 nm.

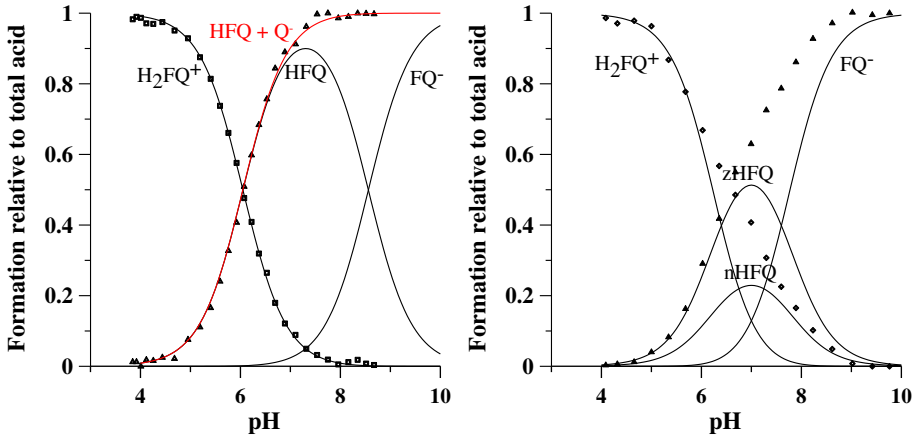

Fig. 7. Speciation plots (full lines) of ciprofloxacin in water (left) and in water-methanol solution (right), with superimposed the normalized heights of the bands at 282 nm (squares) and at 338 nm (triangles).

The speciation plots reported in Fig. 3 for CFX, as a "typical" case and in Fig. S3s for all the four fluoroquinolones, clearly show that at neutral - physiological pH the species HFQ is the predominant one (>90%) together with some percent of both the positively charged H_2FQ^+, and the anionic species FQ^-. The species HFQ, according to the current literature, could exist either as zwitterion form zHFQ with the positive charge on the protonated N4′ and the negative on carboxylate, or as neutral species nHFQ.

According to Ross and Riley (Ross and Riley, 1992) "The zwitterion species and the neutral species are likely to have different distribution properties and therefore to fully understand and interpret differences in bioavailability and the structure-activity relationships of these compounds, it is necessary to consider their microscopic dissociations".

Based on the above considerations several articles proposed a microscopic dissociation scheme (Supplementary Information). These papers can be classified according to the different approaches they used, based on:

1) the assumption that the basic groups are so spatially apart that it is reasonable to assume that the charge of one functional group will not significantly affect the protonation constant of the other group (Ross and Riley, 1990);
2) the knowledge of the protonation macro-constants of parent and model compounds (ester derivatives) can be an adequate set of data for calculating all the protonation micro-constants (Rusu et al., 2012; Lin et al., 2004);

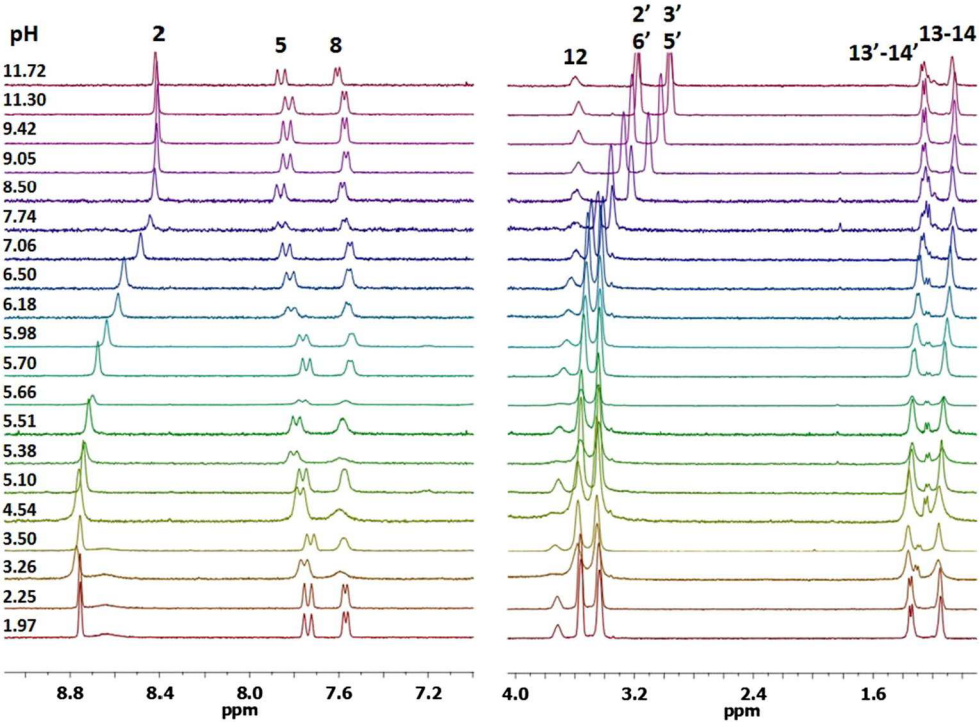

Fig. 8. Selected portion of ^{1}H NMR spectra of CFX quinolone molecule at variable pH.$S2_{NMR}$–$S3_{NMR}$ and Tables $S2_{NMR}$–$S3_{NMR}$). This behavior is in agreement with the first two proposed protonation equilibria. Indeed, the shifts observed in the NMR spectra by increasing the pH, are towards higher fields for the protons neighboring the site of protonation. These shifts are in agreement with the shielding following the process. In particular, the detected trend supports the observation that, whereas the first protonation involves N4′ in the piperazine moiety, to form the charged $HN4'^+$ species, the second protonation involves the carboxylate group to form COOH.

3) the spectral variations, with the assumption that they can be completely associated to the protonation of a single group, the carboxylate group in the case of FQs. The fraction of carboxylate group, independent on N4′ ionization, can be calculated from the equation 4,

$$\alpha_{COO-} = \frac{A_{pH} - A_{COOH}}{A_{COO-} - A_{COOH}} \quad (4)$$

where α_{COO}- is the fraction of FQ as zwitterion, A_{pH} is the absorbance at a given pH value, A_{COOH} is the absorbance at an acid pH value in which the carboxylic group is completely protonated, and A_{COO}- is the absorbance at a pH value in which the carboxylic group is completely deprotonated (Takács-Novák et al., 1990; Hernàndez-Borrell and Montero, 1997).

Some concerns should be raised regarding the points listed above: 1) the total charge of the molecule always influence its protonation equilibria, in different amounts according the distance; 2) although this approach had historical merits in the determination of the complete protonation scheme for simple amino acids (Edsall and Blanchard, 1933; Edsall et al., 1958), it has some limits, taking in mind that the diprotic acids are not equivalent to the ester derivative models; 3) even if potentiometric data alone allow obtaining correct macroscopic protonation constants, they do not contain the necessary information to infer a micro-protonation scheme.

The assumption that a micro-protonation scheme is necessary to correctly describe the studied system should be based on experimental observations appropriate to discriminate between the two opposite situations outlined in the following:

- the macro-protonation constants (calculated from potentiometric data, which depend only on the protonation degree of the molecule) completely describe the system since the first proton is acquired from only one site, leading to a single zHFQ or nHFQ species;
- the introduction of a micro-protonation scheme is necessary to describe the system. In this case, the first proton is acquired from the two different sites leading to the contemporary presence of both the species zHFQ and nHFQ, whose amounts depend on the ratios of micro-constants.

Some simulated examples can be of great aid for defining the spectral trend we should expect during a titration of a diprotic acid in the two different situations, making use of the unique assumption that only the protonation of the carboxylate group is accompanied by measurable spectral variations. A further requirement is that the experimental device allows the collection of a sufficient number of high quality spectra in the pH range $\log K_2 \pm 2$. In the first case we calculated the speciation plots for different couples $\log K_1 - \log K_2$ in which the $\log K_2$ of carboxylic group was held constant ($\log K_2 = 6$) and the $\log K_1$

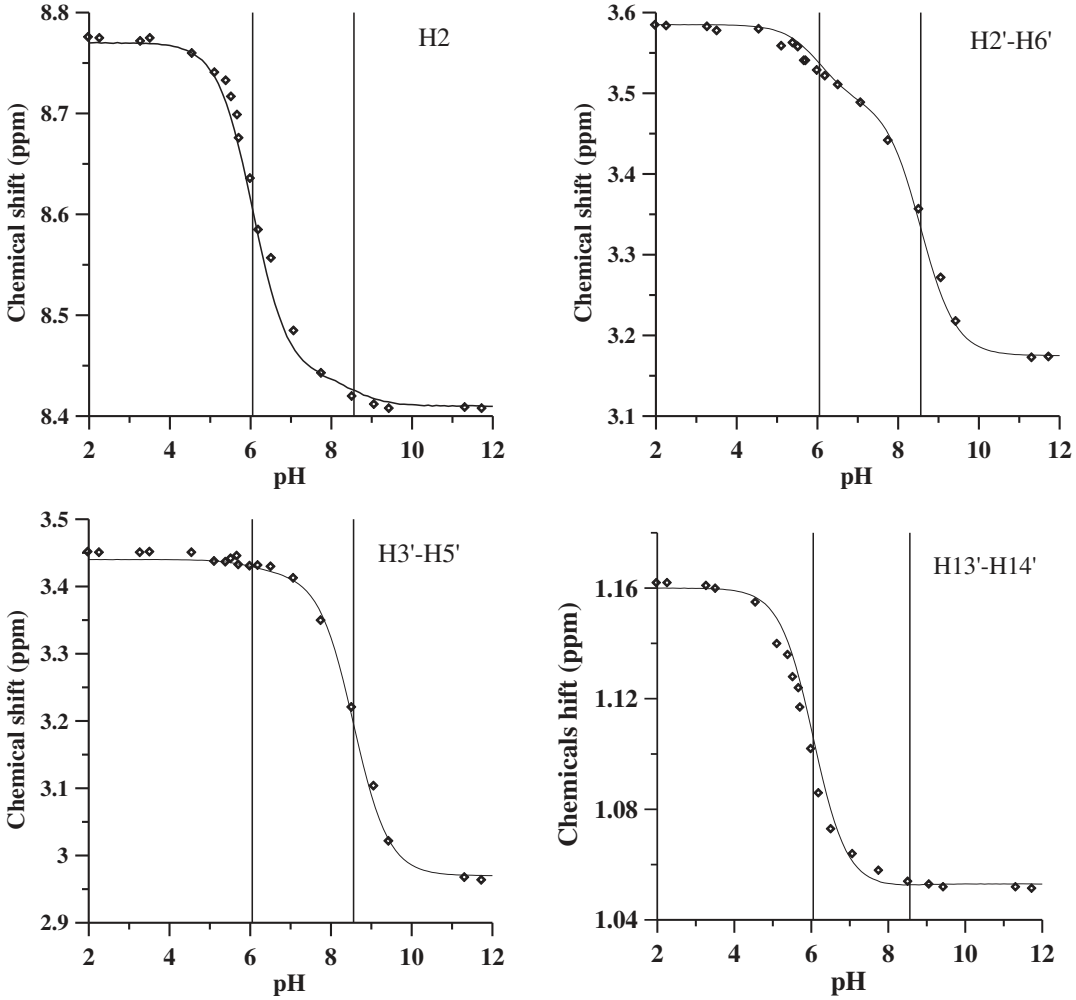

Fig. 9. ^{1}H NMR chemical shifts of some representative protons of CFX vs pH. The experimental chemical shifts are reported as points, and the trends, calculated from the speciation plots and from the intrinsic chemical shifts obtained with the HypNMR software (www.hyperquad.co.uk/hypnmr.htm), as continuous lines. Two grid lines are drown at pH values corresponding to $\log K_1$ and $\log K_2$.

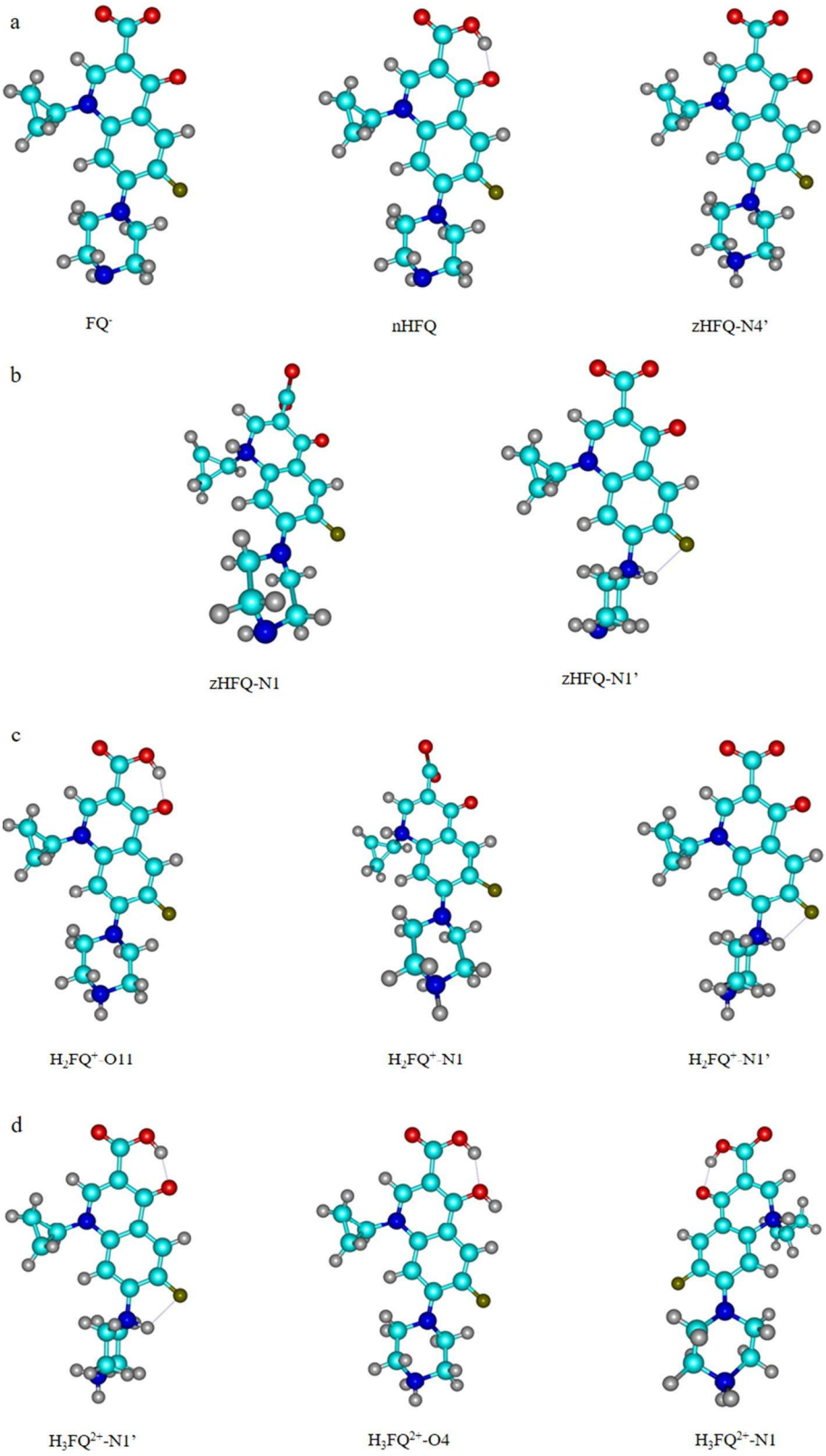

Fig. 10. Minimum energy structures of: a) FQ^{-}, nHFQ and zHFQ—N4′ for CFX; b) zHFQ; c) H_2FQ^{+} and d) H_3FQ^{2+}.

assumed the decreasing values 9, 8.5, 8 and 7.5, i.e. the Δlog K was decreased from 3 to 1.5. The speciation plots in Fig. 4 point out that, as Δlog K decreases, the amount of the mono-protonated species HFQ in its maximum drops from ~96% to ~73%, with corresponding increasing amounts both of the bi-protonated H_2FQ^{+} and of the completely deprotonated form FQ^{-} at the pH value of the maximum of the mono-protonated species HFQ.

If spectral variations depend only on the protonation state of the carboxylic group, the band connected to the protonated form COOH decreases with pH in a way proportional to the blue curve related to the

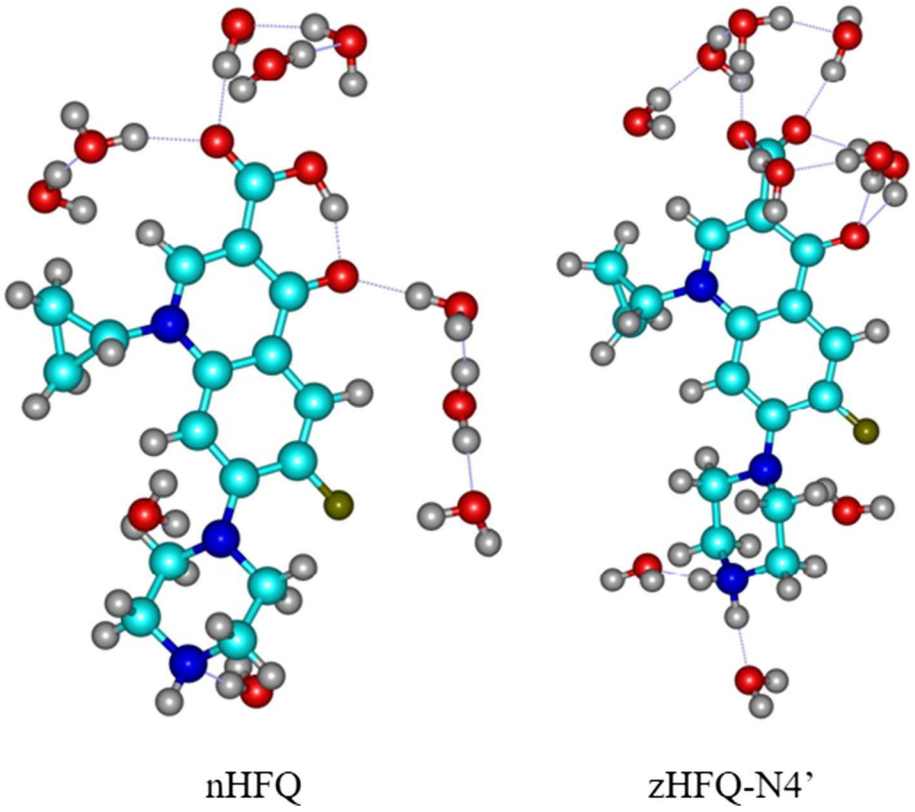

Fig. 11. Optimized nHFQ and zHFQ–N4′ species with 10 solvating molecules in PCM water.

H_2FQ^+ species, while that of carboxylate increases with a trend proportional to the sum of the HFQ and FQ^- curves (red curve). The trend of these curves, which is typical of a monoprotic acid with a log K 6, is identical in all the four cases, not influenced at all by the protonation state of the amino group.

As far as the second case is concerned, in Fig. 5a a typical behavior of a diprotic acid is reported.

This acid is characterized by the macro-protonation constants log $K_1 = 8$ and log $K_2 = 6$ (as in the third case in Fig. 4) and by the micro-constants log $K_{zHFQ} = 7.8$ (chosen by us) and log $K_{nHFQ} = 7.5671$ (calculated with the restraints imposed by the macro-constant, Scheme S1). The species zHFQ represents the zwitterion protonated on the piperazine nitrogen atom N4′ and nHFQ the neutral species protonated on the carboxylate. The band connected to the protonated form COOH decreases with pH in a way proportional to the curve in blue. In this case the blue curve does not correspond to that of H_2FQ^+ species (that can lose the first proton not only from the carboxylic group but also from the nitrogen atom N4′) but to the sum of the H_2FQ^+ and nHFQ species, i.e. to all the species protonated on the carboxylate group. The band of carboxylate increases with a trend proportional to the sum of the zHFQ and FQ^- curves (red curve). The trend of these blue and red curves differs from that of a simple monoprotic acid in an amount that depends on the weight of the nHFQ and of zHFQ species. Furthermore, there is no symmetry between the two curves. In Fig. 5b the sum zHFQ + FQ^- is reported for systems always characterized by the same macro-protonation constants log $K_1 = 8$ and log $K_2 = 6$, and by variable log K_{zHFQ}, and log K_{nHFQ}, in order to have an increasing weight of the nHFQ form. A progressive deviation from the trend of a simple monoprotic acid is apparent. Hence the trend of the absorbance vs pH clearly remarks the presence or not of micro-protonation equilibria in a non-questionable way.

Coming back to our experimental observations, the illustrative case of ciprofloxacin (not different from that of the other examined FQs) is analyzed, by comparing the UV–vis data collected in water (Fig. 2) and in water-methanol solution (Fig. 6).

The spectra in Fig. 2 and in Fig. 6 were decomposed in the constituent Gaussian peaks,[1] and the normalized heights of the bands at 282 nm, attributable to the carboxylic group, and those at 338 nm, attributable to carboxylate, are reported in Fig. 7 together with the species distribution. The estimated heights of the spectral bands are more accurate than the absorbance values measured at the wavelengths of band maxima, since they derive from a large number of experimental points, and are depurated from the contribute of any overlapping band. The experimental points in water perfectly overlap the speciation curves calculated from the macro-constants evaluated from potentiometric data (Fig. 7, left), similarly to the red and blue curves depicted in Fig. 5. This confirms that the acid base equilibria of CFX are completely represented by the macro-constants and no micro-protonation scheme has to be introduced.

When the protonation equilibria of CFX is studied in water-methanol solution a different trend is observed (Fig. 6), where the bands of carboxylate decrease not only in the second protonation step (pH 4–7) but also in first (pH 7–10). The heights of the bands at 282 and 338 nm reported in Fig. 7 right show the characteristic trend of the micro-protonation equilibrium depicted in Fig. 5 and well overlap the sum of the H_2FQ^+ and zHFQ species and the sum of the nHFQ and FQ^- curves.[1] Methanol, less polar than water, stabilizes the neutral form that appears at a concentration about one half that of the zwitterion species. In this case, the trend of spectral data as a function of pH permits to ascertain the existence of a micro-protonation equilibrium in an unequivocal way.

The first two protonation equilibria for FQs have also been studied by using ^{1}H NMR spectroscopy in the pH range 2–12, to substantiate

[1] The values log $k_{1z} = 7.61(2)$, log $k_{1n} = 7.25(2)$ and log $\beta_2 = 14.01(3)$ were estimated from the spectrophotometric measurements using a non-linear least squares procedure

the attribution of the protonation sites made based on the UV spectral results. The ^{1}H spectra and the resonance assignments are reported in Figures $S1_{NMR}$–$S3_{NMR}$ and Tables $S1_{NMR}$–$S3_{NMR}$. In Fig. 8 selected portions of ^{1}H NMR spectra for CFX molecule at variable pH are reported. The δ variations in the aromatic region remark that the H2 proton, close to the carboxylic group in position 3 (Scheme 1b), undergoes the most pronounced changes ($\Delta\delta = -0.228$ ppm from pH 5.98 to pH 9.42, Table $S1_{NMR}$, Fig. 9). Above pH 8, the protons H3′-5′ on the piperazine ring and H2'-6′ in the aliphatic region undergo the highest variation in their chemical shifts ($\Delta\delta$ *H*3'-5′ $= -0.396$ ppm and $\Delta\delta$ H2′-6′ $= -0.269$ ppm from pH 7.06 to pH 11.3 respectively, Figure 9, Table $S1_{NMR}$). The same trend has been also observed for the other FQs here studied (Figures

The remarkable NMR spectral variations with pH related to the first protonation allows to attribute it to the zwitterionic species protonated on N4′ site on piperazine ring, while the second protonation process involves the carboxylate group. These attributions are in good agreement with the other experimental data and the quantum chemical evaluation reported in the following.

3.1. Computational results

3.1.1. First protonation and second protonation

Literature reports that formation of both nHFQ (protonation of O11 oxygen) and zHFQ (protonation of N4′ nitrogen, zHFQ—N4′) species (Scheme S2a, Scheme S2 shows all tautomeric forms studied in this work) occur, following the first protonation in Equation (1), and that zHFQ—N4′ is the most stable tautomeric species for CFX in water (Ross and Riley, 1990; Takács-Novák et al., 1990; Rusu et al., 2012; Ross and Riley, 1992; Wallis et al., 1994; Hernàndez-Borrell and Montero, 1997; Park et al., 2000). The minimum energy structures of the possible protonated species in the first protonation step are shown in Fig. 10a (Fig. 10 shows all structures optimized in this work in water). Small structural changes occur on going from FQ^- to nHFQ, zHFQ—N4′ species and selected bond lengths and angles values are reported in Table S1. The calculated structure of CFX compounds in zHFQ—N4′ is in good agreement with the experimental ones (Turel et al., 1997) (Table S2).

Calculations in gas phase show that the nHFQ is more stable than zHFQ—N4′, being $\Delta G = 90.9$ kcal mol^{-1} ($\Delta G = G_{zHFQ-N4'} - G_{nHFQ}$) and the trend in stability does not change introducing the implicit water ($\Delta G = 24.7$ kcal mol^{-1}). This result is in agreement with other computational works (Musa and Eriksson, 2009; Vitorino et al., 2006) but in contrast with the experimental data (Ross and Riley, 1990; Takács-Novák et al., 1990; Rusu et al., 2012; Ross and Riley, 1992; Wallis et al., 1994; Hernàndez-Borrell and Montero, 1997; Park et al., 2000) reported in the literature. Therefore, the effect of the presence of explicit water molecules solvating the ionisable groups was considered. Water molecules were introduced to obtain a cluster composed by CFX and 10 water molecules. The number of water molecules added to CFX was calculated based on the average number of waters solvating the MD simulations (see Computational Details). The obtained cluster was then optimized in PCM water to produce stable final structures (Fig. 11).

With this last approach, zHFQ—N4′ species is found to be slightly more stable than the nHFQ form ($\Delta G = -2.1$ kcal mol^{-1}) in good agreement with experimental literature (Ross and Riley, 1990; Takács-Novák et al., 1990; Rusu et al., 2012; Ross and Riley, 1992; Wallis et al., 1994; Hernàndez-Borrell and Montero, 1997; Park et al., 2000).

Table 3
Cluster formation Energy (kcal mol^{-1}).

	ΔE
$10H_2O \rightarrow$ Cluster10w (nHFQ)	−18.6
$10H_2O \rightarrow$ Cluster10w (zHFQ—N4′)	−14.4
nHFQ + cluster10w → cluster10w-nHFQ	−31.7
zHFQ—N4′ + cluster10w → cluster10w-zHFQ—N4′	−66.7

Table 4
Relative stability (ΔG in kcal mol^{-1}) of the different zHFQ forms in gas-phase and PCM water.

	Gas-phase	Water
zHFQ isomers		
zHFQ—N4′ → zHFQ—N1	−6.8	34.8
zHFQ—N4′ → zHFQ—N1′	−11.2	9.3
H_2FQ^+ isomers		
H_2FQ^+—O11 → H_2FQ^+—N1	92.4	59.9
H_2FQ^+—O11 → H_2FQ^+—N1′	119.8	45.4

The stabilization of the zHFQ—N4′ species could be related to the energy contribution of hydrogen bonds. To clarify this point, the cluster formation energies for the water cluster in absence of CFX, ($\Delta E = E_{cluster10w} - E_{10w}$), and in presence of CFX ($\Delta X = X_{cluser10w\text{-}HFQ} - X_{cluster10w+HFQ}$) have been for nHFQ and zHFQ—N4′ are reported in Table 3.

The results show that the ΔE without CFX, is negative in both cases, but the ΔE of the nHFQ is about 4 kcal mol^{-1} lower than the zHFQ—N4′. When CFX is present ΔE is much more negative for zHFQ—N4′ than for nHFQ form (35 kcalmol^{-1}). When the clusters shown in Fig. 11 have been optimized using methanol as implicit solvent the computed free energies show that zHFQ—N4′ is slightly more stable than nHFQ ($\Delta G = -1.6$ kcal mol^{-1}). Other possible zHFQ form (Scheme S2b) could be present as the protonation can take place at N1 (zHFQ—N1), N1′ (zHFQ—N1′) or at O4 (zHFQ—O4). The optimized geometries of these species in implicit water are shown in Fig. 10b. When zHFQ—O4 (proton placed in O4 in the starting structure) geometry is optimized a transfer of the proton occurs from O4 to O11 and the nHFQ species is obtained. Small structural changes occur on going from zHFQ—N4′ to zHFQ—N1 and zHFQ—N1′, selected bond lengths and angles values are reported in Table S3.

The relative stability of the forms in Fig. 10b is summarized in Table 4a. The ΔG values were calculated as difference between the zHFQ—N4′ (taken as reference) and other zHFQ forms ($\Delta G = G_{zHFQ\text{-}n} - G_{zHFQ-N4'}$ where zFHQ-n is zHFQ—N1, N1′).

The results show that in gas phase both zHFQ—N1 and zHFQ—N1′ forms are more stable than the zHFQ—N4′ form, with zHFQ—N1′ the most stable species. The introduction of implicit water again leads to an inversion of this trend and the most stable species is now zHFQ—N4′ isomer in agreement with experimental data (Ross and Riley, 1990; Rusu et al., 2012; Ross and Riley, 1992; Wallis et al., 1994; Hernàndez-Borrell and Montero, 1997; Park et al., 2000).

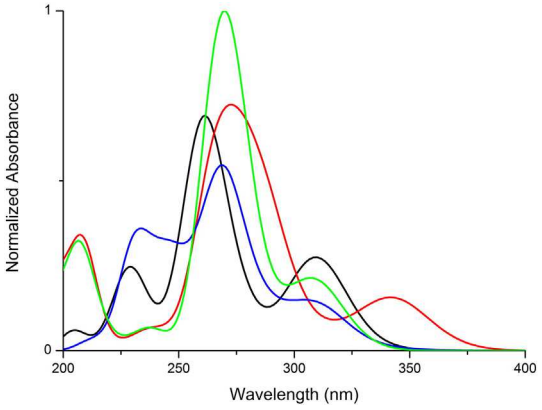

Fig. 12. Computed UV-vis spectra in implicit water of FQ^- (black line), nHFQ (red line), zHFQ—N4′ (blue line) and H_2FQ^+—O11 (green line) species. (For interpretation of the references to color in this figure legend, the reader is referred to the web version of this article.)

Table 5
Relative stability (ΔG in kcal mol^{-1}) of the different H_3FQ^{2+} forms in gas-phase and in PCM water.

Form	Gas-phase	Water
H_3FQ^{2+}—O4 → H_3FQ^{2+}—N1	39.5	33.2
H_3FQ^{2+}—O4 → H_3FQ^{2+}—N1′	41.0	3.7

For the second protonation reaction, the experimental data (Ross and Riley, 1990; Takács-Novák et al., 1990; Rusu et al., 2012; Ross and Riley, 1992; Wallis et al., 1994; Hernàndez-Borrell and Montero, 1997; Park et al., 2000) suggest that there is the formation of the H_2FQ^+ species (protonation of O11, oxygen, H_2FQ^+—O11) reported in Scheme S2c, but also other protonated species could form (Scheme S2d). The minimum energy structures in water are displayed in Fig. 10c, while selected bond lengths and angles values are reported in Table S4 for optimized structures. The calculated structures of the CFX isomers are again in excellent agreement with the available X-ray (Turel et al., 1997) experimental data (Table S5).

The relative stability of these forms are summarized in Table 4b. The ΔG values were calculated as difference between the H_2FQ^+—O11 (taken as reference) and the other H_2FQ^+ forms ($\Delta G = G_{H2FQ^+\text{-n}} - G_{H2FQ^+\text{—O11}}$ where H_2FQ^+-n is H_2FQ^+—N1,N1′,O4).

The results in gas-phase and water show that the H_2FQ^+—O11 is always much more stable than the other possible form, in agreement with the literature data (Ross and Riley, 1990; Takács-Novák et al., 1990; Rusu et al., 2012; Wallis et al., 1994; Hernàndez-Borrell and Montero, 1997; Park et al., 2000).

In summary, for the first protonation it has been observed that the zHFQ is slightly more stable than the nHFQ protonated in N4′. The introduction of methanol as a solvent, leads to a slight decrease in the ΔG with respect to those calculated in water. Furthermore, the zHFQ—N4′ is the most stable species compared to all other possible tautomeric zHFQ forms. The most stable form relative to the second protonation step results to be H_2FQ^+—O11.

4. UV-vis spectra

The UV–vis spectra were simulated to have a comparison with the experimental ones. Calculated absorption spectra are shown in Fig. 12.

The main absorption peak of these species is located in the UV region of the spectrum at 260–280 nm and all species display weaker absorption in the 300–400 nm range. These findings are in good agreement with experimental spectra (Fig. 1) and with previous computational works available for NOR (Musa and Eriksson, 2009).

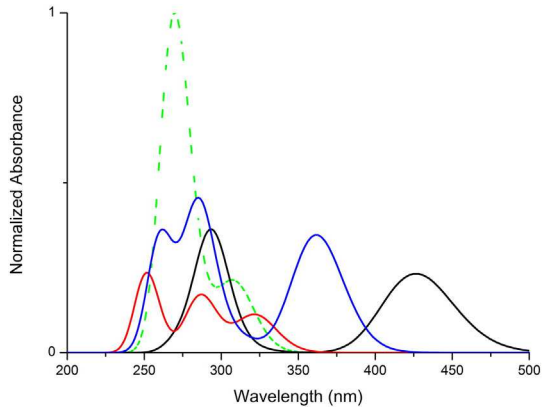

Fig. 13. Computed UV-vis spectra in PCM water of H_3FQ^{2+}—N1 (black line), H_3FQ^{2+}—N1′ (red line), H_3FQ^{2+}—O4 (blue line), H_2FQ^+—O11 (dotted green line) forms. (For interpretation of the references to color in this figure legend, the reader is referred to the web version of this article.)

The larger changes in experimental spectra with decreasing pH correspond to the increase of the intensity of the main peak at around 280 nm accompanied by its shift to higher wavelengths, and the decrease of the intensity of the bands between 320 and 360 nm. To understand the effect of the protonation site on the absorption spectra, the relevant frontier molecular orbitals, which play a dominant role in electronic transitions of FQs, have been reported in Fig. S1 and the main transitions are reported in Table S6. It is interesting to note that the bands at higher wavelength, which corresponds to the HOMO → LUMO excitation is useful to distinguish the zHFQ ($\lambda = 310$ nm) from the nHFQ ($\lambda = 342$ nm). This can be explained by observing that the HOMO of the nHFQ orbital it is localized in the piperazine and quinolone ring, while for zHFQ is located in the carboxyl group (Fig. S1).

With the first protonation step ($FQ^- \rightarrow$ nHFQ + zHFQ—N4′) a shift of the main maximum towards higher wavelengths is observed (+15 nm in the case of nHFQ, +8 nm for zHFQ—N4′ and H_2FQ^+—O11) in agreement with the experimental trend. According to Fig. 12, an absorption peak relative to nHFQ should appear in the high wavelength range by lowering the pH. On the contrary, in the experimental titration (Fig. 2) only a weak shoulder appears in the 360–400 nm range: therefore, it can be proposed that nHFQ species is formed only in small amounts. The formation of a small shoulder in the low wavelength range (~210 nm, Fig. 2) is compatible with the formation of the H_2FQ^+—O11 species (green line in Fig. 12).

5. Third protonation

The experimental data show that H_3FQ^{2+} species can be only formed in extremely acidic conditions. In this case, however, the literature is ambiguous, indicating that this last protonation could take place or in N1′ nitrogen of piperazine ring (H_3FQ^{2+}—N1′) (Rusu et al., 2012; Lin et al., 2004) or in carbonyl oxygen (H_3FQ^{2+}—O4) (Gerasimenko et al., 2008; Polishchuk et al., 2008). The DFT study was extended also to these last species, taking into account also the additional H_3FQ^{2+}—N1 form (Scheme S2e). The optimized structures of the different isomers are displayed in Figs. 10d (some structural parameters reported in Table S7). In Table S8, the more significant calculated atomic distances of H_3FQ^{2+}—O4 are inserted together with the available experimental data (Gerasimenko et al., 2008). The ΔG values were calculated as difference between the H_3FQ^{2+}—O4 (taken as reference) and other H_3FQ^{2+} forms ($\Delta G = G_{H3FQ2^+\text{-n}} - G_{H3FQ2^+\text{—O4}}$ where H_2FQ^{2+}-n is H_3FQ^{2+}—N1 and N1′).

The results shows that the H_3FQ^{2+}—O4 form is the most stable isomer both in gas phase and in water (Table 5). However, the introduction of the implicit solvent leads to a drastic reduction of the energy differences between H_3FQ^{2+}—O4 and H_3FQ^{2+}—N1′.

The electronic spectra of the various H_3FQ^{2+} forms have been calculated and are shown in Fig. 13. The main absorption maxima wavelengths, orbitals involved, relative percentage contribution and the oscillator strength are reported in Table S9. The molecular orbitals involved in the electronic transitions are shown in Fig. S2.

The main experimental absorption peak of these species is located in the 250–290 nm spectral range. The major variations in experimental spectra, passing from the H_2FQ^+ to the H_3FQ^{2+} species (decreasing the pH) is the appearance of the band at 360–400 nm accompanied by a decrease of intensity of the other bands (Fig. 2). The computed spectrum that best reproduces this trend seems to be the H_3FQ^{2+}—O4 form (Fig. 13, Table S9). In conclusion, by the relative stability data, of the various forms of H_3FQ^{2+}, and the computed UV-vis spectra, we can propose that the most probable species formed at very low pH is H_3FQ^{2+}—O4.

6. Conclusion

The protonation sequence of four different fluoroquinolones has been fully evaluated with the aid of different complementary techniques. In

particular, the experimental observations necessary to discriminate between a protonation scheme represented by macro-constants alone, and one that requires the introduction of a micro-protonation scheme, are clearly delineated based on careful analysis of experimental and simulated data. This should overcome the contrasting literature evaluations of the existence of tautomeric forms of mono-protonated species (neutral form or zwitterion), described by a set of protonation micro-constants.

The comparison of the trend of spectral data as a function of pH of CFX in water and in water-methanol solution allows ascertaining in an unequivocal way the existence of a micro-protonation equilibrium in the mixture, whereas no micro-protonation scheme must be introduced in water. The trend of NMR spectra as a function of pH in water substantiates the formation of the zHFQ species alone in the first protonation step.

DFT calculations carried out for CFX indicate the predominance of the zNHFQ—N4′ form in water solution, and this is confirmed also by comparing the calculated and experimental absorption spectra. A slight decrease of relative stability of the zHFQ—N4′ species with respect to the nHFQ was observed by passing from water to methanol as implicit solvent, due to the lower polarity of the last solvent.

Theoretical stabilities and electronic spectra suggest that O11 and O4 should be protonated in the H_2FQ^+ and H_3FQ^{2+} species respectively.

As a concluding comment, we have remarked the existence of the zwitterionic species alone at physiological pH in water, and an increase of the neutral species with the lipophilicity of the medium. This property will surely affect the bioavailability of FQs, causing an increase of the neutral species when the molecules approach the local lipophilic environment close to the cellular membranes.

Appendix A. Supplementary data

Supplementary data to this article can be found online at http://dx.doi.org/10.1016/j.ejps.2016.08.053.

References

Albert, A., Serjeant, E., 1984. The Determination of Ionization Constants. Springer.
Alner, D., Greczek, J., Smeeth, A., 1967. J. Chem. Soc. A 1205–1211.
Aragoni, M.C., Arca, M., Crisponi, G., Nurchi, V.M., 1995. Anal. Chim. Acta 316, 195–204.
Barbosa, J., Bergés, R., Sanz-Nebot, V., 1998. J. Chromatogr. A 823, 411–422.
Becke, A.D., 1993. J. Chem. Phys. 98, 1372–1377.
Comuzzi, C., Melchior, A., Polese, P., Portanova, R., Tolazzi, M., 2003. Inorg. Chim. Acta 355, 57–63.
Crisponi, G., Caredda, A., Cristiani, F., Diaz, A., Nurchi, V.M., Pinna, R., Pivetta, T., Silvagni, R., 2004. Ann. Chim. 94, 147–153.
Del Piero, S., Di Bernardo, P., Fedele, R., Melchior, A., Polese, P., Tolazzi, M., 2006. Eur. J. Inorg. Chem. 2006, 3738–3745.
Edsall, J.T., Blanchard, M.H., 1933. J. Am. Chem. Soc. 55, 2337–2353.
Edsall, J.T., Martin, R.B., Hollingworth, B.R., 1958. Proc. Natl. Acad. Sci. 44, 505–518.
Emmerson, A., Jones, A., 2003. J. Antimicrob. Chemother. 51, 13–20.
Endrizzi, F., Melchior, A., Tolazzi, M., Rao, L., 2015. Dalton Trans. 44, 13835–13844.
Fan, J.Y., Sun, D., Yu, H., Kerwin, S.M., Hurley, L.H., 1995. J. Med. Chem. 38, 408–424.
Fries, P.H., Imbert, D., Melchior, A., 2010. J. Chem. Phys. 132, 044502.
M.J.T. Frisch, G. W.; Schlegel, H. B.; Scuseria, G. E.; Robb, M. A.; Cheeseman, J. R.; Scalmani, G.; Barone, V.; Mennucci, B.; Petersson, G. A.; Nakatsuji, H.; Caricato, M.; Li, X.; Hratchian, H. P.; Izmaylov, A. F.; Bloino, J.; Zheng, G.; Sonnenberg, J. L.; Hada, M.; Ehara, M.; Toyota, K.; Fukuda, R.; Hasegawa, J.; Ishida, M.; Nakajima, T.; Honda, Y.; Kitao, O.; Nakai, H.; Vreven, T.; Montgomery, J. A., Jr.; Peralta, J. E.; Ogliaro, F.; Bearpark, M.; Heyd, J. J.; Brothers, E.; Kudin, K. N.; Staroverov, V. N.; Kobayashi, R.; Normand, J.; Raghavachari, K.; Rendell, A.; Burant, J. C.; Iyengar, S. S.; Tomasi, J.; Cossi, M.; Rega, N.; Millam, J. M.; Klene, M.; Knox, J. E.; Cross, J. B.; Bakken, V.; Adamo, C.; Jaramillo, J.; Gomperts, R.; Stratmann, R. E.; Yazyev, O.; Austin, A. J.; Cammi, R.; Pomelli, C.; Ochterski, J. W.; Martin, R. L.; Morokuma, K.; Zakrzewski, V. G.; Voth, G. A.; Salvador, P.; Dannenberg, J. J.; Dapprich, S.; Daniels, A. D.; Farkas, Ö.; Foresman, J. B.; Ortiz, J. V.; Cioslowski, J.; Fox, D. J., Wallingford, C. T., (2009).
Gerasimenko, A., Karaseva, E., Polishchuk, A., 2008. Acta Crystallogr. Sect. E: Struct. Rep. Online 64, m378.
Gran, G., 1952. Analyst 77, 661–671.
Hammett, L.P., Deyrup, A.J., 1932. J. Am. Chem. Soc. 54, 2721–2739.
Hernàndez-Borrell, J., Montero, M.T., 1997. J. Chem. Educ. 74, 1311.
http://www.hyperquad.co.uk/HQ2013.htm.
Lambert, A., Regnouf-de-Vains, J.B., Ruiz-López, M.F., 2007. Chem. Phys. Lett. 442, 281–284.
Lee, C., Yang, W., Parr, R.G., 1988. Phys. Rev. B 37, 785.
Lin, C.E., Deng, Y.J., Liao, W.S., Sun, S.W., Lin, W.Y., Chen, C.C., 2004. J. Chromatogr. A 1051, 283–290.
Melchior, A., Peressini, S., Portanova, R., Sangregorio, C., Tavagnacco, C., Tolazzi, M., 2004. Inorg. Chim. Acta 357, 3473–3482.
Melchior, A., Peralta, E., Valiente, M., Tavagnacco, C., Endrizzi, F., Tolazzi, M., 2013. Dalton Trans. 42, 6074–6082.
Mendonça, A.C., Martins, A.F., Melchior, A., Marques, S.M., Chaves, S., Villette, S., Petoud, S., Zanonato, P.L., Tolazzi, M., Bonnet, C.S., 2013. Dalton Trans. 42, 6046–6057.
Musa, K.A., Eriksson, L.A., 2009. J. Phys. Chem. A 113, 10803–10810.
Nurchi, V.M., Lachowicz, J.I., Crisponi, G., Murgia, S., Arca, M., Pintus, A., Gans, P., Niclos-Gutierrez, J., Domínguez-Martín, A., Castineiras, A., Remelli, M., Szewczuk, Z., Lis, T., 2011. Dalton Trans. 40, 5984–5998.
Nurchi, V.M., Crisponi, G., Crespo-Alonso, M., Lachowicz, J.I., Szewczuk, Z., Cooper, G.J., 2013. Dalton Trans. 42, 6161–6170.
Park, H.R., Chung, K.Y., Lee, H.C., Lee, J.K., Bark, K.M., 2000. Bull. Kor. Chem. Soc. 21, 849–854.
Park, H.R., Kim, T.H., Bark, K.M., 2002. Eur. J. Med. Chem. 37, 443–460.
Paul, M., Long, F., 1957. Chem. Rev. 57, 1–45.
Peana, M., Medici, S., Nurchi, V.M., Crisponi, G., Zoroddu, M.A., 2013. Coord. Chem. Rev. 257, 2737–2751.
Polishchuk, A., Gerasimenko, A., Gayvoronskaya, K., Karaseva, E., 2008. Acta Crystallogr. Sect. E: Struct. Rep. Online 64, m931–m932.
Ross, D.L., Riley, C.M., 1990. Int. J. Pharm. 63, 237–250.
Ross, D.L., Riley, C.M., 1992. Int. J. Pharm. 83, 267–272.
Rusu, A., Tóth, G., Szőcs, L., Kökösi, J., Kraszni, M., Gyéresi, Á., Noszál, B., 2012. J. Pharm. Biomed. Anal. 66, 50–57.
Scalmani, G., Frisch, M.J., Mennucci, B., Tomasi, J., Cammi, R., Barone, V., 2006. J. Chem. Phys. 124, 094107.
Schmid, N., Eichenberger, A.P., Choutko, A., Riniker, S., Winger, M., Mark, A.E., van Gunsteren, W.F., 2011. Eur. Biophys. J. 40, 843–856.
Takács-Novák, K., Noszál, B., Hermecz, I., Keresztúri, G., Podányi, B., Szász, G., 1990. J. Pharm. Sci. 79, 1023–1028.
Tomasi, J., Mennucci, B., Cammi, R., 2005. Chem. Rev. 105, 2999–3094.
Turel, I., Bukovec, P., Quirós, M., 1997. Int. J. Pharm. 152, 59–65.
Vitorino, G.P., Barrera, G.D., Mazzieri, M.R., Binning, R., Bacelo, D.E., 2006. Chem. Phys. Lett. 432, 538–544.
Wallis, S.C., Gahan, L.R., Charles, B.G., Hambley, T.W., 1994. Aust. J. Chem. 47, 799–806.
Zoroddu, M.A., Peana, M., Medici, S., 2007. Dalton Trans. 379–384.
Zoroddu, M.A., Kowalik-Jankowska, T., Medici, S., Peana, M., Kozlowski, H., 2008. Dalton Trans. 6127–6134.
Zoroddu, M.A., Peana, M., Medici, S., Anedda, R., 2009. Dalton Trans. 5523–5534.
Zoroddu, M.A., Medici, S., Peana, M., Anedda, R., 2010. Dalton Trans. 39, 1282–1294.
Zoroddu, M.A., Peana, M., Medici, S., Potocki, S., Kozlowski, H., 2014. Dalton Trans. 43, 2764–2771.
摇Hess, J.C., 2008. Theory Comput 4, 435–437.